DEVELOPMENT OF MICRO/NANO-SCALE SENSORS FOR INVESTIGATION OF HEAT TRANSFER IN MULTI-PHASE FLOWS

A Dissertation

by

SAE IL JEON

Submitted to the Office of Graduate Studies of
Texas A&M University
in partial fulfillment of the requirements for the degree of

DOCTOR OF PHILOSOPHY

August 2011

Major Subject: Mechanical Engineering

Development of Micro/Nano-Scale Sensors for Investigation of Heat Transfer in
Multi-Phase Flows

DEVELOPMENT OF MICRO/NANO-SCALE SENSORS FOR INVESTIGATION OF HEAT TRANSFER IN MULTI-PHASE FLOWS

A Dissertation

by

SAE IL JEON

Submitted to the Office of Graduate Studies of
Texas A&M University
in partial fulfillment of the requirements for the degree of

DOCTOR OF PHILOSOPHY

Approved by:

Chair of Committee,	Debjyoti Banerjee
Committee Members,	Nicole S. Zacharia
	Eric L. Petersen
	Frederick J. Strieter
Head of Department,	Dennis O'Neal

August 2011

Major Subject: Mechanical Engineering

ABSTRACT

Development of Micro/nano-scale Sensors for Investigation of Heat Transfer in Multi-Phase Flows. (August 2011)

Sae Il Jeon, B.E., Korea Aerospace University;
M.S., Seoul National University

Chair of Advisory Committee: Dr. Debjyoti Banerjee

The objective of this investigation was to develop micro/nano-scale temperature sensors for measuring surface temperature transients in multi-phase flows and heat transfer. Surface temperature fluctuations were measured on substrates exposed to phase change processes. Prior reports in the literature indicate that these miniature scale surface temperature fluctuations can result in 60-90% of the total heat flux during phase change heat transfer.

In this study, DTS (Diode Temperature Sensors) were fabricated with a doping depth of ~100 nm on n-type silicon to measure the surface temperature transients on a substrate exposed to droplet impingement cooling. DTS are expected to have better sensor characteristics compared to TFTs (Thin Film Thermocouples), due to their small size and faster response (which comes at the expense of the smaller operating temperature range). Additional advantages of DTS include the availability of robust commercial micro fabrication processes (with diode and transistor node sizes currently in the size range of ~ 30 nm), and that only 2N wire leads can be used to interrogate a set of N x N array of sensors (in contrast thermocouples require 2 N x N wire leads for N x N sensor array).

The DTS array was fabricated using conventional semi-conductor processes. The temperature response of the TFT and DTS was also calibrated using NIST standards. Transient temperature response of the DTS was recorded using droplet impingement cooling experiments. The droplet impingement cooling experiments were performed for two different test fluids (acetone and ethanol). An infrared camera was used to verify the surface temperature of the substrate and compare these measurements with the temperature values recorded by individual DTS.

PVD (Physical Vapor Deposition) was used for obtaining the catalyst coatings for subsequent CNT synthesis using CVD (Chemical Vapor Deposition) as well as for fabricating the thin film thermocouple (TFT) arrays using the “lift-off” process. Flow boiling experiments were conducted for three different substrates. Flow boiling experiments on bare silicon wafer surface were treated as the control experiment, and the results were compared with that of CNT (Carbon Nano-Tube) coated silicon wafer surfaces. Similar experiments were also performed on a pure copper surface. In addition, experiments were performed using compact condensers. Micro-scale patterns fabricated on the refrigerant side of the compact heat exchanger were observed to cause significant enhancement of the condensation heat transfer coefficient.

DEDICATION

To my wife Bora, my sweet angels Ryeowon(Kate) & Ryeojin(Kaley) and beloved parents for their endless support.

ACKNOWLEDGEMENTS

I would like to thank my committee chair, Dr. Banerjee, and my committee members, Dr. Strieter, Dr. Petersen, and Dr. Zacharia, for their guidance and support throughout the course of this research.

Thanks also go to my friends and colleagues and the department faculty and staff for making my time at Texas A&M University a great experience. Finally, thanks to my mother and father for their encouragement and to my wife for her patience and love.

I would like to acknowledge the support of the Office of Naval Research (Thermal Management Program), Aspen Systems (Thermal Division) through the ONR SBIR (Small Business Innovative Research) Phase II Program and the Qatar National Research Foundation (QNRF). I also want to extend my gratitude to the National Instruments and Keithley, who provided me with the survey instruments and technical support throughout my research.

I would like to express special thanks to Tom Lovell (Aspen), who patiently advised me while I was performing the compact condenser experiments. Also, thanks to Dr. Bizrat and Dr. Young, who have showed me how to use a wide range of equipment in MCF. Finally, I would like to thank Microscopic Imaging Center (MIC) for the FE-SEM acquisition that was supported by the NSF grant DBI-0116835, through the Vice President (VP) for Research Office, and the Texas Engineering Experiment Station (TEES).

NOMENCLATURE

Greek Symbols

α	Thermal diffusivity of air $[m^2/s]$
β	Thermal expansion coefficient of air $[1/K]$
υ	Kinematic viscosity of air $[m^2/s]$
υ	Forward voltage [V]
ω	Relative uncertainty [%]
Δ	Difference

Roman Symbols

g	Gravity $[m/s^2]$
h	Heat Transfer Coefficient $[W/m^2 \cdot K]$
I	Current [A]
k	Thermal Conductivity $[W/m \cdot K]$
L	Wafer Thickness [cm]
Nu	Nusselt Number
q''	Heat Flux $[W/m^2]$
R	Resistance $[m^2 \cdot K/W]$
Ra	Rayleigh Number
T	Temperature [°C]
V	Voltage [V]

x	Position [m]
x	Vector (boldface) or its component

Subscripts

2P	Two Phase
air	Air
avg	Average
c	Contact
DTS	Diode Temperature Sensor
HP	Hot Plate
NC	Natural Convection
room	Room
s	Saturation
surf	Surface
T	Thermal
w	Wall

Other Symbols

∞	Bulk / Ambient
ϵ	Error of $\frac{\Delta \boldsymbol{\varepsilon}}{\boldsymbol{\varepsilon}}$

TABLE OF CONTENTS

CHAPTER Page

LIST OF FIGURES

Page

Page

Page

LIST OF TABLES

Page

CHAPTER I

INTRODUCTION

As we enter the era of nanotechnology, a primary challenge is to cool these novel devices in industries which include transportation, microelectronics, solid-state lighting and manufacturing. Smaller chips and faster performance (microprocessor speed or clock frequency) in the electronic industry and optical devices with higher power ratings are producing devices / platforms with higher thermal loads which cannot subsist on conventional fin-fan cooling. Thermal loads as high as 100-1000 W/cm^2 have been reported for various electronic chips [1] and the current methods of cooling (which mostly use single phase convective heat transfer air/liquid cooling) have reached their limits and failed to meet these high levels of cooling loads. Consequently a resurrected interest in multi-phase flows (boiling and condensation heat transfer) has occurred in the past decade due to the high fluxes that can be achieved in cooling systems that utilize phase change phenomena.

A. Review of Boiling on Micro / Nano Surfaces

Both pool and flow boiling are very effective in delivering high heat fluxes with a small temperature difference between the heated surface and the cooling fluid. Boiling is a highly non-linear phenomenon where the underlying mechanisms for transport

---

This dissertation follows the style of Journal of Heat Transfer.

processes are intricately coupled. For a given working fluid, the variables affecting the boiling heat flux include wall superheat, nucleation site density, bubble diameter, bubble departure frequency, contact angle, heater orientation etc. [2]. Higher heat fluxes are obtained in boiling (than that of natural or forced convection) due to mass transfer associated with latent heat transfer, sensible heat transfer as well as periodic transient conduction by direct liquid-solid contact and “micro-layer” effects. While nucleating and departing from the surface, the bubbles absorb large amounts of thermal energy through phase change phenomena and also promote circulation of colder bulk fluid to the heater surface resulting in an increase in the overall convective heat transfer.

A vast body of correlations has been reported in the literature for predicting the various experimental parameters, such as heat flux, bubble departure diameter and bubble departure frequency. However, the intricate nature of the non-linear coupling of the experimental parameters (and thermo-physical properties) as well as large variability in the experimental data has created the need for development of more intricate metrology platforms as well as more sophisticated and comprehensive correlations that are based on the fundamental transport mechanisms (including at the micro/nano-scales).

Jensen and Memmel [3] compared twelve correlations from the current literature for estimating bubble departure diameter and concluded that Kutateladze and Gogonin [4] had the best-fitting correlation with an average absolute deviation (AAD) of 45.4%. Thus, it is obvious that we are still in need of a comprehensive correlation for predicting bubble departure diameter and frequency. Besides this, recently invented techniques to fabricate engineered micro/nano-scale surfaces have put forth new challenges in front of existing models. Miller et al. [5] tested hexagonal dimples on a silicon chip using FC-72 as the working fluid. Phadke et al [6] tested reentrant cavities on a vertical silicon chip with R-113. O’Connor et al [7] investigated sprayed aluminum particles and painted diamond particles on an aluminum foil and silicon chip in FC-72. Chang and You [8] studied painted diamond particles on a copper chip in FC-72. Honda et al [9] tested pin fins with submicron-scale roughness on a silicon chip in FC-72.

Also, boiling on surfaces coated with carbon nanotubes, which possess high thermal conductivity and mechanical strength, has shown significant enhancement in boiling heat transfer coefficient and critical heat flux (CHF) along with a decrease in boiling incipience superheat [10-12]. Furthermore, low density (compared to metals) and high specific heat capacity values (similar to graphite) make carbon nanotubes (CNT) suitable candidates for surface texturing with the intent of enhancing heat transfer in multi-phase flows. Therefore, in this study various aspects of heat transfer in multi-phase flows have been investigated. The aim of this study is to extend the boundaries of scientific research by investigation of transport phenomena during phase change at smaller spatial scales (with a concomitant ability to gather data at higher frequencies for the transport processes). Hence, the scope of this study is focused on the investigation of coupled thermal-hydraulic transport phenomena during phase change heat transfer on micro/nano-structured surfaces, through the development and testing of high density – high speed micro/ nano-sensors, and the development of high speed digital flow visualization techniques.

In the following sections, literature studies have been performed and reported. The literature study has been classified into four different types of engineered surfaces, which include: (1) Micro-finned surfaces, (2) Micro-porous structures, (3) CNT coated surfaces and (4) Other nano-structured surfaces.

(1) Micro-finned surfaces

Micro-pin-fins were fabricated on a silicon chip by a dry etching process with the dimension of $50 \times 50 \times 60$ µm^3 (width × thickness × height) [9]. The effect of the micro-pin-fins on pool boiling with different geometries and dimensions were also studied by other authors [13]. Square micro-pin-finned chip with an inline array of 10, 20, 30 and 50 µm thick (and 60 µm in height) were used in these studies. Distances between the fins were identical to the fin thickness [9]. O'Connor et al. [7] prepared an aluminum foil coated with diamond. Anderson and Mudawar [14] used a vapor-blasted copper chip with 0.305 mm thick and 0.506 mm high square pins. Oktay [15] tested a dendritic heat sink with 1 mm high brush-like structure on a silicon chip. Table 1.1 summarizes the previous studies on boiling heat transfer enhancement using micro-fin structures.

(2) Micro-porous structures

As an alternative technique for enhancing boiling heat transfer, micro-porous coatings have been investigated by various researchers. The effect of micro-porous coating itself and the various parameters that affect boiling performance are discussed next. O'Connor and You [7] introduced a painting technique where 1.5 g of silver flakes of 3 -10 µm size were used to prepare the surface of the heater. An aluminum foil surface was used as the control experiment for comparison purposes. The thickness of the paint was under 25 μm and the working fluid was FC-75. The boiling incipience was drastically reduced from ~20 - 27 °C (on the reference surface) to ~3 - 8.5 °C (on micro-porous coated surfaces). Furthermore, the critical heat flux (CHF) was enhanced by more than 100% from 14.3 W/cm^2 for the reference surface to 30 W/cm^2 for the enhanced surface.

Table 1. 1 Literature review for boiling on micro-finned surfaces.

Author	*Material & Heater Type*	*Fluid*	*Result*
Honda et al. (2002)	Silicon Chip	FC-72	Effect of micro-pin fin dimensions, and sub-cooling on CHF
Honda and Wei (2004)	N/A N/A	N/A	Effect of surface microstructures on CHF (Review paper)
Miller (1990)	Silicon Chip	FC-72	Effect of hexagonal dimples on incipient superheat and temperature overshoot
Wei et al. (2009)	Silicon Chip	FC-72	Effect of micro-pin finned surface, and with sub-cooling in flow boiling on CHF
Wei and Honda (2002)	Silicon Chip	FC-72	Effect of height and thickness of square micro-pin fin on CHF
Wei et al. (2005)	Silicon Chip	FC-72	Effect of micro-pin fins on CHF
Guglielmini (1996)	Finned Copper Flat	Gladen Ht-55	Effect of non-boiling waiting period, pressure and spine dimensions on boiling behavior

The heat flux was also enhanced significantly in the nucleate boiling regime. The bubble diameter at departure was also reduced significantly on the micro-porous surface in the nucleate boiling regime. Larger bubbles were formed on the reference surface whereas tinier bubbles were observed to form on the painted surface. This is due to early nucleation (boiling inception) on the painted surface. The authors obtained the difference in bubble diameters by analytical calculations using the given pressure and superheat conditions for their experiment.

Alumina particles were coated to enhance the boiling heat transfer in other studies [8,16,17]. Chang and You applied this surface treatment technique and investigated the effects of fin length on boiling characteristics focusing on the critical heat flux [8]. In their study, the performance of the pinned surface was compared with a machined surface for comparison. Rainey and You coated heater surfaces using “ABM method” [17]. They named the ABM coating from the initial letters of its three components: Aluminum particles/Devcon Brushable Ceramic epoxy/Methyl-Ethyl-Keytone (M.E.K.). Three components were mixed and sprayed over the heater surfaces. In this study, aluminum particles with a size range of 1 to 20 μm were used and the total thickness of this coating was about 50 μm. The authors reported that the plain and roughened surfaces were placed between the micro-porous and the highly polished surfaces. The results from these experiments showed that the roughness of a surface was not the dominant parameter that affected the boiling performance in the nucleate boiling regime and the critical heat flux (CHF). The authors concluded that the enhancement of the nucleation site density due to the increased volume of entrapped gasses in the porous surface resulted in enhancement in pool boiling heat transfer. The effects of micro-porous coating on boiling heat transfer were also studied using wire shaped heaters [17, 18]. Micro-porous coating was applied on a platinum wire using DOM method. DOM coating was named from the three components of the coating: (1) synthetic Diamond particles (8-12 μm); (2) Omegabond 101 epoxy binder; and (3) Methyl-ethyl-keytone carrier. The effect of the micro-porous coating on a wire heater were even more pronounced that of the horizontal plate heaters. A significant increase in the critical heat flux was reported in this study. Experimental investigations for boiling heat transfer enhancement on a heater with micro-porous coatings were also reported by Kim et al. [19]. The authors summarized from their experimental results that the microporous coatings: (1) enhanced the active nucleation site density; (2) reduced bubble departure diameters; and (3) enhanced the bubble departure frequency. However, at higher heat fluxes, the transient conduction from the heater surface to the superheated liquid layer enhanced the boiling heat transfer. The enhancement of this micro convection transport processes delayed the onset of the critical heat flux by increasing the hydrodynamic stability of the vapor leaving the surface. Other reports in the literature on the micro-porous coatings are summarized in Table 1-2.

(3) CNT coated surfaces

In this section, reports in the literature involving boiling on CNT coated surfaces are discussed [10, 12, 13, 20]. The effect of coating silicon and copper substrates with CNT was reported [20]. Different CNT array densities and area coverages were tested on $1.27 \times 1.27\ mm^2$ silicon and copper samples in FC-72. The density of the light CNT array is estimated to be 30 CNTs/μm^2 and a dense CNT array had twice the density which is 60 CNTs/μm^2. ‘Grid-’ and ‘Island-‘ patterned surfaces were used to differentiate the area coverage using the CNT coated surfaces. The dense array shows a noticeable decrease in

Table 1. 2 Literature review of micro-porous surfaces (Note: NB denotes nucleate boiling and SH denotes superheat.)

Author	*Material & Heater Type*	*Fluid*	*Result*
You et al. (1990)	Si, $SiO_2Al_2O_3$ Cylinder	FC-72 R-113	Effect of liquids on the wall SH at the incipience and surface materials on the surface energy.
O’Connor and You (1995)	Alumina, Diamond Rect.Flat plate	FC-72	85 % reduction in incipient SH 70 % to 80 % decrease in NB SH 100% increase in critical heat flux
Chang and You (1997-a)	Diamond Square Flat Plate	FC-72	Classifying ‘micro-porous’ and ‘porous’ coating. The most enhanced CHF in the largest particle size. The smallest incipient SH at the smallest particle coating.
Chang and You (1997-b)	ABM, CBM Square Flat Plate	FC-72	80 - 90 % reduction of incipience SH 30 % enhancement of the NB heat transfer coefficient. Comparing two different coating methods.
Rainey and You (2000)	ABM Pin Finned Plate	FC-72	Comparing micro-porous surfaces and roughened surfaces. Effect of fin length on boiling heat transfer characteristics. More than 100 % enhanced heat transfer coefficient by micro-porous coating on the finned surfaces.
Rainey and You (2001)	DOM Square Plate	FC-72	Effect of heater inclination on the CHF and nucleate boiling (Decreased CHF as increased inclination of heater). Heater size effect (No significant effect on both CHF and nucleate boiling region).
Kim et al. (2002)	DOM Wire	FC-72	Confirmation of the similar effect of micro-porous coating. 130% enhancement in CHF and 600% enhancement in NB region.

the boiling incipience superheat as well as a shift of the entire nucleate boiling region towards lower wall superheats (to the left in the boiling curve) [21]. Thome reported that nucleate boiling heat transfer can be enhanced by increasing nucleation site density (per unit area) [22]. However, the CHF value for the light array revealed boiling superior performance compared to that of the dense array. The general perception in the boiling literature is that CHF enhancement is commonly achieved by increasing boiling surface area using various kinds of fin shapes and sizes [20]. However, it appears that the dense array provides less accessible surface area compared to the lightly packed array. This may partially explain the inferior CHF value on the densely packed CNT coated surface. A study from Reed and Mudawar [23] showed that the CNT mesh provides reservoir-type cavities that are ripe for nucleation with minimal superheat. Also, the high thermal conductivity of CNTs is believed to aid the boiling process augmentation by the enhanced surface area, thus facilitating the reduction of resistance to conduction heat transfer [24-26]. In addition, the grid patterned CNT coated surface did not show heat transfer enhancement compared to the lightly coated CNT surface. Hence, the authors concluded that the macro-scale attempts to manipulate the CNT area coverage and layout are ineffective in enhancing CHF.

Another study on CNT coated surfaces was reported by Ahn et al. [10]. In this study the height of the CNT coating on the substrate was controlled. Two types of CNT coated surfaces were introduced, which where Type-A (for a CNT height of 9 μm) and Type-B (for a CNT height of 25 μm), where the CNT diameter ranged from 8-16 nm (i.e., these were multi-walled CNT). The working fluid for this study was PF-5060 (which is a dielectric refrigerant, and is a commercial version of FC-72). The experiments were conducted in the nucleate boiling regime as well as in the film boiling regime. Boiling heat transfer enhancement was observed in nucleate boiling regime, which is consistent with the result from Ujereh et al. (2007) [20]. The height of the CNT did not seem to play a key role in the nucleate boiling regime. In contrast, the film boiling regime was strongly sensitive to the height of the CNT. The dynamic values of the minimum vapor film thickness in film boiling of PF-5060 were predicted to be less than 15 μm [27, 28]. As a result, if the surface micro/nano-structures are engineered to a height exceeding 15 μm, they can disrupt the vapor film leading to a possible collapse of the film boiling into a hybrid boiling phenomena representative of transition boiling (i.e., a significant part of the boiling surface is in the nucleate boiling regime). Thus, Type-B (with a CNT height of 25 μm) can augment the boiling heat transfer compared to that of the bare silicon wafer. The boiling heat flux for Type-A in film boiling was identical to that of bare silicon surfaces. Figure 1-1 schematically demonstrates the different disruption behavior of two different samples.

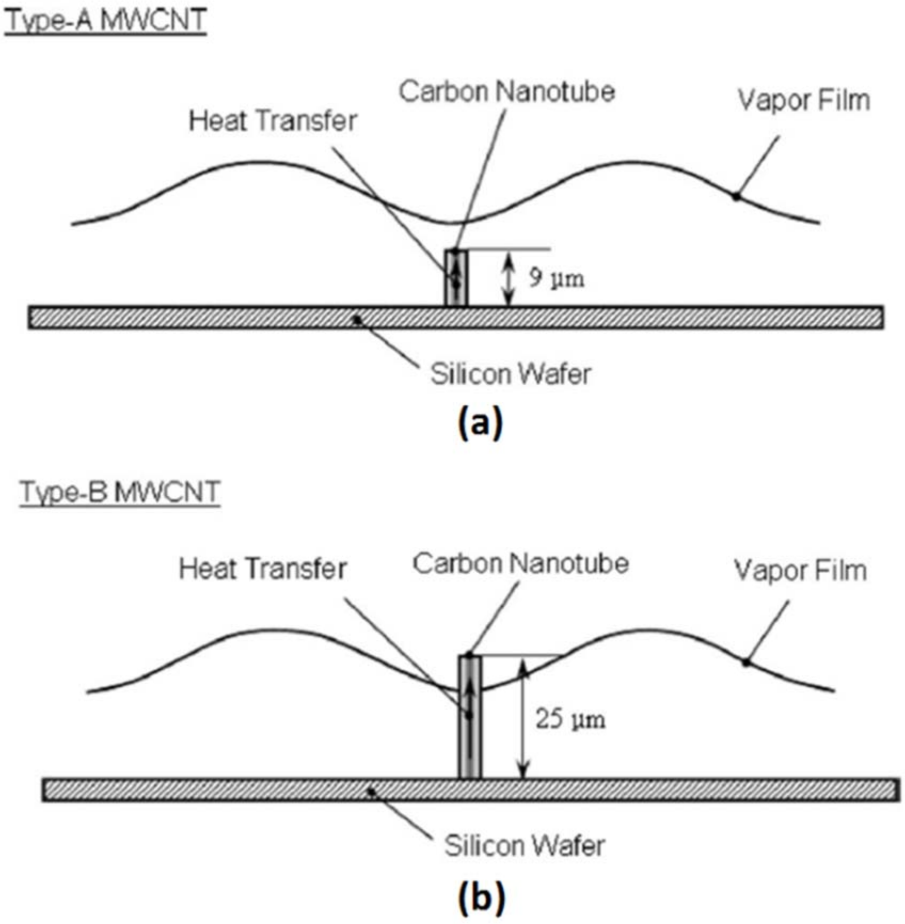

Figure 1. 1 Schematic of the heat transfer mechanism for carbon nanotubes in film boiling: (a) Type-A (9 µm thickness), and (b) Type-B (25 µm thickness) MWCNT [29]

(4) Other nano-structured surfaces

Several studies have been performed for boiling performance on inorganic nano-coatings on heater surfaces (or for engineered nano-structures on heater surfaces). Sriraman reported boiling characteristics on silicon (Si) pin finned surfaces where the diameter of the silicon pins was ~ 200 nm and the height of the fins was varied from 10 - 600 nm [30]. The nano-finned surfaces exhibited higher heat fluxes as well as CHF in the nucleate boiling regime compared to the bare silicon surfaces. The CHF was enhanced by 120% (in contrast, the CHF was enhanced by ~60% for pool boiling on CNT coated heaters). This demonstrated that the interfacial thermal resistance (Kapitza resistance) was the dominant parameter in controlling the level of CHF. The Kapitza resistance for silicon is predicted to be 1000 times smaller than that of CNT.

Chen et al. also performed pool boiling experiments on nano-finned surfaces using randomly oriented Si-nanowires and Cu-nanowire coatings and using deionized water as the working fluid [31]. Small sized heaters were used in this study where the edge effects are likely to have modified the true values of the boiling heat flux resulting in apparent enhancement of the results. In the study performed by Sriraman [30] a "large heater" was used (Heater Size: 5.8738 cm × 3.175 cm). However, Chen et al. [31] used "small heater" (heater size: 1cm × 1cm). In the "small heater" regime, as the heater size decreases the boiling heat flux increases, for all other parameters remaining constant. Hence the observed boiling heat flux enhancements reported by Chen et al. [31] needs to be qualified for the heater size, when comparisons are made with other reports in the literature. Similar arguments are also valid for other studies reported in the literature for nanostructured surfaces (e.g., [10, 12, 13, 20, 23, 24, 26]).

The Taylor instability wavelength (λ_T) and length of scale in boiling(l_0) are [32, 33]:

$$\lambda_T = 2\pi \left[\frac{\sigma}{g(\rho_f - \rho_g)}\right]^{\frac{1}{2}} \tag{1.1}$$

$$l_0 = \sqrt{\frac{\sigma}{g(\rho_f - \rho_g)}} \tag{1.2}$$

where λ_T and l_0 are the Taylor instability wavelength and length of scale in boiling, respectively. The length of scale in boiling is estimated to be 2.5 mm and 0.8 mm for saturated water and PF-5060 at one atmosphere, respectively.

The most dangerous wavelength (λ_D) is approximately ten times larger than the length scale (l_0) in boiling, and is expressed as:

$$\lambda_D = \lambda_T\sqrt{3} = l_0\,(2\,\pi\,\sqrt{3}\,) \tag{1.3}$$

Hence, the most dangerous wavelength in pool boiling has a magnitude of 2.5 cm and 0.8 cm, for saturated water and PF-5060, respectively. The heater size needs to be at the minimum ~5-10 times the size of the most dangerous wavelength to be classified as a "large heater". If the heater size is below this limit – it is qualified as a "small heater". Hence, from this discussion it is apparent that the experiments reported by Chen et al. [31] were for the "small heater" regime and therefore the heat flux values reported are not representative of the true boiling heat flux values.

Hence, in this study, the sub-cooled flow boiling experiments were conducted for "large heater" substrates consisting of Copper, Silicon and Multi Walled Carbon Nanotube (MWCNT) coated Silicon surfaces. The experiments were conducted in a horizontal rectangular channel and water was used as the working fluid in these studies.

B. Review of Condensation on Micro / Nano Surfaces

Microchannels are widely used in industry due to its advantage of yielding compact packaging for heat transfer applications. Abundant literature [34-37] exists on single-phase flow, pressure drop and heat transfer in microchannels. Various reports in the literature discuss in boiling and evaporation phenomena such as pool boiling and flow boiling in microchannels, for the heat removal at high heat fluxes in different applications. However, limited research has been conducted on the measurement of pressure drop and heat transfer coefficient during condensation in microchannel geometries especially in the sub-millimeter range of hydraulic diameters. The rejection of the large heat fluxes using compact condensers has not been addressed adequately in the literature. The research challenge in micro scale condensation is that two phase flow and flow regime transitions in these tiny channels are different from the conventional larger scale channels. The relative magnitude of gravity, surface tension effects, and shear which determine the flow regime at a given liquid and vapor phase are different in micro scale compared with the macro-scale. Coleman and Garimella experimentally demonstrated and interpreted these differences in flow mechanisms and transitions for air-water flows [38] as well as for the condensation of refrigerants [39-42]. In addition, they developed a model for condensation pressure drop in annular flow [43] and further extended it to a comprehensive multiregime pressure drop model [44] for circular microchannels.

The present work investigates the heat transfer enhancement with different surface treatment for a compact condenser. The design includes novel microchannel geometries to efficiently transfer heat from condensing R-134a to liquid water in a counter flow configuration. Low thermal resistances from both the refrigerant and water sides were needed to achieve high values of overall heat transfer coefficient.

Two unique microchannel enhancement geometries were tested using R-134a and water in a counter flow condensing test section. A flatchannel baseline design with the cross section of 200 μm height and 8.2 mm width was used for the control experiments.The results from the control experiments were compared to that of the micropost microchannel configuration which had the same cross sectional dimensions as the flat channel configuration but had in addition 2500 microfins micromachined onto the substrate. Each channel design was tested with identical inlet conditions. The micropost geometry microchannel showed better performance for heat transfer.

C. Review of Micro / Nano Sensors

Cooling technologies for high heat flux devices are required for the next generation of cutting edge platforms ranging from energy harvesting applications to applications in electronics chip cooling. Other applications include: fuel cells, high performance compact heat exchangers, chemical synthesis/ refining processes, batteries used for EV(electric vehicles) and biomedical devices. Such applications also rely on precise measurement and control of operating temperatures using sensors that need to be fabricated in-situ. However, current commercial sensors may not meet these requirements and technical specifications, due to the constraints arising from the challenges of interfacing with these devices of interest and due to the limitations imposed on the size and speed of operation arising from the conventional fabrication techniques used for manufacturing these sensors [45].

In order to overcome these challenges, various approaches have been proposed for developing integrated temperature, pressure and flow sensors [46-48]. For commercial applications - thermocouples have been of interest for their wide range of operating temperatures, durability in harsh conditions as well as ease of use (e.g., standardized calibration procedures and sensor responses). However, conventional wire bead thermocouples are expected to affect boiling and condensation studies by acting as nucleating spots which will in turn affect the local heat flux and the transient response of the surface temperature transients. Hence the geometry and size of the temperature sensors need to be altered to have minimal impact on the transport processes during investigation of the local values of heat flux and temperature transients.

In order to compensate for these disadvantages, many investigators have developed various thermal sensors such as micro-RTD (resistance temperature detector) sensors [26, 49-51]. Nguyen and Kiehnscherf [52] and Rasmussen et al [53] used RTD sensors for measuring temperature difference between the upstream and downstream locations in microfluidics devices.

A micro/nano-scale temperature sensor with a simpler fabrication method and a simpler calibration process was developed to overcome the drawbacks of the sensors mentioned previously. Sunder and Banerjee [54] developed thin-film thermocouples (TFT) and employed for surface temperature measurements with high spatial and temporal resolution.

In this study the TFT (Thin film thermocouples) were fabricated using Alumel and Chromel alloys to form a K-type junction at the point of interest. The TFT were fabricated by using Physical Vapor Deposition (PVD) for deposition of the alloys. Lift-off process was used in conjunction with photolithography techniques to pattern the metal traces on the silicon substrates. The thickness of the TFT was 250 nm for each material resulting in 500 nm at the junction of the two materials (Chromel and Alumel) An adhesion layer (either Cr or Ti) was used before deposition of Chromel or Alumel.

In addition, the feasibility of using Diode Temperature Sensors (DTS) for measuring surface temperature transients in multiphase flows was demonstrated using droplet impingement cooling experiments. An array of DTS was fabricated using standard semi-conductor processes. Kersjes et al [50] and Van der Wiel et al [51] developed micro-thermal flow sensors that employed diode temperature sensors for detecting a temperature difference between the upstream and downstream flows. The DTS array used in this study consisted of 100 temperature sensors in an area of 1.87 mm × 1.87 mm on a silicon wafer. The DTS provides two primary advantages compared with other nano-sensors mentioned previously. The first advantage is that the packaging requirements are reduced dramatically. An array of N*N sensors can be addressed by only 2*N wires. This simplifies the effort for packaging the temperature nano-sensors dramatically. The second advantage is that the sensors are located flush under the surface which does not perturb of the hydrodynamic and thermal transport processes on the surface exposed to phase change heat transfer phenomena. In this study, flow boiling experiments were also conducted for CNT coated surfaces with deionized water (“DI Water” or “DIW”) as the working fluid.

The aim of this study is to develop the instrumentation for miniaturized temperature measurements and the associated experimental capabilities for exploring the role of various micro/nano-scale transport mechanisms in multi-phase flows and heat transfer. The effect of the micro/nano-scale coating on a surface for enhancing flow boiling heat transfer enhancement was also explored. A flow boiling apparatus and droplet impingement cooling apparatus were developed and used in this study.

D. Review of Droplet Cooling

Both experimental and theoretical studies have been reported for droplet impingement cooling. Understanding the physics of impingement dynamics as well as developing the models for predicting the behavior of the evaporating droplet has been of interest in predicting the cooling (phase change) heat flux values. Some of the studies are focused on the parameters such as spreading diameter, dynamic contact angle and crown evolution [55-58] while others have focused on the surface conditions [59, 60] such as surface roughness and surface temperatures.

Droplet to surface interactions during the impact and during the boiling / evaporation process is crucial to understanding the transport processes. Fingering and splashing can take place under certain conditions that make the behavior difficult to predict. Various studies on fingering and instability propagation have been reported in the literature [61, 62]. Also, correlations developed in terms of Reynolds and Weber numbers have been reported [63, 64]. Dynamic contact angle is often used as a defining parameter in investigation of the impinging process. Chandra et al. [65] documented that the enhancement of heat transfer occurred with increased wetting of a surface. Several studies were reported for predicting the dynamic contact angle as a function of contact line velocity [66], wetting theory model [67] and the molecular-kinetic theory of wetting model [68]. In addition, maximum spreading diameter is an important parameter that is based on surface energy analysis of the droplet before the impact at maximum spreading speed [69-71].

Droplet impingement on a heated surface is a fundamental topic for investigation of spray cooling. Typically three stages are identified during the evaporation process for a single droplet impingement. Stage 1 refers to when the droplet impacts the surface until flow oscillations subside. Stage 2 refers to when the droplet evaporates mostly with a decrease in the dynamic contact angle. Stage 3 refers to the flow phenomena when the contact angle remains invariant after the droplet has reached a critical size.

Many studies have focused on experiments involving single droplet impact, in order to obtain a better handle on the droplet impact dynamics [68, 69] because the single droplet behavior can be representative of the spray cooling phenomena. This is also of considerable interest in designing platforms for electronics cooling as well as for enumerating the performance of fuel spray injectors in high performance internal combustion engines.

From reports in the literature, four regimes were identified for spray cooling heat transfer - that are similar to that of the pool boiling phenomena that is often described based on the surface temperature (or wall superheat). (1) Single phase film evaporation occurs when the heat transfer is driven by conduction and convection without phase change. (2) As the temperature increases to the critical heat flux (CHF) condition - multiphase phenomena plays a major role in defining the overall magnitude of the heat transfer. (3) This is followed by the transition boiling regime where a vapor layer is formed at the liquid-solid interface, thus reducing the heat transfer while the temperature increases rapidly to reach the Leidenfrost temperature. (4) Finally, in the film boiling region the vapor layer becomes stable – thus causing conduction and radiation to be the dominant mechanisms for the overall heat transfer.

In this study the droplet impingement cooling experiments were performed using single droplet impingement configuration. The transient measurement of the surface temperature fluctuations were performed using temperature nano-sensors (DTS) for experiments involving impinging droplets.

E. Significance of the Current Study

The research results are expected to make contributions to the field of heat transfer metrology (and associated instrumentation capabilites) using integrated nano-scale devices/ sensors and to the field of heat transfer enhancement using micro/nano-scale surface texturing (by involving engineered surfaces and nano-caoted surfaces).

This study will contribute to existing heat transfer literature in multiphase flows, particularly for flow boiling and droplet impingement cooling. The fabrication techniques, experimental apparatus/ procedure and results in this study are expected to make contributions to the heat transfer research in the following ways:

1. Make contributions to nano-fabrication techniques, testing methods and development of novel infrastructure for heat transfer research.
2. Design, fabricate and test nano-scale devices (temperature nano-sensors and nano-coatings) for heat transfer research involving multiphase flows. This study will prove the feasibility of employing these nano-scale devices for heat transfer research involving multiphase flows.
3. Assess the impact of various parameters (wall superheat, liquid subcooling, flow rates, surface conditions, heat flux) on the dynamics of flow boiling and droplet impingement cooling.
4. Develop compact condensers using plain and micro-scale structures machined inside microchannels for enhancing condensation heat transfer.
5. Assess the impact of various parameters (wall superheat, liquid subcooling, flow rates, surface conditions, heat flux) on the dynamics of condensation heat transfer.
6. Nano-sensors will be employed in these experiments to obtain experimental data for surface temperature transients during phase change and to analyze the spatio-temporal variation of surface temperature distribution.

CHAPTER II

EXPERIMENTAL SETUP AND PROCEDURE

A. Flow Boiling

a. Introduction

Better cooling technologies are required for development of the next generation of devices and platforms in various industries which include transportation, microelectronics, opto-electronics (e.g., lasers), communications, and advanced manufacturing (e.g., laser cutting). The smaller footprints and faster clock speeds in micro-chips in the electronic industry as well as the brighter and more efficient optical devices have enhanced the cooling loads for these platforms. These cooling loads are exceeding the capabilities of the fan-cooling platforms typically used for such systems. Thermal (cooling) loads as high as ~10^2-10^3 W/cm^2 have been reported for the next generation of electronic chips and devices under development. The current methods of cooling which mostly use single phase convective heat transfer (such as air or liquid cooling) have reached their fundamental limits and have failed to meet the required cooling loads. Phase change heat transfer (such as pool and flow boiling, condensation, ablation, etc.) is considered to be an attractive option for application in these future generations of cooling systems.

Both pool and flow boiling is very effective in achieving a high heat flux with a small temperature difference between the heated surface and the cooling fluid. Luttich et al. [72] indirectly measured the local temperature fluctuations during pool boiling on horizontal heaters and predicted the maximum heat flux to be over 6 MW/m^2 (~10^4 W/cm^2). These predictions were based on near surface optical measurements of temperature fluctuations and inverse conduction methods [72]. Flow boiling delivers higher levels of heat fluxes compared to pool boiling since the total heat flux is then a sum of phase change heat flux and forced convection heat flux. Hence, cooling platforms utilizing flow boiling designs provide compact components that have smaller space (or volume) footprints compared to passive air-cooling or fan-cooling platforms. However, the work input (e.g., power input for the motors and pumps) for these cooling platforms utilizing phase change heat transfer are usually higher than for fan cooling.

Boiling is a highly non-linear phenomenon where the underlying mechanisms for transport processes are intricately coupled. For a given working fluid, the variables affecting the boiling heat flux include wall superheat, nucleation site density, bubble diameter, bubble departure frequency, contact angle, heater orientation etc. [2]. Higher heat fluxes obtained in boiling than natural or forced convection involve mass transfer associated with latent heat transfer, sensible heat transfer as well as periodic transient conduction by direct liquid-solid contact and “micro-layer” effects. During bubble nucleation, growth and departure cycles, higher magnitudes and rates of thermal energy are absorbed and transported in the phase change processes. In each cycles, and for each bubble departure and re-flooding of the heater surface with colder fluid - higher amounts of transient heat fluxes also occur (compared to air-cooling). These cyclical variations in induced or forced convective heat flux (in single phase) as well as the phase change heat flux, results in the enhancement of the total heat flux.

Numerous studies can be found in the existing literature that are focused on predicting the correlations for bubble departure diameter and frequency as well as the associated heat fluxes as a function of flow rate, wall superheat and liquid subcooling. These studies provide space and time averaged information – thus losing out on the intricacies of the transport mechanisms associated with the spatial and temporal fluctuations that are manifested by these transport processes. Also these correlations are only valid within the limitations of the geometry, configurations and experimental parameters used in each study and are not universally applicable. This limits the repatability of these experiments to very narrow range of conditions. Jensen and Memmel [3] compared twelve correlations from current literature for estimating bubble departure diameter and concluded that Kutateladze and Gogonin [4] had the best-fitting correlation with an average absolute deviation (AAD) of 45.4%. Thus, it is obvious that there is a need for a comprehensive correlation for predicting bubble departure diameter and frequency in flow boiling. Besides, recently invented techniques (such as using microfabricated and engineered surfaces with micro/ nano-scale textures and particle-coatings) have set new challenges for the applicability of the existing models which are often based on continuum assumptions. However, the flow regimes within these nano-textured surfaces are often in the non-continuum regime. Hence, new experimental techniques need to be developed to explore the transport phenomena on these novel surfaces and coatings that are considered attractive for enhancing heat transfer in mutli-phase flows. In association with the new experimental techniques new theoretical and fundamental frameworks also need to be developed that can provide new models and correlations to account for the non-continuum flow regimes on the heater surface as well as the spatio-temporal fluctuations that are responsible for the bulk of the total heat flux.

One such invention is to coat a heater surface with multi-walled carbon nanotubes (MWCNTs). Boiling heat fluxes measured on surfaces coated with MWCNT were found to be enhanced by ~30-300% (depending on the boiling regime – such as boiling incipience, fully developed boiling and critical heat flux or “CHF”) compared to that on bare uncoated surfaces. A decrease in boiling incipience superheat was also observed in these experiments [10-12]. MWCNT are reported to possess high thermal conductivity and mechanical strength. Furthermore, low density (compared to metals) and high specific heat similar to graphite make MWCNT attractive materials for surface texturing (and nano-coatings).

Visualization studies for pool boiling heat transfer were reported by Luke and Cheng [73], Diao et al. [74-76], Williamson [77] and Jo et al. [78]. Khanikar [79] reported flow boiling experiments on CNT coated copper micro channels. Most of these studies used high speed camera to visualize flow configuration but they did not characterize the variations in bubble departure diameter and frequency with change in the experimental parameters (such as wall superheat, flow rates, liquid subcooling, etc.).

In this study, by using high speed photographic techniques, bubble characteristics (bubble departure height with time) were measured for sub-cooled flow boiling of water over MWCNT coated Silicon surfaces in a horizontal rectangular channel with a designated region heated electrically. Measurement sensors used previously is the TFT (Thin Film Thermocouple) that was fabricated using photolithography and metal evaporation processes. The details of the experiment setup and experimental procedure are described in this chapter.

b. Test Surface Preparation & Description of Working Fluid

The test substrates were prepared starting from a 3” diameter silicon wafer. All the substrates were purchased and diced to the dimension shown as below in Figure 2.1.

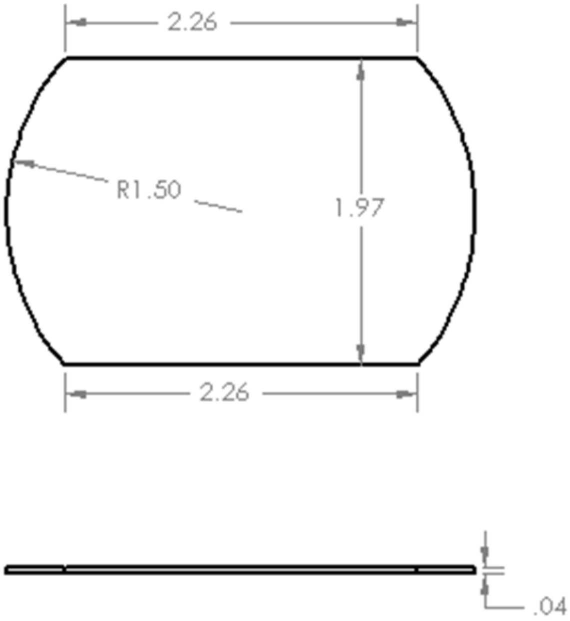

Figure 2. 1 Geometry of the heater (test) surface. All dimensions in inches.

The test substrates were diced to obtain the dimensions shown in Figure 2.1. These dimensions were chosen to be consistent with the dimensions of the copper heating block (which is described in the next section). The dicing operations were performed using a dicing saw located in the MCF (Material Characterization Facility) at Texas A&M University.

CNT synthesis can be performed using a variety of techniques which include: Arc discharge, Laser ablation, CVD (Chemical vapor deposition), and Super-growth CVD. Arc discharge method is a classical way of synthesizing the CNT since this method was the pioneering technique for discovery of CNT. Carbon soot of graphite electrodes during arc discharge produced nanotubes at a current of 100 amps that were intended to produce fullerenes. Arc discharge method yields a high-quality mixture of MWCNT and SWCNT (Single Walled CNT) which are usually 1 ~ 30 nm in diameter and 10 microns in length. Laser ablation method uses a pulsed laser that vaporizes a graphite target in a high-temperature reactor while an inert gas is bled into the chamber. The nanotubes are condensed on the cooler surface and collected. This method primarily yields SWCNT and the diameter of the nanotubes can be controlled by controlling the reaction rates. However, this method is more expensive than the arc discharge or the CVD method.

In the CVD method a substrate is coated with a layer of a catalyst material, such as Fe, Ni, Co, Pt, Pd, etc. The substrate coated with the catalyst material is typically heated to approximately 700°C. A process gas and a carbon-containing gas are blown into the chamber for the CVD reaction. The direction of the nanotube growth can be controlled by imposing an electric field in the vicinity of the substrate surface. The size of the synthesized nanotubes depends on the size of the catalyst layer or the catalyst nanoparticles. CVD is an attractive method for commercial synthesis of CNT coatings because of the cost-effectiveness and that the synthesis process is amenable for direct synthesis of CNT on the desired substrates.

The super-growth CVD is a water-assisted chemical vapor deposition process where the activity and the lifetime of the catalyst are enhanced by introduction of water vapor into the CVD reactor. The temporal growth of CNT., i.e., height of CNT, *H*, as a function of time, *t*, in the CVD process can be expressed as (K. Hata *et al.* (2005)):

$$H\left(t\right)=\beta\tau_0\left(1-e^{-t/\tau_0}\right) \tag{2.1}$$

β is the initial growth rate and τ_0 is the characteristic catalyst lifetime.

In this study, a tube furnace (Manufacturer: Blue-M) as shown in Figure 2.2 was used for performing the CVD synthesis of MWCNT coating on silicon substrates. Acetylene and nitrogen were used as process gases. The temperature of the furnace typically ranged from 750°C ~ 800°C during the synthesis step. MWCNT synthesis using CVD suffers from large amount of crystal lattice defects but it enables rapid synthesis of long and aligned nanotubes. The lattice defects can affect the electrical properties of the MWCNT while the thermal and mechanical properties are not as strongly sensitive to the lattice defects. Hence, for boiling experiments using MWCNT coatings – the CVD synthesis provides a quick and economical method for realizing these nano-coatings.

Figure 2. 2 Blue-M CVD furnace used for MWCNT coating of various substrates.

c. Description of Experimental Apparatus

The experimental setup that was used in this study for measuring flow boiling heat flux consists of a flow boiling test section integrated with a calorimeter platform and pumping and metrology devices. The dimensions of the copper block are shown in Figure 2.3. The dimensions were designed to fit flush with the bottom surface of the flow boiling test section. The dimensions of the top surface of the copper block were designed to accommodate the diced 3” diameter silicon wafers (as depicted in Figure 2. 1). The silicon wafers were diced to this size so that they could be placed inside the CVD tube furnace (which had a diameter of 2.5 inches). Eight cartridge heaters were embedded into the copper block to serve as the heat sources. A DC power supply from AMREL was used to supply electrical power to the heaters. The power supply was programmed to supply a fixed current and voltage. Figure 2.3 shows the schematic of the copper block and the experimental setup.

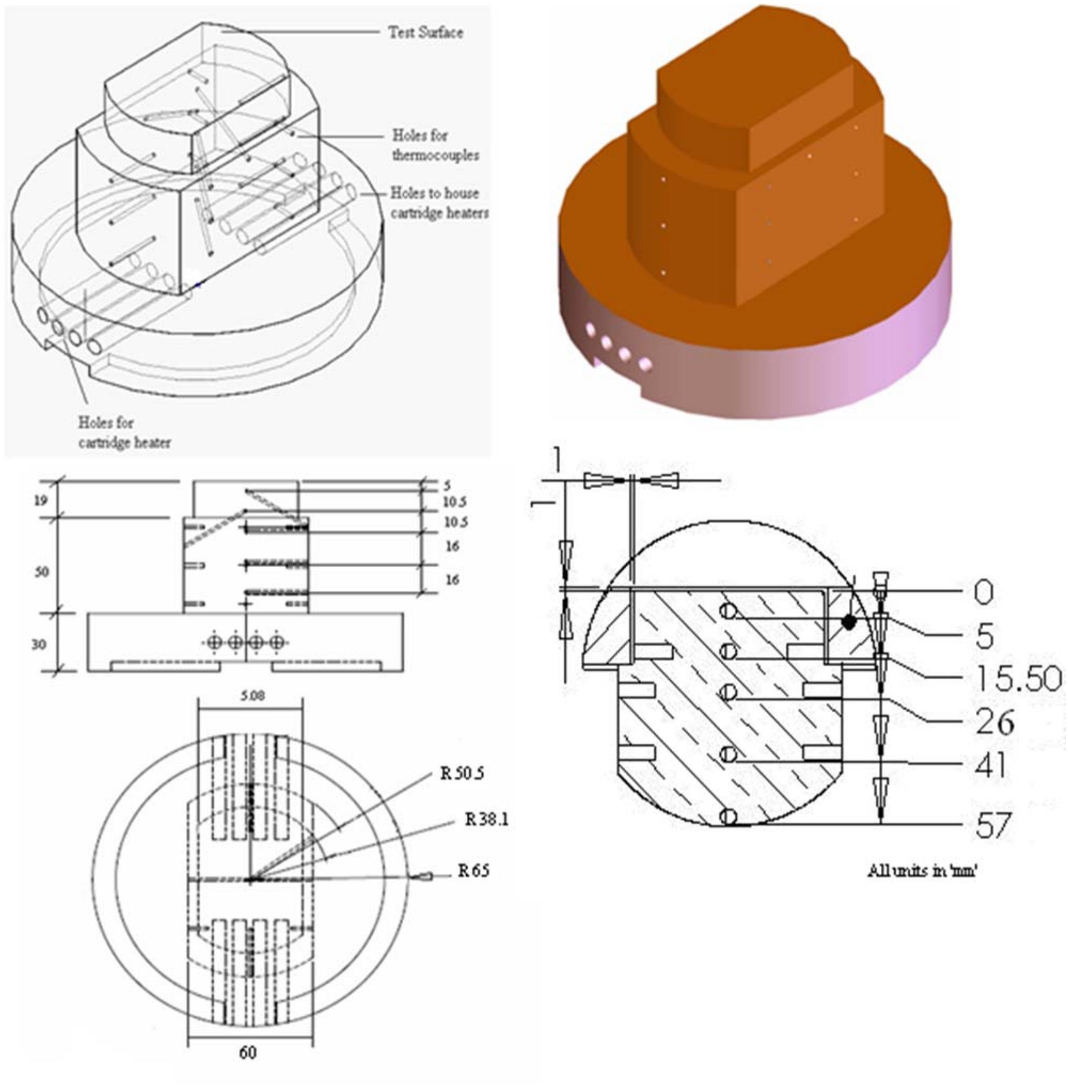

Figure 2. 3 Schematic of the copper block geometry with embedded cartridge heaters and thermocouples for heat flux measurements. All dimensions in mm.

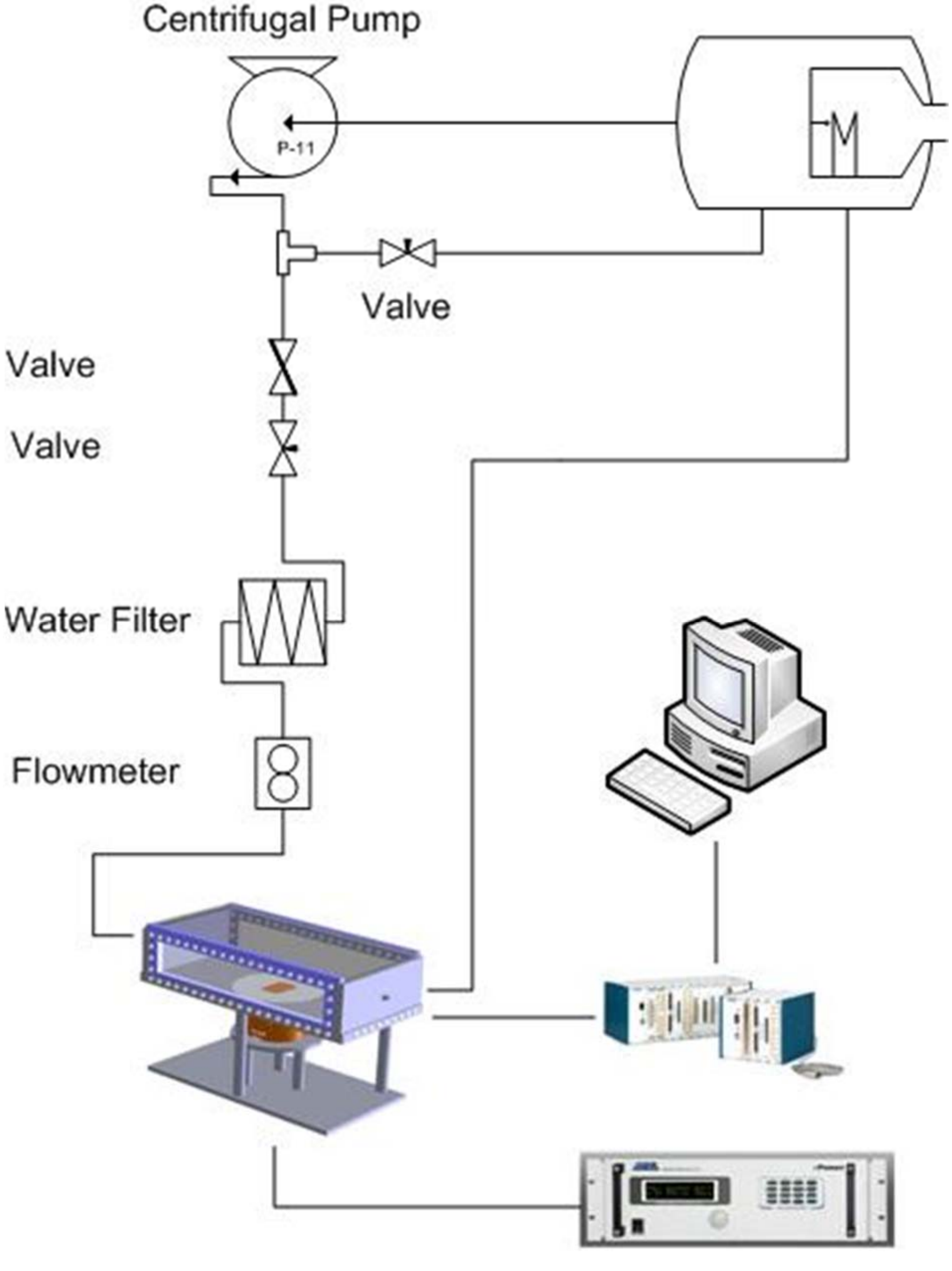

Figure 2. 4 Schematic view of the experiment setup.

Figure 2.4 shows the overall setup of the flow boiling experiment. The flow boiling test section is comprised of the rectangular flow chamber where the copper block heater is mounted flush with the bottom surface of the test section. A water tank with an immersion heater is used to preheat the water (for degassing as well as to supply the water at a fixed subcooling to the inlet of the test section). A centrifugal pump is used to pump the water into the test section. Flow rate meters and differential pressure sensors are used to monitor the flow rates and pressure drops in the test section. A high speed camera is used for high speed digital image acquisition for the bubble growth rates and departure. A high speed data acquisition system (National Instruments) is used to record the temperature data from the temperature nano-sensors as well as the embedded thermocouples in the calorimeter apparatus as well as in the inlet and outlet of the test section.

- Flow Boiling Test Section

The flow boiling test section was fabricated using 1 inch thick high grade aluminum plates. The two side walls were machined to enable the location of a transparent window (using plexiglass windows). This provided optical access for viewing the boiling surface (top surface of the copper block that was mounted flush with the bottom surface of the test section). Two different side walls were fabricated with two different window sizes. The walls of the test section were assembled by fastening to the bottom plate and using o-rings that were installed in machined grooves for achieving leak proof sealing. A stainless steel plate was press fitted onto a circular aluminum plate in a hot chamber (the copper block was inserted into the aluminum plate and mounted flush using o-rings).

Stainless steel was chosen for its lower thermal conductivity than aluminum. A vent hole with a valve was fabricated on the top cover to eliminate the gas (air) during degassing operation at the start of the experiment. The top cover also had a viewing window for image acquisition as well for using a halogen lamp to illuminate the boiling surface. Circular pipes were welded to provide the inlet and outlet to the test section. The copper block was heated using 750 W cartridge heaters made from Omega. Total of 8 cartridge heaters were embedded into the copper block to provide a total of 6 KW thermal power input to the test section. The power to the cartridge heaters were controlled using a DC power supply (manufacturer: AMREL, Ratings: 6.6 KW 125 Volts – 53 Amperes). In order to record the temperature at different locations of the copper block, 17 holes each of 1.5 mm diameter were drilled into the copper block and sheathed K-type thermocouples were inserted into these holes, as shown in Figure 2.3. The K-type thermocouples (Chromel-Alumel thermocouples) are rated for temperature measurements up to 700 °C. Five of these thermocouples were used to monitor the temperature at the center core of the copper block. These thermocouples were separated by a distance of 5, 10.5 and 16 cm from the top of the copper block (as shown in Figure 2. 3). The copper block was mounted with a 1mm clearance from base plate to enable the silicon wafer (mounted on the copper block) to be flush with the inside surface of the base plate. The thermocouples were connected to a high speed data acquisition system (Manufacturer: National Instruments).

- Water Tank

A horizontal leg type tank (Manufacturer: Norwesco) was used to store the deionized (DI) water that were used in the flow boiling experiments. The water tank has a diameter of 0.58 m, is 0.66 m in height, and is 1.09 m long with the maximum volume capacity of 246 L and is made of polyethylene.

A hole was machined at the bottom of the water tank and an adapter (Model: 1MKH9, connecting to a 2 ¼" diameter pipe, Material: polypropylene, Temperature Rating: -20 to 150 °F, Connection Type: FNPT.) was used to connect the water tank to the centrifugal pump. This adapter was selected since it had a threaded end on one side that can be used for connecting to a standard sized pipe whereas the other side of the adapter had a vortex breaker that enabled uniform supply of water to the centrifugal pump to minimize flow oscillations to the test section.

An immersion heater (Manufacturer: TEMPCO) was also installed in the water tank to preheat the water and for degassing the water at the beginning of the experiment. This enabled the supply of water to the test section at a fixed value of liquid subcooling. The immersion heater was designed to preheat the water to a maximum temperature of 200 °F (~ 90 °C).

- Centrifugal Pump and Piping Installation

A centrifugal pump (Manufacturer: Goulds Pumps Inc.; Model: G&L Series NPO) was used for pumping water from the storage tank to the flow boiling test section. The pump has a variable port positioning anatomy so that the outlet direction in the circumferential position of the impeller can be positioned according to the user's needs.

Table 2. 1 provides the parts list for the pump (this was obtained from the manufacturer's website). After the main test section, a water filter and a turbine type flow meter were installed.

- Data Acquisition System

A data acquisition system (Manufacturer: National Instruments) consisting of a thermocouple amplifier, a signal conditioning module, isothermal terminal block and an M-series multifunction DAQ device that can record data at 5 KHz was used in this study. The data collection and DAQ interfacing was performed by using LABVIEW® software (Manufacturer: National Instruments).

- High Speed Imaging System

A Fastec Imaging Corp. Troubleshooter high-speed video camera with an INFINITY Model KC 991260 lens (focus from infinity to 985 mm), an INFINITY IF-3 91107 objective (1.71x to 2.13x, 100 mm to 86 mm working distance), and a Lowel P2-10 Prolight tungsten halogen lamp were used for high speed digital image acquisition. This image acquisition apparatus was used for video capture of the bubble nucleation, growth and departure from the test surfaces that were mounted on the copper block (calorimeter apparatus).

Table 2. 1 List of components for the centrifugal pump.

Item No.	*Description*	*Materials*
100	Casing	AISI 304 SS
101	Impeller	AISI 316L SS
108	Motor adapter	AISI 316L SS
108A	Motor adapter seal vent / flush	AISI 316L SS
123	Deflector	BUNA-N
184	Seal Housing	AISI 316L SS
184A	Seal housing seal vent / flush	AISI 316L SS
240	Motor support	STEEL
304	Impeller locknut	AISI 304 SS
349	Seal ring, guidevane	VITON
370	Socket head screws, casing	AISI 410 SS
371	Bolts, motor	PLATED STEEL
283	Mechanical seal	
408	Drain and vent plug	AISI 316L SS
412B	O-ring, drain and vent plug	VITON
513	O-ring, casing	VITON
Motor	NEMA standard, 56J flange	
	Beating frame, greased for life	IRON

d. Experimental Procedure

The experimental procedure consists of the preparation step for the flow boiling test section (including degassing of the DI water test liquid), setting up the data acquisition and high-speed image acquisition.

- Preparation Step for Flow Boiling Test Section

The top surface of the copper block is cleaned prior to mounting the test surface (coated or uncoated silicon wafer) on the top surface of the copper block. Thermal paste (Manufacturer: Omega, Figure 2.6) is applied between the copper block and the silicon wafer. A uniform force of 50 N is applied on the silicon wafer for an hour under ambient room temperature conditions to eliminate the trapped air gaps in the thermal paste. A mixture of Teflon and silicone paste is applied around the perimeter of the copper block surface that is mated to the flow boiling test section for preventing any leaks. The copper block with the wafer is then precisely docked onto the main test section with a manual jack and leveled using a level gauge (to obtain a horizontal orientation for the boiling surface). The assembled apparatus is then allowed to dry for ~ 6 hours. A leak test is performed subsequently. Figure 2.5 shows an image of the top surface of the copper block after the application of the thermal paste. Additional details on the preparation and assembly of the experimental apparatus are provided in the Appendix.

- Degassing Step

After leak test is performed - the apparatus is allowed to dry. The test fluid is then boiled for 20 minutes at its boiling point (~100 °C) within the test section and the storage tank for performing degassing operation - in order to remove the trapped gases and dissolved air from the test fluid and to prevent premature nucleation.

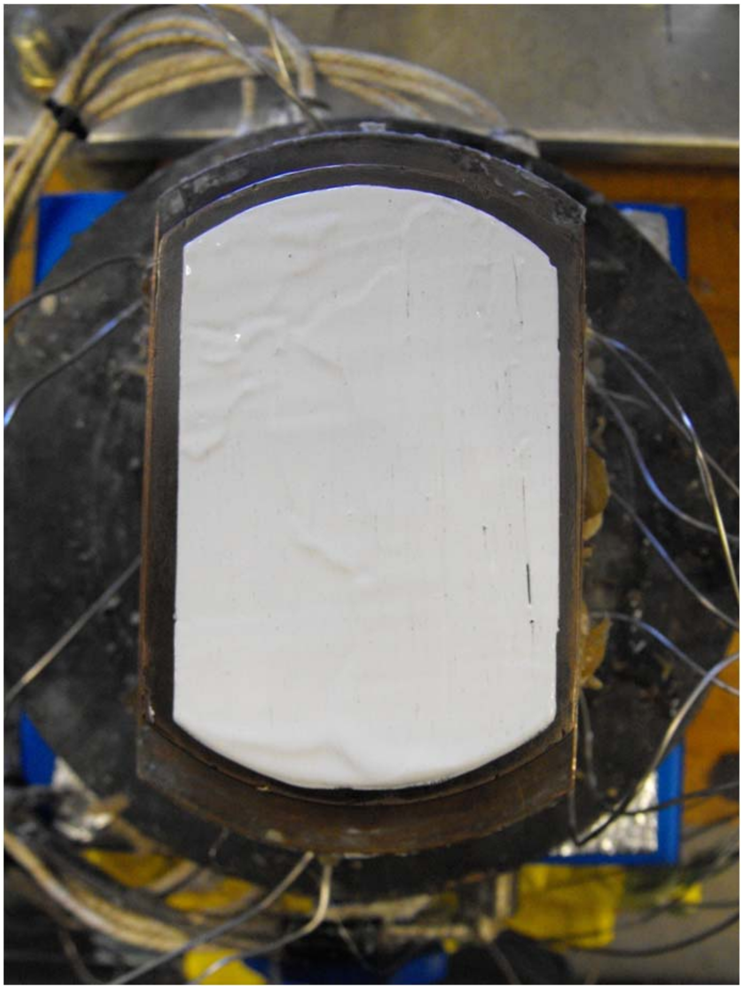

Figure 2. 5 Thermal paste on the copper block.

- Data Acquisition

The temperature of the water tank is then fixed to achieve the desired liquid subcooling. The immersion heater power supply is then disconnected (for the sub-cooled flow boiling experiments). The AMREL power supply is used to control the power input to the cartridge heaters. The system is allowed to reach steady state conditions for each power setting. The temperature of the test fluid is carefully monitored using LABVIEW® and adjustments to the liquid temperature level are made accordingly during the time taken to reach steady state. The temperatures within the copper block are also monitored simultaneously in LABVIEW®. Once steady state conditions are achieved, the DAQ system is used to record the thermocouple readings for a period of two minutes at a rate of 200 Hz. The temperature readings are used to evaluate the heat fluxes and wall superheats. These are then used to construct the flow boiling curves for the experiments. The current and voltage supplied to the cartridge heaters are recorded to obtain the power input values. In addition the temperature of the water storage tank is also recorded. The input voltage for the cartridge heaters is then increased in steps of approximately 3 or 5 volts and the aforementioned data acquisition procedure is repeated.

- High Speed Digital Image Acquisition

High speed digital image acquisition was performed at 250, 500 and 1000 frames per second (fps) at a resolution of 1280 x 512 pixels. The shutter speed was varied from 1X to 10X (of the image acquisition speed) depending on the intensity of the light source and the quality of the image. After reaching steady state conditions, the tungsten halogen lamp was turned on and the digital recording by the camera was initiated for approximately 2 to 3 seconds. The lamp was immediately turned off to minimize the thermal perturbation of the test section.

B. Condensation

a. Compact Condensation Test Section

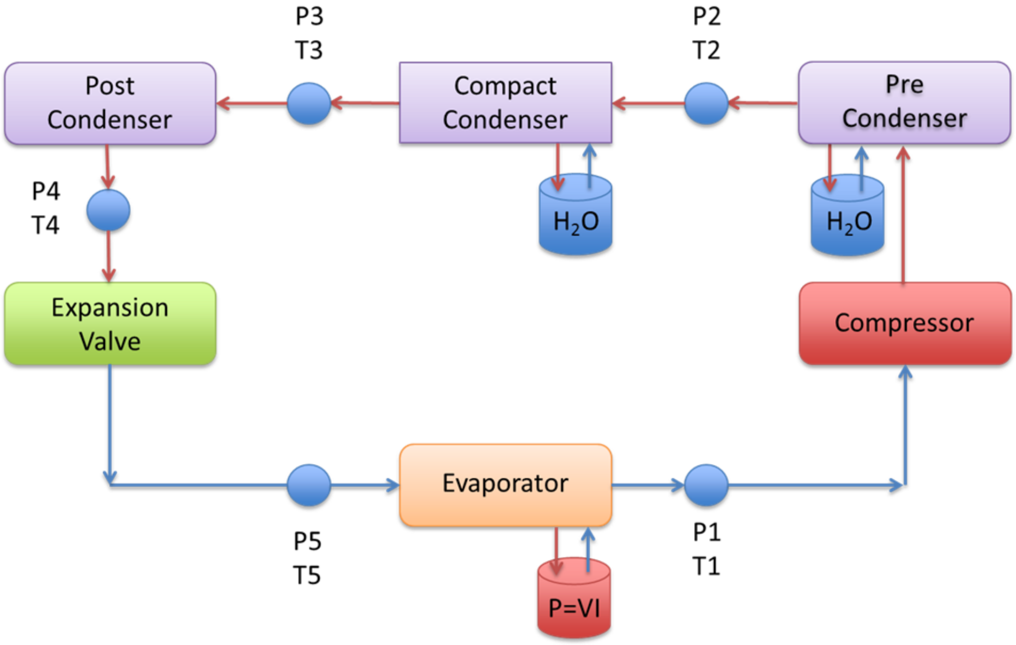

Figure 2. 6 Condensation experiment schematic.

Figure 2.6 shows the refrigeration flow loop apparatus used for testing the compact condenser configurations. The refrigeration flow loop consists of an evaporator, compressor, pre-condenser, compact condenser, post condenser and the expansion valve. A variac power supply is connected to the evaporator to supply electrical power to two heating pads that are mounted on the evaporator section (and insulated to prevent substantial heat loss to the ambient). A miniature compressor (Model 19-24-000X, Aspen Compressor, LLC) was used to actuate the refrigeration loop. A pre-condenser (a counter flow heater exchanger for water cooling) is placed after the compressor to control the inlet quality of the compact condenser. The water loop is driven by a mini centrifugal pump (Model 809-2, March MFG, Ltd). The flow rate is controlled with a needle valve that is located at the outlet of the mini pump. The compact condenser is located between the pre-condenser and the post-condenser. The refrigerant is cooled in the compact condenser heat exchanger using counter current water flow. The compact condenser test section is termed as the “Coupon”. The post-condenser (heat exchanger) was located right after the compact condenser and is connected to the expansion valve. The expansion valve was a needle type valve where the opening was precisely controlled (with provisions for both manual and automatic control). P1 - P5 in Figure 2.6 indicates the location of pressure sensor stations. T1 - T5 follows identical nomenclature for the location of the temperature sensors stations.

b. Description of Experimental Apparatus

- Mini Compressor

The mini-compressor (Manufacturer: Aspen, Model number of 19-24-00X) was used to drive the refrigeration flow loop in the condenser testing test rig, originally developed at Aspen. Aspen thermal systems introduced the smallest and lightest rotary compressor (Figure 2.7) for refrigeration systems. The variable speed refrigeration compressor was designed for a 24V DC power supply and primary use with refrigerant R-134a. Its size, weight, and durability made it ideally suited for mobile or portable application including kitchen appliances, miniature refrigerator or freezer systems, thermally-controlled transit containers, electronics cooling systems, medical devices, beverage dispensers, and mini-chilled water systems. Table 2.2 lists the technical specifications while the following graph shows the operating characteristics for the mini compressor (courtesy of Aspen Systems Inc.).

Table 2. 2 Mini compressor technical details

Application Information		*Design*	
Refrigerant	R-134a	Motor	Brushless DC (BLDC)
Voltage Range	20 ~ 30 VDC	Drive	Advanced Sensorless
Evaporator Temp Range°C (°F)	-24 ~ +65 (-10 ~ +75)	Speed Range	2000 ~ 6000
Condenser Temp Range°C (°F)	+26 ~ +65 (79 ~ 149)	Pump Displacement cm^3 (in^3)	1.9 (0.1159)
Max. Discharge Temp °C (°F)	130 (266)	Oil Quantity cm^3	21
Max. Compression Ratio	8:1	Housing Volume cm^3 (in^3)	171.2 (10.5)
Max. Compartment Temp °C (°F)	55 (131)	Total Weight kg (lb)	0.59 (1.3)
Protection Systems	Voltage, Thermal, Rotor	Diameter cm (in) Height cm(in)	5.58 (2.20) 7.74 (3.05)

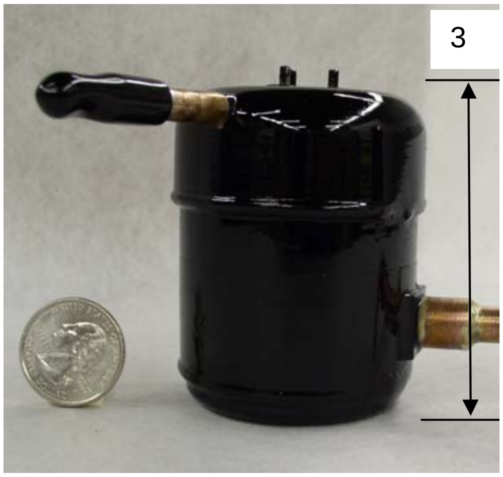

Figure 2. 7 Picture of the mini-compressor.

The following graph (Figure 2.8) represents the rpm of the compressor with the given DC voltage to the compressor.

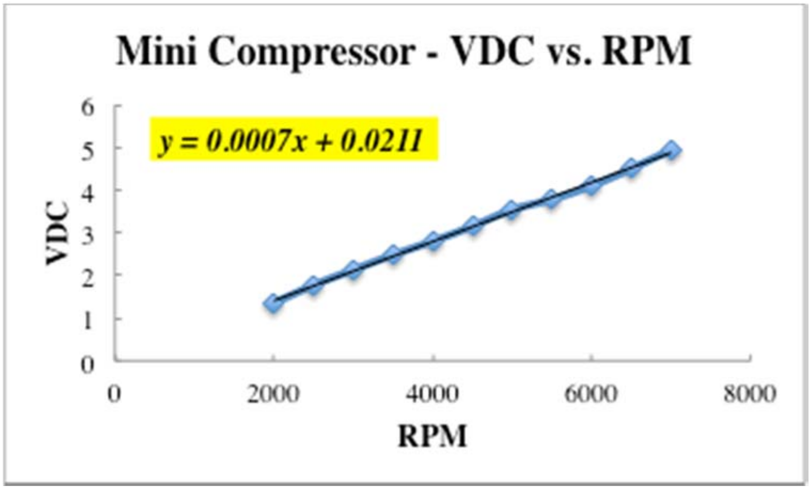

Figure 2. 8 Operating characteristics (VDC vs. RPM) of the mini compressor.

- Compact Condenser

The compact condenser sections were fabricated and assembled for two different design configurations that were used in this study. Prototype design variations are listed in the following table along with a list of the key design parameters. The first design (Design F) is the Flatchannel baseline to be used as the control experiment. The other design (Design M) includes 2,500 microfins. The microfins were designed to enhance the surface area in order to perform efficient wicking of the condensed liquid refrigerant and to augment the condensation heat transfer with minimal effect on the pressure drop in the compact condenser. Both designs have unique heat transfer (HT) enhancement characteristics and were designed to measure the flow characteristics. The following picture (Figure 2.9) shows the microchannel coupon with the machined microfins. An image with enhanced magnification (using a microscope) is also shown in Figure 2.10 where the microfins can be identified more clearly. Table 2.3 summarizes the details for coupon F and M designs.

Table 2. 3 Specification of the condenser test section.

Coupon Design	*Micro-posts [number]*	*Height [mm]*	*Width [mm]*	*Surface Area [cm^2]*
F	0	0.20	8.2	14.7
M	2500	0.20	8.2	20.0

Figure 2.9 shows the surface of the flatbed and the coupon with the micro-posts. A microscope picture follows where the micro-posts are seen from the top.

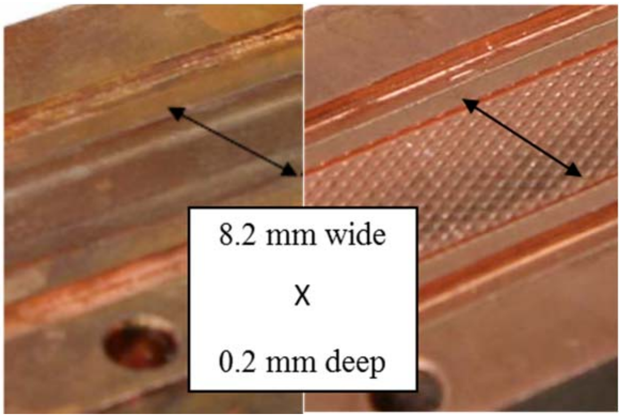

Figure 2. 9 Image of microchannel compact condenser configurations: (Left) F: Flatbed; and (Right) M: Microfin.

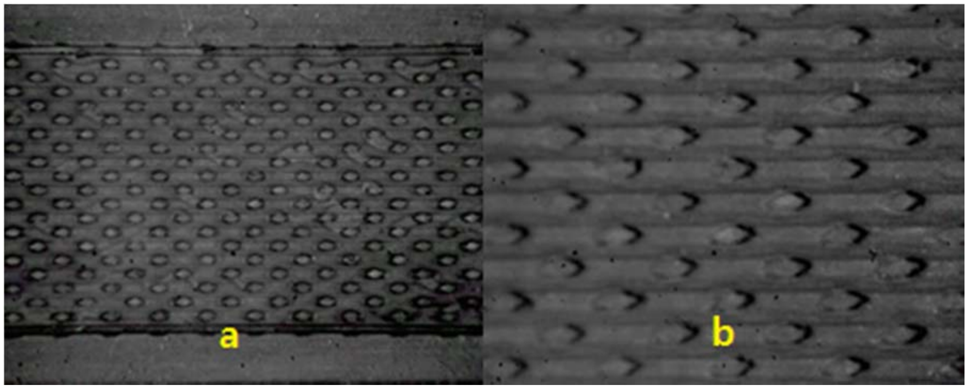

Figure 2. 10 Image of microfins that were machined inside the microchannel of the compact condenser, that were used in the experiments. (a) Low magnification, (b) Enhanced magnification (using a microscope).

c. Data Acquisition System

Temperature and pressure data were recorded using the data acquisition system that was connected to each sensor. The thermocouples and the pressure transducers were connected separately to the terminal blocks. LabView © was used for the data acquisition program for the measurement as well as to monitor the experimental parameters (Figure 2.11). The sensor data from the measurements were used to calculate the enthalpy of the refrigerant at each measurement station (with the aid of the Mollier diagram for R-134a). Table 2.4 summarizes the hardware configuration.

Table 2. 4 List of data acquisition hardware used in this study (Manufacturer: National Instruments)

Part No.	Detail	Remark
776570-01	SCXI-1000 4 Slot Chassis (120 VAC)	Chassis
776572-02	SCXI-1102 32-Channel Thermocouple Amplifier. Signal Conditioning Module for thermocouples and low bandwidth millivolt, volt, and current inputs.	Thermocouple Module
777687-03	SCXI-1303 32-Channel Isothermal Terminal Block. Connects thermocouples and signals to SCXI-1100 / SCXI-1102 Modules.	Thermocouple Connection
776572-02C	SCXI-1102C 32-Channel Amplifier, 10 kHZ Bandwidth. Signal Conditioning Module with gain and filters on each 32 channels.	Pressure Module
777687-00	SCXI-1300 General Purpose Screw Terminal Block, Cast.	Pressure Connection
776576-60	SCXI-1360 Front Filler Panel. Covers one empty slot (Front).	Cover
776576-61	SCXI-1351 Rear Filler Panel. Covers one empty slot (Rear).	Cover
182671-01	SCXI-1349 Bracket / Adapter Assembly. Connects the modules to the PC.	Adapter
192061-02	SHC68-68-EPM Shielded Cable, 68-D-Type to VHDCI Offset, 2m.	Cable
781048-01	NI PCIe-6351, X Series Multifunction DAQ (16 Al, 24 DIO, 2 AO), 1.25 MS/s single-channel sampling.	PCIe Card

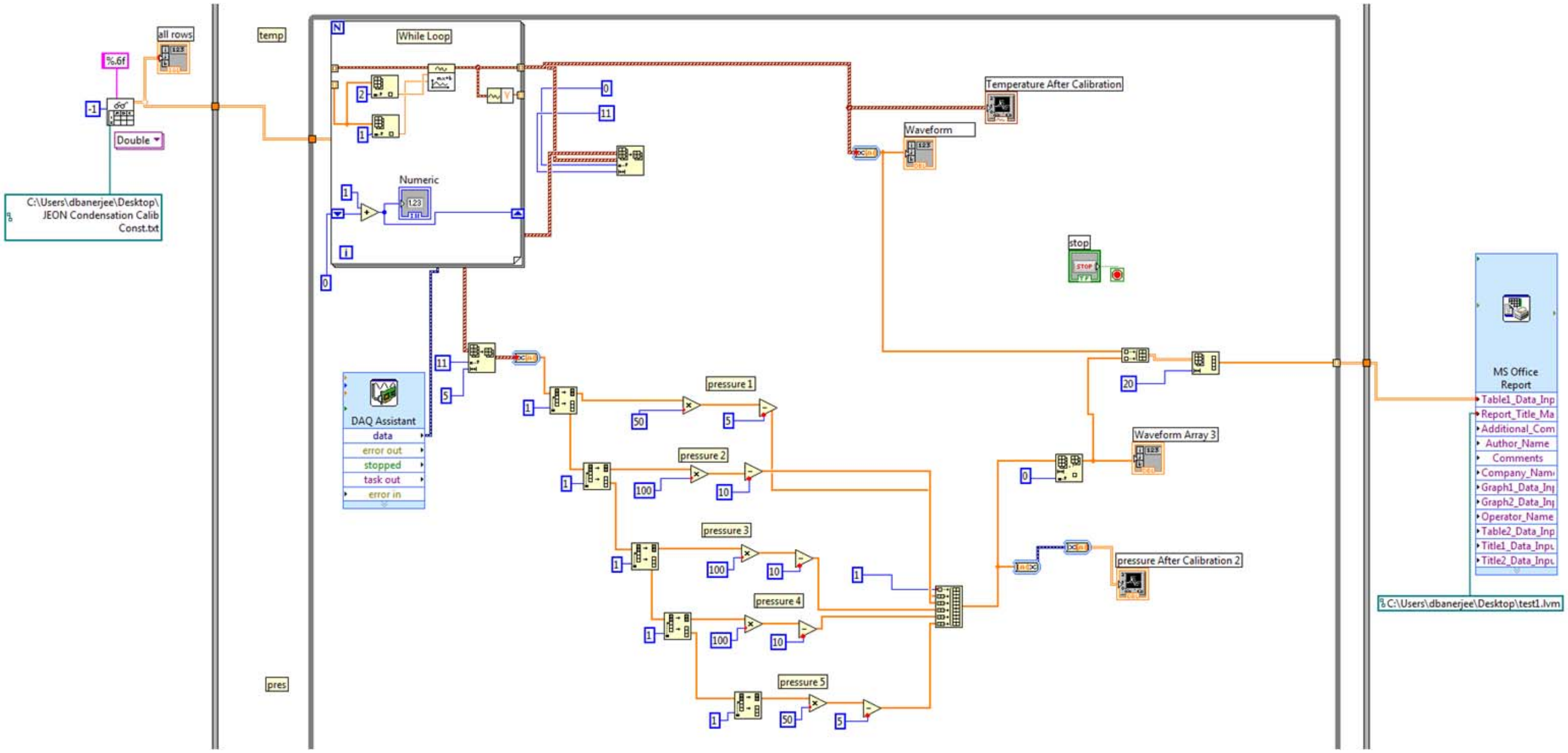

Figure 2. 11 Virtual instrument (VI)™ from the Labview® that was used to record the temperature and pressure in the compact condenser testing rig.

d. Data Analysis

This section describes the calculation procedure for the obtaining the average heat transfer coefficient in the refrigerant side as well as for estimating the overall heat transfer coefficient for the compact condenser. The experimental apparatus was assembled to include two heating pads which were installed around the evaporator. Double-layered HVAC piping heat insulation was used to minimize heat loss from the heating pads to the ambient. Since the power supply to the heating pads was modulated using a variac power supply, the power from the power supply to the evaporator may be expressed as (assuming negligible heat loss):

$$P = VI = \dot{m}(h_1 - h_5) \tag{2.2}$$

The subscripts represent stations that are shown in Figure 2.6. Then the mass flow rate of the refrigerant can be expressed as:

$$\dot{m} = \frac{VI}{(h_1 - h_5)} \tag{2.3}$$

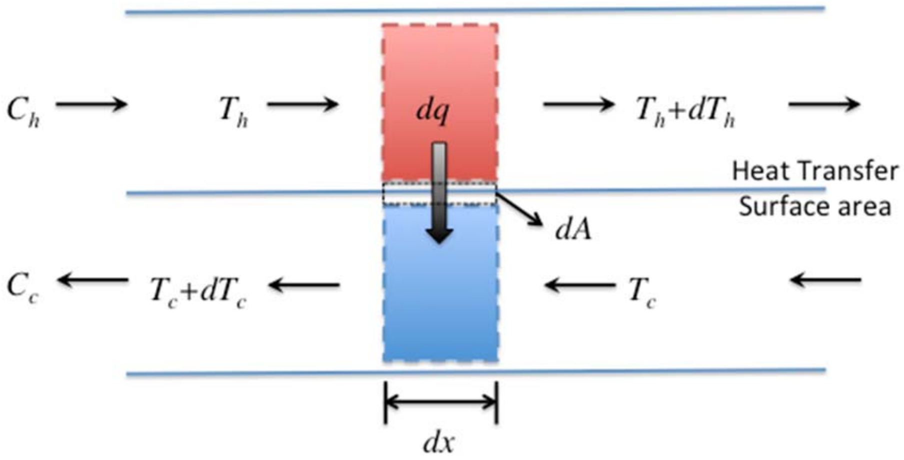

Figure 2. 12 Schematic of the counter flow heat exchanger analysis used in this study.

Figure 2.12 shows the schematic for performing a counter flow heat exchanger analysis involving the use of log mean temperature difference (LMTD) to calculate the device performance. For counter flow heat exchangers, the endpoint temperature differences at the inlet and outlet of the compact condenser are defined as:

$$\begin{gathered} \Delta T_{in} = T_{ref,in} - T_{w,out} \\ \Delta T_{out} = T_{ref,out} - T_{w,in} \end{gathered} \tag{2.4}$$

where

$$\begin{gathered} T_{ref,in} = T_2 \\ T_{ref,out} = T_3 \end{gathered} \tag{2.5}$$

Hence the LMTD for the compact condenser may be expressed as:

$$T_{LMTD} = \frac{(T_{ref,in} - T_{w,out}) - (T_{ref,out} - T_{w,in})}{ln\left(\frac{T_{ref,in} - T_{w,out}}{T_{ref,out} - T_{w,in}}\right)} \tag{2.6}$$

Since heat is rejected to the water side of the heat exchanger, the total heat transfer is expressed as:

$$q_w = c_p \dot{m}_w (T_{w,out} - T_{w,in}) = UA_{cond} T_{LMTD} \tag{2.7}$$

$$\text{U} = \frac{c_p \dot{m}_w (T_{w,out} - T_{w,in})}{A_{cond} T_{LMTD}} \tag{2.8}$$

where, u is the overall heat transfer coefficient for the compact condenser, and A_{cond} is the surface are of the refrigerant side of the compact condenser. For heating of a fluid under turbulent flow conditions (where the surface temperature exceeds the fluid temperature) the Dittus Boelter correlation can be used to estimate the heat transfer coefficient on the water side of the compact heat exchanger as:

$$Nu_D = 0.023\, Re_D^{0.8}\, Pr^{0.4} \tag{2.9}$$

Also,

$$Nu = \frac{h_w D_h}{k_w} \tag{2.10}$$

In these calculations the thermal conductivity of water (k_w) is used for property values at 50°C (which is the mean fluid temperature on the water side). The hydraulic diameter is calculated using the following expression:

$$D_h = \frac{4A_{water}}{P} \tag{2.11}$$

where, A_{water} refers to the cross sectional area of the microchannels for flow of water, P is the wetted perimeter of the cross-section. After obtaining the heat transfer coefficient for the water side (h_w) from equation 2.10, and the overall heat transfer coefficient (u) from 2.8, the heat transfer coefficient for the refrigerant side (h_{ref}) is calculated from the following equation 2.12.

$$\frac{1}{U} = \frac{1}{h_{ref}} + \frac{1}{h_w} \tag{2.12}$$

C. Fabrication & Calibration of Micro / Nano Sensor

a. Introduction

Conventional thermocouples are widely used for their wide range of temperature measurement applications. However, the size of these conventional thermocouples usually is in the order of hundreds of microns – which makes them unsuitable for metrology of phase change processes since these are affected even by surface roughness as small as 1 micron.

To obviate these issues TFT (Thin film thermocouple) have been developed. TFT uses identical principle as the conventional wire-bead type thermocouple which is the Seebeck effect. The Seebeck effect causes a potential to develop at a junction of dissimilar materials and the potential developed is proportional to the temperature of the junction. The proportionality constant is known as the Seebeck coefficient. The TFT sensor is realized by deposition of different materials (metals or alloys) on a semi-conducting or electrically non-conducting substrate (such as wafer or a glass surface). Typically the Physical Vapor Deposition (PVD) technique is used for metal evaporation or metal deposition process followed by the lift-off process to pattern the deposited layers of metals to realize a junction of dissimilar materials. However, each sensing node requires two lead wires and two interconnection bond pads for transferring the sensing (electrical potential) signals to the external data acquisition system. For instance, in order to measure 100 sensor nodes located within a small area, 200 lead wires (and 200 bond pads) are required. Hence, TFT sensors are useful when only a small number of sensing locations are required for high speed temperature sensing. For high speed and high spatial density sensing needs (with minimal perturbation of the transport mechanisms) TFT sensors are cumbersome due to the need for packaging high number of interconnects to the data acquisition system. Furthermore, a fundamental limitation of is that the thickness of the deposited metal layers need to be higher than ~ 200 nm, since below this size limit phonon dispersion causes these metal traces to behave as resistors rather than thermocouples (i.e., emf sources).

In order to overcome the drawbacks of the TFT, a DTS (Diode Temperature Sensor) array was developed in this study. With the DTS, it is possible to sense temperature fluctuations with high spatial density (~ 1 micron pitch) and high speed (~ 1 MHz), while the packaging requirements for the interconnects are minimized. Since the DTS does not require individual lead wires for each location while the individual sensing nodes can be addressed using a novel semiconductor based addressing scheme (i.e., using the diode principle of much reduced backward bias current compared to forward bias current). Hence, when the DTS array is fabricated geometrically in an array of 10 columns and 10 rows forming 100 sensing node locations, only 20 bond pads (or interconnects) are required for addressing all of the sensing nodes. In this study, DTSA (Diode Temperature Sensor Array) were fabricated. The feasibility of applying these sensors for transient measurement of the surface temperature fluctuations during heat transfer in multi-phase flows has been demonstrated by performing droplet impingement cooling experiments on a substrate with DTSA fabricated in-situ and flush beneath the surface of the substrates.

b. Principle of Sensing Using DTS

The diode equation expresses the working principle of a diode and is closely approximated by

$$i = I_s\left(e^{\upsilon/V_T} - 1\right) \tag{2.13}$$

where, I_s is a constant for a given diode at a given temperature and is usually called the **saturation current** or **scale current**. I_s is proportional to the cross-sectional area of the diode. υ is the given forward voltage. V_T is a constant called the thermal voltage and is expressed as

$$V_T = \frac{kT}{q} \tag{2.14}$$

where,

$k = 8.62 \times 10^{-5} \left[eV/K \right] = 1.38 \times 10^{-23} \left[J/K \right]$: Boltzmann's constant

T: Absolute temperature in Kelvin; $T = 273 + temperature\left[{}^{\circ}C \right]$

$q = 1.60 \times 10^{-19} \left[coulomb \right]$: Magnitude of electronic charge

Equation (2.13) shows that

$$V_T = 0.0862T \left[mV \right] \tag{2.15}$$

substituting the constants above. For instance, at room temperature of $25\,{}^{\circ}C$ the value of V_T is $25.7\left[mV \right]$. The *i*-*v* characteristic in the forward region (Figure 2.13) of the diode reveals that for a fully-conducting diode the voltage drop lies in a narrow range, approximately $0.6\left[V \right]$ to $0.8\left[V \right]$. It is assumed that a conducting diode has approximately a $0.7\left[V \right]$ potential drop across it.

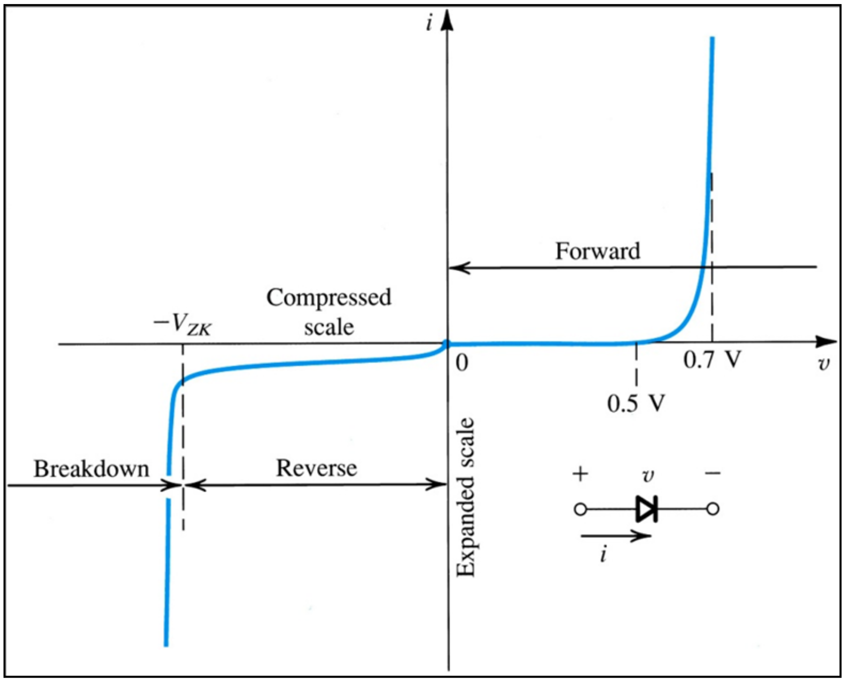

Figure 2. 13 The diode *i-v* relationship with some scales expanded and others compressed in order to reveal details.

I_s and V_T are functions of temperature. The forward *i-v* characteristic varies with temperature as can be seen in Figure 2.13 and Figure 2.14. Generally, silicon diodes have a forward voltage drop of 0.7V. Near room temperature, this voltage decreases by 2mV for every 1 °C increase in the operating temperature of the diode.

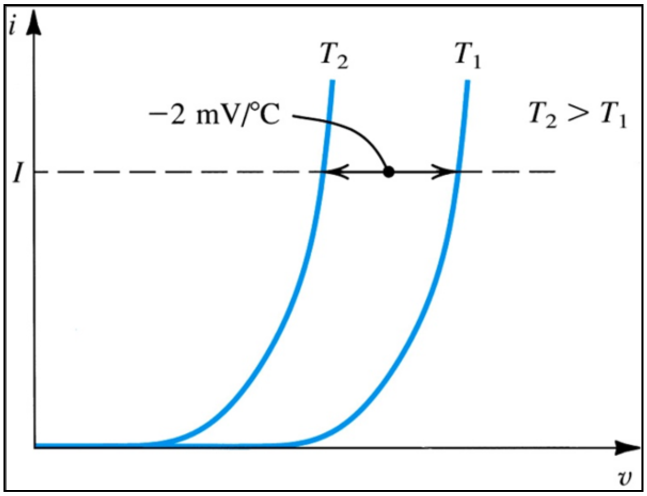

Figure 2. 14 Temperature dependence of the diode forward characteristic. At a constant current, the voltage drop decreases by approximately 2 mV for every 1°C increase in temperature.

Due to variations in the fabrication process as well as variations in the spatial distribution of the dopants and impurities, diodes can display different temperature characteristics. Hence, the individual diode sensors must be calibrated in order to determine the relationships between the temperature and the forward voltage drop. The calibration can be performed using a heated chuck (with precise temperature control) placed in a probe station with micropositioners (for achieving electrical contacts with the bond pads to address individual diode sensors in an array). Details of the sensor characterization are discussed in the next chapter.

c. Sensor Design (DTS)

Diode temperature sensors were fabricated using classical methods. The design of the sensor array was performed with an aim to locate one hundred sensing nodes in the array with a small spatial footprint (~ 5 mm square) which can be addressed with only 20 bond pads (thus requiring the packaging operation for only 20 interconnects). Figure 2.15 shows an image of DTS array that was fabricated in this study. Each row in the image has an array of 100 DTS. The image shows 8 rows of DTSA, each array containing 100 DTS.

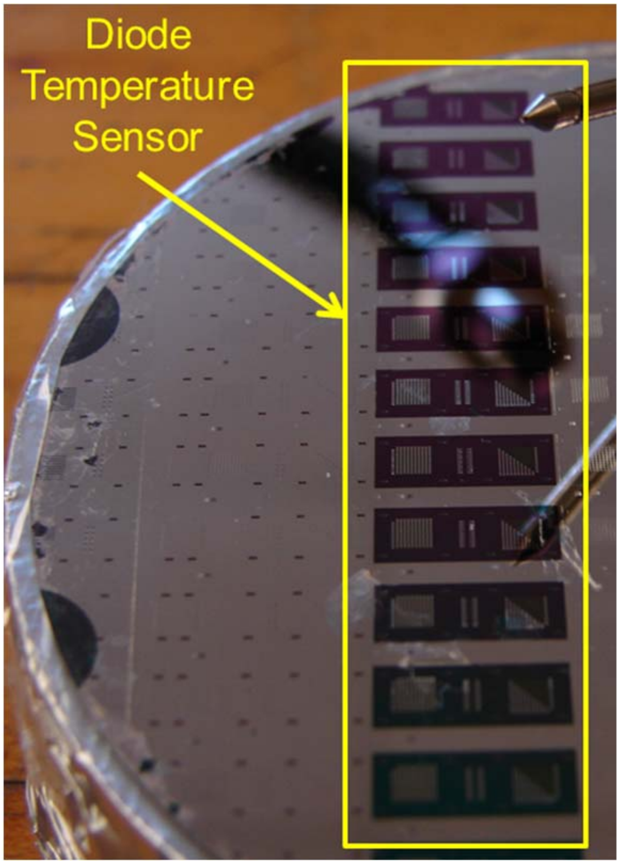

Figure 2. 15 Image of silicon wafer with DTS fabricated under the surface of the wafer.

d. Fabrication Sequence

- Wafer Selection

The DTSA were fabricated using a 3” diameter n-type silicon wafer as the substrate. Table 2.5 summarizes the properties of the 3” diameter n-type silicon wafer.

Table 2. 5 Properties of the n-type silicon wafer.

Properties	*Details*
Diameter	76.2 mm (3”)
Type / Dopant	N / phos.
Orientation	< 1 0 0 >
Slice Align	±0.5 deg.
Resistivity	1.0 ~ 10.0 Ω-cm
Thickness	330 ~ 430 μm
Flats	SEMI std.
Grade	SSP/E - Test
Growth Method	CZ

- Photo Mask Layout Design

The fabrication process is categorized into two parts. Mask layout design is the first step followed by photolithography. In order to fabricate the DTSA, 4 masks were necessary for the photolithography sequence. Since the substrate was selected as an n-region, Mask #1 was used to open a p-region onto the substrate. Mask #2 was used to open a n-region on top of the p-region to create n-p-n layer. Mask #3 and Mask #4 were used for obtaining the contact opening and metallization layer (for bond pads) respectively.

Figure 2.16 shows the mask layout design used in this study. One photo-mask was used to realize the four mask sequence. The strategy was to shift the wafer by one masking step (using the same photo-mask) from Mask #1 through Mask #4 by repositioning and aligning on the mask aligner during the fabrication (and photolithography) sequence. Figure 2.17 shows a detailed view of the mask features and the feature dimensions.

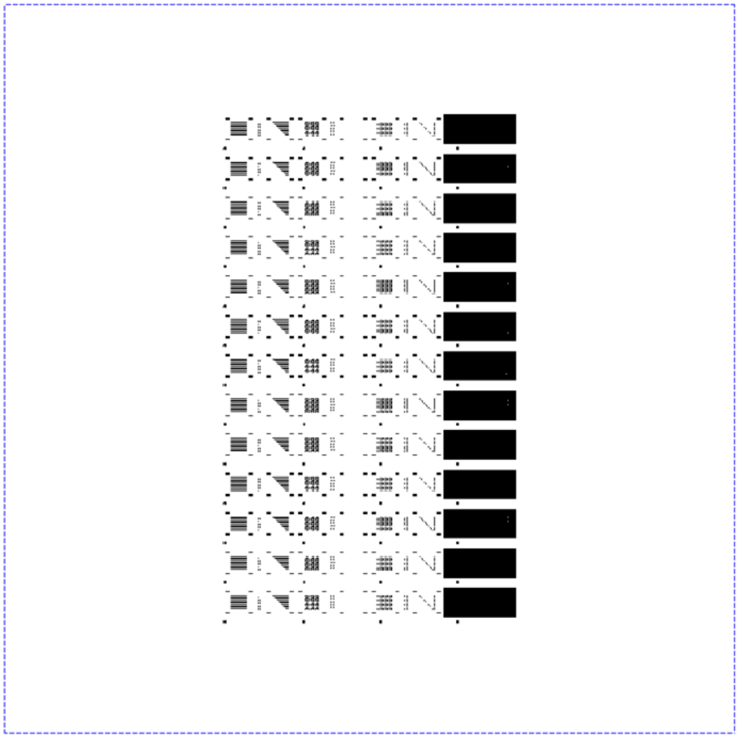

Figure 2. 16 Photo-mask layout design used for fabrication of the DTSA.

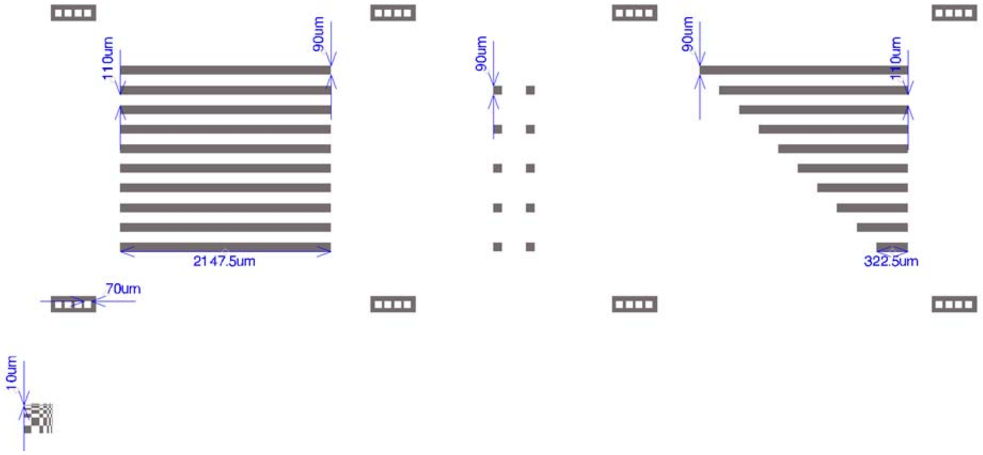

(a) Mask 1 : p-layer

Figure 2. 17 Details of the dimensions and features for the four photolithography steps integrated into one photo-mask layout. (a) Mask 1, (b) Mask 2, (c) Mask 3, (d) Mask 4

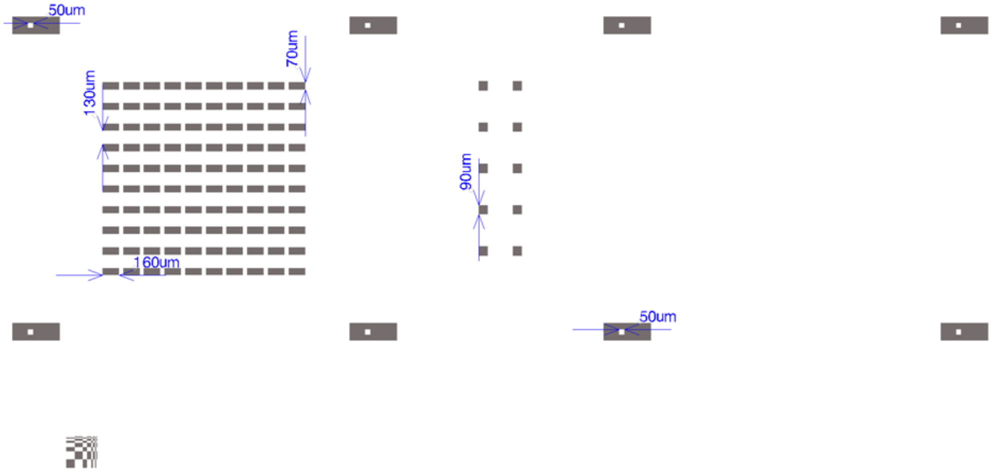

(b) Mask 2 : n-layer

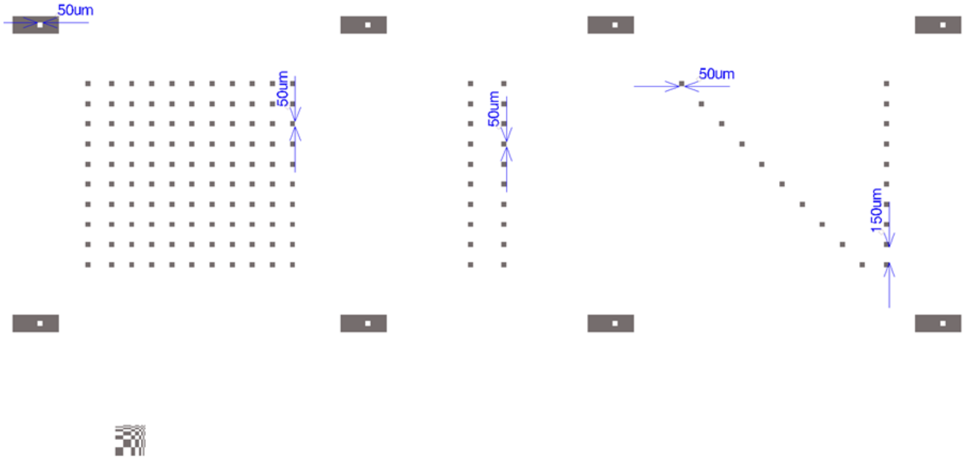

(c) Mask 3 : Contact opening

Figure 2. 17 Continued.

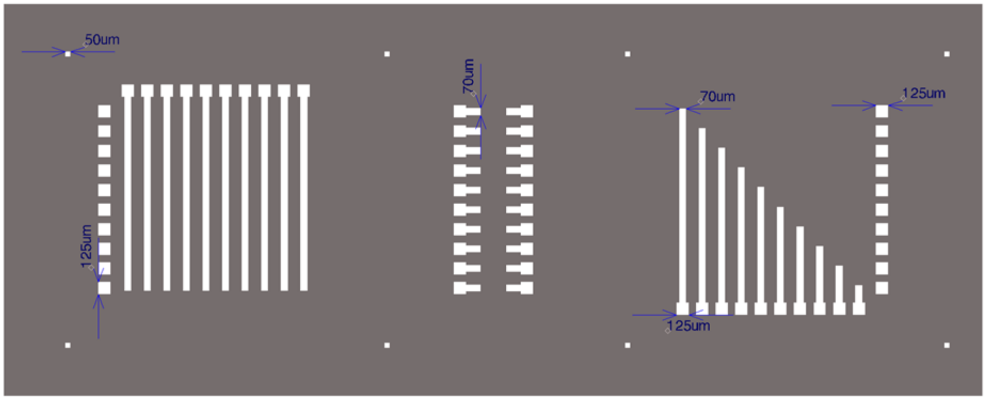

(d) Mask 4 : Metallization layer

Figure 2. 17 Continued.

- Initial Oxidation

Process chemicals that are needed for the various fabrication steps are summarized in Table 2.6.

All the fabrication process steps start with the cleaning of the wafer in piranha solution. Each time a fresh piranha solution is prepared by mixing 3 portions of sulfuric acid (by volume) and 1 portion of hydrogen peroxide. For instance, 300 ml of sulfuric acid was prepared in Pyrex © beaker and 100 ml of hydrogen peroxide was slowly added to the sulfuric acid. The preparation must be performed in a clean room facility along with use of all the protective gears and required safety practices/ protocols in performing these operations. When the hydrogen peroxide is slowly poured into the sulfuric acid, oxidizing fumes are created within the solution. The mixture was then

Table 2. 6 List of process chemicals used for fabrication of DTSA.

Name	*Chemical Formula*	*Usage*
BOE (Buffered Oxide Etchant)	1 part HF to 7 parts H_2O	Oxide layer etching
Hydrogen Peroxide 30%	H_2O_2	To make piranha
Sulfuric Acid	H_2SO_4	To make piranha
Positive Photoresist (AZ4512)		
μ-posit MF-312 Developer (tetramethylammonium hydroxide)	$(CH_3)_4NOH$	Positive photoresist developer
Aluminum Etchant		

placed on a hot plate set at 50 °C and mixed uniformly using a Teflon ™ stirrer. Two additional beakers with deionized water were prepared to rinse the wafer that was immersed in the piranha solution for the cleaning protocol. The wafers were immersed in the heated piranha for 5 minutes on the stirrer. After 5 minutes, the wafer was carefully removed from the piranha solution using tweezers and then immersed in the first beaker with deionized water for another 5 minutes. Then the second rinsing step for the wafer was performed by immersing in the fresh deionized water. Specially designed tweezers were used to move the wafers from one solution bath to the next while ensuring that they were rinsed in separate deionized water sprays every time the tweezers were used. After the two-step rinsing process was performed, the cleaned wafer was dried using ultra high pure nitrogen (N_2) gun with micro-pored filter attached to the nozzle. The drying step was performed until no water marks were visible on the wafer surface. The proper handling procedure requires that during the drying step the wafer is held at an angle while resting at an angle on a wafer wipe cloth while the nitrogen gun was pointed at the wafer surface. Resting the edge of the wafer on the wipe cloth helps with faster drying of the wafer surface. Figure 2.18 shows a wafer in piranha and demonstrates the proper procedure for handling a wafer during the drying step. After the drying process is accomplished, the wafer was placed in a closed convection oven (that is set at 120 °C) for 15 minutes to enable complete elimination of water on the wafer surface. At this point, the wafer cleaning was completed and the wafer is ready to be inserted into the oxidation furnace.

Initially, the n-type wafer does not have any oxide layer on the surface (other than a native oxide layer that is a few nanometers thick). An oxidation process is used to realize a thick layer of SiO_2. A “Thermco Mini-Brute 70” furnace was used as an oxidation furnace. A bubbler apparatus with a heater (for heating the water through which oxygen is bubbled) was used for wet oxidation.

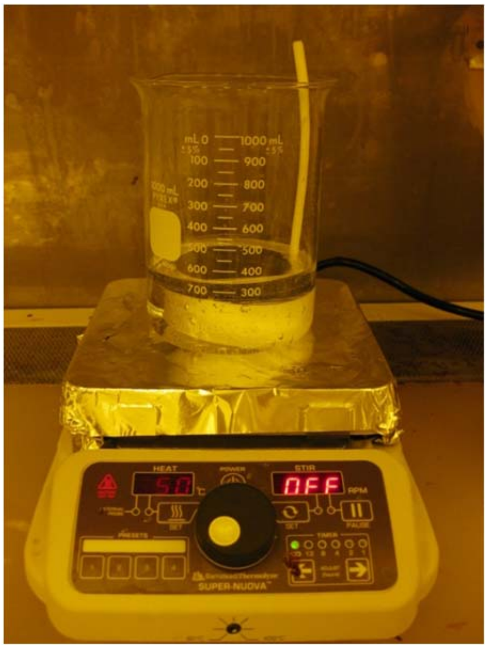

(a) Wafer in piranha.

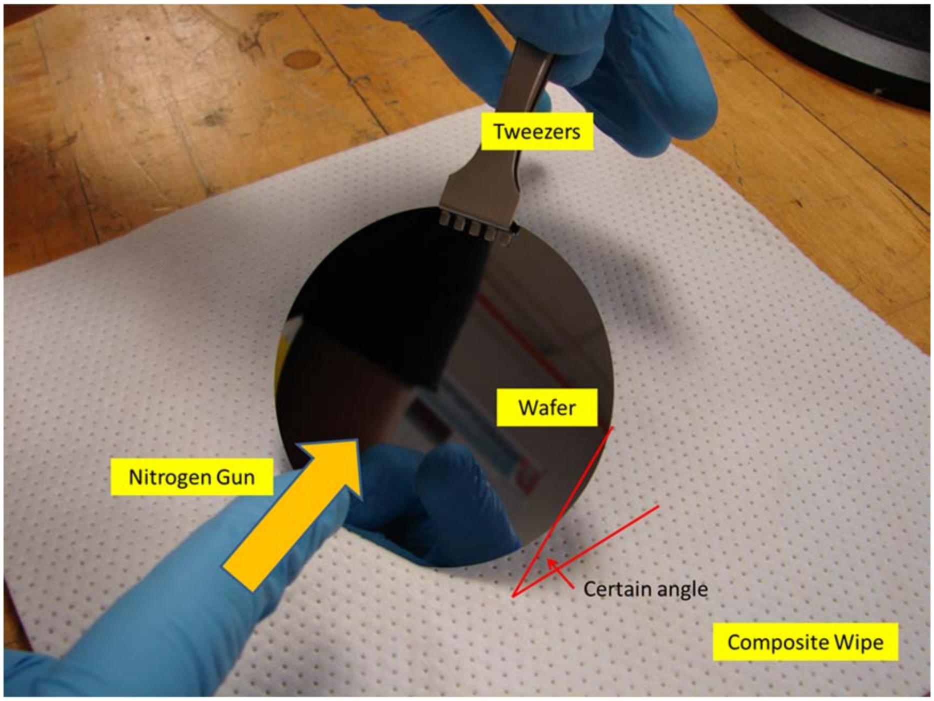

(b) Wafer position when drying using a N_2 gun.

Figure 2. 18 (a) Wafer in piranha, (b) Wafer position when drying using a N_2 gun.

Table 2. 7 Initial oxidation process.

Steps	*Oxidation Type*	*Time*	*Temperature*	*Pressure*
1	Dry O_2	10 min.	1100 °C	1 atm
2	Wet O_2	130 min.	1100 °C	0.9 atm
3	Nitrogen (N_2) only	10 min.	1100 °C	1 atm

The bubbler apparatus is connected to the oxygen supply line (from an oxygen cylinder). Table 2.7 summarizes conditions needed for the furnace operation in order to achieve approximately 1 μm thickness of SiO_2 layer on the cleaned n-type silicon wafer. The cleaned wafer was loaded onto a quartz boat (Figure 2.19) and a quartz rod for insertion into the furnace. Safety equipment such as the heat resistant gloves and eye protector with mask were used, when the wafer on the boat was pushed into the furnace. The boat was pushed slowly into the furnace in order to prevent a sudden heat shock to the wafers loaded on the boat. The boat was positioned at the entrance of the furnace tube for 2 minutes. With nitrogen gas flowing in the furnace, the wafer was then pushed approximately to the middle of the furnace tube. The furnace cap was closed and the springs were secured. The oxygen valve was controlled with a flow meter gauge and opened slowly to achieve the process conditions described in Table 2.7.

A dummy wafer was placed at the front of the stack of wafers on the quartz boat, with the polished surface reversed to the flow direction inside the furnace. The other cleaned process wafers were inserted approximately 1.5” behind the dummy wafer. After the oxidation process was finished, the quartz boat containing the stack of wafers was taken out of the furnace slowly and positioned at the entrance for 2 minutes (for temperature equilibration). The wafer was then cooled under natural circulation conditions in the clean room ambient temperature (in the open air) before resuming the next process step. Figure 2.20 presents a flow chart for the fabrication process steps.

Figure 2. 19 Quartz boat to load 3" wafers.

- P-Layer Opening

The silicon wafer with the oxide layer is then processed for the photolithography step. To obtain the p-layer strips in the n region, the first mask layer is used in the photolithography step. This process is the initial usage of the mask and therefore no alignment was necessary. The wafer with the oxide layer can get contaminated with organic materials and natural oxidation may also occur, hence the first photolithography step was performed only after cleaning the wafer in freshly prepared piranha solution.

As before, the wafer was immersed in piranha and dried with nitrogen gun followed by heating in an oven at 120°C for removal of water. After mounting the wafer on a spin coater, a small quantity of photoresist (AZ-5214) was then dispensed using a pipette.

The wafer was placed on the chuck of the spin coater and centered. A vacuum pump was used to suction mount the wafer. Photoresist was dispensed to cover the entire surface of the wafer and visibly ensuring that no significant bubbles were present. If any bubbles were visible, they were eliminated by using the pipette to physically suction them out. The spin coater was programmed to rotate at 3000 rpm for 30 seconds. When the wafer was set on the chuck and photoresist was properly applied, the lid was closed and the spin coater was turned on for operation. After the spin coating process, any extraneous particles or other foreign materials could be detected by the visible striation marks and traces that were formed after the spinning process. In such a situation, the wafer was cleaned again using acetone and isopropanol followed by rinsing in deionized water and the spin coating operation was repeated. If no striation marks were detected on visual inspection after the spin coating process - the wafer was placed on a hot plate (set at 110°C) for 3 minutes for soft-bake. This step is known as the “pre-exposure bake” and is performed before the wafer is placed on the mask aligner. The conditions for the soft-bake are usually determined based on the manufacturer recommendation for the photoresist. The mask aligner (Manufacturer: Karl Suss) used in this study is operated manually and has four power settings. The first power setting is used to turn on the main

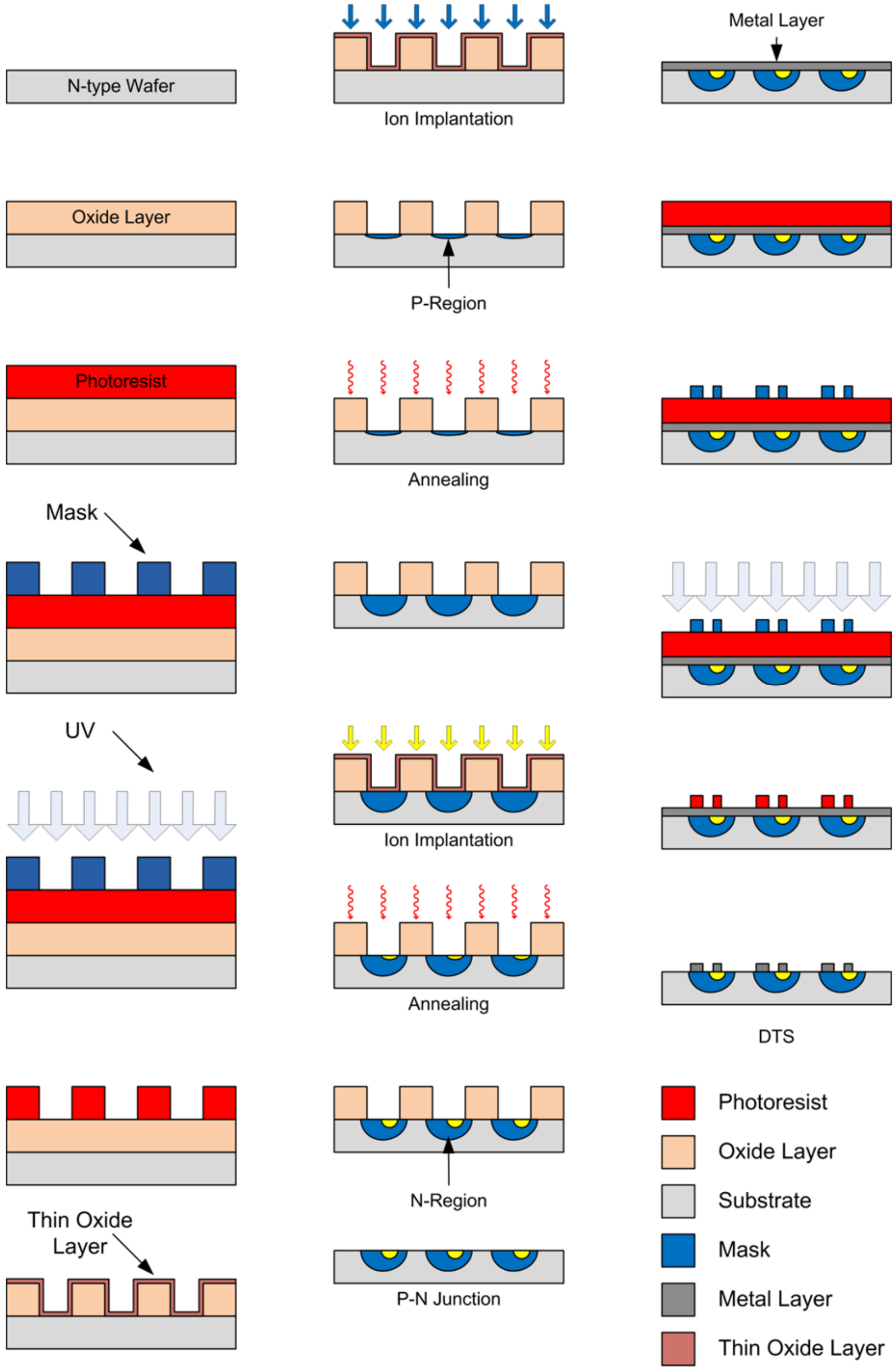

Figure 2. 20 Diode temperature sensor fabrication flow chart.

power. The second power setting is used to turn on the vacuum pump for suction mounting of the wafer on the aligner chuck. The third power setting is used for setting the pressure toggles switches. The fourth power setting is used for turning on the light source for the microscope. The photomask was cleaned using IPA and suction mounted onto the mask-tray. Then the soft-baked wafer was placed in the sliding wafer-tray on the mask aligner. Control knobs were used to elevate the wafer closer to the mask. Interference optical ripples appear at certain proximity of the wafer to the mask – at which point the adjustment of the control knobs should be stopped. At this time, the mask and the wafer are in the contact mode. When the ripples are observed, the separation lever needs to be engaged to change the status from contact mode to separation mode. This is needed to enable a small gap between the photomask and the wafer in the event the mask needs to be shifted for performing alignment procedures.

To open the oxide mask for obtaining the p-layer, the wafer did not require any mask alignment and thus was ready to be exposed when the ripples were observed. The exposure time was calculated from the intensity of the main power and the dose required for the photoresist for developing step. The following equation was used to calculate the exposure time for the wafer.

$$\text{Intensity}\left({}^{mW}\!/_{cm^2}\right) \times \text{Time} = \text{Dose}$$

For the mask aligner (Karl Suss), the intensity was $7.5\left[mW/cm^2\right]$ and the dose required for the photoresist was 150. Hence, the exposure time was set for 22 seconds.

After the exposure step the exposed photoresist was developed by immersing in a photoresist developer solution. The solution was prepared by mixing 3 volume portions of the developer and 2 volume portions of deionized water. Light agitation of the wafer on top of a Teflon© stirrer was needed to ensure uniform mixing. As soon as the exposed features were visibly apparent, the wafer was immediately removed from the developer bath for rinsing in afresh bath of deionized (DI) water and drying step with nitrogen gun. The wafer was checked under the microscope to make sure that it was exposed and developed properly. A quick strategy for checking the adequacy of the yield of the photolithography step is to focus the microscope on the resolution mark when observing under the microscope. The resolution marks designed in the mask layout are shown in Figure 2.21. The image of the wafer observed using a 3-D microscope is shown in Figure 2.22.

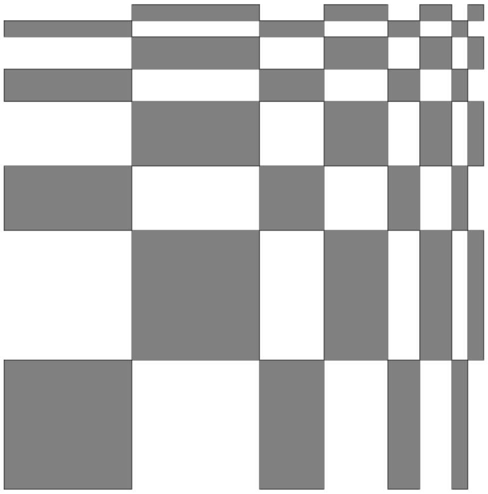

Figure 2. 21 Exploded view of resolution test pattern (designed in the mask layout for the alignment marks). The largest of the diagonal squares is 80 µm on a side, and the smallest is 10 µm.

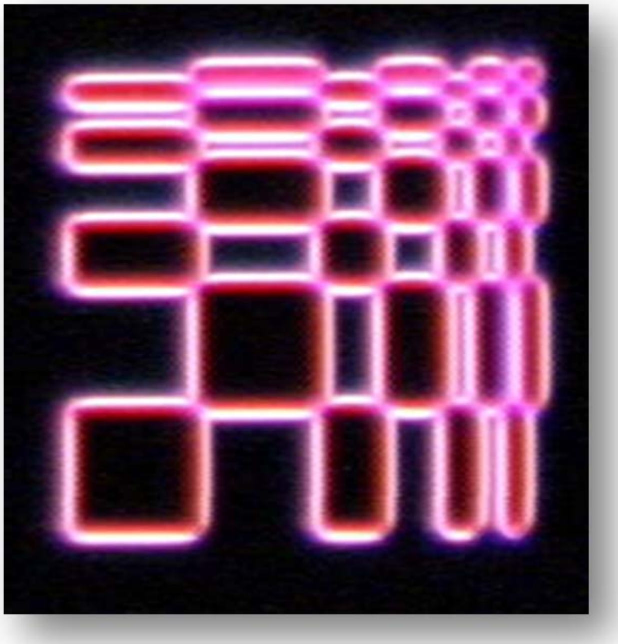

Figure 2. 22 Image of the resolution mark after developing process using a 3D microscope.

Once the success (and yield) of the photolithography step was checked, it was placed into the oven to hard-bake at 120 °C for 10 ~ 15 minutes. As soon as the wafer was hard-baked and cooled under natural convection in room temperature conditions, it was etched using the BOE (Buffered Oxide Etch) solution. After etching in BOE solution the wafer was cleaned in piranha and was loaded onto the quartz boat for gate oxidation. The purpose of the gate oxidation was to form a very thin oxide layer to act as a damper for the ion implantation step. The oxidation process was identical to the ones described previously but the conditions were different, as mentioned in Table 2.8. The wafer was packaged into a specialized container to be shipped for commercial processing for ion implantation step (performed by Core Systems Inc.). The ion implantation was performed for obtaining the p-layer in the wafer. Boron was used to form a region of the p-layer on the n-type wafer. The conditions for the boron ion implantation are summarized in Table 2.9.

Table 2. 8 Gate oxidation process conditions.

Steps	*Oxidation Type*	*Time*	*Temperature*	*Pressure*
1	Dry O_2	10 min.	1100 °C	1 atm
2	Wet O_2	10 min.	1100 °C	0.9 atm
3	Nitrogen (N_2) only	10 min.	1100 °C	1 atm

.

Table 2. 9 Ion implantation condition (B+).

Item	*Detail*
Machine	3015
Wafer Size / Scan	3”
Side	Front
Species	B+
Dose	1.2 e14
Energy (keV)	100

Table 2. 9 Continued

Item	Detail
Offset	7
Current (μA)	75
Area (cm^2)	1821
Mode	Hybrid
Vacuum (Torr)	7.0 e -07

- Annealing of Implanted Boron and "Emitter" Process

Upon receiving the ion implanted wafer back from Core Systems (with implanted Boron), the wafer was cleaned in piranha and annealed in a furnace. The processing conditions for this step are listed in Table 2.10.

Table 2. 10 Steps for annealing boron.

Steps	*Oxidation Type*	*Time*	*Temperature*	*Pressure*
1	Nitrogen (N_2) only	200 min.	1100 $^\circ C$	1 atm
2	Wet O_2	10 min.	1100 $^\circ C$	0.9 atm
3	Nitrogen (N_2) only	10 min.	1100 $^\circ C$	1 atm

After the annealing process, the wafer was cleaned and subsequent steps were performed to realize the “Emitter” device. Photolithography was performed to open the oxide layer for realizing the n-region in the p-well. In short, an opening in the oxide layer was performed create the n-region window on top of the p-layer. The opening in the oxide layer was devised for either ion implantation of Arsenic or by Phosphorous diffusion.

- Arsenic Ion Implantation

The wafer was sent to the same company (Core Systems) for ion implantation of As for the n-layer through the window created from the emitter process. The conditions for the arsenic ion implantation are summarized in Table 2.11. Upon receiving the wafer after the As ion implantation, the wafer was first cleaned in piranha and annealed in the furnace using the processing conditions described in Table 2.12.

Table 2. 11 Ion implantation condition (As+).

Item	*Detail*
Machine	3015
Wafer Size / Scan	3”
Side	Pattern
Species	As+

Table 2. 12 Continued

Item	Detail
Dose	1.0 e16
Energy (keV)	100
Offset	70
Current (μA)	200
Area (cm^2)	62.55
Mode	X4
Vacuum (Torr)	2 e -06

Table 2. 13 Steps for annealing arsenic.

Steps	*Oxidation Type*	*Time*	*Temperature*	*Pressure*
1	Dry O_2	10 min.	1000 $^\circ C$	1 atm
2	Wet O_2	60 min.	1100 $^\circ C$	0.9 atm
3	Nitrogen (N_2) only	15 min.	1100 $^\circ C$	1 atm

- Contact Opening

The annealed wafer was prepared for subsequent processing steps. The wafer was cleaned using the cleaning protocol described earlier, followed by spin coating of photoresist. The contact opening in the oxide layer was obtained by photolithography using Mask #3. This was followed by etching of the oxide layer using BOE solution.

- Metallization

With the contact opening on the wafer, a metal layer was deposited and patterned in order to obtain the bond pads (for connecting the lead wires). Metallization was performed by evaporating Al onto the wafer using the metal evaporator at MCF (Material Characterization Facility) at Texas A&M University. The target thickness of the metal layer is 3000Å~4000Å. In this study the target thickness for metal deposition using PVD was set to 3500Å. The metal evaporation was performed at the chamber pressure of $4 \times 10^{-7} \left[torr \right]$. Five pure Al targets were placed on a tungsten boat. The thickness of the metal layer was monitored using a crystal monitor/ indicator. After the metal evaporation step, the wafer was ready for the final processing step. Since the pattern for the metallization step used a negative mask, the wafer was coated with the Al layer prior to the photolithography to realize the required pattern. The wafer was spin-coated with photoresist after the metal deposition, followed by exposure on the mask aligner and immersion in developer bath (along with rinsing in DI water). The developer solution was prepared by mixing 1 portion of A400K and 4 portions of DI water. The exposed Al layer was etched using Al etchant using an etching time of 4 minutes. After the etching process, the wafer with the metal features was cleaned in piranha and dried. Fabrication for the diode temperature sensor is finalized. Figure 2.23 shows the oxide opening for metallization under the 3D microscope.

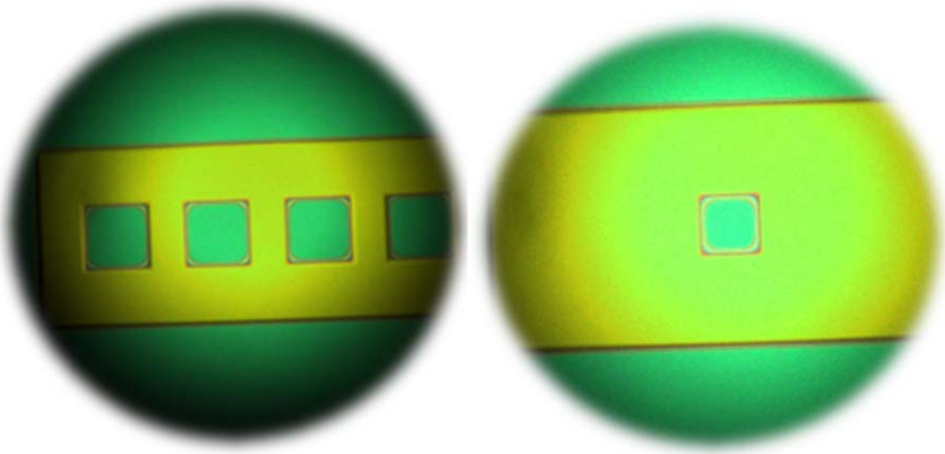

Figure 2. 23 Image of the oxide opening for metallization. The image was obtained using a 3D microscope.

D. Droplet Cooling Experiment

a. Introduction

The diode temperature sensor's electrical output was calibrated and correlated to the surface temperature of the silicon substrate. The correlation constants were obtained by measuring the steady state response of the sensors. The electrical response of DTS can be affected by illumination, humidity, ambient temperature, electro-magnetic interference (emi) from the distant power cables as well as other devices in the proximity of the probe station. In addition, continued oxidation of the diode temperature sensor itself and the heat transfer from (or to the) diode can affect the calibration as well as temperature measurements. The primary objective was to evaluate the feasibility of the fabricated DTSA for transient measurements of the surface temperature fluctuations during droplet impingement cooling experiments. Hence, calibration curves were generated by applying different bias voltages. In this chapter the experimental hardware and the data acquisition equipment are described that were used for the calibration step. Thermal measurement using the infrared camera was performed simultaneously for minimizing the measurement uncertainty during calibration.

b. Description of Experimental Apparatus

The experimental apparatus consists of a probe station with 2 micro-positioners that are connected to the data acquisition device (DAQ). A syringe pump is positioned next to the probe station to supply the droplet using a tube placed directly above the DTSA. The data was recorded using PC which was connected to the DAQ. A black box was used to minimize the illumination of the DTSA from external light sources. The silicon wafer was placed on a hot plate that was maintained at a fixed temperature for each experiment. Figure 2.24 shows the image of the fabricated Diode Temperature Sensor. Figure 2.25 shows the droplet cooling experiment picture within the probe station. Figure 2.26 shows additional K-type thermocouples attached onto the test substrate for surface temperature monitoring and calibration purposes.

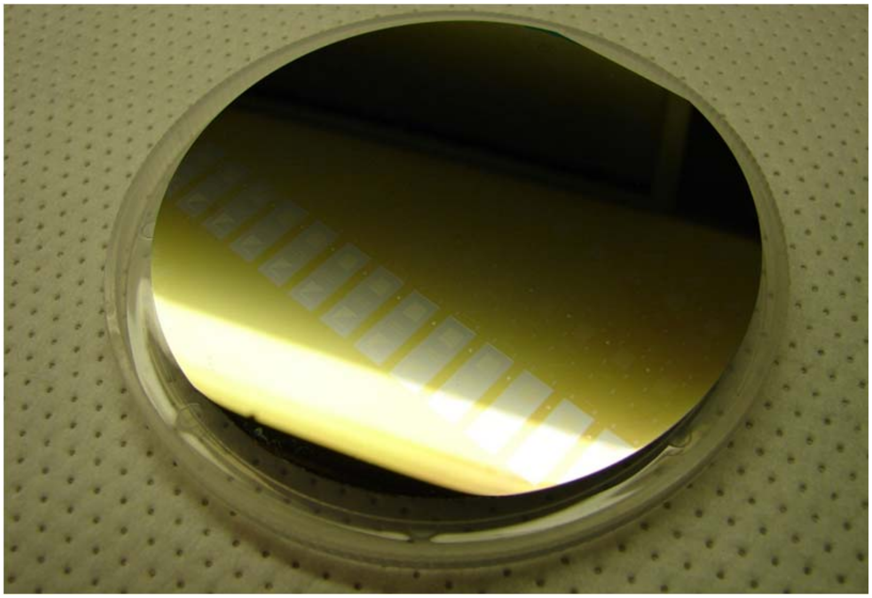

Figure 2. 24 Image of diode temperature sensor array fabricated on a silicon wafer.

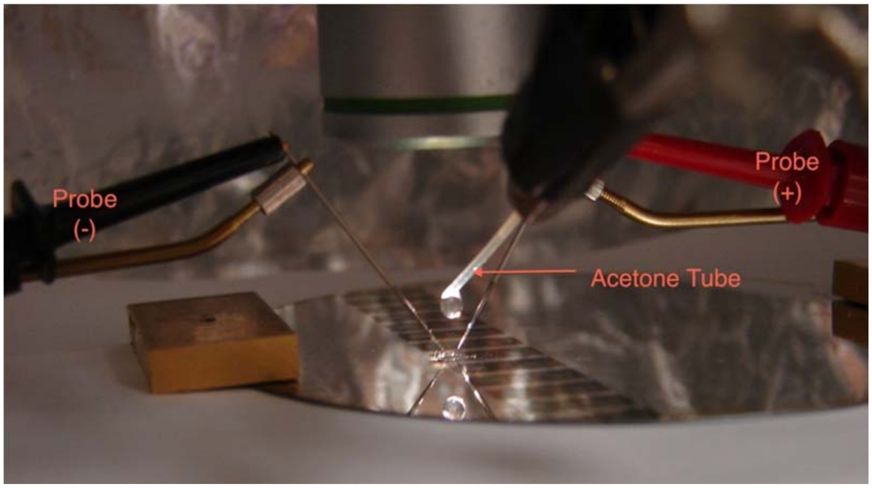

Figure 2. 25 Droplet impingement experiment using acetone.

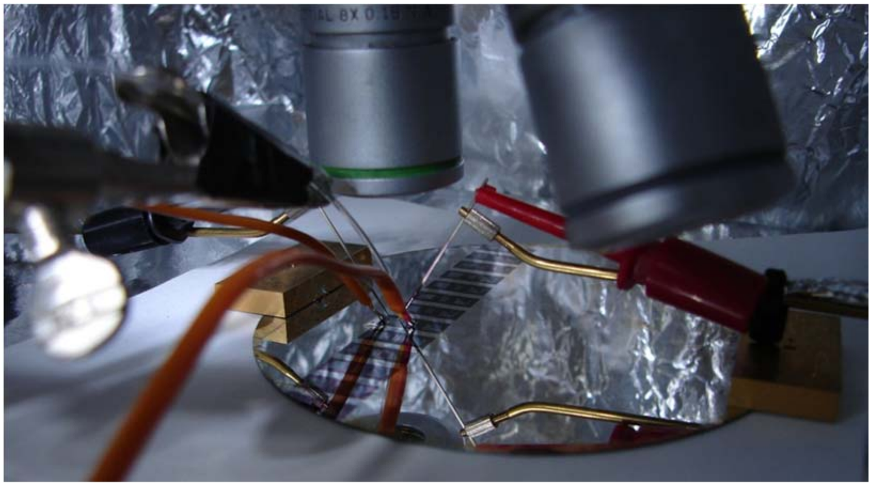

Figure 2. 26 Image showing a close-up view of the experimental apparatus.

c. Experimental Procedure

The experiments were performed in the dark by enclosing the experimental apparatus in a black box to avoid illumination of the DTS. The flow rate in the syringe pump was fixed to a constant value and the time from one droplet to the other was measured using the stop watch before the experiment. In each experiment 10 droplets were fed through the syringe pump continuously and the data was saved into a text file for each drop. The raw experimental data in ASCII text format was then imported into MS-Excel® spreadsheet for further analysis. K-type thermocouple was installed on the surface of the wafer for continuous monitoring of steady state conditions. The surface temperature monitoring using K-Type thermocouples was performed with a separate data acquisition device (from National Instruments using SCXI module with a sampling rate of 200Hz). The surface temperature was monitored in real time. As soon as the steady state conditions were detected for the surface temperature, the droplet impingement cooling experiments were resumed.

d. Data Acquisition System

Two measurement instruments were used in the calibration for the DTS as well as the actual droplet cooling experiment. NI DAQ was used to detect the steady state response of the DTS. Keithley 2400 SMU was used to measure the transient current response at a fixed biased voltage. NI DAQ that was used in this study consisted of a thermocouple amplifier, a signal conditioning module, isothermal terminal block and an M-series multifunction DAQ device that can record data at 5 KHz. The data collection and DAQ interfacing was performed by LABVIEW® software. Keithley 2400 SMU was used for characterizing the current versus voltage plot as well as the transient current output at a fixed bias voltage applied to the DTS.

The temperature of the hot plate was fixed to achieve a desired temperature level for each experiment. The actual temperature on the surface of the wafer (measured by the DTS) was different from the temperature set on the hot plate. Hence a K-Type thermocouple was used to monitor the steady state surface temperature of the silicon wafer. The hot plate was allowed to reach steady state conditions for each temperature setting. The temperature on the surface of the wafer (from the K-type thermocouple) was carefully monitored in LABVIEW® in real time for monitoring the steady state conditions. After steady state conditions were achieved, the DAQ system is used to record the thermocouple readings for a period of two minutes at a rate of 200 Hz. The raw data was then checked and averaged. The hotplate temperature was increased in steps of 10 °C or 15 °C and the calibration procedure was repeated.

When steady state condition was reached, the Keithley 2400 SMU was used to measure the output current from the diode temperature sensor with bias voltages ranging from -5.0V to 5.0V in steps of 0.5V increment. The calibration process was repeated for 3 times to ensure the repeatability. Table 2.13 summarizes the data acquisition hardware from national instruments.

Table 2. 14 NI DAQ equipment details.

Part No.	*Detail*	*Remark*
776570-01	SCXI-1000 4 Slot Chassis (120 VAC)	Chassis
776572-02	SCXI-1102 32-Channel Thermocouple Amplifier. Signal Conditioning Module for thermocouples and low bandwidth millivolt, volt, and current inputs.	Thermocouple Module
777687-00	SCXI-1300 General Purpose Screw Terminal Block, Cast.	Pressure Connection
776576-60	SCXI-1360 Front Filler Panel. Covers one empty slot (Front).	Cover
776576-61	SCXI-1351 Rear Filler Panel. Covers one empty slot (Rear).	Cover
182671-01	SCXI-1349 Bracket / Adapter Assembly. Connects the modules to the PC.	Adapter
192061-02	SHC68-68-EPM Shielded Cable, 68-D-Type to VHDCI Offset, 2m.	Cable
781048-01	NI PCIe-6351, X Series Multifunction DAQ (16 Al, 24 DIO, 2 AO), 1.25 MS/s single-channel sampling.	PCIe Card

e. Calibration

The calibration curves were obtained by placing the wafer with the DTSA on a hot chuck. The performance of the diode temperature sensor was measured using the Alessi probe station with micro-positioners that were connected to the source meter. Steady state temperature conditions were ensured before recording the sensor response with the source meter. Surface temperature monitoring for the steady state conditions was performed using the NI SCXI DAQ. As soon as the steady state temperature conditions were reached, the bias voltage was varied in the range of -5.0 V to 5.0 V in steps of 0.5V. The resulting current output was recorded in a text file. The following picture shows the measurement devices without the dark chamber in place (Figure 2.27).

In order to conduct the droplet cooling experiment, two fluids were selected. One is Acetone and the other Ethanol. The following graphs represent the calibration curves for each of the fluids. A forward bias of 1.5V for Acetone and 2V for Alcohol was selected. Figure 2.27 shows the general setup of the droplet cooling experiment without the black chamber cover over the probe station. Figure 2.28 and 2.29 represent the calibration curves for acetone and ethanol respectively.

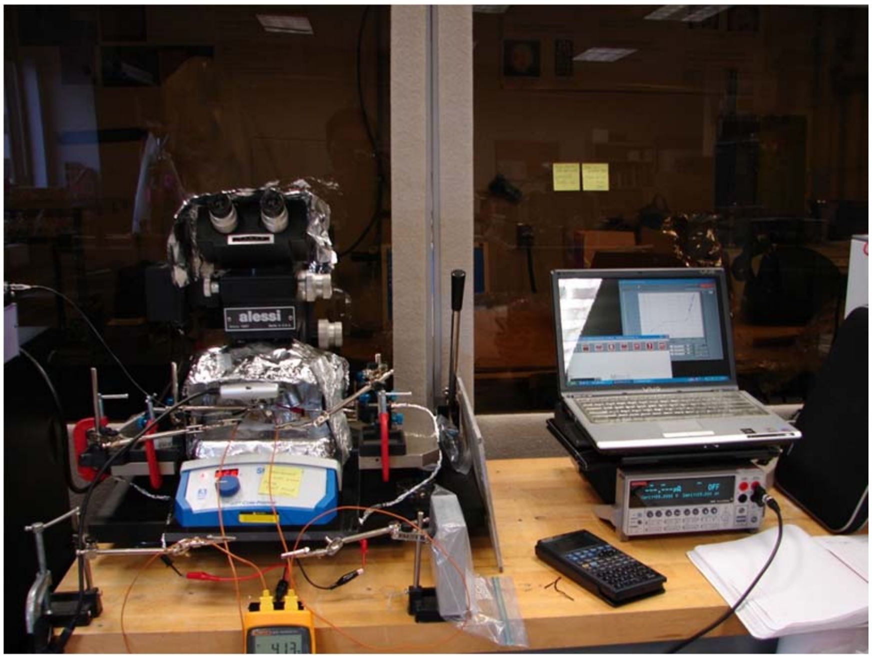

Figure 2. 27 Droplet cooling experiment rig.

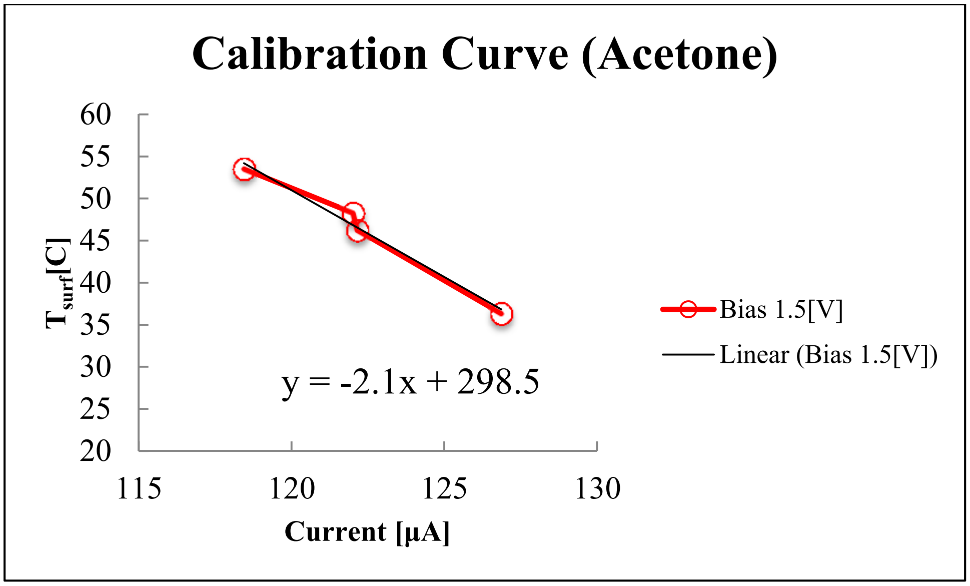

Figure 2. 28 Calibration curve (Acetone)

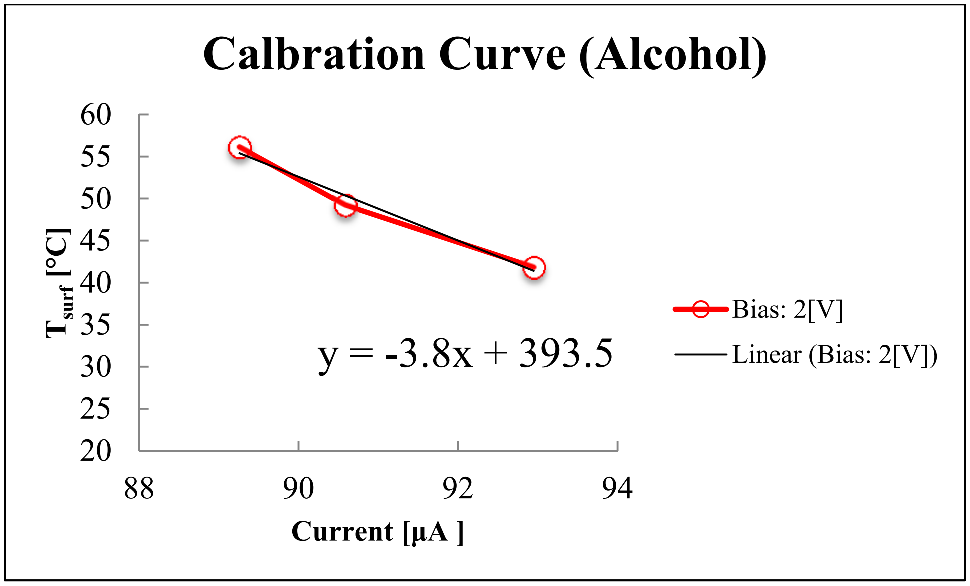

Figure 2. 29 Calibration curve (Ethanol)

f. Comparison with the IR Data

Infrared camera (Manufacturer: Fluke) was used to calibrate the surface temperature of wafer at the location of the DTS. As mentioned before a K-type thermocouple was placed on the silicon surface for monitoring the steady state surface temperature. After reaching steady state conditions, the IR images were obtained and edited using the SmartView 3.1.82.0 software (provided by Fluke Thermography Inc.). The following IR images are presented for each hot plate temperature setting and the corresponding surface temperature values are summarized below (in °F).

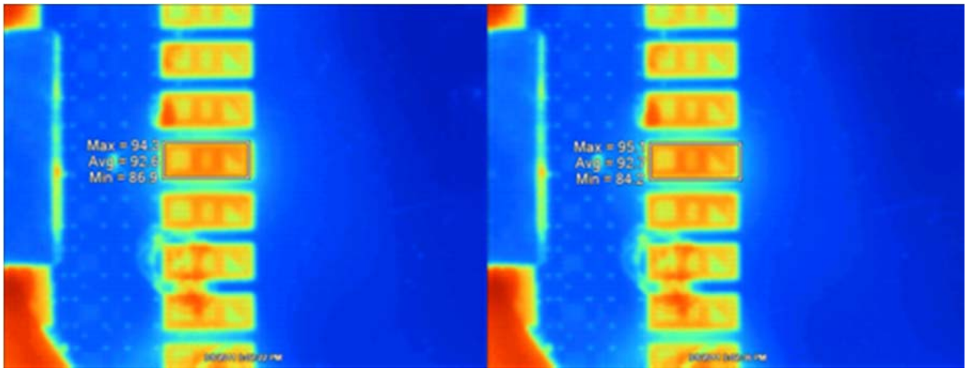

Figure 2. 30 Hot plate indicator 40°C – thermocouple 35.7°C

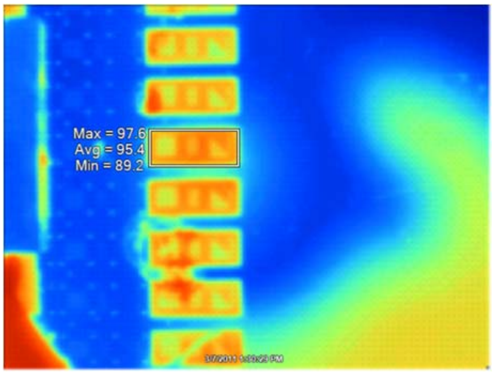

Figure 2. 31 Hot plate indicator 45°C – thermocouple 38.6°C

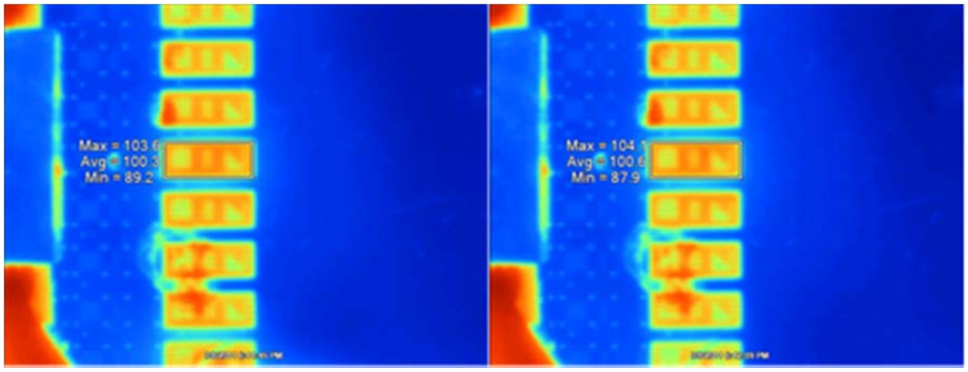

Figure 2. 32 Hot plate indicator 50°C – thermocouple 41.3°C

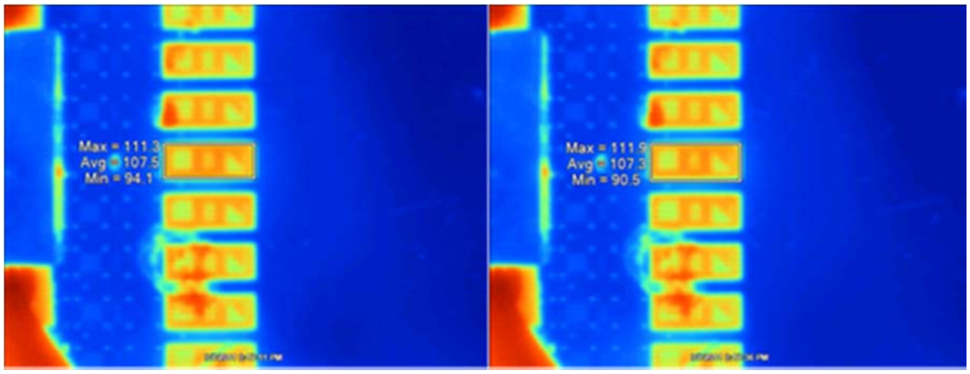

Figure 2. 33 Hot plate indicator 55°C – thermocouple 48.3°C

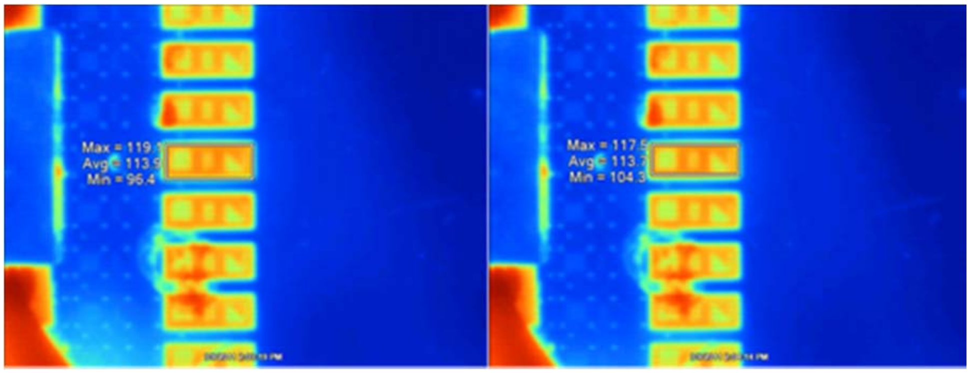

Figure 2. 34 Hot plate indicator 60°C – thermocouple 52.5°C

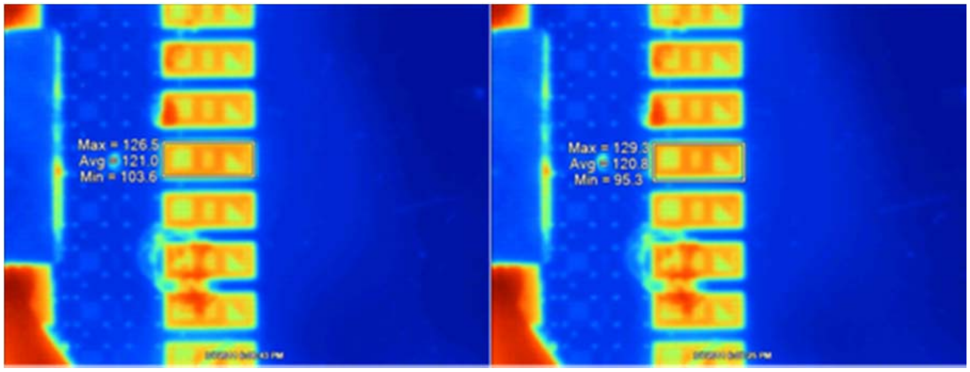

Figure 2. 35 Hot plate indicator 65°C – thermocouple 57.1°C

For each image, Row #4 of the DTSA was chosen as the region for measurement. The square indicates temperature measurement for Row #4 in the images. The average, maximum and minimum value of the IR data for temperature is shown in the images. The units are in °F. Table 2.14 summarizes the data in °C. Figures 2.30 – 2.35 represents the infrared camera image taken for each surface temperature of 35.7ºC, 38.6 ºC, 41.3 ºC, 48.3 ºC, 52.5 ºC and 57.1 ºC. Each image was taken at a steady state of the surface temperature at the identical distance between the infrared camera and the diode temperature sensor.

Table 2. 15 IR calibration for DTSA.

Hot Plate Ind. [°C]	*Thermocouple [°C]*	*IR Camera [°C] avg.*	*IR Camera [°C]*
40	35.4	33.7	35.1
45	36.8	35.2	36.4
50	40.5	37.9	40.1
55	44.7	42.0	44.1
60	48.9	45.4	48.4
65	54.7	49.4	54.1

From Table 2.14, the difference in temperature for the thermocouple and the IR camera is observed to range from 0.3°C ~ 0.6°C. Since the thermocouple for monitoring the surface temperature was positioned at the perimeter of the wafer, where higher temperature were observed from the IR images, it was expected that the thermocouple would record slightly higher values compared to the temperature recordings by the IR Camera.

g. Data Analysis

In this section, temperature results with respect to time are plotted as the result of the experiment. To setup the schematic for calculation, Figure 2.36 depicts a schematic of the single droplet impingement experiments.

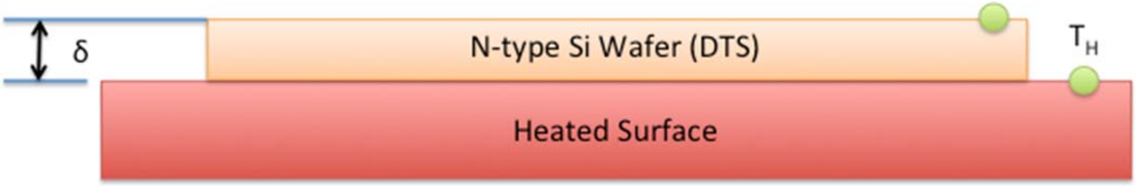

Figure 2. 36 Schematic of droplet impingement experiments and analysis (T_w: measurement by DTS, T_H: hot plate temperature).

T_w and T_H correspond to the surface temperature of the Silicon wafer where the DTS is fabricated and the surface of the heated surface where the DTS is on. δ refers to the thickness of the wafer provided by the manufacturer.

The surface temperature of the DTS was recorded as a current while performing the droplet impingement test. The current data was then converted into temperature using the calibration curve of each fluid. The data was analyzed for natural convection and the two phase region which refers to before the actual drop impact on the surface and after the impact on the surface respectively.

For natural convection region which is before the droplet impacts the surface, the time when the droplet actually hit the surface was recorded to identify the region for the natural convection. Then, the duration of the natural convection was separated into three identical time period regions. The second portion of the total natural convection region was selected for the calculation of the DTS surface temperature. With the averaged DTS surface temperature in natural convection region, the Rayleigh number (Ra) was calculated according to the following formula;

$$\mathrm{Ra} = \frac{g\beta(T_{DTS,avg} - T_{room}) \times L^3}{\upsilon\alpha} \tag{2.16}$$

where, $T_{DTS,avg}$ is the average value surface temperature data recorded by the DTS prior to start of the droplet impingement experiments, and T_{room} is the ambient temperature, L is the characteristic length of the wafer (hot surface), ν is the dynamic viscosity and α is the thermal diffusivity of air.

The thermophysical properties were obtained from the standard air thermophysical table for the corresponding DTS average temperature in the natural convection regime.

The Nusselt number for this experiment was computed as:

$$\mathrm{Nu_{NC}} = 0.54 \times \mathrm{Ra}^{0.25} \tag{2.17}$$

The Nusselt number value was then used to obtain the heat transfer coefficient:

$$\mathrm{h_{NC}} = \frac{\mathrm{k_{air} \cdot Nu_{NC}}}{\mathrm{L}} \tag{2.18}$$

where the $\mathrm{k_{air}}[\mathrm{W/m \cdot K}]$ refers to the thermal conductivity of the air.

The natural convection heat flux was calculated by using the temperature difference between the average value of DTS measurements for the surface temperature in natural convection region and the room temperature, as:

$$\mathrm{q''_{NC}} = \mathrm{h_{NC}} \times \left(\mathrm{T_{DTS,avg}} - \mathrm{T_{room}}\right) \tag{2.19}$$

Thermal contact resistance $\mathrm{R_c}$, between the hotplate and the wafer is expressed as:

$$\mathrm{R_c} = \frac{\mathrm{T_{HP}} - \mathrm{T_{DTS,avg}}}{\mathrm{q''_{NC}}} \tag{2.20}$$

where , $T_{DTS,avg}$ is the average value surface temperature data recorded by the DTS prior to start of the droplet impingement experiments, and T_{HP} is the hot plate temperature programmed to be at a constant value on the hot plate controller.

The two phase heat flux was then expressed in terms of the thermal contact resistance as:

$$q''_{2P} = \frac{T_{HP} - T_{DTS}}{R_c} \tag{2.21}$$

where , T_{DTS} is the transient surface temperature data recorded by the DTS during the droplet impingement experiments.

The heat transfer coefficient for two phase droplet impingement cooling experiments was then calculated using the following equation.

$$h_{2P} = \frac{(T_{HP} - T_{DTS})}{q''_{2P}} \tag{2.22}$$

The raw data was imported into a spreadsheet (using MS-Excel®) and the calculation mentioned above was performed. Graphs for transient value of temperature, heat flux (q''_{2P}) and heat transfer coefficient (h_{2P}) were plotted.

CHAPTER III

RESULTS AND DISCUSSION

A. Flow Boiling

a. Infra-Red (IR) Image Analyses for Surface Temperature Calibration

IR images were obtained using an IR camera (Manufacturer: Fluke, Model: IQ50) to calibrate the surface temperature of the test surface as a function of the thermocouple reading from the copper block. The images were acquired when the temperature fluctuation of the copper block was observed to decay to a minimum value (assuring steady state conditions were reached). When steady conditions were achieved the temperature fluctuations were observed to be less than ±0.3°C of the mean value. Figure 3.1 shows the sequence of the IR images that were used for calibrating the surface temperature of the test surface to that of the copper block temperature.

b. High Speed Digital Image Acquisition

The high speed digital image acquisition apparatus was used to record the bubble nucleation, growth and departure cycles on the boiling surface. Figure 3.2 shows the sequence of images obtained from a representative flow boiling experiment.

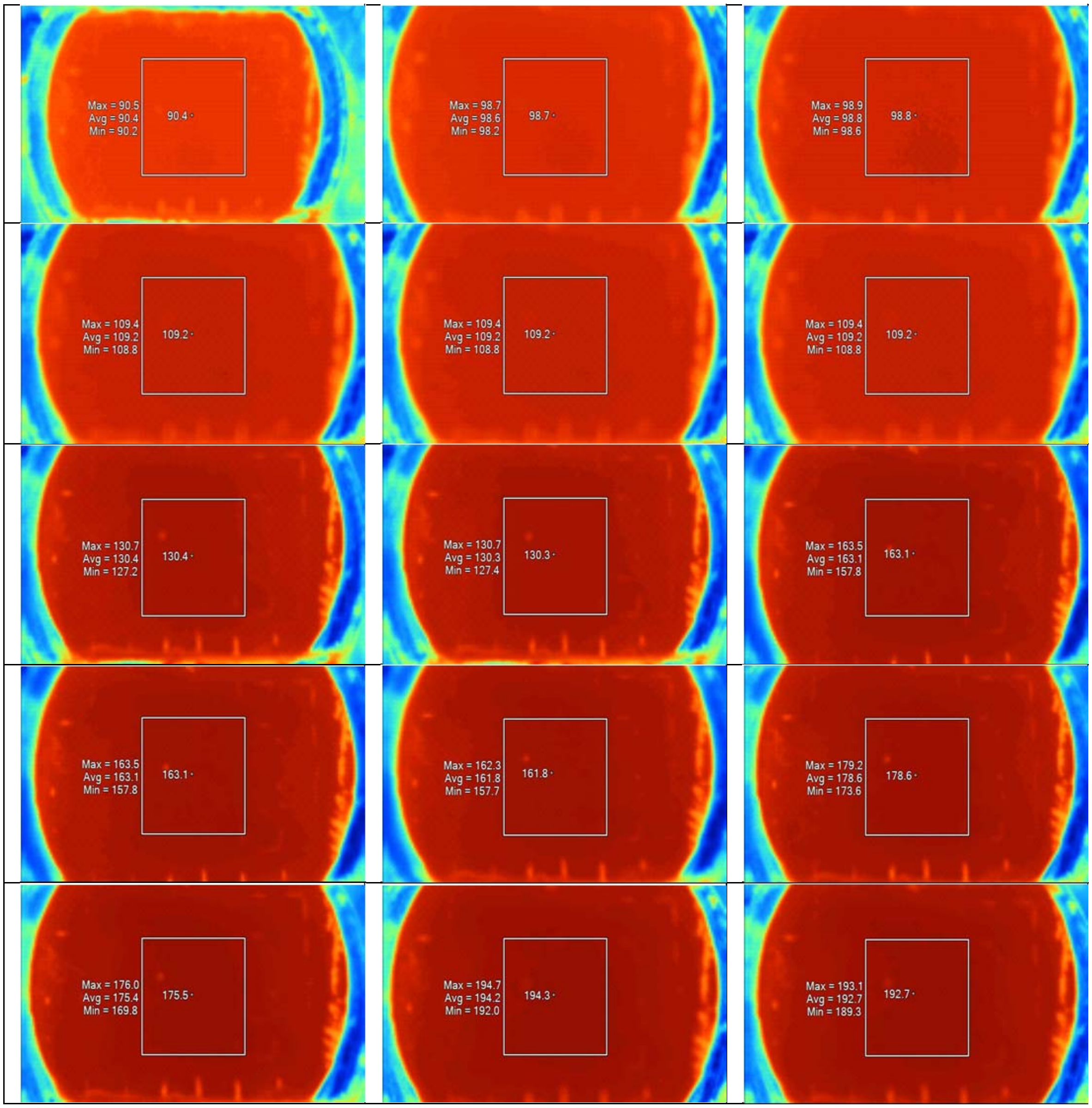

Figure 3. 1 IR images of the surface of the copper block.

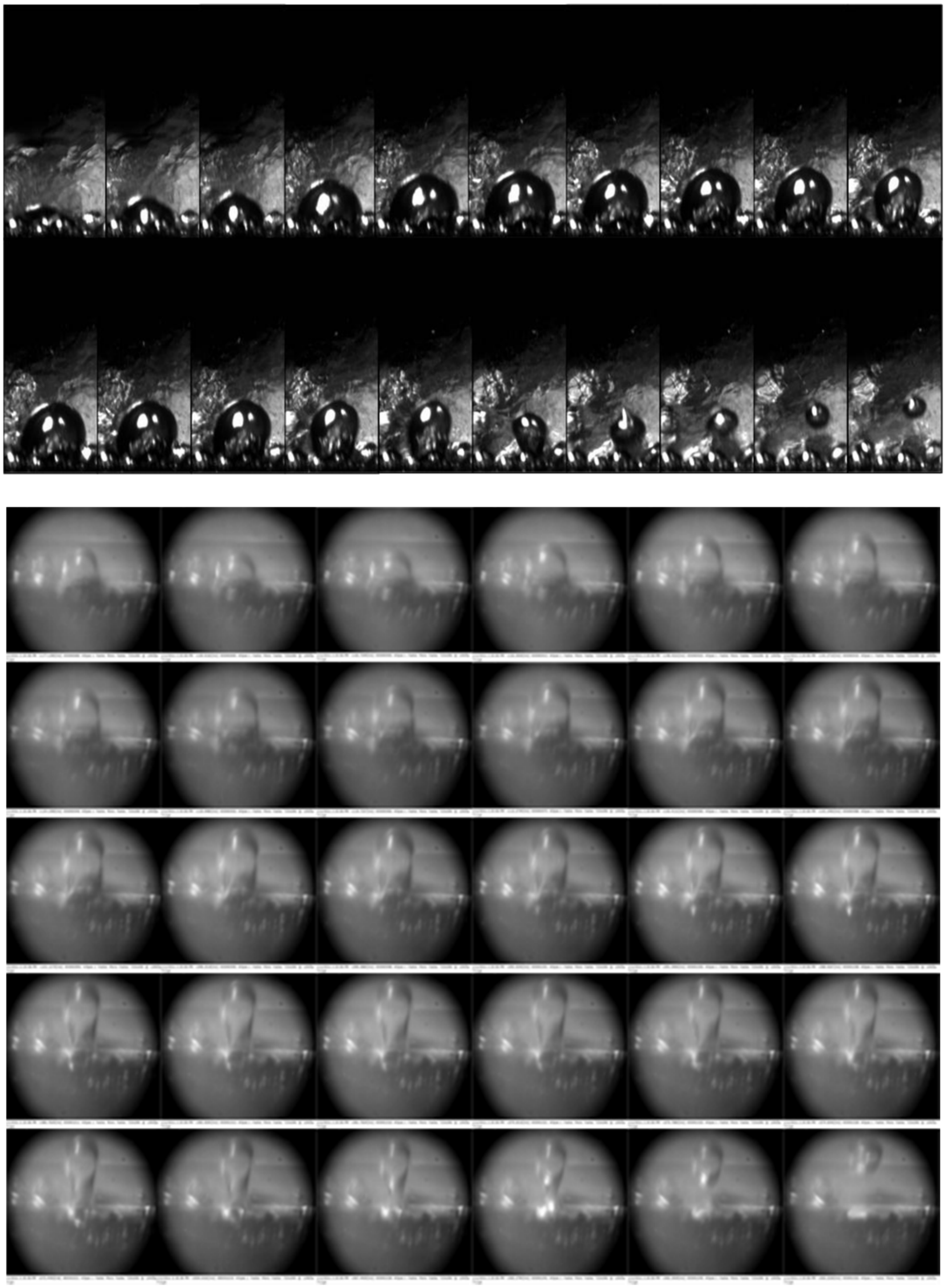

Figure 3. 2 Sequence of high speed digital images for bubble growth and departure.

c. Characterization of MWCNT Coated Silicon Wafer Substrates

A set of silicon wafer were coated with MWCNT. The silicon wafer surface was initially dices to the dimensions shown in Figure 2.1. A layer of iron was deposited using PVD to a thickness of ~ 20nm. The wafer was then placed in the CVD furnace to obtain the MWCNT coating. Figures 3.3 and 3.4 show the Scanning Electron Microscopy (SEM) images of the MWCNT coating showing that the MWCNT were ~ 20-30 nm in diameter. The SEM images were obtained using an FE-SEM instrument located at the Microscopy and Imaging Center (MIC) at the Texas A&M University (The FE-SEM image acquisition was supported by the NSF grant DBI-0116835, the Office of the Vice President for Research, and the Texas Engineering Experiment Station).

d. Heat Flux Measurements

The heat flux data was analyzed by using the temperature gradients within the copper block in the calorimetry apparatus. The heat flux data was plotted as a function of the wall superheat from the flow boiling experiments in figure 3.5 for the three different test surfaces: bare copper surface, bare silicon substrate and MWCNT coated silicon substrate. From figure 3.5 it is observed that among all the surfaces Copper surface exhibits the highest wall heat flux (at a fixed wall superheat). Significant enhancement in the values of wall heat flux are observed for the case of MWCNT coated surface compared to that on bare Silicon surface. As the surface temperature increases, the enhancement in heat flux also increases.

This enhancement can be explained to be due to the following transport mechanisms: (a) higher thermal conductivity of MWCNT compared to Silicon, (b) disruption of microlayer by the presence of MWCNT, (c) increase in number of active nucleation sites (enhancement of number of nucleating bubbles per unit projected area of the boiling surface), and (d) “nano-fin” behavior of the MWCNT coating resulting in enhancement of the effective surface area for heat transfer. (e) The augmentation of the surface area due to the MWCNT coating also results in an enhancement of transient solid-liquid contact causing enhancement of transient heat conduction transfer (that is much smaller in magnitude for the bare silicon surfaces).

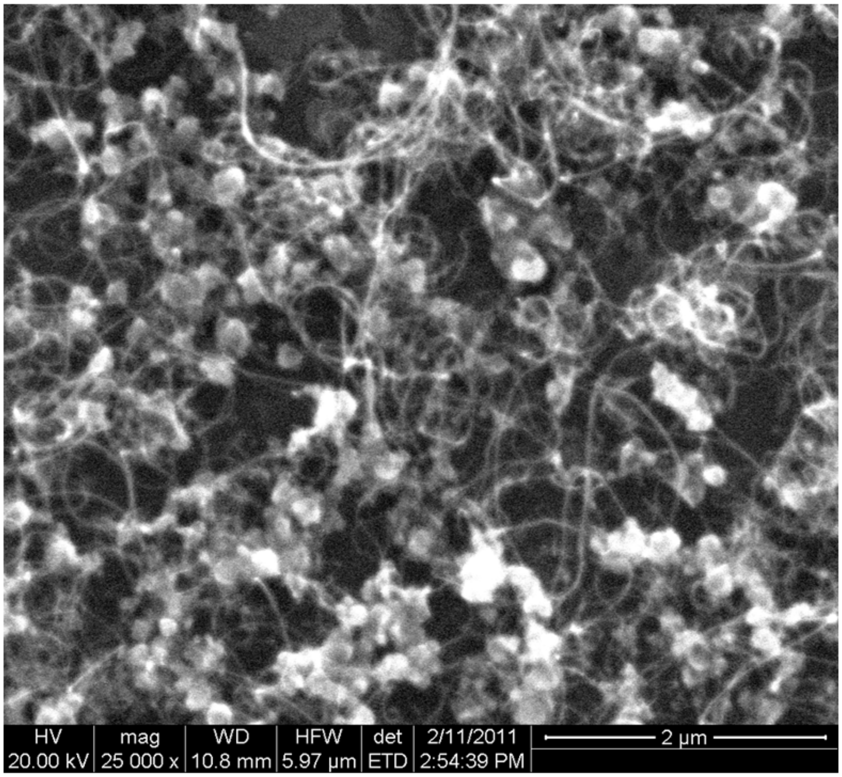

Figure 3. 3 CNT Forest on CNT coated silicon wafer (magnification 25,000X)

In nucleate boiling, the MWCNT tends to disrupt a thin layer of liquid film or “microlayer” that is believed to exist under the vapor bubbles leading to enhanced heat transfer. The number of nucleation sites is observed to increase for the wafers coated with MWCNT than that of a bare silicon wafer. This could be responsible for the significant enhancement in the heat transfer for nucleate pool boiling and flow boiling. The high thermal conductivity of MWCNT results in a very small temperature differential between the base and tip of the MWCNT. The presence of MWCNT enhances the effective heat transfer area thus acting as nano-fins.

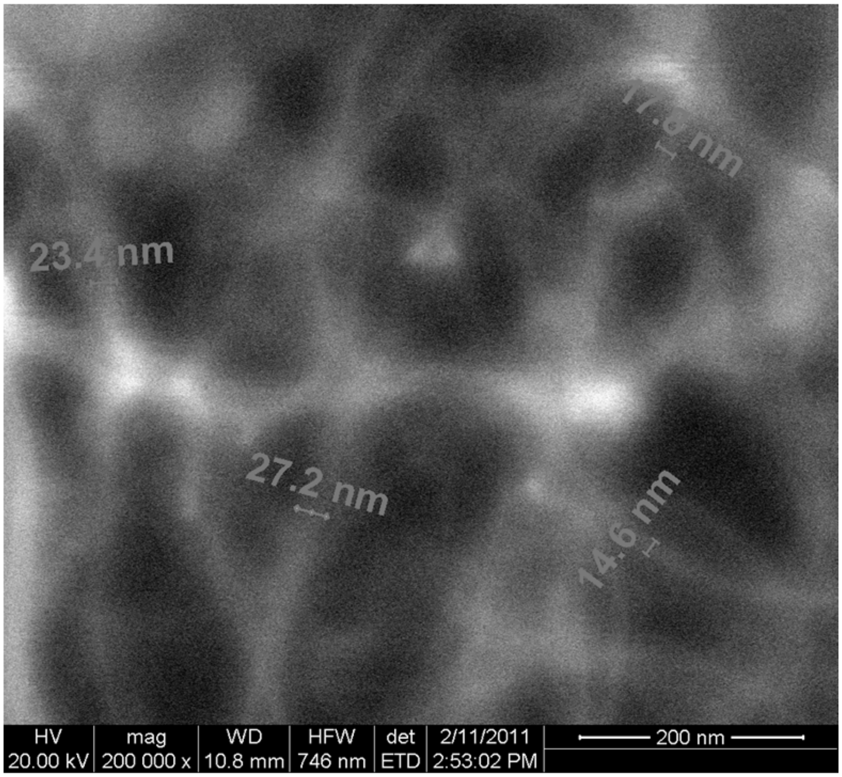

Figure 3. 4 CNT Forest on CNT coated silicon wafer (magnification 200,000X)

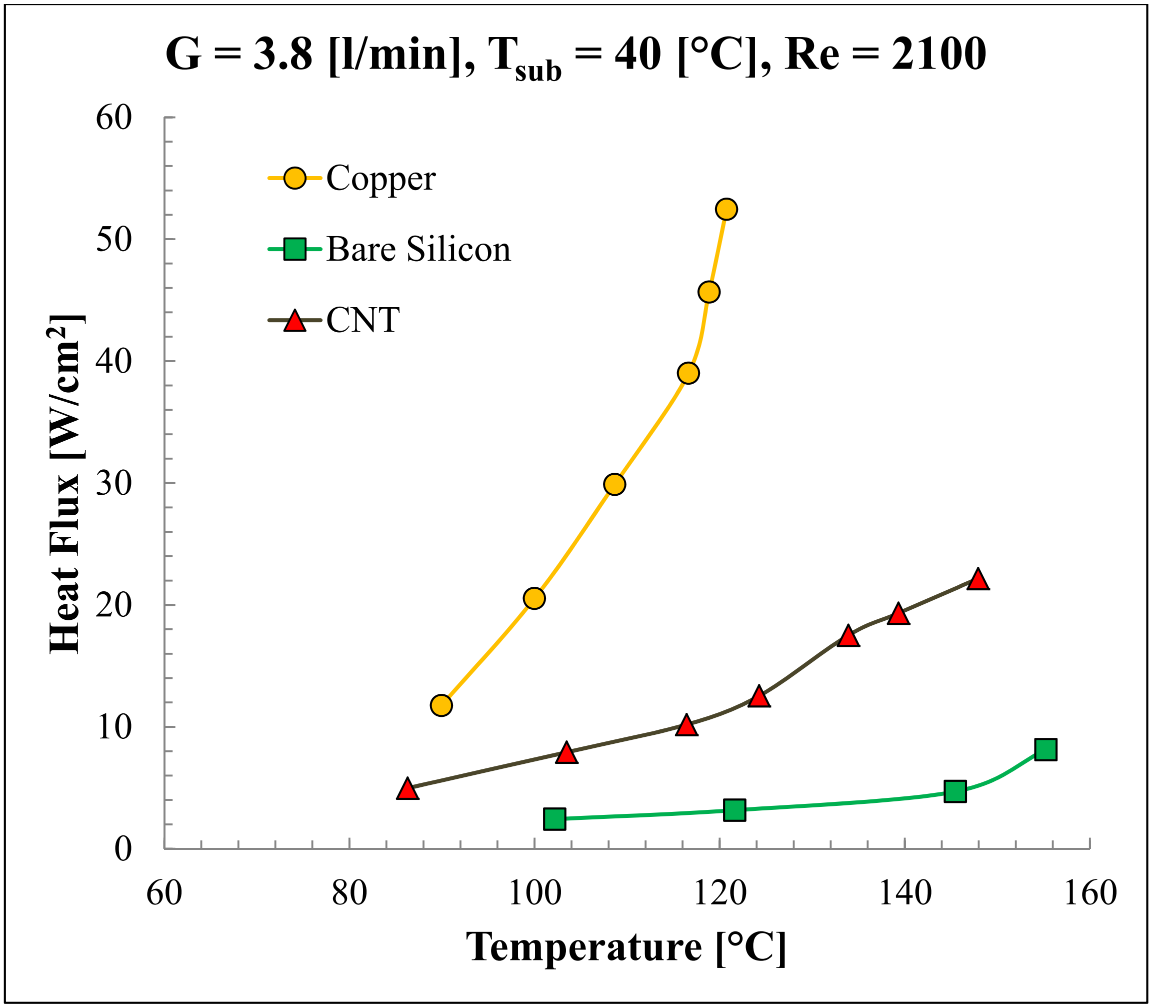

Figure 3. 5 Heat transfer performance curve for three different surfaces.

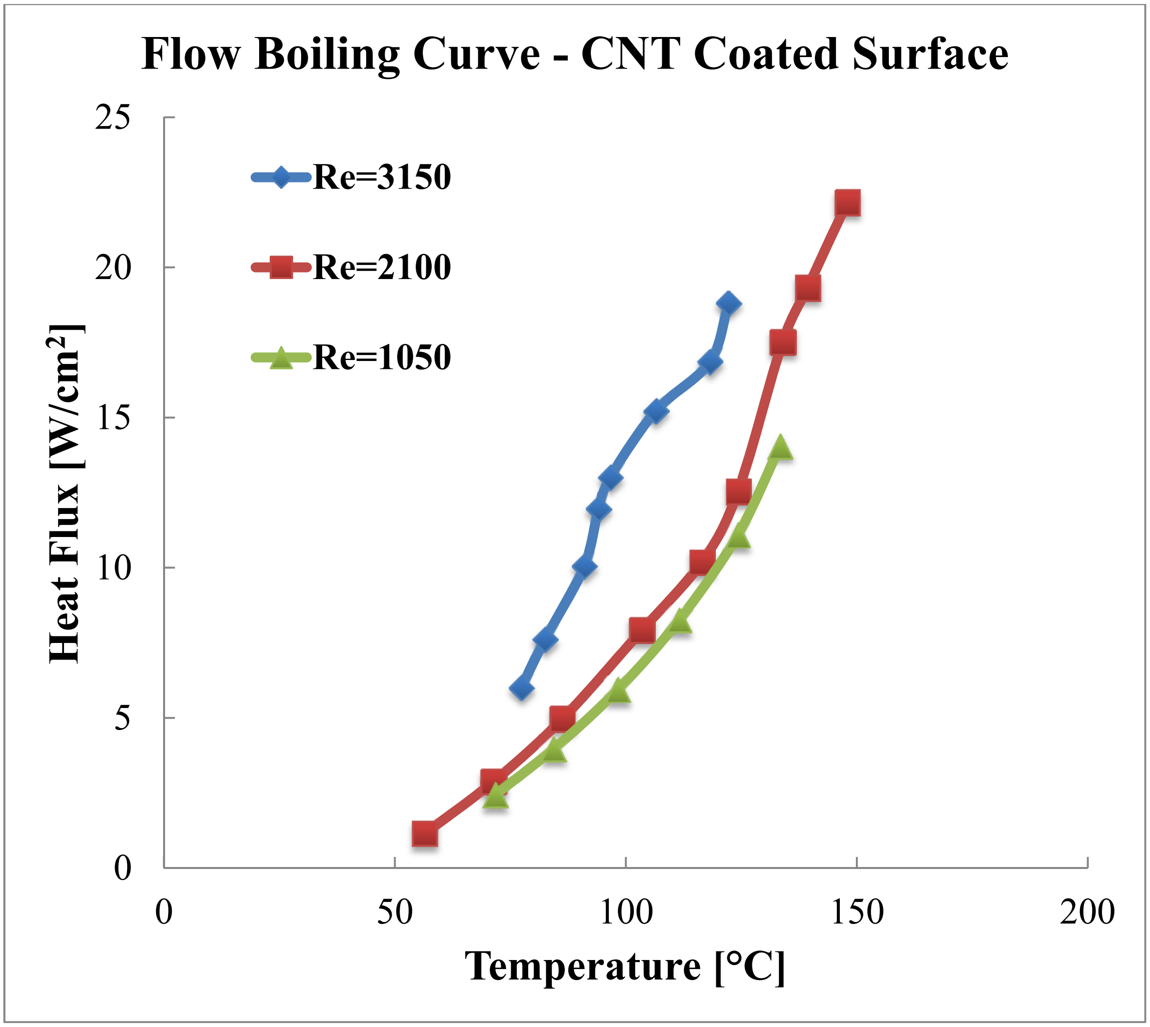

Figure 3. 6 Heat transfer performance curve for three different flow rates on CNT coated wafer.

Figure 3.6 shows the heat transfer performance for a CNT coated wafer with different Reynolds number. From Figure 3.6 it is observed that at higher Reynolds number, the heat flux is enhanced dramatically. Figures 3.7 – 3.11 show the bubble analysis results.

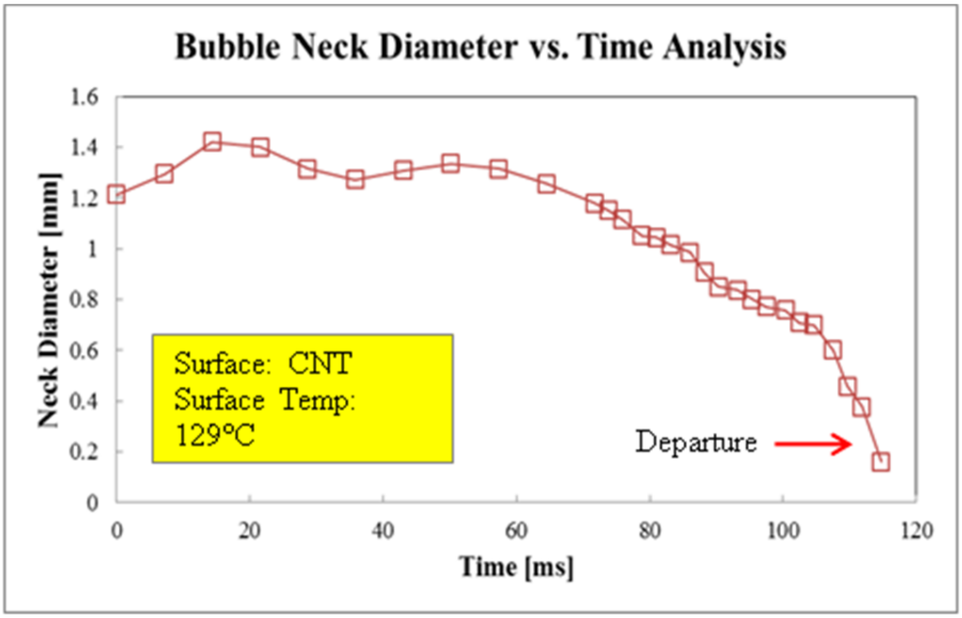

Figure 3. 7 Bubble neck diameter analysis with the time for a MWCNT coated substrate.

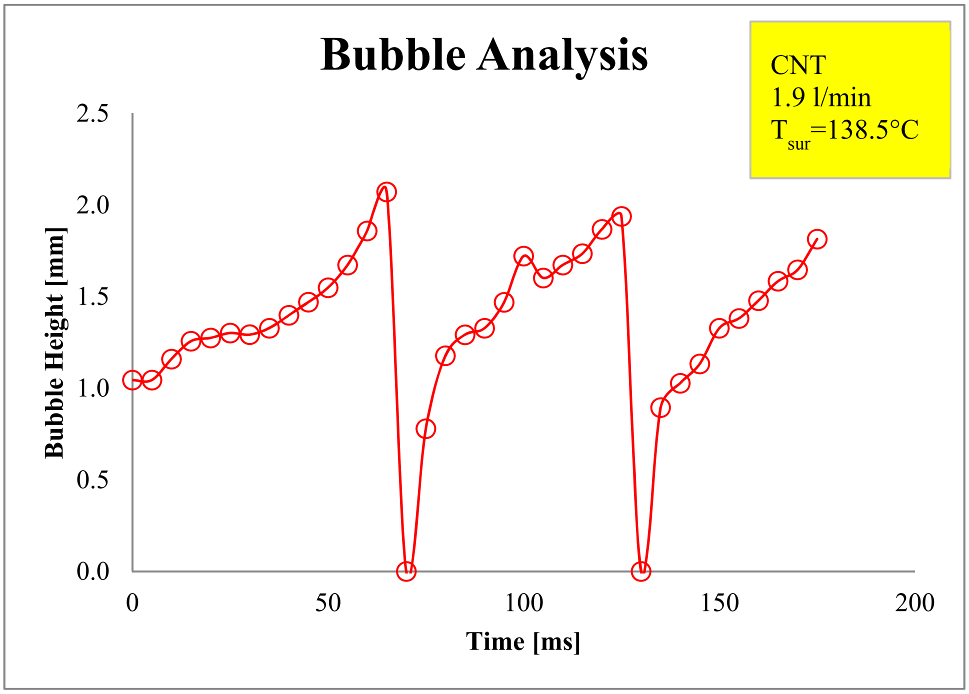

Figure 3. 8 Variation of bubble height with time in nucleate boiling regime for MWCNT coated substrate at 1.9 l/min.

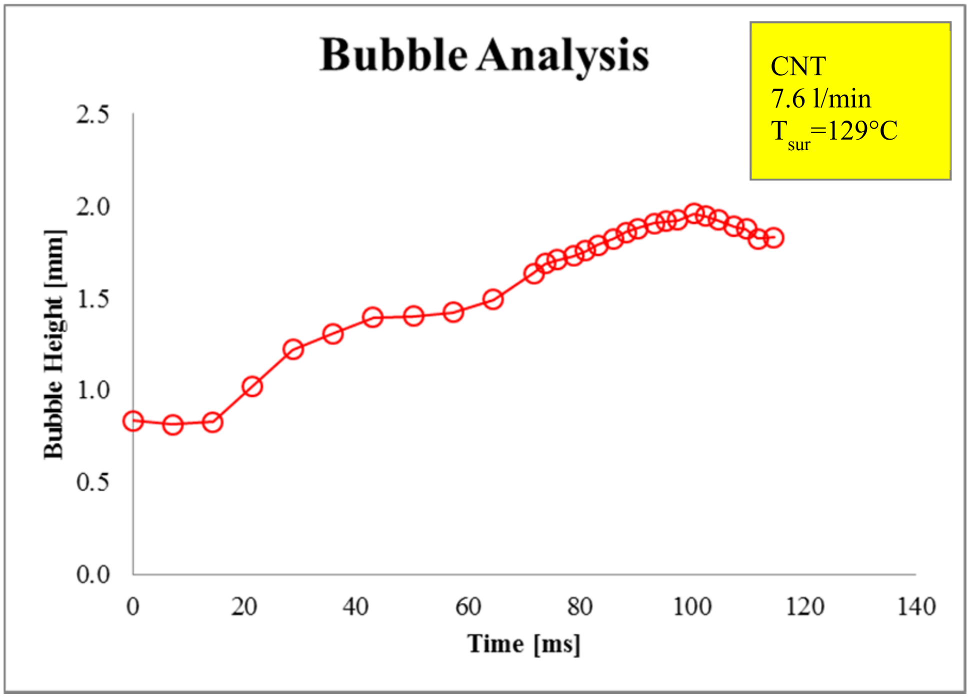

Figure 3. 9 Variation of bubble height with time in nucleate boiling regime for MWCNT coated substrate at 7.6 l/min.

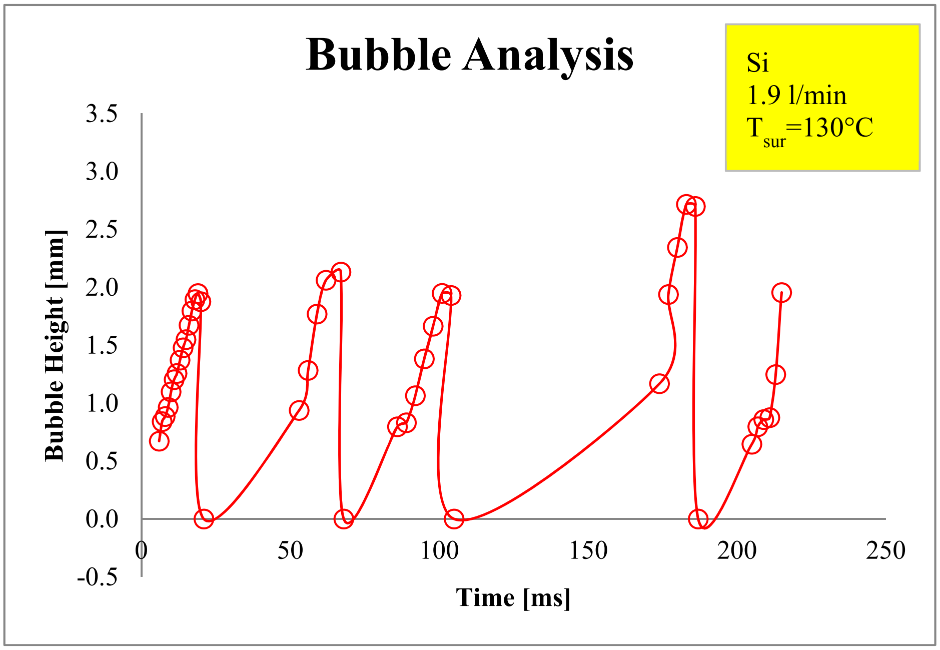

Figure 3. 10 Variation of bubble height with time in nucleate boiling regime for bare silicon wafer at 1.9 l/min.

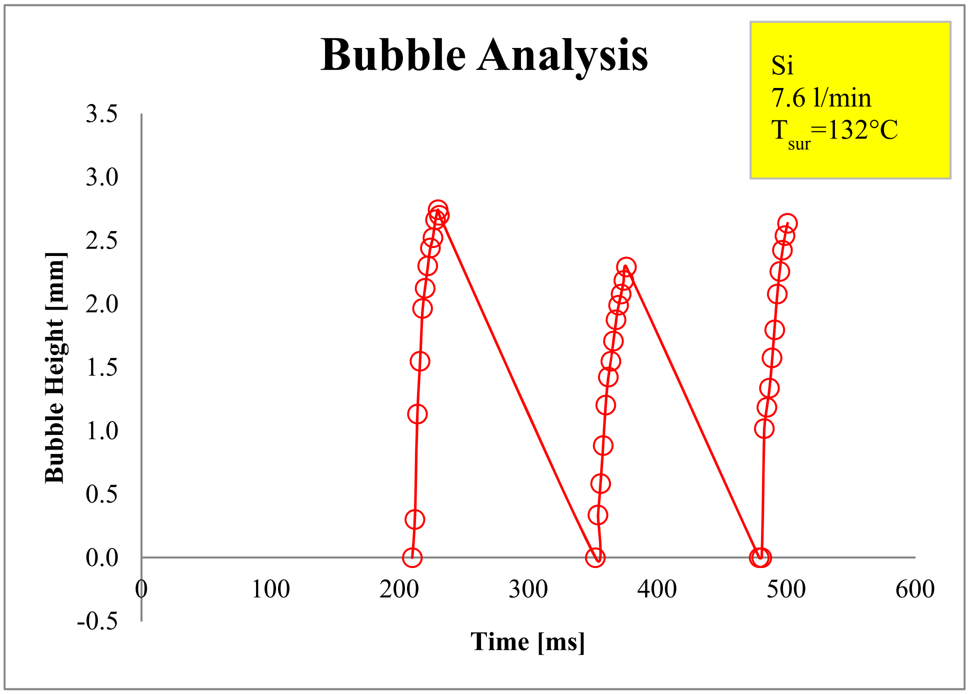

Figure 3. 11 Variation of bubble height with time in nucleate boiling regime for bare silicon wafer at 7.6 l/min.

e. Summary

The effect of MWCNT (Multi Wall Carbon Nano Tube) coating on flow boiling was experimentally investigated. Flow boiling experiments were conducted for three different surfaces which are pure copper, bare silicon wafer and MWCNT coated silicon wafer using deionized water as the working fluid. All the surfaces were tested in the nucleate boiling regime at 40°C sub-cooling. High speed video at 1000 ~ 1300 frames per second (FPS) was used to capture the bubble images.

Boiling curves were obtained from the experiments showing 230% of heat transfer enhancement on the substrate with CNT compared to the bare silicon wafer at the higher wall superheat. Experiments were also conducted with different flow rate of the working fluid for CNT coated substrate. It was observed that with a flow rate of 2GPM enhanced the heat transfer performance as much as 67% compared with lower Reynolds number.

Significant heat flux enhancement for CNT coated Silicon wafer in comparison with bare Silicon wafer was observed. This enhancement can be explained to be due to high thermal conductivity of the carbon nano-tubes, micro-layer effect, increase in solid-liquid contact area due to presence of CNT “nano-fins” (enhancement of transient conduction) and enhancement of active nucleation site density. As the surface temperature increases, the enhancement in heat flux was also observed to increase. The possible reasons for this phenomenon are higher thermal conductivity of MWCNT compared to Silicon surface, disruption of microlayer by the presence of MWCNT, increase in number of active nucleation sites, augmented surface area resulting in an enhancement of solid liquid contact in the form of nano-fins (the “nano-fin” effect). In nucleate boiling, the CNT tends to disrupt the vapor film or “microlayer” under the bubbles leading to enhanced heat transfer. The number of nucleation sites in case of the wafer coated with CNT was observed to be higher than that of a bare silicon wafer. This could be responsible for the significant enhancement in the heat transfer for nucleate pool boiling and flow boiling. The high thermal conductivity of CNT results in a very small temperature differential between the base of the CNT and its tips. The presence of CNT enhances the effective heat transfer area thus acting as nano-fins.

High-speed video measurements showed the behavior of the bubble departure for the bubble height with time for two different surfaces (Figures 3.7 – 3.11). Due to difficulties in flow visualization, the bubble images recorded in this study were not obtained from the actual test surface. The images were obtained for bubbles nucleating in the gap between the copper block and the mating parts for the main test section – as shown in Figure 3.12.

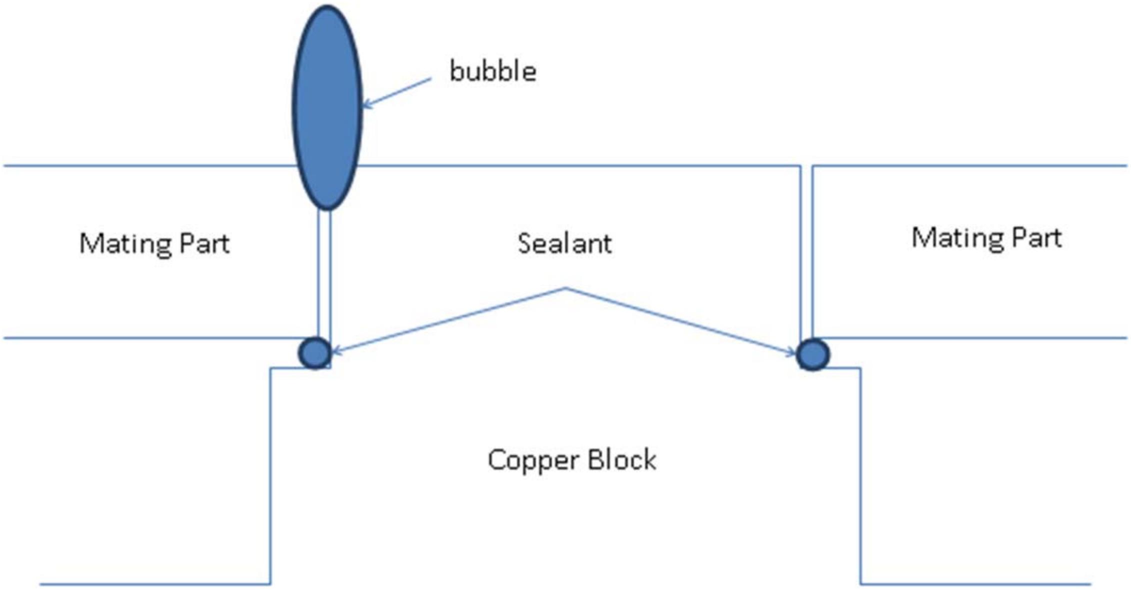

Figure 3. 12 Cross sectional view of the bubble image recorded location.

B. Condensation

Prototype M (Micropost) is similar to F (Flatbed) except that the Prototype F is populated with over 2500 microfins. The design provides a third more surface area for heat transfer than the baseline. The design was expected to increase the pressure drop due to the unique geometry of the fins. Figure 3.13 shows the micropost model in detail. The design for the spacing of the microposts was explored in advance of fabrication – with the intent to minimize the pressure drop (due to flow separation and friction losses). It is expected that the microfins will increase the heat transfer coefficient compared to the flatbed. Table 3.1 shows the summary of the design difference and numerical results for both designs of the microfin spacing. The purpose was to investigate and determine the most optimal design for the compact condenser geometry.

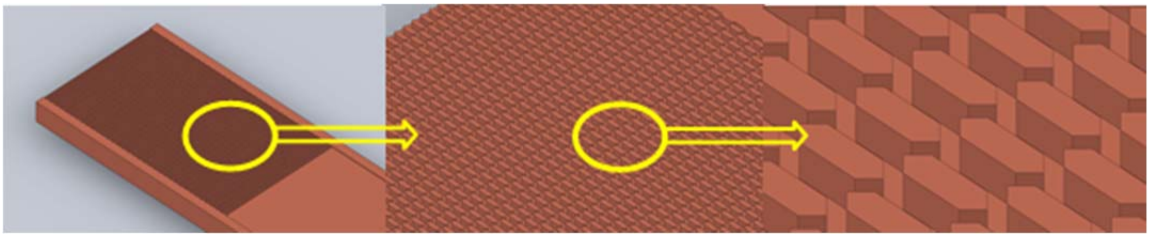

Figure 3. 13 Compact condenser micropost model

Table 3. 1 Design difference between design 6 and design 6B.

Design	*μ-posts (Width)*	*Rows (Length)*	*Total*	*%open (Volume)*	*D_h [mm]*	*Re*
6	55	70	3850	53.9	0.19	1293
6B	55	64	3520	58.4	0.20	1311

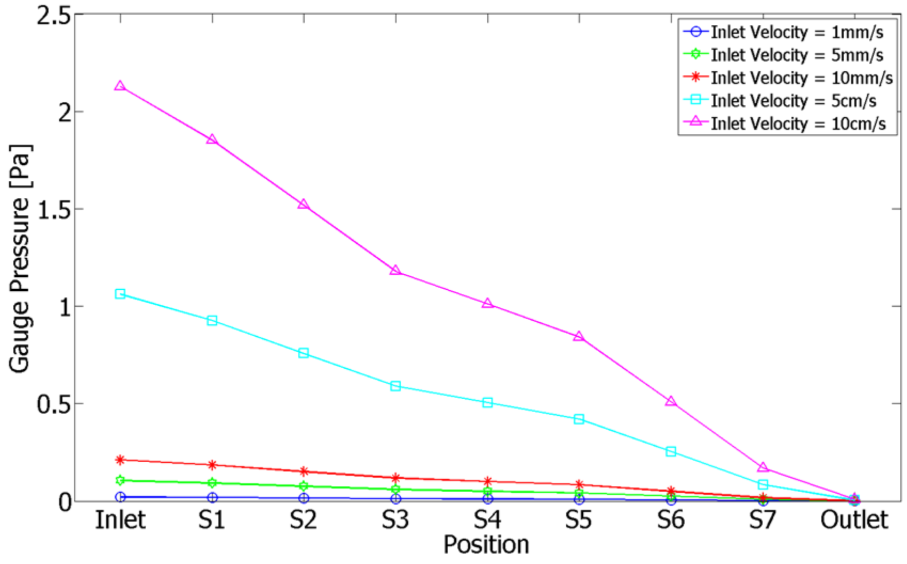

Design 6

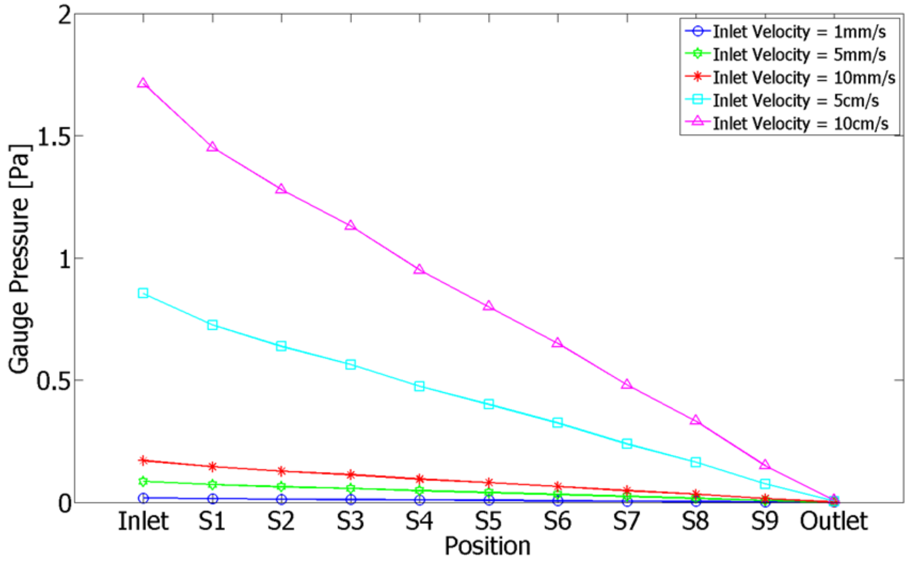

Design 6B

Figure 3. 14 Averaged pressure in cross sections (a) Design 6 (b) Design 6B.

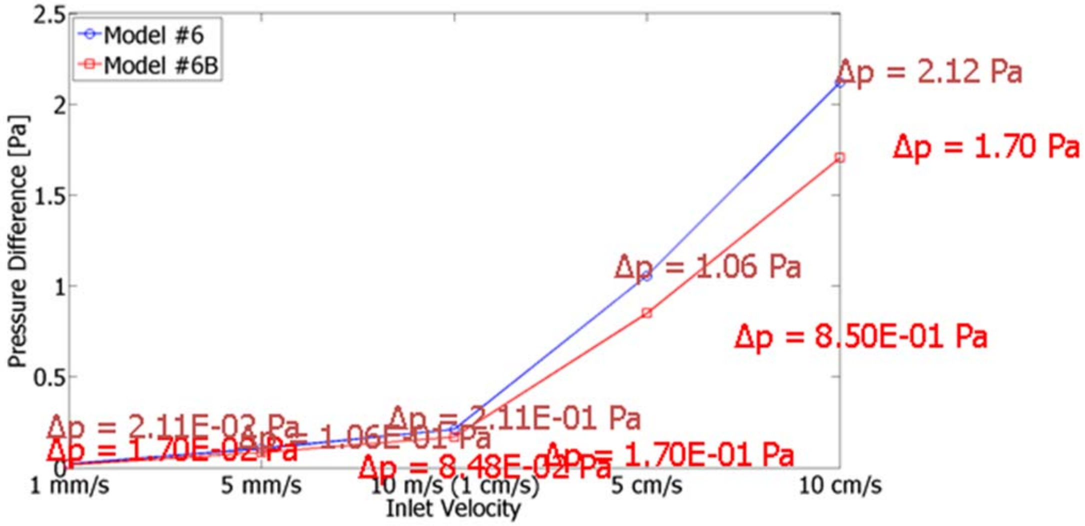

Figure 3. 15 Pressure drop between the inlet and outlet of a single flow element.

According to the numerical analysis (Figure 3.14 and Figure 3.15), model 6 and 6B are different in the aspect of the row numbers. The differences in the row numbers arise from the differences in the design of the layout. However, the single elements (individual microfin) had the same dimensions in both designs. From the results, the pressure drop of model 6B was found to be less than that of model 6 for all the inlet velocities. In addition, there is a slight difference in the velocity and Reynolds number for the two designs, where the pressure drop for flow around a single microfin was calculated to be 2.12 Pa for model 6 and 1.70 Pa for model 6B (for an inlet velocity of 10 cm/s). Hence model 6B was chosen for this study.

Two condenser plate designs were experimentally investigated in the refrigeration loop, starting with the flatbed channel as a baseline (Design F). Each condenser plate was tested at least five times to ensure the repeatability. Table 3.2

summarizes the key results for the most important performance parameters of the tested microchannel designs. Important performance parameters are namely, the heat transfer coefficient (kW/m^2-K) and the pressure drop (Pa or psi). The value of the heat transfer coefficient is the average value calculated from the net conductance, (*hA*) as mentioned before in the data analysis section.

Table 3. 2 Test results summary of key performance parameters.

Parameter	Design M Micropost	Design F Flatbed
Heat transfer coefficient "h" (W/m^2-K)	3873.2	2672.6
Pressure Drop "ΔP" [kPa]	81.4 (11.8 psi)	7.6 (1.1 psi)
Standard Deviation (h / ΔP)	241.18 / 0.15	192.65 / 0.48

C. Droplet Cooling

The transient measurement of surface temperature fluctuations by DTS during droplet impingement experiments are shown in Figure 3.17 for acetone and alcohol. The transient values of heat flux and the heat transfer coefficient were also calculated and shown in figure 3.16. Additional results can be found in Appendix.

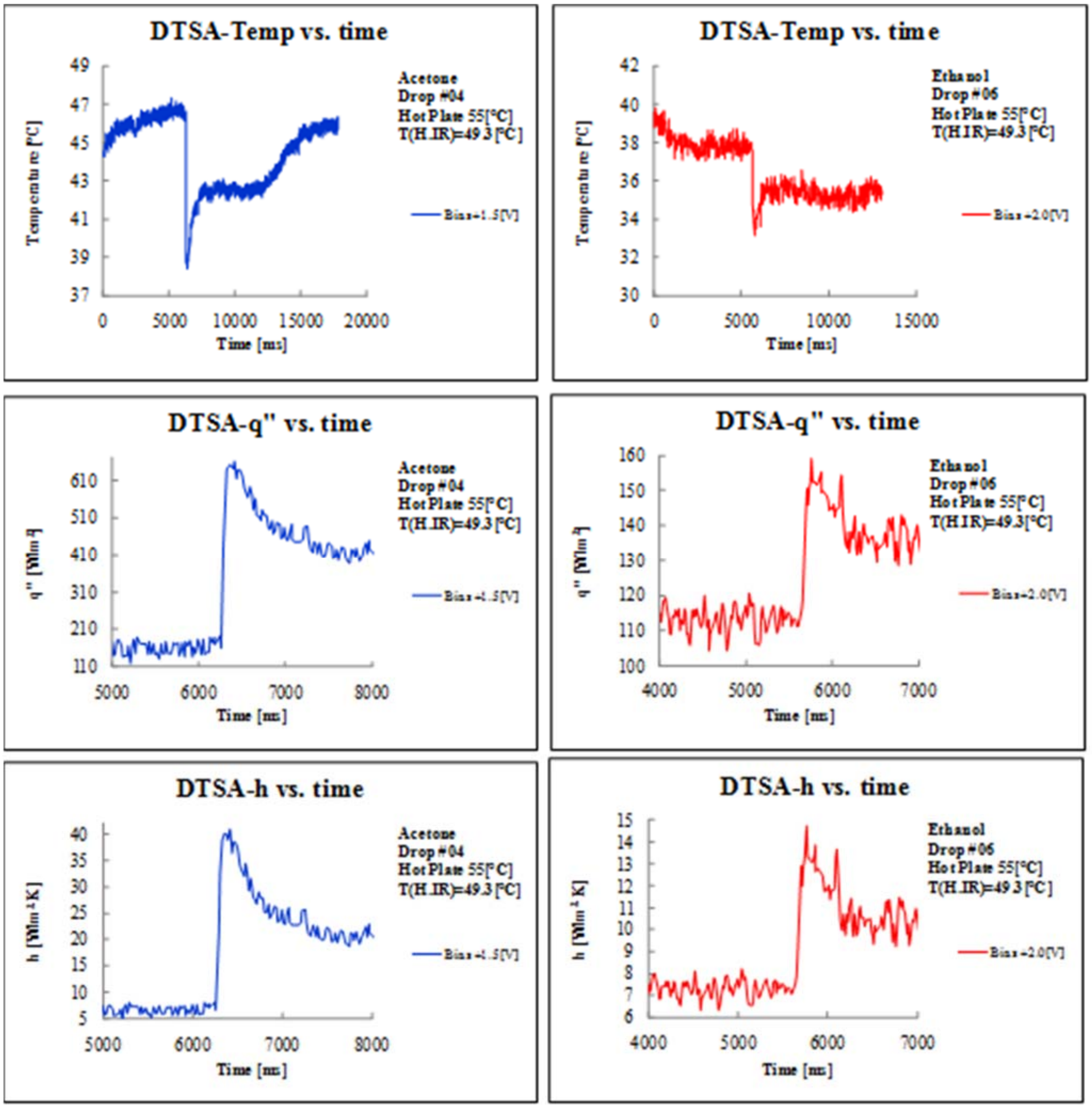

Figure 3. 16 Transient heat flux calculations for droplet impingement cooling experiments for acetone (LEFT) and ethanol (RIGHT).

D. Uncertainty Calculation

a. Measurement Uncertainty (Flow Boiling)

For estimating the measurement uncertainty for heat flux calculations the method of Kline and Mc-Clintock (1953) (Kine and Mc-Clintock, 1953) was used. For two vertically aligned thermocouples 1 and 2, the relative uncertainty (ω) in the heat flux (q”) is estimated as:

$$\frac{\omega_{q''}}{q''} = \left[\left(\frac{\omega_k}{k}\right)^2 + \left(\frac{\omega_{T_1}}{T_2 - T_1}\right)^2 + \left(\frac{\omega_{T_2}}{T_2 - T_1}\right)^2 + \left(\frac{\omega_{\Delta x}}{\Delta x}\right)^2\right]^{\frac{1}{2}} \quad (3.1)$$

where, k is the thermal conductivity of the copper block, T is the temperature recorded by the thermocouples and x is the distance between the two vertically aligned thermocouples.

The uncertainty in estimating the various parameters are enumerated next. The resolution of the data acquisition system (National Instrument) used for this study was set to a 16-bit accuracy. This is equivalent to an absolute error of 0.0046 ºC ~ 0.005 ºC in the temperature range of 0-300 ºC. The standard deviation of the temperature fluctuations in steady state conditions was ~0.05 ºC. Therefore the total uncertainty of the temperature measurement was ~ 0.055 ºC. In addition, the uncertainty values for the copper thermal conductivity and from the machining accuracy were ~1.0% and ~3.0% respectively. Hence the estimated maximum uncertainty of the heat flux values was 6~25%.

b. Measurement Uncertainty (Bubble Height)

The bubble height was calculated using:

$$h_B = \frac{y_{top} - y_{bottom}}{CF} \tag{3.2}$$

where y_1 and $y_2$are measured vertical coordinates of the bottom and top of each bubble in pixels and CF is the calibration factor. CF is associated with the frame resolution which is 113.04 pixels/mm or 1280 × 511 resolution.

The dominant uncertainty for bubble height measurement originated from the blurry edges of the captured bubble images. The uncertainty ω_y of the measurements y_{top} and y_{bottom} was estimated as ±5 pixels. The Kline-McClintock method was used to derive the following equation for 2 measurements.

$$\omega_{h_B} = \sqrt{2}\frac{\omega_y}{CF} \tag{3.3}$$

The uncertainty for the 2 measurement was ±0.03 mm. All the high speed camera images were recorded at 1280 × 511 resolution with the Troubleshooter high speed camera.

c. Measurement Uncertainty (Condensation)

The measurement uncertainty for the calculation of the heat transfer coefficient on the refrigerant side is primarily affected by the measurements errors originating from the temperature measurement. The uncertainty for estimating heat transfer coefficient may be calculated using the method of Klein and McClintock (1953) as:

$$\frac{\Delta h_{ref}}{h_{ref}} = \frac{\Delta \mathrm{U}}{\mathrm{U}} + \frac{\Delta h_w}{h_w} \tag{3.4}$$

where, the measurement error terms in the numerator for heat transfer coefficient refers to the $\pm 3\sigma$ (standard deviation) variation on the average temperature of the inlet and outlet of the compact condenser under steady state conditions (99% confidence level) and the denominator refers to the average value for each parameter. The error in estimating U is expressed as:

$$\frac{\Delta \mathrm{U}}{\mathrm{U}} = \frac{\Delta \mathrm{T}_{w,\mathrm{out}}}{\mathrm{T}_{w,\mathrm{out}}} + \frac{\Delta \mathrm{T}_{w,\mathrm{in}}}{\mathrm{T}_{w,\mathrm{in}}} + \frac{\Delta \mathrm{T}_{LMTD}}{\mathrm{T}_{LMTD}} \tag{3.5}$$

As for the contact $\mathrm{T}_{\mathrm{LMTD}}$, the corresponding error in estimating this value is expressed as:

$$\frac{\Delta \mathrm{T}_{LMTD}}{\mathrm{T}_{LMTD}} = \frac{\Delta \mathrm{T}_{ref,in}}{\mathrm{T}_{ref,in}} + \frac{\Delta \mathrm{T}_{ref,out}}{\mathrm{T}_{ref,out}} + \frac{\Delta \mathrm{T}_{w,in}}{\mathrm{T}_{w,in}} + \frac{\Delta \mathrm{T}_{w,out}}{\mathrm{T}_{w,out}} \tag{3.6}$$

Since the heat transfer coefficient on the water side is calculated from equation 2.9 and 2.10 where the mass flow rate of the cooling water was driven by a pump, the relative error for the water flow rate was small enough to be neglected.

$$\frac{\Delta h_w}{h_w} \sim 0 \tag{3.7}$$

Hence, the uncertainty in estimating heat transfer coefficient on the refrigerant side may be expressed as:

$$\frac{\Delta h_{ref}}{h_{ref}} = \frac{\Delta \mathrm{U}}{\mathrm{U}} \tag{3.8}$$

Hence, the measurement uncertainty for the heat transfer coefficient on the refrigerant side is expected to be ~5.7% for the flatbed coupon experiments and ~7.6% for the micropost coupon experiments.

d. Measurement Uncertainty (Droplet Cooling Experiment)

The measurement uncertainty for the calculation of the 2 phase heat flux values is primarily affected by the measurements errors originating from the calibration of the DTS. The uncertainty for estimating natural convection heat flux may be calculated using the method of Klein and McClintock (1953) as:

$$\frac{\Delta q''_{NC}}{q''_{NC}} = \frac{\Delta h_{NC}}{h_{NC}} + \frac{\Delta T_{DTS,avg}}{T_{DTS,avg}} \tag{3.9}$$

where, the measurement error terms in the numerator for DTS temperature refers to the $\pm 3\sigma$ (standard deviation) variation on the average temperature of the surface under steady state conditions (99% confidence level) and the denominator refers to the average value for each parameter. The error in estimating h_{NC} is expressed as:

$$\frac{\Delta h_{NC}}{h_{NC}} = \frac{\Delta T_{DTS,avg}}{T_{DTS,avg}} \tag{3.10}$$

As for the contact resistance (R_c) between the hot plate and wafer substrate, the corresponding error in estimating this value is expressed as:

$$\frac{\Delta R_c}{R_c} = \frac{\Delta T_{HP}}{T_{HP}} + \frac{\Delta T_{DTS,avg}}{T_{DTS,avg}} + \frac{\Delta q''_{NC}}{q''_{NC}} \tag{3.11}$$

The hot plate temperature is maintained at a constant value by an active controller. Hence, the relative error for the hot plate temperature was small enough to be neglected.

$$\frac{\Delta T_{HP}}{T_{HP}} \sim 0 \tag{3.12}$$

Finally, the uncertainty in estimating the two phase heat flux is expressed as:

$$\frac{\Delta q_{2P}^{''}}{q_{2P}^{''}} = \frac{\Delta T_{HP}}{T_{HP}} + \frac{\Delta T_{DTS}}{T_{DTS}} + \frac{\Delta R_C}{R_C} \qquad (3.13)$$

The uncertainty for the surface temperature by the diode temperature sensor and the heat flux is summarized in the following Table 3.3 and Table 3.4.

Table 3. 3 Measurement uncertainty for temperature (°C) in droplet impingement experiments.

	T_{DTS}[min]	T_{DTS}[max]	(%)
Acetone - 45	24.9	27.4	0.06
Acetone - 50	34.3	35.0	0.05
Acetone - 55	37.8	39.6	0.04
Ethanol -45	21.6	24.2	0.07
Ethanol - 55	31.7	33.8	0.05
Ethanol -65	40.3	45.0	0.04

Table 3. 4. Measurement uncertainty for two phase heat flux (W/m^2) in droplet impingement experiments.

	q''_{2P} [Min]	q''_{2P} [Max]	(%)
Acetone - 45	65.7	99.1	10.15
Acetone - 50	250.7	400.7	7.65
Acetone - 55	571.3	769.2	6.50
Ethanol -45	8.7	52.7	13.80
Ethanol - 55	116.5	217.5	10.14
Ethanol -65	249.3	633.8	14.84

Hence, the measurement uncertainty for heat flux is expected to be ~6-10% for the acetone experiments and ~10-15% for the ethanol experiments.

CHAPTER IV

CONCLUSION AND FUTURE DIRECTIONS

A. Summary

In this study, flow boiling experiments have been conducted under sub-cooled conditions on plain substrates and nano-structured surfaces (substrate coated with MWCNT). Nano-structured surfaces were found to enhance the flow boiling heat flux by more than 200%. Several transport mechanisms were identified to be responsible for the enhancement in heat fluxes observed in multi-phase flows. It is expected that small-scale surface temperature transients are responsible for a major proportion of the total heat flux.

To enumerate the micro/nano-scale transport mechanisms for heat transfer in multi-phase flows miniaturized temperature sensors were developed as a part of this study. Diode temperature sensors (DTS) were designed, fabricated, and calibrated. Calibration of the steady state response of the DTS was performed simultaneously using a wire bead thermocouple as well as using an IR camera. The feasibility of using the DTS for high speed transient measurements of the surface temperature fluctuations for heat transfer phenomena in multi-phase flows was demonstrated for droplet impingement cooling experiments. The droplet cooling experiments were performed for acetone and alcohol. From the droplet cooling experiments it was observed that the transient peak in two-phase heat flux was enhanced by ~100-200% for ethanol and ~200-500% for acetone (over that of single-phase natural convection heat flux values).

For both acetone and alcohol, the peak heat flux was found to occur over time-scales that lasted for less than ~10-100 ms. This shows the need for miniaturized high speed temperature sensors with high spatial density.

TFT are comparatively easier to fabricate than the DTS. However, the efforts required for packaging of TFT are considerably more laborious than DTS, especially for measurements involving a large array of sensors in layout designs involving a potentially high spatial density.

A compact condenser with micropost surface was numerically studied to determine the optimal geometry for better heat exchanger performance. The micropost surface compact condenser was compared with a flatbed surface to observe the heat transfer enhancement. The heat transfer performance was experimentally investigated. From the results, the heat transfer coefficient was enhanced by 30% for the micropost surface compared to a flatbed surface which was the control experiment for the compact condensation experiment.

B. Future Directions

The following topics are identified for future explorations as a part of this study:

The flow boiling studies need to be repeated by varying the experimental parameters (wall superheat, flow rate, and liquid sub-cooling) for the various substrates considered in this study. Better insulation of the heated copper can extend the range of the experimental parameters (wall superheat, het flux, flow rate, etc.). Though the existing heater is surrounded by low thermal conductivity 0.25” thick acrylic walls and an additional fiber glass insulation pad, heat loss to the bottom of the heater limits the range of wall superheating used in this study. An enhanced insulation pad or even high performance electric heating pad can be explored.

The experiments using the temperature nano-sensors need to be repeated for surface temperatures exceeding the saturation temperature of acetone and alcohol. The existing fabrication protocol for the temperature nano-sensors (DTS and TFT) can also be improved. Ion implantation as well as the diffusion method to form the p and n region should be taken into consideration and characterized. The performance of the sensors with different fabrication processes need to be compared and optimized.

Use of DTS for flow boiling studies can also be explored. However, there are a large number of challenges in the existing experimental apparatus that need to be resolved. A flip chip circuit must be developed for mounting the DTSA in the flow boiling apparatus. The sensor itself cannot be integrated directly in the boiling experiment yet. An adaptor can be installed in the main test section for providing ease of access for the sensor output. Instead of depending on the wire bonding that can fail easily, a snap and connect type of flip packaging may be needed for future studies.

A heated vacuum chuck with a stable electrical ground is required for better characterization and calibration of the DTSA. This would help to minimize the electrical noise floor of the signal output. In addition to the equipment proposed for developing the DTS, an isolated dark box for housing the probe station is needed. An SMU instrument such as Keithley 2612a (or similar) can be explored to improve the temporal resolution of the sensor data collection. Since, DTS has faster response than the TFT, SMU is recommended for characterizing the sensor output.

The response of the two different temperature nano-sensors (DTS and TFT) need to be compared for similar experiments (e.g., droplet cooling experiments and potentially for flow boiling experiments as well).

REFERENCES

[1] Mudawar, I., 2001, “Assessment of High Heat Flux Thermal Management Schemes,” IEEE Transactions on Components and Packaging, **24**, pp. 122–141.

[2] Dhir, V.K., 1998, “Boiling Heat Transfer,” Annual Review of Fluid Mechanics, **30**, pp. 365-401.

[3] Jensen, M.K., and Memmel, G.J., 1986, “Evaluation of Bubble Departure Diameter Correlations,” *Proceedings of Eighth International Heat Transfer Conference*, **4**, pp. 1907–1912.

[4] Kutateladze, S.S., and Gogonin, I.I., 1979, “Growth Rate and Detachment Diameter of a Vapor Bubble in Free Convection Boiling of a Saturated Liquid,” High Temperature, **17**, pp. 667-671.

[5] Miller, W.J., Gebhart, B., and Wright, N.T., 1990, "Effects of Boiling History on Microconfigured Surface in a Dielectric Liquid," International Communications in Heat and Mass Transfer, **17**(4), pp. 389-398.

[6] Phadke, N.K., Bhavnani, S.H., Goyal, A., Jaeger, R.C., and Goodling, J.S., 1992, "Re-entrant Cavity Surface Enhancements for Immersion Cooling of Silicon Multichip Packages," IEEE Transactions on Components, Hybrids, and Manufacturing Technology. **15**, pp. 815–822.

[7] O'Connor, J.P., and You, S.M., 1995, "A Painting Technique to Enhance Pool Boiling Heat Transfer in Saturated FC-72," Journal of Heat Transfer, **117**(2), pp. 387-393.

[8] Chang, J.Y., and You, S.M., 1997, "Enhanced Boiling Heat Transfer from Micro-Porous Surfaces: Effects of a Coating Composition and Method," International Journal of Heat and Mass Transfer, **40**(18), pp. 4449-4460.

[9] Honda, H., Takamastu, H., and Wei, J.J., 2002, "Enhanced Boiling of FC-72 on Silicon Chips with Micro-Pin-Fins and Submicron-Scale Roughness," Journal of Heat Transfer, **124**(2), pp. 383-390.

[10] Ahn, H. S., Sinha, N., Zhang, M., Fang, S., Baughman, R. H., and Banerjee, D., 2006, “Pool Boiling Experiments on Multi-Walled Carbon Nanotube (MWCNT) Forests,” Journal of Heat Transfer, **128**(12), pp. 1335-1342.

[11] Sebastine, O., Ujereh, O.S., Mudawar, I., Amama, P.B., Fisher, T.S, and Ou, W., 2005, “Enhanced Pool Boiling on Carbon Nanotube Arrays on a Silicon Surface,” *Proceedings of ASME International Mechanical Engineering Congress and Exposition*, Orlando, FL, IMECE2005-80065.

[12] Sathyamurthi, V., 2006, “Pool Boiling Studies on Nanostructured Surfaces Under Highly Subcooled Conditions,” M.S.Thesis, Texas A&M University, College Station, TX.

[13] Honda, H., and Wei, J.J., 2004, "Enhanced Boiling Heat Transfer from Electronic Components by Use of Surface Microstructures," Experimental Thermal and Fluid Science, **28**(2-3), pp. 159-169.

[14] Anderson, T.M., Mudawar, I., 1989, “Microelectronic Cooling by Enhanced Pool Boiling of a Dielectric Fluorocarbon Liquid,” Journal of Heat Transfer, **111**(3), pp. 752-759.

[15] Oktay, S., and Schmeckenbecher, A.F., 1972, "Method for Forming Heat Sinks on Semiconductor Device Chip," US Patent, 32,237(3,706,127).

[16] You, S.M., Bar-Cohen, A., and Simon, T.W., 1990, "Boiling Incipience and Nucleate Boiling Heat Transfer of Highly Wetting Dielectric Fluids from Electronic Materials," IEEE Transactions on Components, Hybrids, and Manufacturing Technology, **13**(4), pp. 1032-1039.

[17] Rainey, K.N., and You, S.M., 2000, "Pool Boiling Heat Transfer from Plain and Microporous, Square Pin-Finned Surfaces in Saturated FC-72," Journal of Heat Transfer, **122**(3), pp. 509-516.

[18] Kim, J.H., Rainey, K.N., and You, S.M., 2002, "Mechanism of Nucleate Boiling Heat Transfer Enhancement from Microporous Surfaces in Saturated FC-72," Journal of Heat Transfer, **124**(3), pp. 500-506.

[19] Kim, J.H., You, S.M., and Pak, J.Y., 2006, "Effects of Heater Size and Working Fluids on Nucleate Boiling Heat Transfer," International Journal of Heat and Mass Transfer, **49**(1-2), pp. 122-131.

[20] Ujereh, S., Fisher, T., and Mudawar, I., 2007, "Effects of Carbon Nanotube Arrays on Nucleate Pool Boiling," International Journal of Heat and Mass Transfer, **50**(19-20), pp. 4023-4038.

[21] Cai, Q., and Chen, C.L., 2010, "Design and Test of Carbon Nanotube Biwick Structure for High-Heat-Flux Phase Change Heat Transfer," Journal of Heat Transfer, **132**(5), pp. 052403-052411.

[22] Thome, J.R., 1990, *Enhanced Boiling Heat Transfer*, Hemisphere, New York.

[23] Reed, S.J., and Mudawar, I., 1997, "Enhancement of Boiling Heat Transfer Using Highly Wetting Liquids with Pressed-on Fins at Low Contact Forces," International Journal of Heat and Mass Transfer, **40**(10), pp. 2379-2392.

[24] Hone, J., Whitney, and M., Piskoti, C., 1999, "Thermal Conductivity of Single-Walled Carbon Nanotubes," Physical Review B (Condensed Matter), **59**(4), pp. 2514-2516.

[25] Berber, S., Kwon, Y., and Tomanek, D., 2000, "Unusually High Thermal Conductivity of Carbon Nanotubes," Physical Review Letters, **84**(20) pp. 4613-4616.

[26] Kim, S.J., and Jang, S.P., 2001, “Experimental and Numerical Analysis of Heat Transfer Phenomena in a Sensor Tube of a Mass Flow Controller,” International Journal of Heat Mass Transfer, **44**, pp. 1711–1724.

[27] Banerjee, D., and Dhir, V.K., 2001, "Study of Subcooled Film Boiling on a Horizontal Disc: Part 1 Analysis," Journal of Heat Transfer, **123**(2), pp. 271-284.

[28] Banerjee, D., and Dhir, V.K., 2001, "Study of Subcooled Film Boiling on a Horizontal Disc: Part 2 Experiments," Journal of Heat Transfer, **123**(2), pp. 285-294.

[29] Sathyamurthi, V., 2009, “Experimental & Numerical Investigation of Pool Boiling on Engineered Surfaces with Integrated Thin-Film Temperature Sensors,” Ph.D. Dissertation, Texas A&M University, College Station, TX.

[30] Sriraman, S., 2007, “Pool Boiling on Nano-Finned Surfaces,” M.S Thesis, Texas A&M University, College Station, TX.

[31] Chen, R., Lu, M., and Srinivasan, V., 2009, "Nanowires for Enhanced Boiling Heat Transfer," Nano Letters, **9**(2), pp. 548-553.

[32] Taylor, G., 1950, "The Instability of Liquid Surfaces When Accelerated in a Direction Perpendicular to Their Planes I," Proceedings of the Royal Society of London, Series A (Mathematical and Physical Sciences), **201**, pp. 192-196.

[33] Sharp, D.H., 1984, "An Overview of Rayleigh-Taylor Instability," *Proceedings of the Third Annual International Conference of the Centre for Nonlinear Studies*, Amsterdam, The Netherlands, **12D**, pp. 3-18.

[34] Sobhan, C.B., and Garimella, S.V., 2001, “A Comparative Analysis of Studies on Heat Transfer and Fluid Flow in Microchannels,” Microscale Thermophysics Engineering., **5**(4), pp. 293–311.

[35] Garimella, S.V., and Sobhan, C.B., 2003, “Transport in Microchannels-A Critical Review,” Annual Review Heat Transfer, **13**, pp. 1–50.

[36] Garimella, S.V., and Singhal, V., 2004, “Single-Phase Flow and Heat Transport and Pumping Considerations in Microchannel Heat Sinks,” Heat Transfer Engineering, **25**(1), pp. 15–25.

[37] Liu, D., and Garimella, S.V., 2004, “Investigation of Liquid Flow in Microchannels,” Journal Thermophysics and Heat Transfer, **18**(1), pp. 65–72.

[38] Coleman, J.W., and Garimella, S.V., 1999, “Characterization of Two-Phase Flow Patterns in Small Diameter Round and Rectangular Tubes,” International Journal of Heat and Mass Transfer, **42**(15), pp. 2869–2881.

[39] Coleman, J. W., and Garimella, S.V., 2000, “Two-Phase Flow Regime Transitions in Microchannel Tubes: The Effect of Hydraulic Diameter,” American Society of Mechanical Engineers Heat Transfer Division, **HTD-366**, pp. 71–83.

[40] Coleman, J. W., and Garimella, S.V., 2003, “Two-Phase Flow Regimes in Round, Square and Rectangular Tubes During Condensation of Refrigerant R134a,” International Journal of Refrigeration, **26**(1), pp. 117–128.

[41] Garimella, S.V., Killion, J.D., and Coleman, J.W., 2002, “An Experimentally Validated Model for Two-Phase Pressure Drop in the Intermittent Flow Regime for Circular Microchannels,” Journal of Fluids Engineering, **124**(1), pp. 205–214.

[42] Garimella, S.V., Killion, J.D., and Coleman, J. W., 2003, “An Experimentally Validated Model for Two-Phase Pressure Drop in the Intermittent Flow Regime for Noncircular Microchannels,” Journal of Fluids Engineering, **125**(5), pp. 887–894.

[43] Garimella, S.V, Agarwal, A., and Coleman, J.W., 2003, “Two-Phase Pressure Drops in the Annular Flow Regime in Circular Microchannels,” *21st IIR International Congress of Refrigeration*, Washington, DC, Paper No. ICR0360.

[44] Garimella, S.V., Agarwal, A., and Killion, J.D., 2005, “Condensation Pressure Drop in Circular Microchannels,” Heat Transfer Engineering, **26**(3), pp. 1–8.

[45] Wu, S., Lin, Q., Yuen, Y., and Tai, Y., 2001, “MEMS Flow Sensors for Nano-Fluidic Applications,” Sensors Actuators, **A 89**, pp. 152–158.

[46] Ashauer, M., Closch, H., Hedrich, F., Hey, N., Sandmaier, H., and Lang, W., 1999, “Thermal Flow Sensor for Liquids and Gases based on Combinations of Two Principles,” Sensors Actuators, **A 73**, pp. 7–13.

[47] Ernst, H., Jachimowicz, A., and Urban, A., 2002, “High Resolution Flow Characterization in Bio-MEMS,” Sensors Actuators, **A 100**, pp. 54–62.

[48] Glaninger, A., Jachimowicz, A., Kohl, F., Chabicovsky, R., and Urban, G., 2000, “Wide Range Semiconductor Flow Sensors,” Sensors Actuators, **A 85**, pp. 139–46.

[49] Han, I.Y., Kim, D., and Kim, S.J., 2005, “Study on the Transient Characteristics of the Sensor Tube of a Thermal Mass Flow Meter,” International Journal of Heat and Mass Transfer, **48**, pp. 2583–2592.

[50] Kersjes, R., Eichholz, J., Langerbein, A., Manoli, Y., and Mokwa, W., 1993, “An Integrated Sensor for Invasive Blood-Velocity Measurement,” Sensors Actuators, **A 37–38**, pp. 674–678.

[51] Van der Wiel, A.J., Linder, C., and de Rooij, N F., 1993, “A Liquid Velocity Sensor Based on the Hot-Wire Principle,” Sensors Actuators, **A 37–38**, pp. 693–697.

[52] Nguyen, N. T., and Kiehnscherf, R., 1995, “Low-Cost Silicon Sensors for Mass Flow Measurement of Liquids and Gases,” Sensors Actuators, **A 49**, pp. 17–20.

[53] Rasmussen, A., Mavriplis, C., Zaghloul, M.E., Mikulchenko, O., and Mayaram, K., 2001, “Simulation and Optimization of a Microfluidic Flow Sensor,” Sensors Actuators, **A 88**, pp. 121–132.

[54] Sunder, M., Banerjee, D., 2009, "Experimental Investigation of Micro-Scale Temperature Transients in Sub-Cooled Flow Boiling on a Horizontal Heater," International Journal of Heat and Fluid Flow, **30**, pp. 140-149.

[55] Moita, A.S., and Moreira, A.L., 2002, "The Dynamic Behavior of Single Droplets Impacting onto a Flat Surface", *ILASS-Europe*, Zaragoza, Spain.

[56] Chow, C.K. and Attinger, D., 2003, "Visualization and Measurements of Microdroplet Impact Dynamics on a Curved Substrate," *Proceedings of FEDSM, 4th ASME JSME Joint Fluids Engineering Conference*, Honolulu, Hawaii, FEDSM2003-45153.

[57] Cossali, G.E., Brunello, G., and Marengo, M., 1999, "Impact of a Single Drop on a Liquid Film: Experimental Analysis and Comparison with Empirical Models", Italian Congress of Thermofluid Dynamics UIT, Ferrara, Italy.

[58] Sangplung, S., and Liburdy, J.A., 2007. "Effect of Dynamic Contact Angle on Single/Successive Droplet Impingement," *Proceedings of ASME IMECE 2007*, Seattle, WA, IMECE 2007-41603.

[59] Liu, J., Franco, W., and Aguilar, G., 2008, "Effect of Surface Roughness on a Single Cryogen Droplet Spreading," Journal of Fluids Engineering, **130** (4), pp. 041402-041411.

[60] Bernardin, J.D., Mudawar, I., Walsh, C.B., and Franses, E.I., 1997, “Contact Angle Temperature Dependence of Water Droplets on Practical Aluminum Surfaces,” International Journal of Heat and Mass Transfer, **40**, pp. 1017-1033.

[61] Lajeunesse, E., and Couder, Y., 2000, “On the Tip-Splitting Instability of Viscous Fingers,” Journal of Fluid Mechanics, **419**, pp. 125-149.

[62] Navid, Z., Mehdizadeh,al., Chandra, S., and Mostaghimi, J., 2004, “Formation of Fingers around the Edges of a Drop Hitting a Metal Plate with High Velocity,” Journal of Fluid Mechanics, **510**, pp. 353-373.

[63] Stow, C.D., and Hadfield, M.G., 1981, “An Experimental Investigation of Fluid Flow Resulting from the Impact of a Water Drop with an Unyielding Dry Surface,” Proceedings of Royal Society London A, **373**, pp. 419-441.

[64] Zhang, X., and Basaran, O.A., 1997, “Dynamic Surface Tension Effects in Impact of a Drop with a Solid Surface,” Journal of Colloid and Interface Science, **187**, pp. 166-178.

[65] Chandra, S., di Marzo, M., Qiao, Y.M. and Tartarini, P., 1996, “Effect of Liquid-Solid Contact Angle on Droplet Evaporation,” Fire Safety J., **27**, pp. 141-158.

[66] Hoffman, R.L., 1975, “A Study of the Advancing Interface,” Journal of Colloid and Interface Science, **50**, pp. 228-241.

[67] Cox R.G., 1998, “Inertial and Viscous Effects on Dynamic Contact Angles,” Journal of Fluid Mechanics, **357**, pp. 249-278.

[68] Blake T.D., 1993, *Dynamic Contact Angles and Wetting Kinetics,* Marcel Dekker, New York.

[69] Chandra, S., and Avedisian, C.T., 1991, “On the Collision of a Droplet with a Solid-Surface,” Proceedings of Royal Society London A **432**, pp. 13-41.

[70] Pasandideh-Fard, M., Qiao, Y.M., Chadra, S., and Mostaghimi, J., 1996 “Capillary Effects during Droplet Impact on a Solid Surface,” Physics of Fluids, **8**, pp. 650-659.

[71] Mao, T., and Kuhn, D., 1997, “Spread and Rebound of Liquid Droplets upon Impact on Flat Surfaces,” American Institute of Chemical Engineers Journal, **43**, pp. 2169-2179.

[72] Luttich, T., Marquardt, W., Buchholz, M., and Auracher, H., 2006, “Identification of Unifying Heat Transfer Mechanisms along the Entire Boiling Curve,” International Journal of Thermal Sciences, **45**, 284-298.

[73] Luke, A., and Cheng, D., 2005, “High Speed Video Recording of Bubble Formation with Pool Boiling,” International Journal of Thermal Sciences, **45** (3), 310-320.

[74] Diao, Y., Zhao, Y., and Wang, Q., 2007, "Photographic Study of Bubble Dynamics for Pool Boiling of Refrigerant R11," Journal of Heat and Mass Transfer, **43** (9), 935-947.

[75] Diao, Y., and Zhao, Y., and Wang, Q., 2005, "High Speed Photographic Analysis of Saturated Nucleate Pool Boiling at Low Heat Flux," Journal of Thermal Science, **15** (1), 79-84.

[76] Diao, Y., Zhao, Y., and Wang, Q., 2005, "Bubble Dynamics and Heat Transfer Mechanism of Pool Boiling of R113," Journal of Chemical Industry and Engineering, **56** (2), 227-234.

[77] Williamson, C.R., and El-Genk, M.S., 1991, " High-Speed Photographic Analysis of Saturated Nucleate Pool Boiling at Low Heat Flux," ASME Winter Annual Meeting, ASME, New York, pp. 1-7.

[78] Jo, B.N., Jeon, P.S., Yoo, J.S., and Kim, H.J., 2009, "Wide Range Parametric Study for the Pool Boiling of Nano-fluids with a Circular Plate Heater," Journal of Visualization, **12** No. 1, pp. 37-46.

[79] Khanikar, V., Mudawar, and I., Fisher, T., 2008, "Flow Boiling in a Micro-channel Coated with Carbon Nanotubes", IEEE Transactions on Components and Packaging Technologies, **32**(3), pp. 639-649.

APPENDIX A

FABRICATION AND ASSEMBLY OF EXPERIMENTAL APPARATUS FOR FLOW BOILING STUDIES

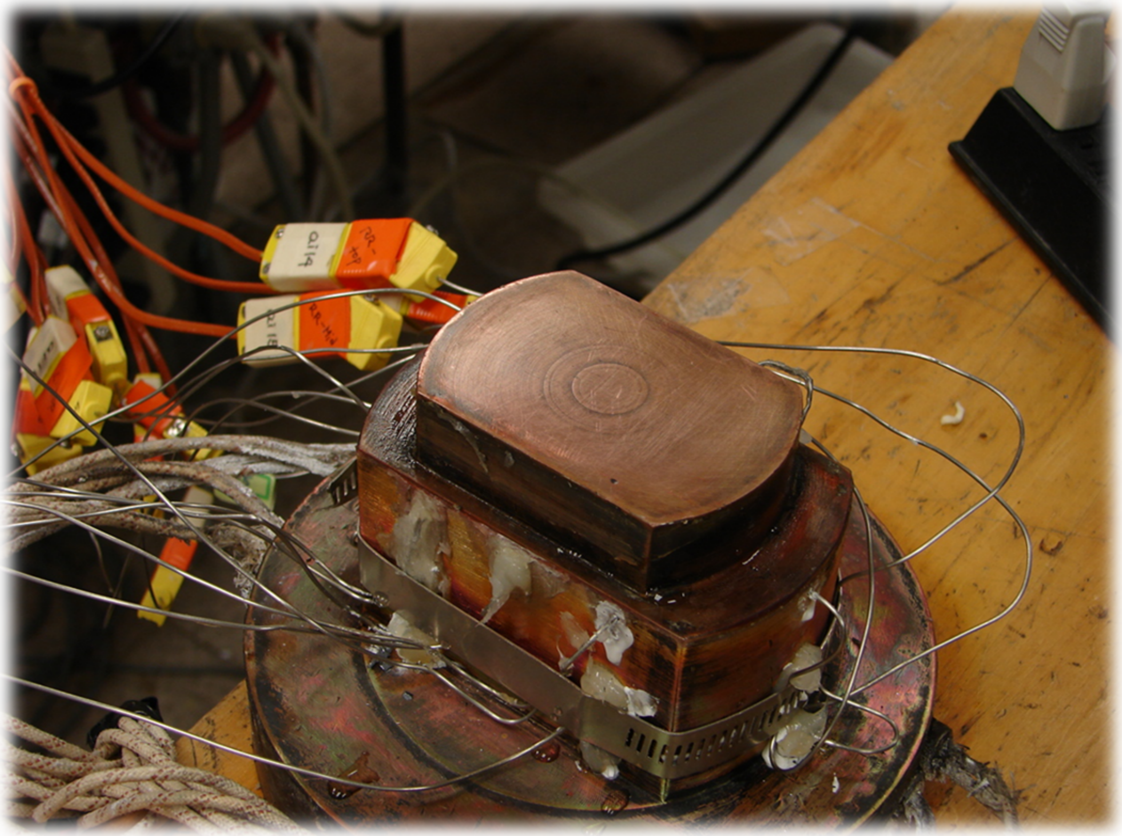

Figure A.1 Copper Block prepared for surface attachment.

Figure A.1 shows the copper block with thermocouples inserted. In order to attach various substrates, the copper block needs to be cleaned thoroughly. In the picture, orange lines are the thermocouples that are installed at different locations with numbered tags on them. On the bottom of the copper block where the largest circular disk is visible, eight cartridge heaters are inserted that are connected to the AMREL power supply.

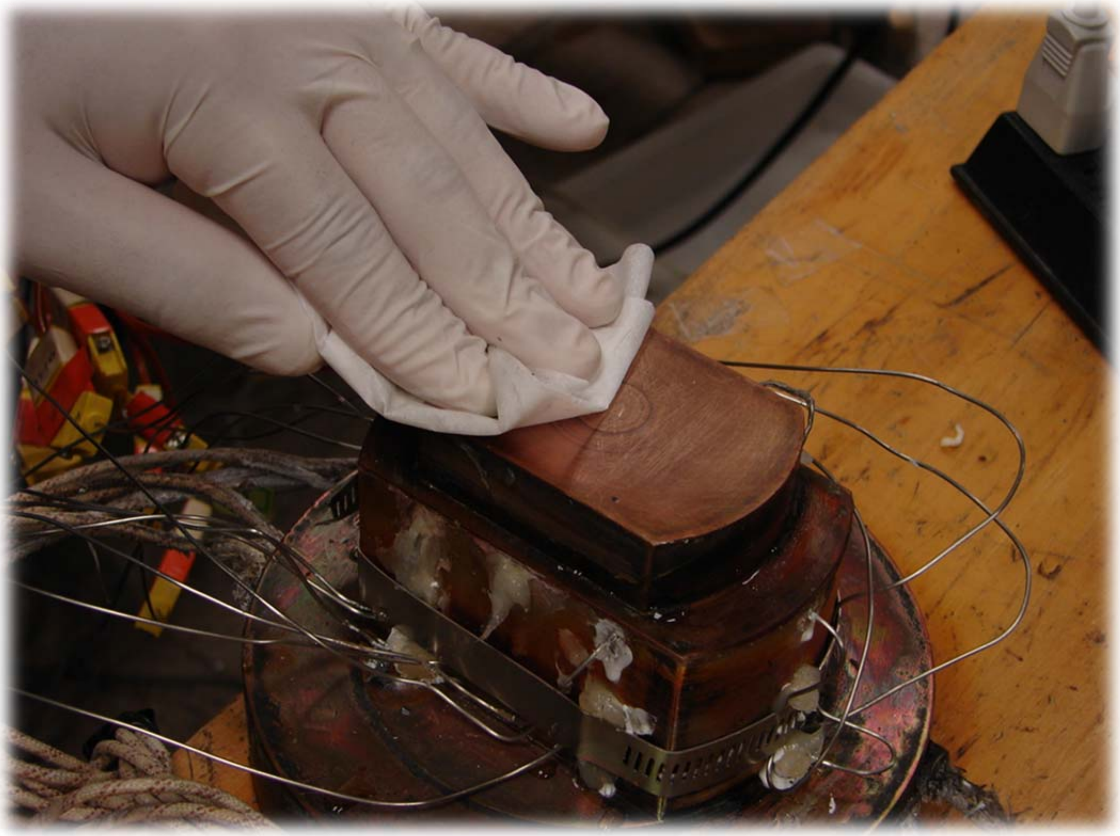

Figure A.2 Surface cleaning.

The surface of the copper block needs to be cleaned using Kimwipe©. The wipe should partially soaked in Isopropanol before physically wiping the surface of the copper block surface. After wiping off the surface couple times with the Isopropanol, repeat the step using Acetone soaked Kimwipe. Redo the Isopropanol and Acetone cleaning 3~4 times until no debris or dirt is captured on the wipe. While wiping off the surface, try to apply pressure on the edges of the surface as well as on the surface itself.

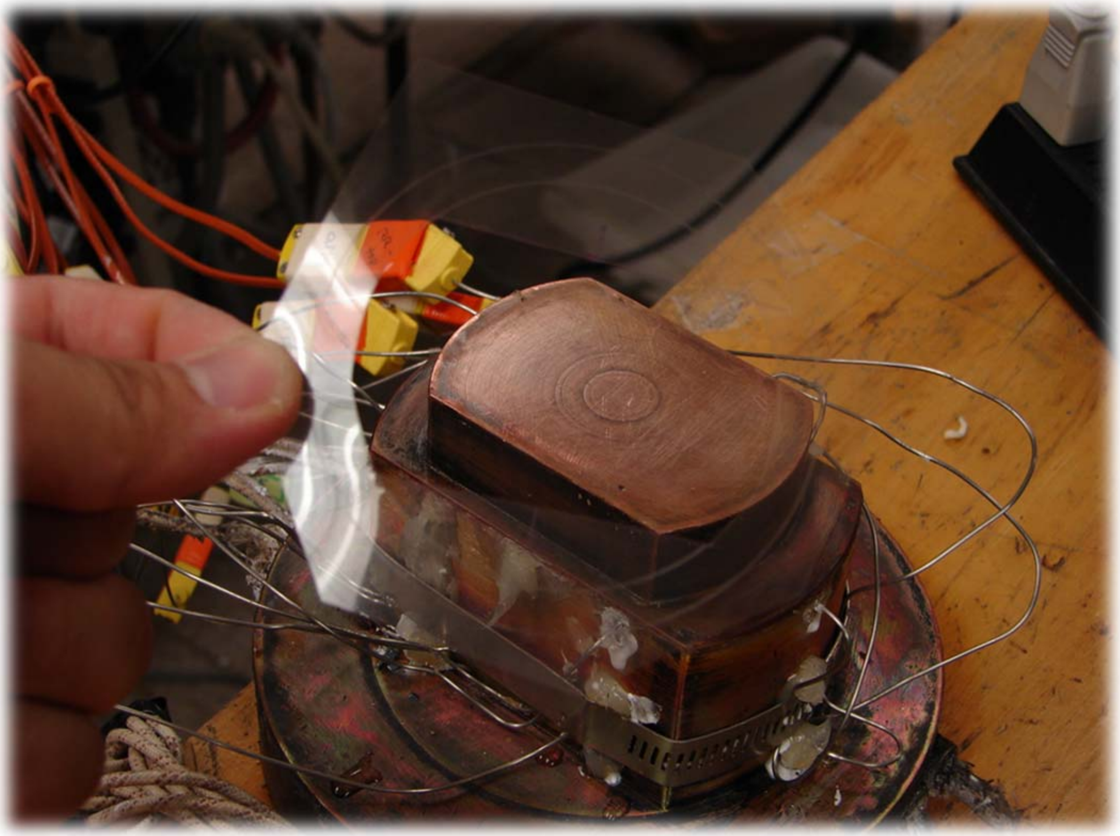

Figure A.3 Transparency Mask.

A transparency film cut from a conventional OHP film is used to mask the cleaned copper block surface partially before applying the thermal paste. The transparency film should be sketched before cutting out the part where the paste should be applied. First, draw a circle with the diameter of 2.7~2.8”. Draw a line that crosses the center of the circle. Make a perpendicular line that is 2.5 cm away from the center of the circle. Another line is sketched on the other side of the center. The final film with the sketch should look similar to the copper block surface but a bit smaller. This is to secure the outer perimeter to apply the silicone.

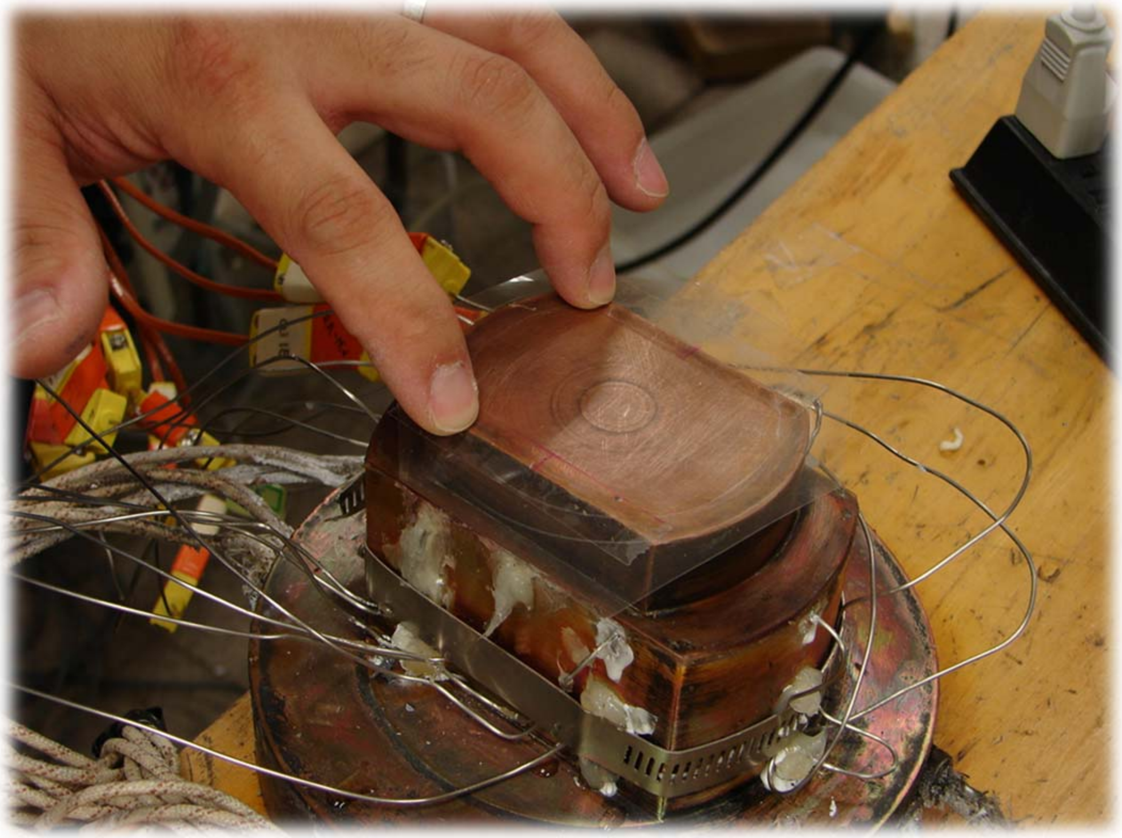

Figure A.4 Setting the transparency film.

After the sketching on the transparency film, cut the inner part of the transparency film with a scissor. The edges need not be sharp. Apply double sided tape at the surface that needs to be fixed to the copper block. Press couple times on the double sided tape to secure adhesion. The transparency film after all will be used as a stencil while applying the thermal paste.

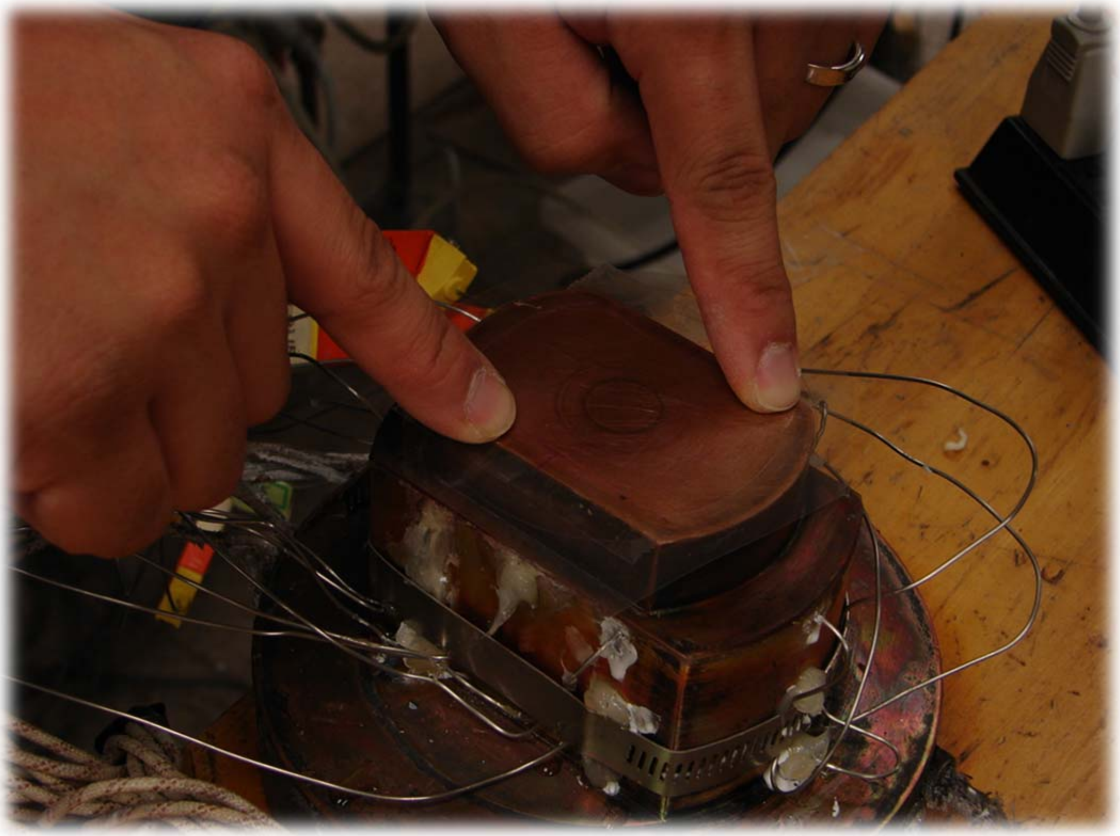

Figure A.5 Pressing the transparency film .

Figure A.5 shows the transparency film pressed onto the copper block. Use your fingers to press uniformly along the edges.

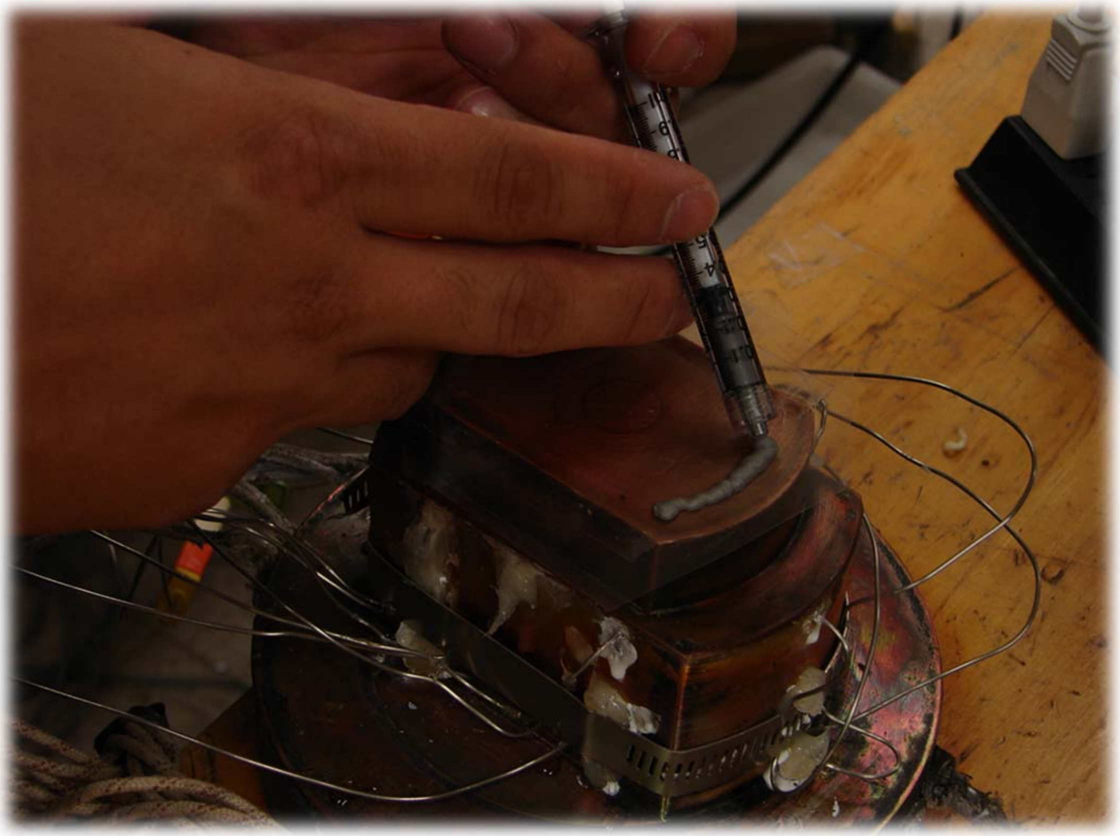

Figure A.6 Applying thermal paste.

Apply the thermal paste at one end of the copper block top surface. The thermal paste may be stored in a can which the user needs to scoop out using a spoon-like utensil or in a form of syringe that is shown in the picture. Since the thermal paste is going to be spread evenly downstream, it is important not to apply too much at the starting location.

Figure A.7 Spreading the thermal paste using joint knife.

Using a joint knife, try to spread the thermal paste in one direction. Do not reverse the direction until you have covered the area of interest. One good tip would be pressing firmly with one of your finger on the joint knife shown in figure A.7. After the first application, wipe of any excessive thermal paste that is sticking on the joint knife.

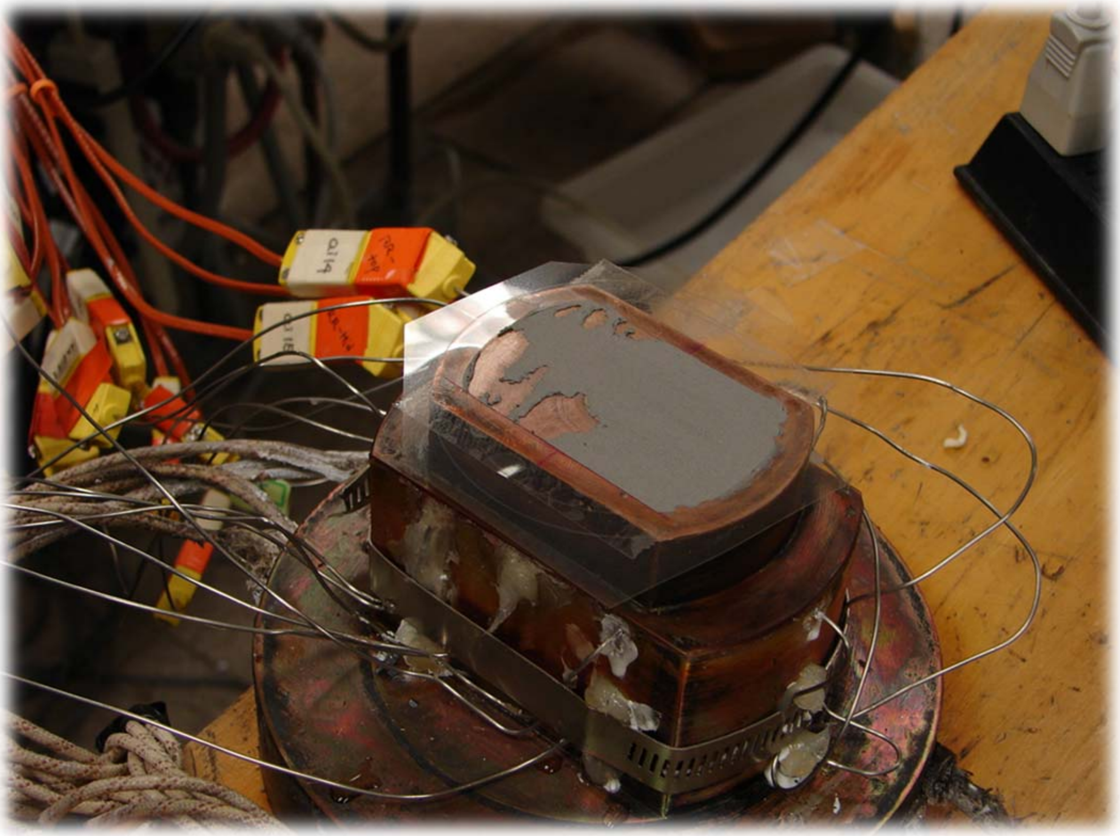

Figure A.8 Thermal paste applied for the first time.

Figure A.8 shows how it might look like after the first application of the thermal paste. As seen from the picture, part of the area is not coated with the thermal paste yet and needs to be reapplied until the whole surface of interest is covered evenly with the thermal paste. If there are insufficient thermal pastes, it is recommended to add some more at the same location where the thermal paste was initially applied. However, try to spread evenly using the joint knife as before to cover the whole surface.

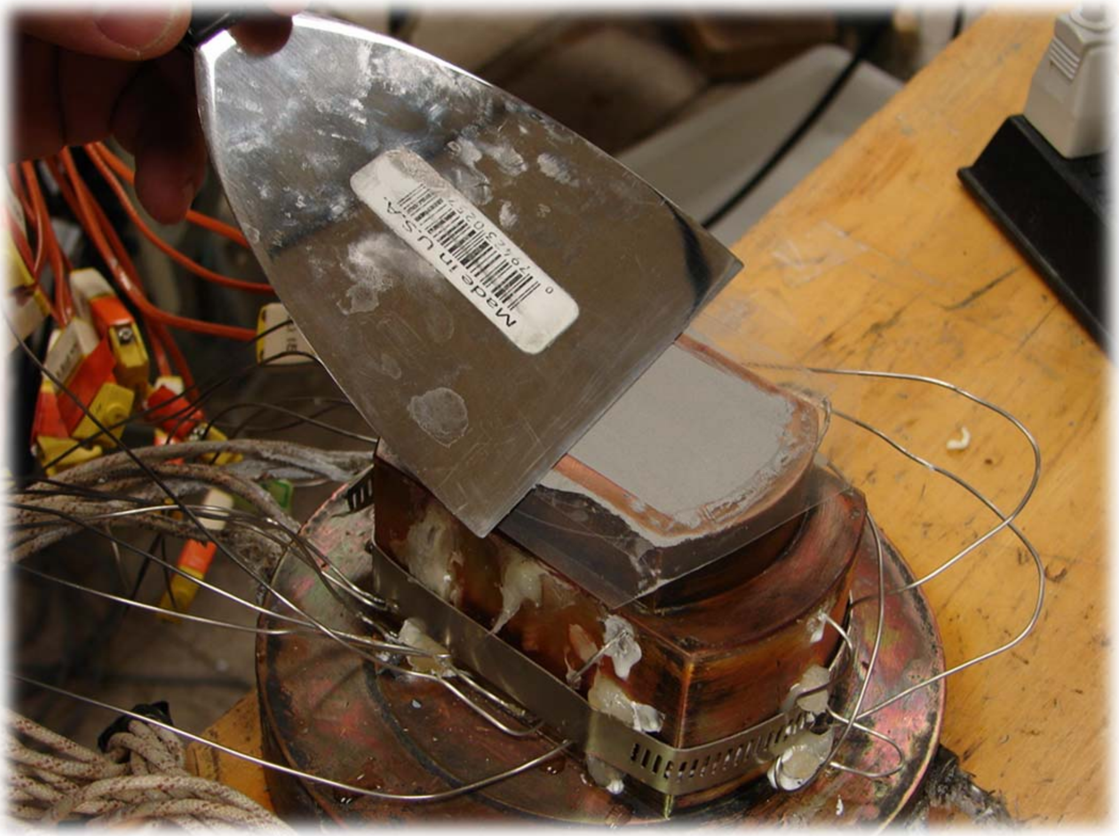

Figure A.9 Reapplying the thermal paste.

Figure A.9 shows the reapplication of the thermal paste using the joint knife.

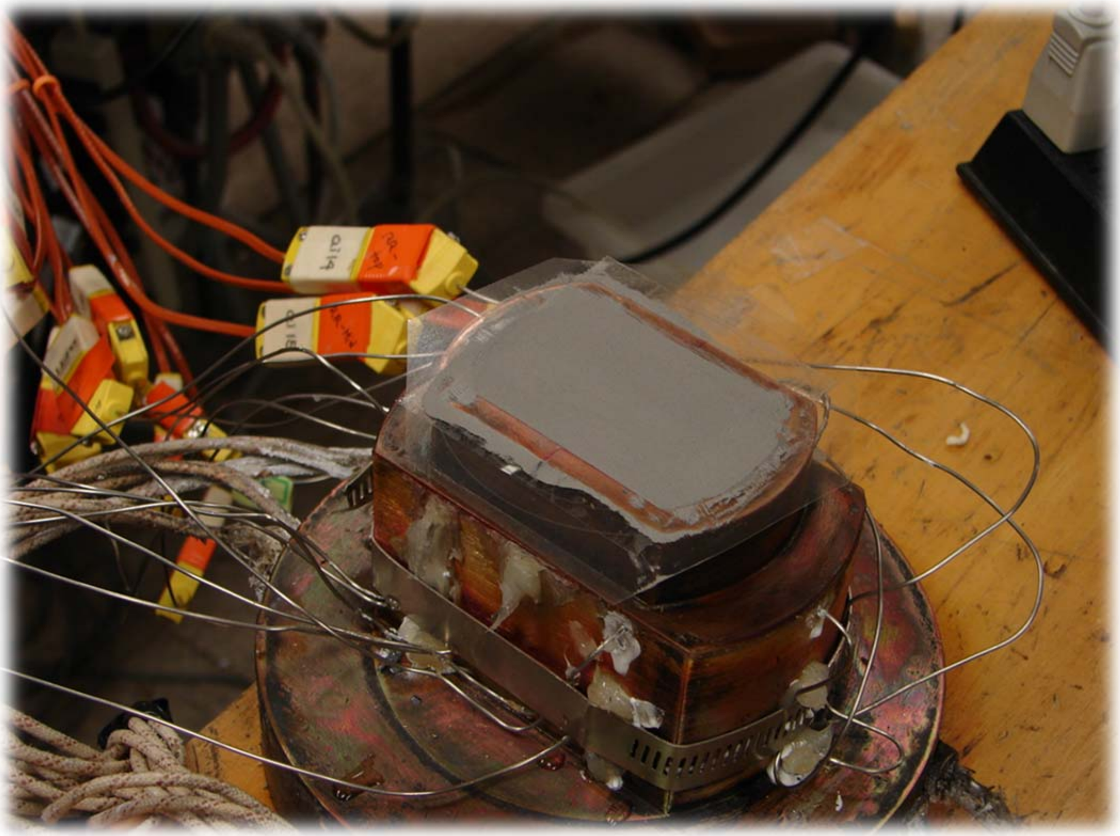

Figure A.10 Thermal paste coated.

Use the joint knife multiple times until the surface of interest is covered uniformly as seen in figure A.10.

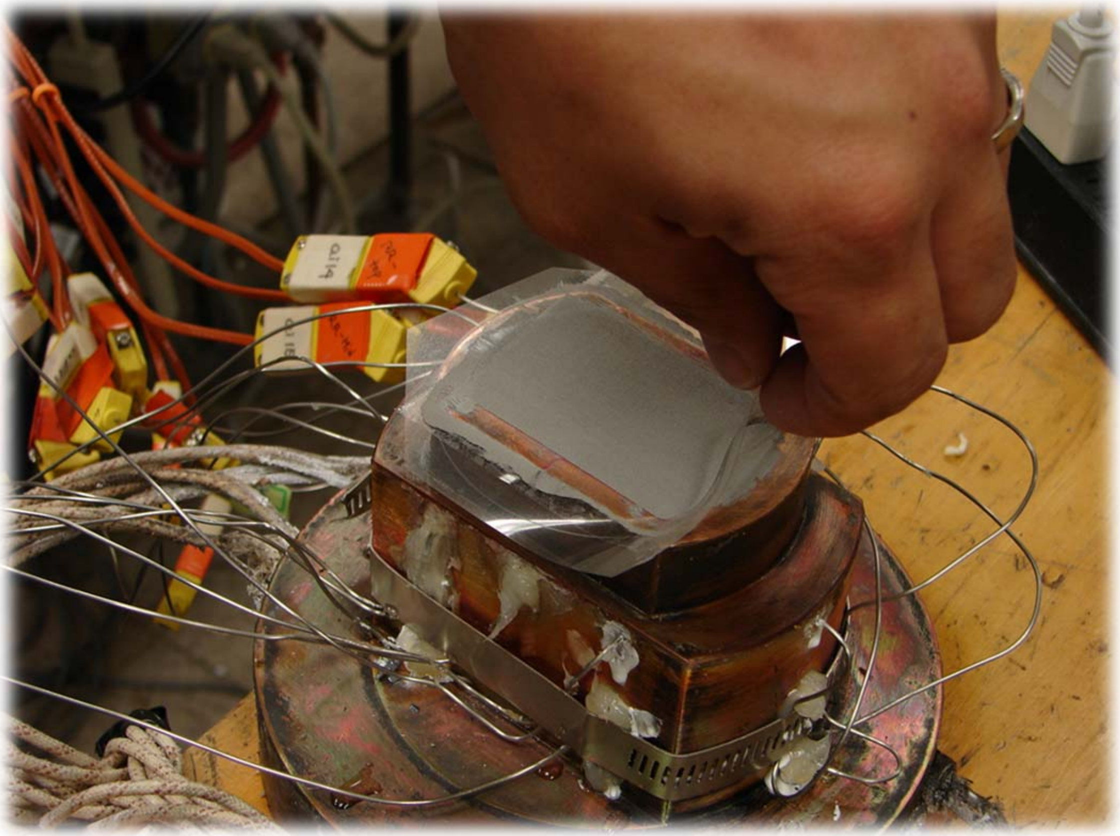

Figure A.11 Peeling off the transparency.

After making sure that the thermal paste is covered fully, start to peel off slowly from one end of the transparency film. While peeling off the transparency, it is acceptable to have some of the thermal paste smeared into the space between the film and the copper block.

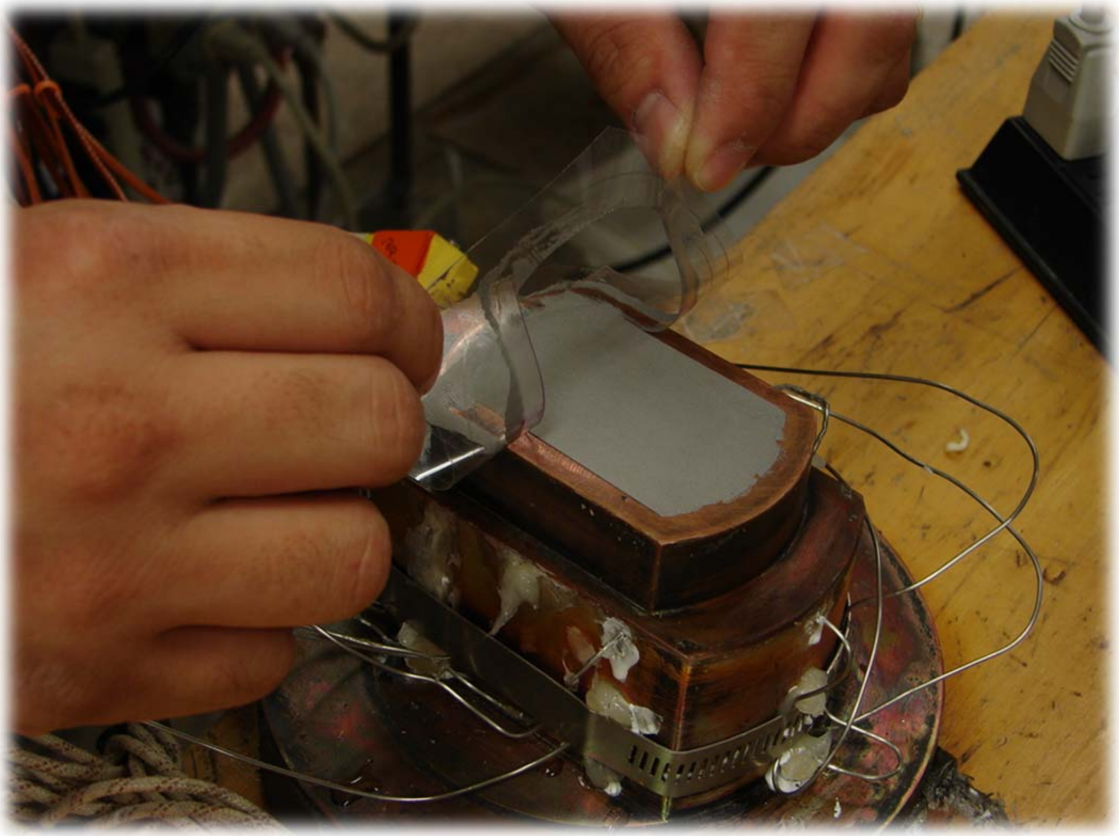

Figure A.12 Removing the transparency.

Use both of your hands to peel off the transparency as shown in figure A.12.

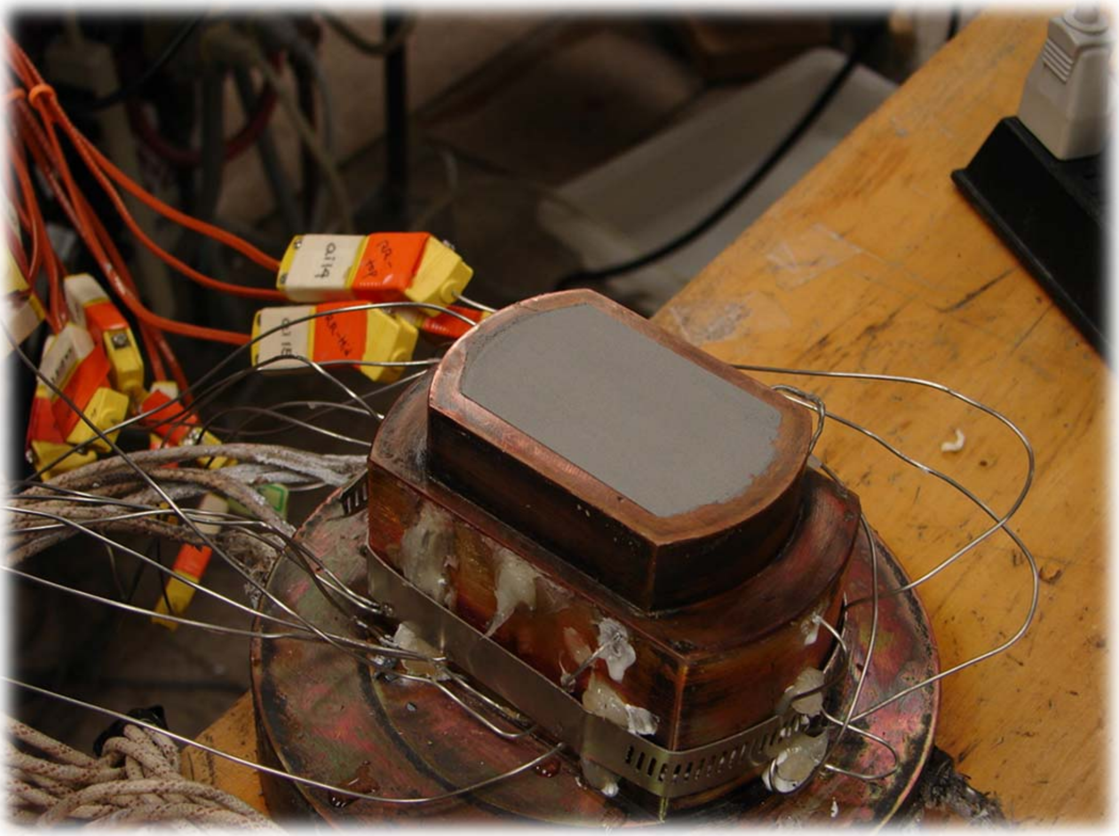

Figure A.13 Thermal paste coated on the copper block.

Figure A.13 shows how it should look like after the thermal paste is applied properly on the copper block.

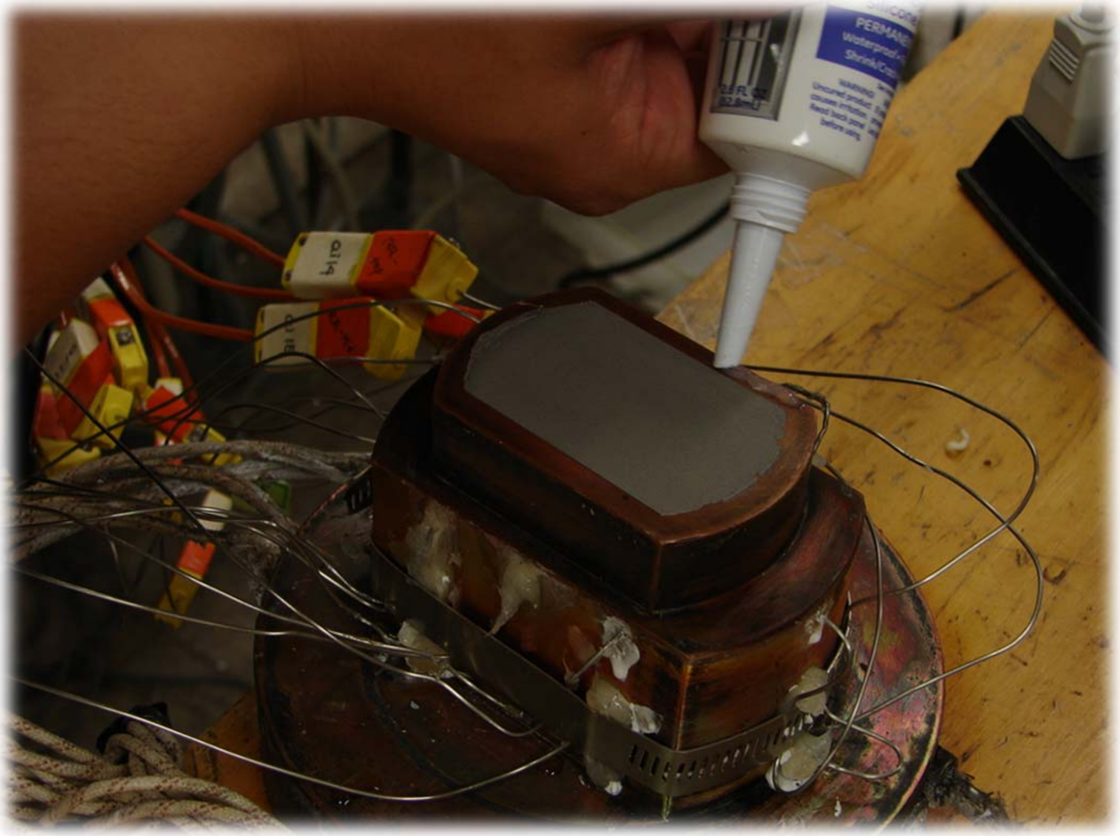

Figure A.14 Applying silicon at the edge of the thermal paste coated copper block.

Now, use the premium silicone paste and apply it at the perimeter of the uncoated area on the copper block. The reason for using the transparency film is to apply the thermal paste with even thickness on the copper block and to secure the perimeter for application of the silicone paste. The main reason for the application of the silicone paste is to promote the adhesion of the silicon wafer on the copper block. At high heat fluxes during the experiment a high temperature region is formed in the center of the copper block, causing the wafer to dislodge from the top of the copper block (due to mismatch caused by thermal expansion). This strategy was implemented to enhance the adhesion of the silicon wafer to the copper block.

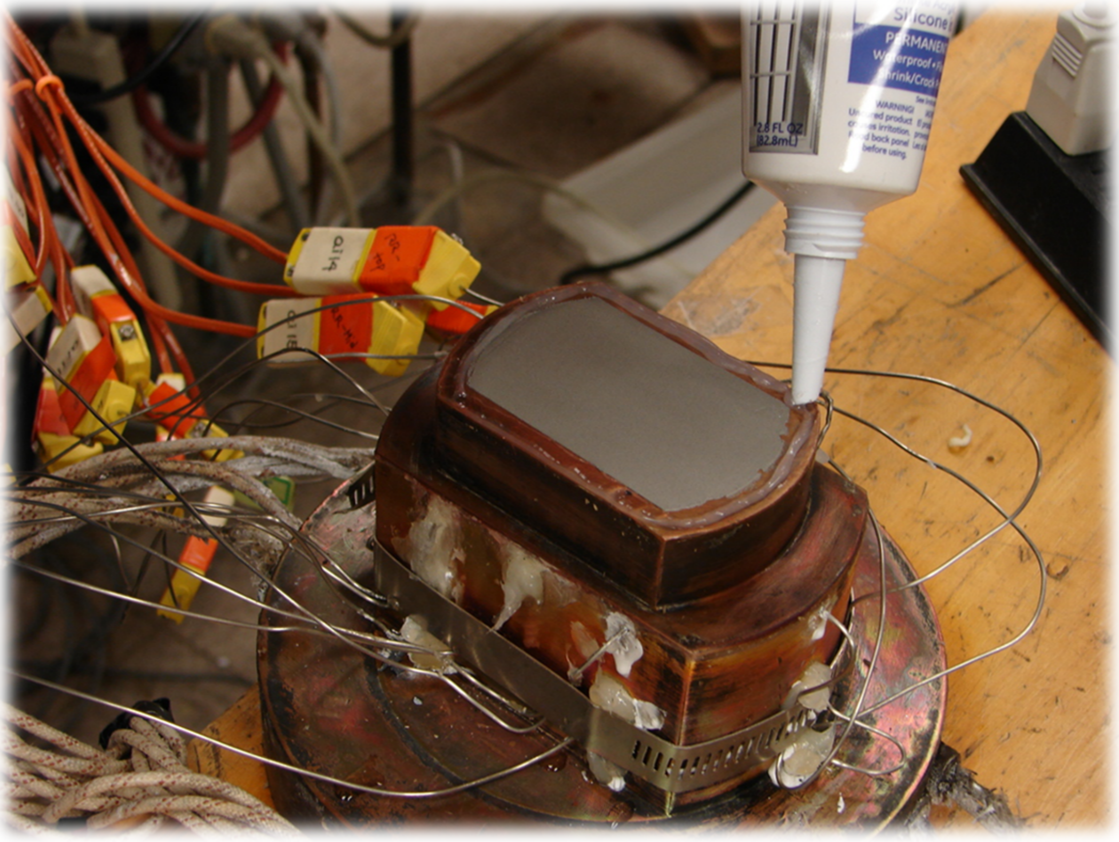

Figure A.15 Applying the silicon around the perimeter.

Apply the silicone paste around the perimeter. In this process, premium transparent silicone (Manufacturer: GE) was used. Instead of using the squeezing tool for applying large pressures to dispense the silicone paste, this brand of silicone was available in a single tube which the user could apply manually.

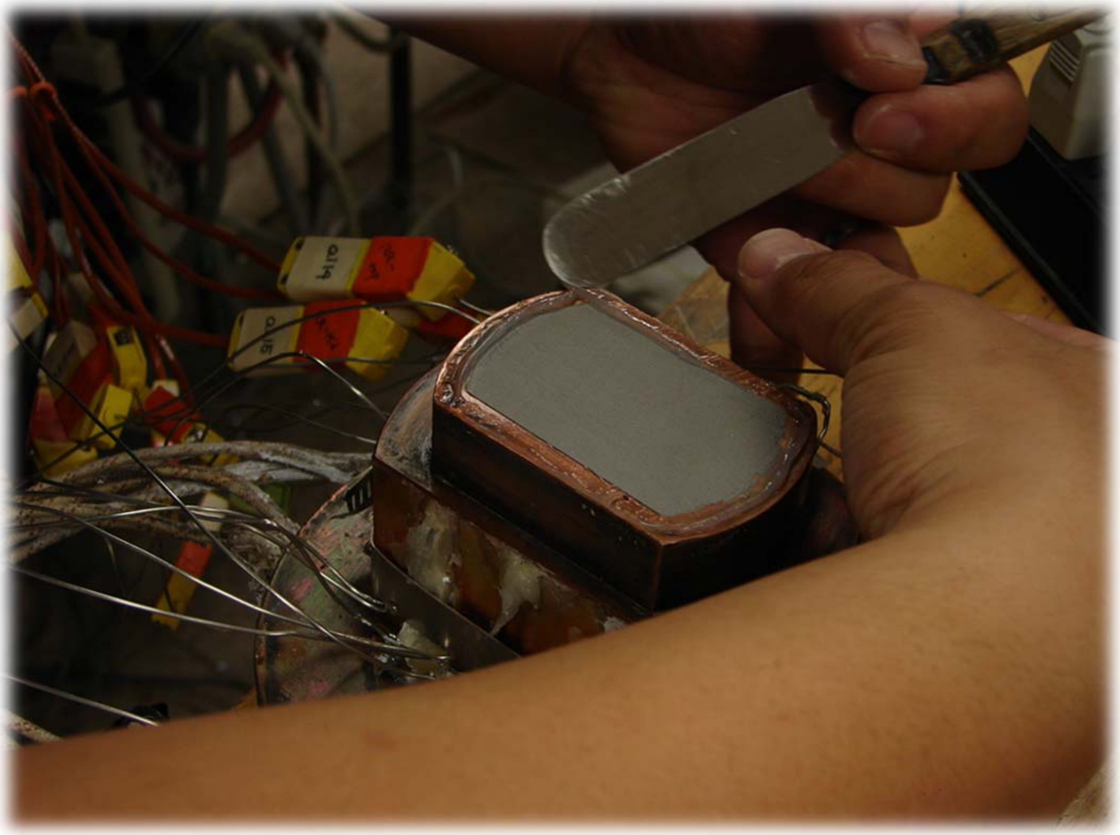

Figure A.16 Spreading the silicon around the perimeter.

After the silicone paste is applied on the perimeter of the copper block, use a smaller joint knife to spread it in a thin layer by partially mixing with the thermal paste at the boundary.

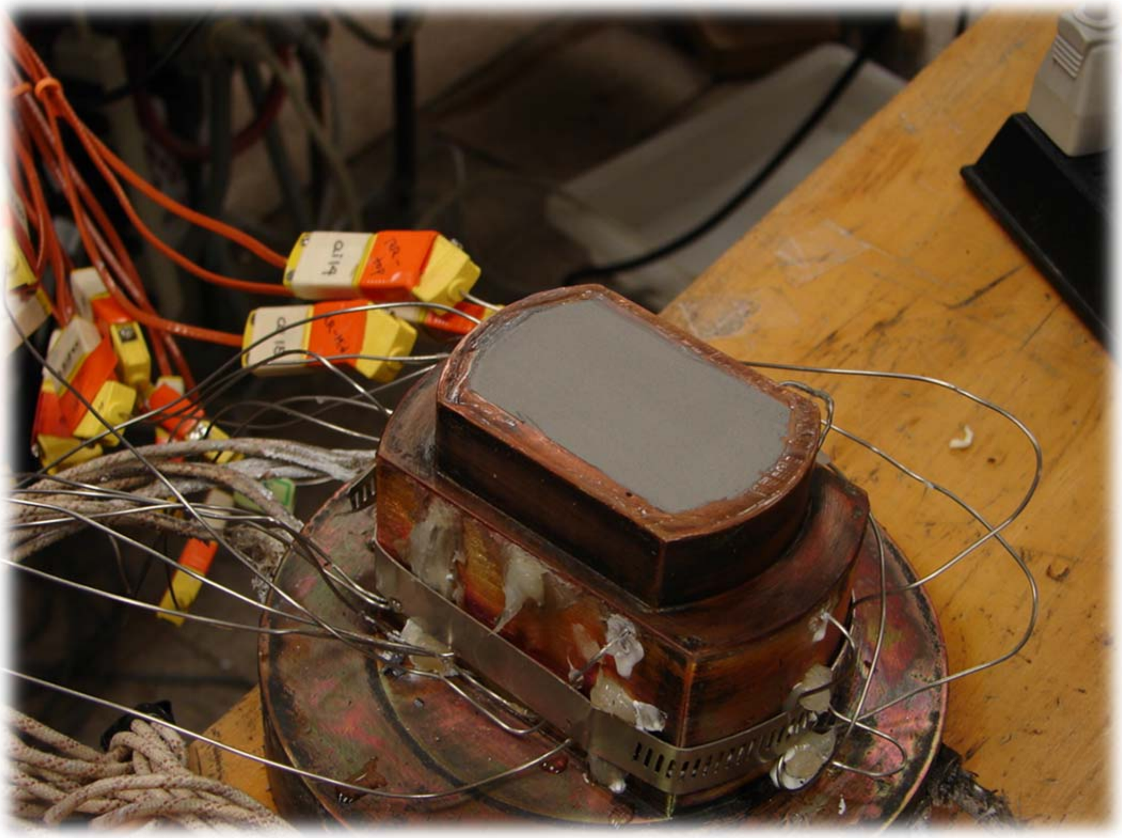

Figure A.17 Final look with the thermal paste and the silicon applied.

Figure A.17 shows the final picture with the thermal paste and the silicone paste applied before the silicon wafer is mounted on the copper block.

Figure A.18 Wafer to be used for the experiment.

CNT coated silicon wafer needs to be placed on to the heater surface.

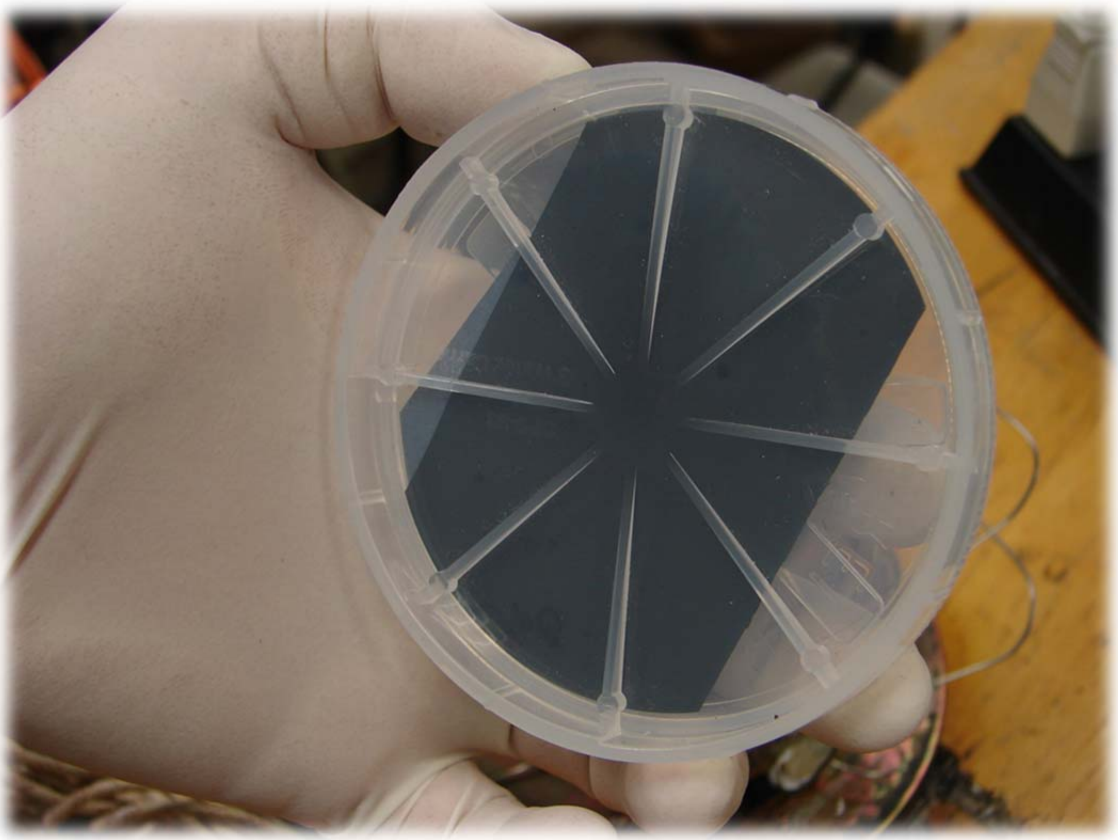

Figure A.19 CNT coated wafer seen in the wafer carrier (container).

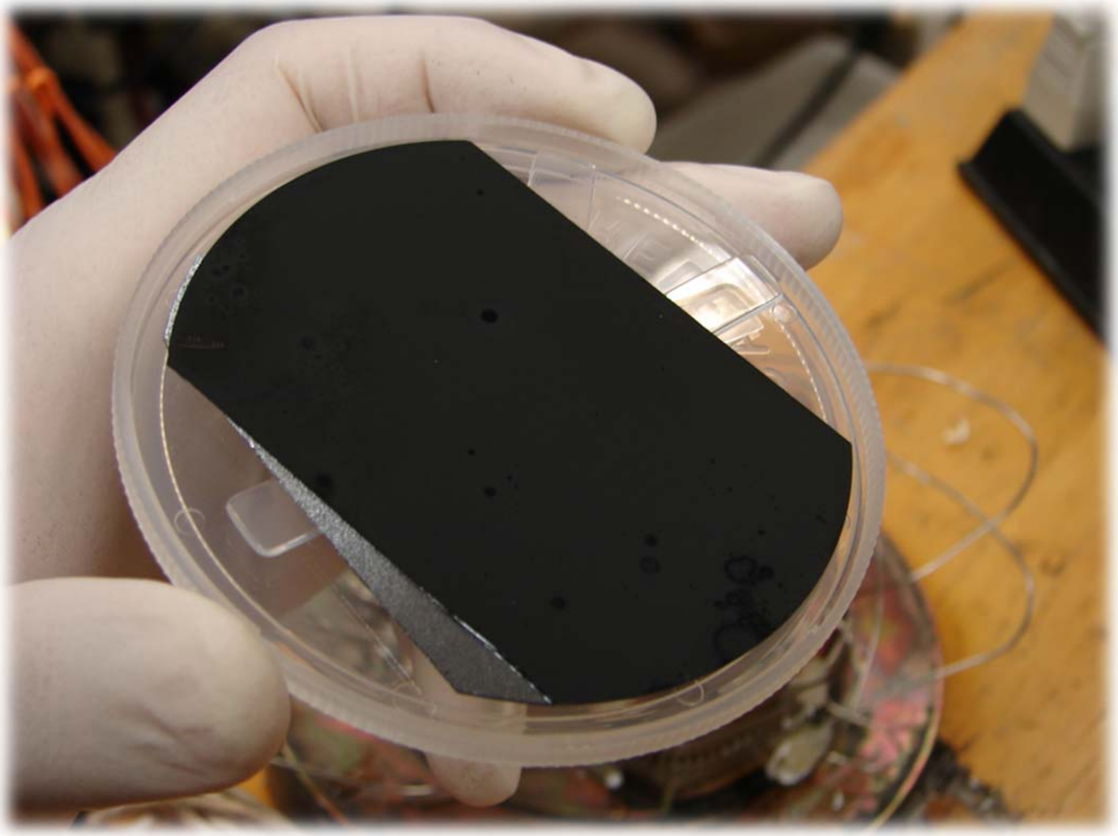

Figure A.20 CNT coated wafer.

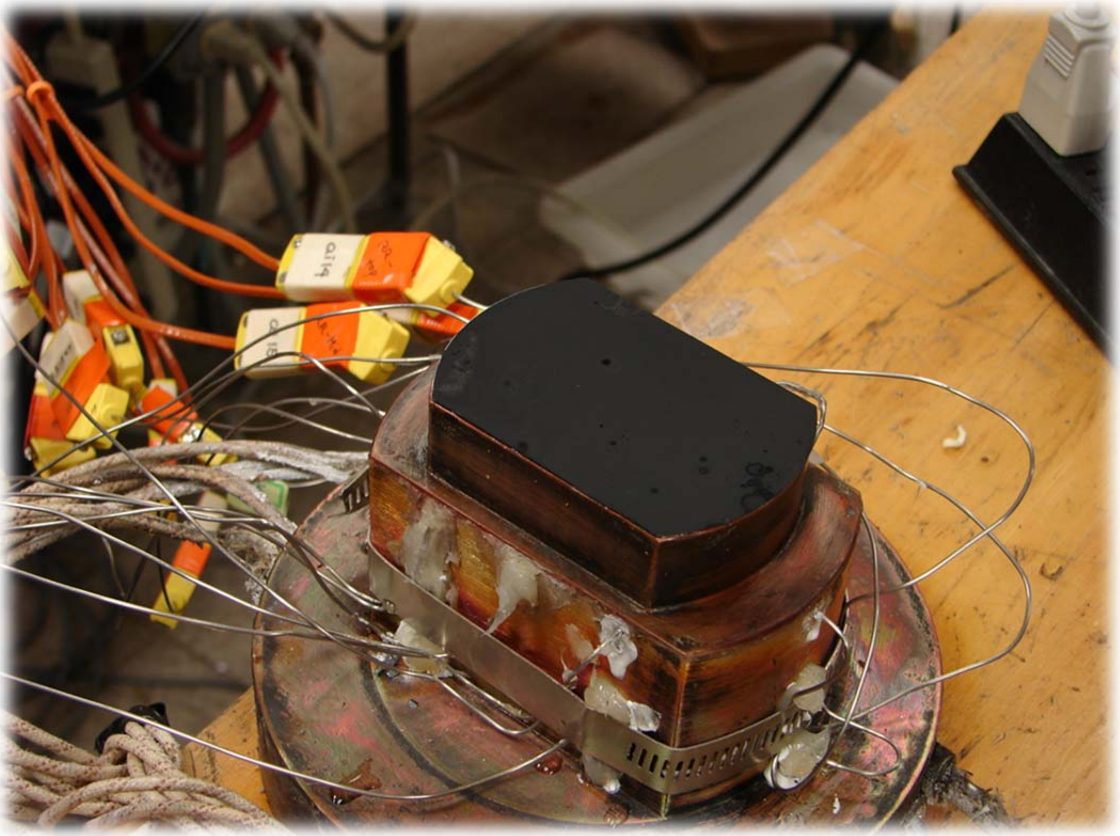

Figure A.21 CNT coated wafer placed on the heater.

Place the CNT coated wafer on the heater surface contacting from one end and slowly let it settle. Do not push or press as the wafer as it may break since it is brittle.

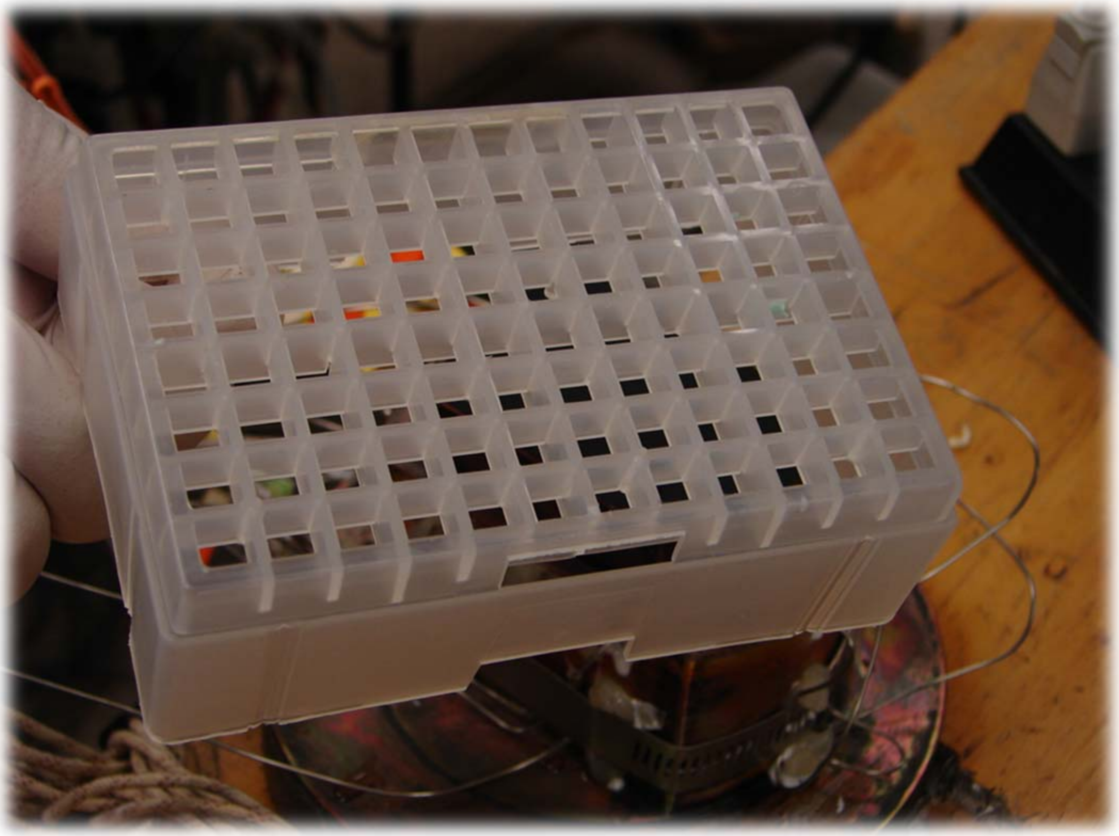

Figure A.22 Mesh acting as adapter.

Use the mesh as shown in figure A.22 to apply load onto the CNT coated wafer. This is necessary because the wafer needs to be pressed down but at the same time it should not be destroyed by the surface.

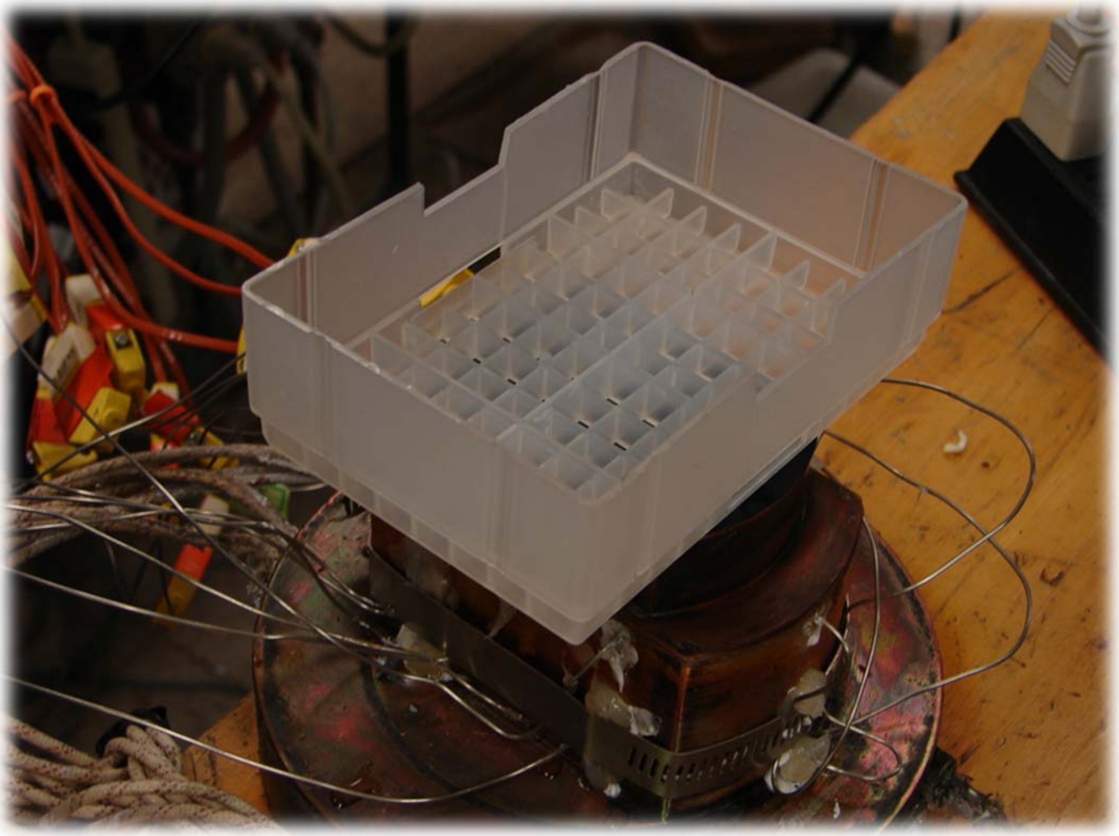

Figure A.23 Adapter before placing load on the wafer.

Carefully center the adapter on the wafer and place it as shown in figure A.23. Do not move or adjust once the adapter is on the CNT coated wafer as it will destroy or smear the coating.

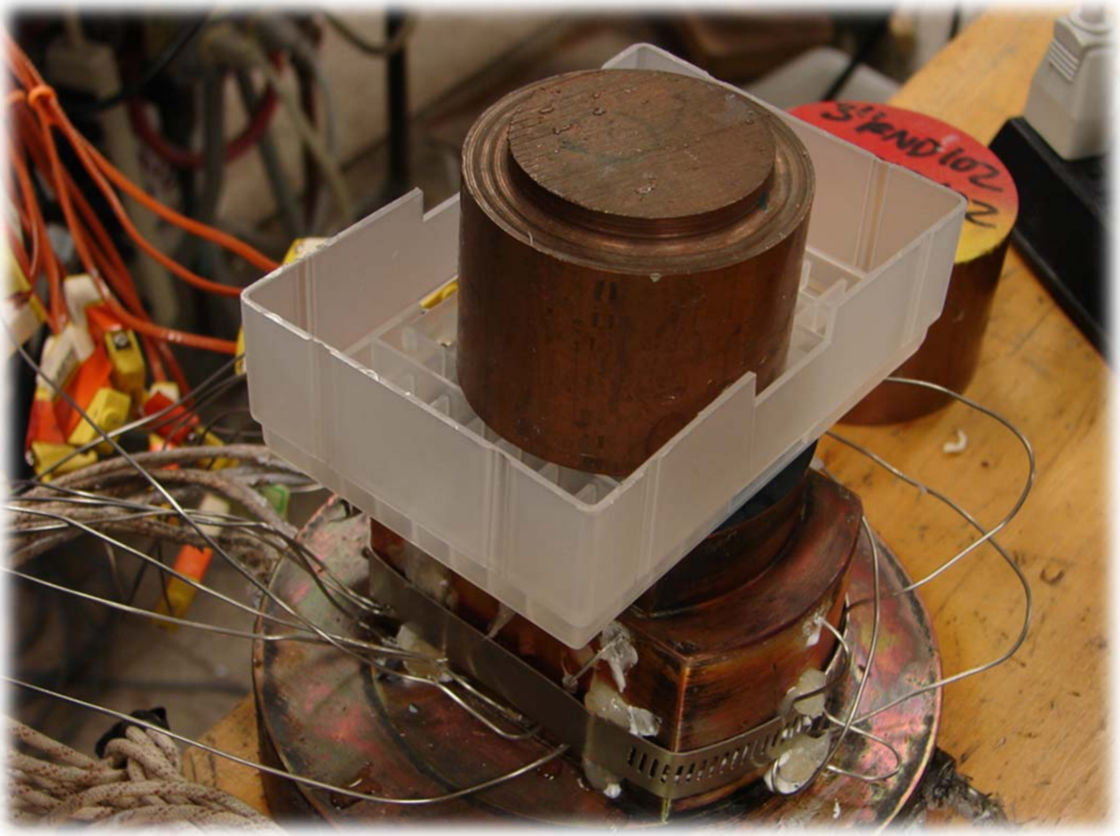

Figure A.24 Weight on the adapter.

Place a weight on the adapter slowly at the center as shown in Figure A.24. After the weight has been applied, turn on the power supply to approximately 5V to add a small heat flux on the copper block surface in order to let the thermal paste and the silicon cure to obtain better quality of adhesion. The CNT coated wafer and the copper block needs to me monitored every 5 minutes to avoid the weight from slipping to one side or causing the wafer to shift on the copper block. If a shift or movement of the wafer is found, adjust it with your hand by pushing it to the original location. The monitoring and adjusting should be performed until the thin film between the copper block and the wafer is cured fully. The wafer must be placed in proper orientation to avoid interference when the copper block is docking into the main test section by raising the mini jack.

APPENDIX B

CONSTRUCTION OF THE FLOW BOILING TEST SECTION

This section will introduce the design for the main test section used for the flow boiling experiments. Raw material that was used for the main test section is 1” thick aluminum plate which was machined in the Mechanical Engineering Department Work Shop using Bridgeport 3D milling machine. Related images and drawings are included for better clarity. The design is a modified construction of the phase-I model that had acrylic windows. At phase-I, since the walls were made out of acrylic frequent leakage and bulging of the main test section at higher flow rates was observed. In addition, since the cross section was large, the flow in the chamber was not uniform. In addition, due to the high heat flux from the halogen lamps, part of the top cover was melted locally. In order to overcome these problems, in phase-II the main test section for the flow boiling was modified according to the design shown here.

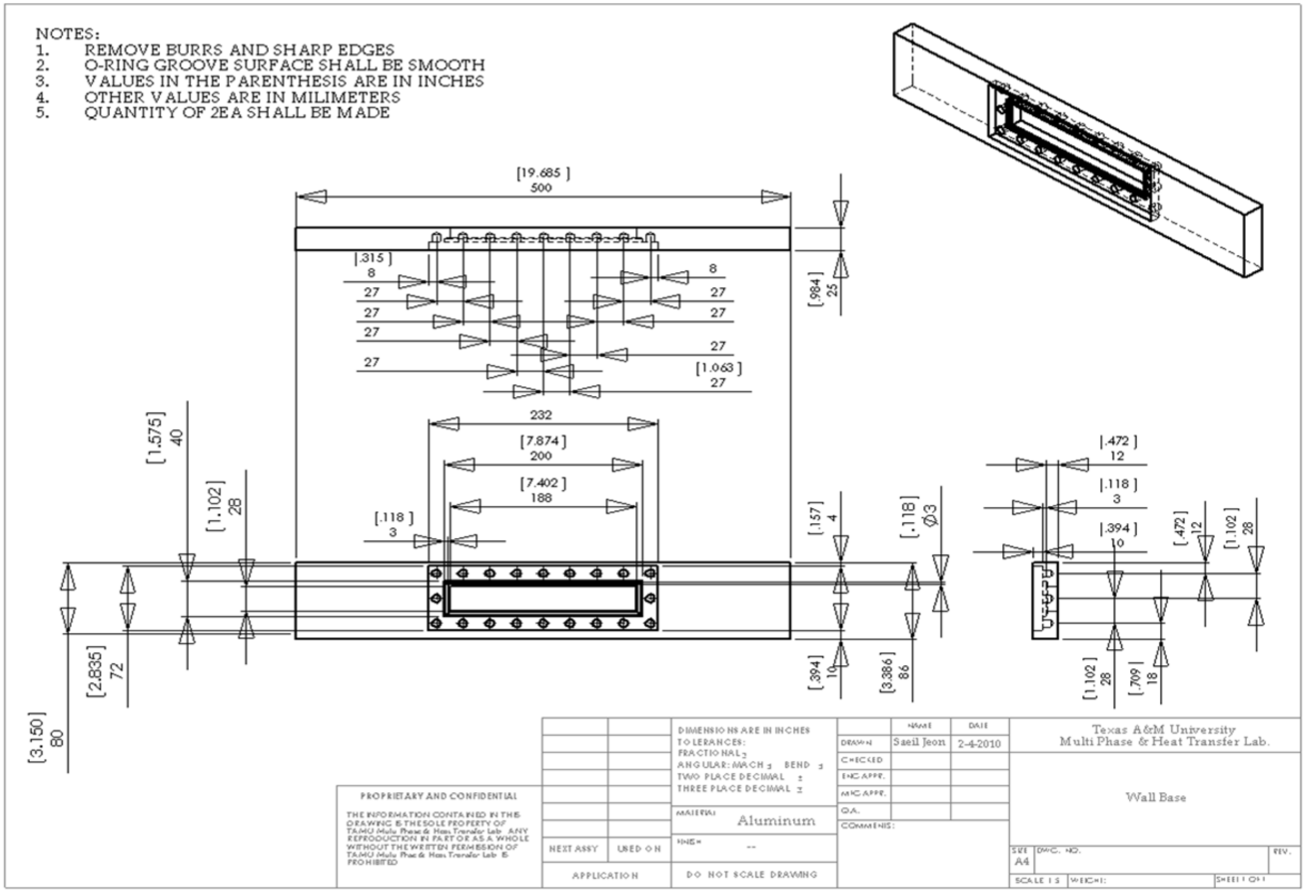

Figure B.1 Drawing – Side wall.

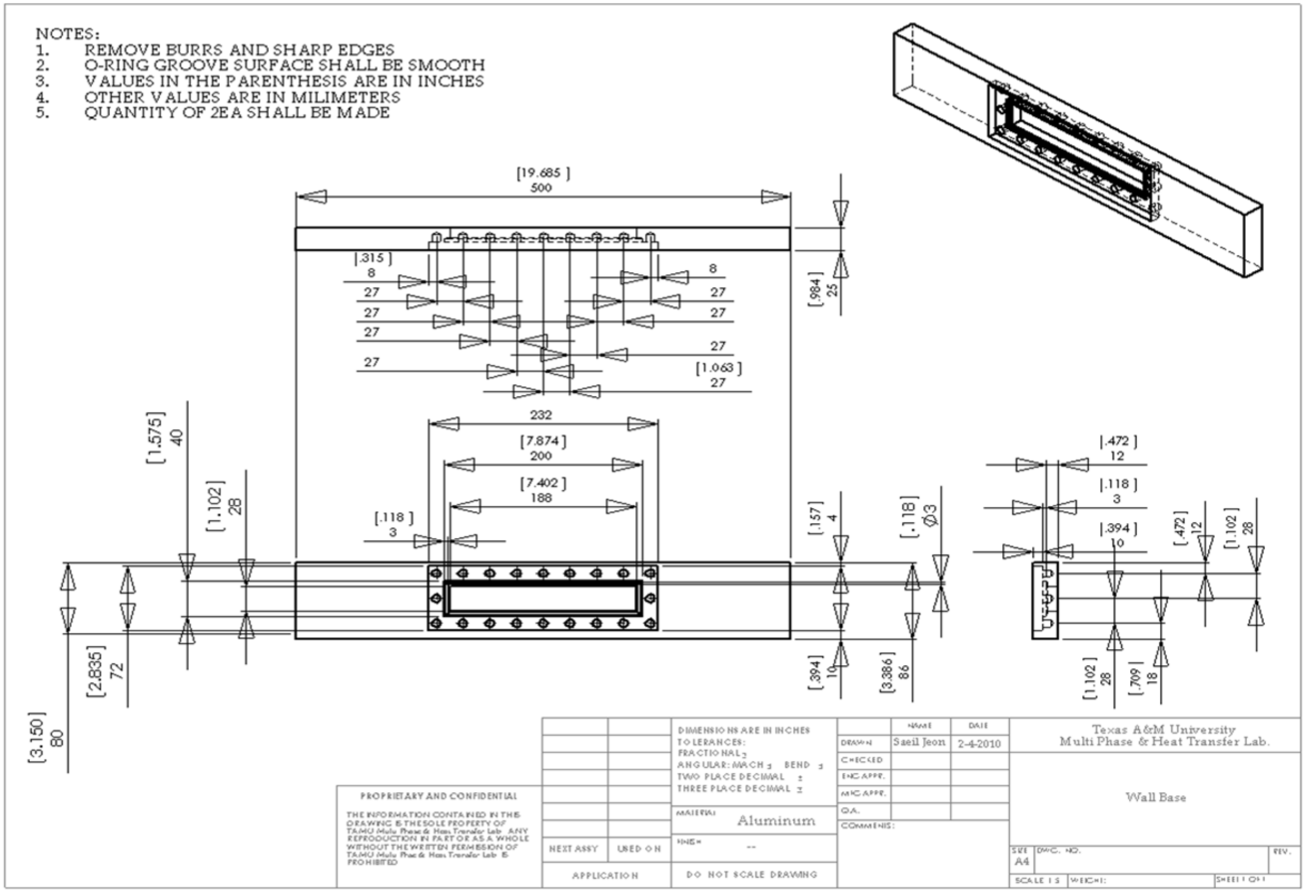

Figure B.1 Drawing – Side wall.

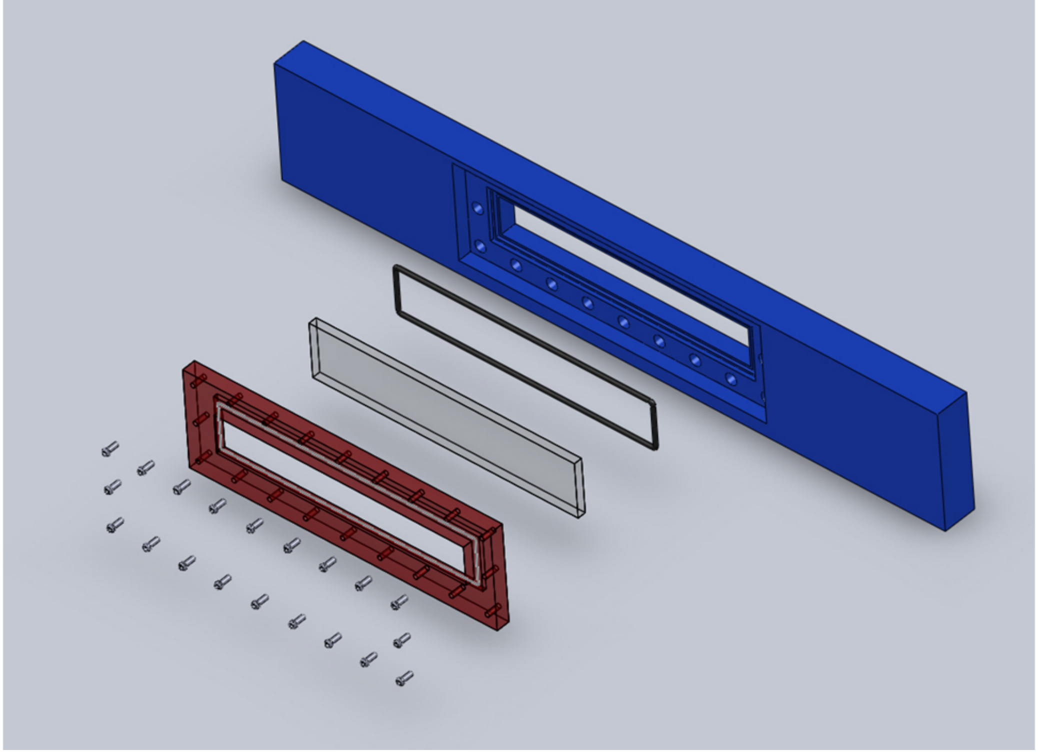

Figure B.2 Assembly diagram of the side wall for the flow boiling test section.

The side wall is made out of 1” thickness aluminum (Blue). As shown in the figure above, an O-ring (Black) is fitted within the groove of the wall before attaching the acrylic transparent window (Gray). Another O-ring is attached on the outer cover (Red). When assembled using the button head bolts the thrust of the bolts will automatically compress the O-rings on both sides of the clear window in order to achieve proper sealing. The side walls of the flow boiling section are constructed using the above design. This enables the mounting and dismounting of the viewing window to be easier and without having to disassemble the whole wall from the main test section.

APPENDIX C

HEAT FLUX DATA AND HEAT TRANSFER COEFFICIENT CALCULATION FOR DROPLET IMPINGEMENT EXPERIMENTS

(1) Acetone – 45, Drop #01

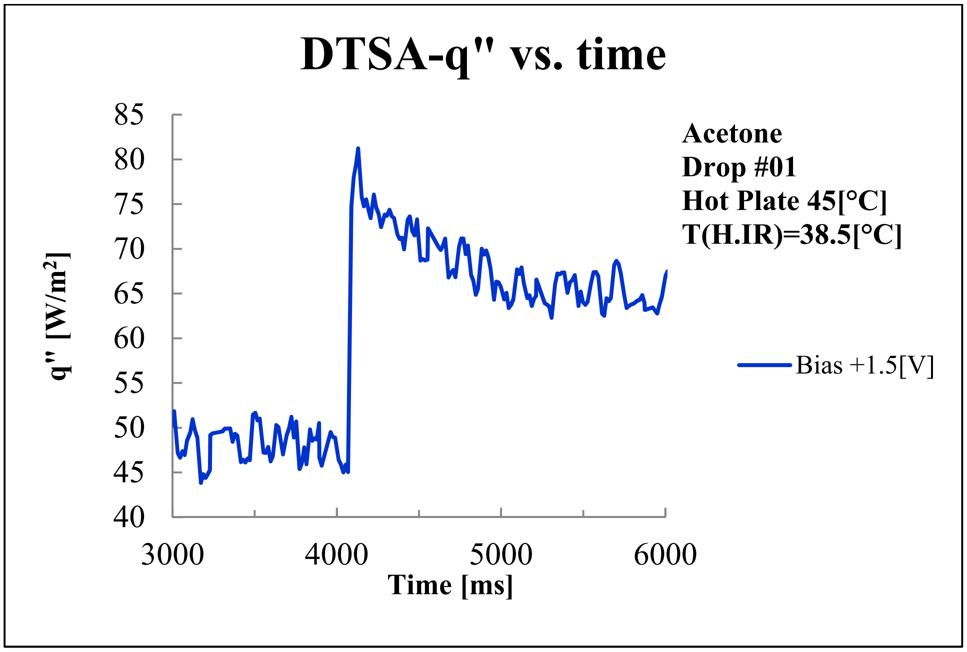

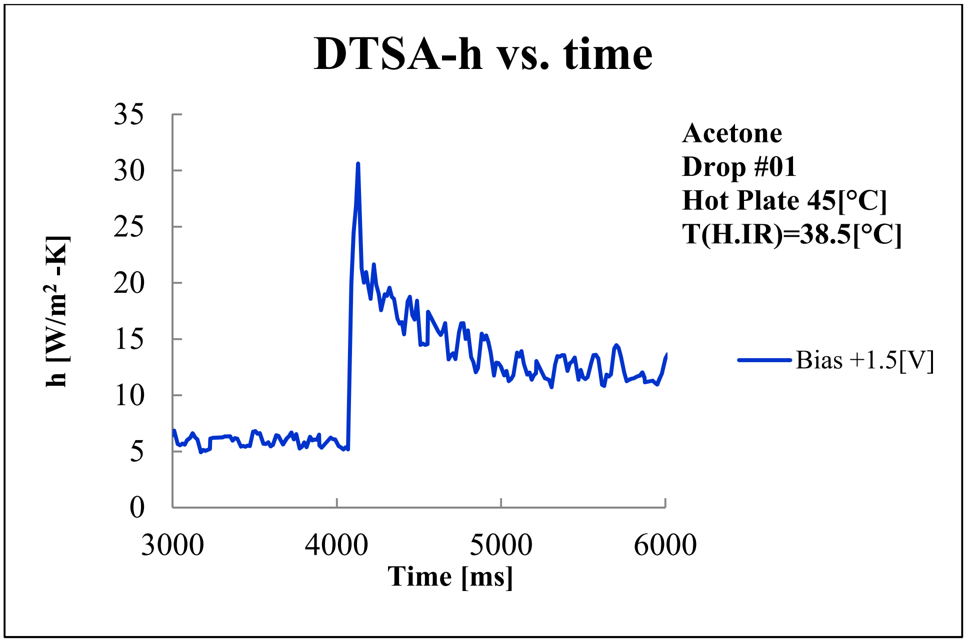

Drop #02

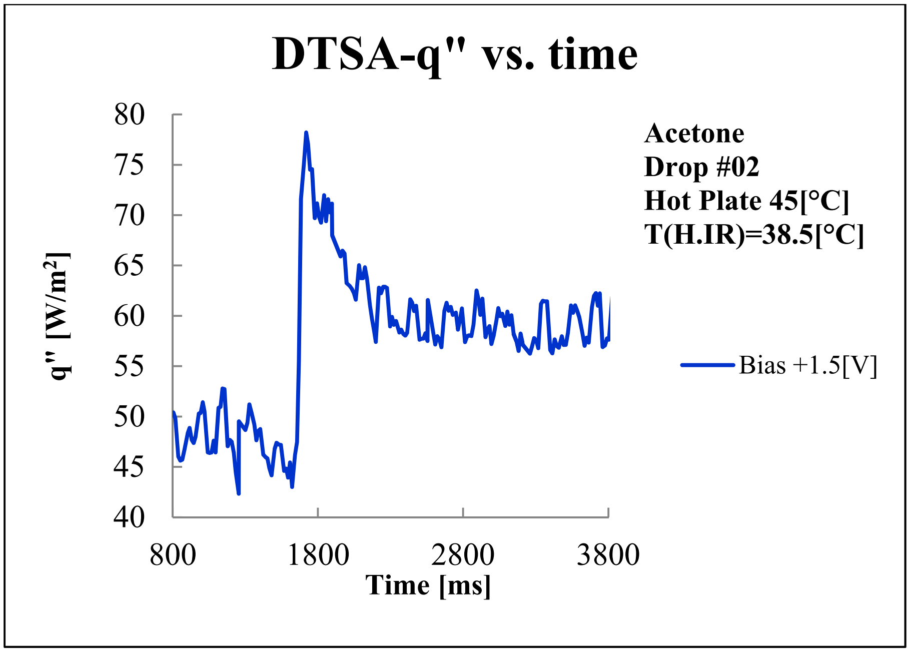
DTSA-q" vs. time
80
75
70
65
60
55
50
45
40
q" [W/m^2]
800
1800
2800
3800
Time [ms]
Acetone
Drop #02
Hot Plate 45[°C]
T(H.IR)=38.5[°C]
Bias +1.5[V]

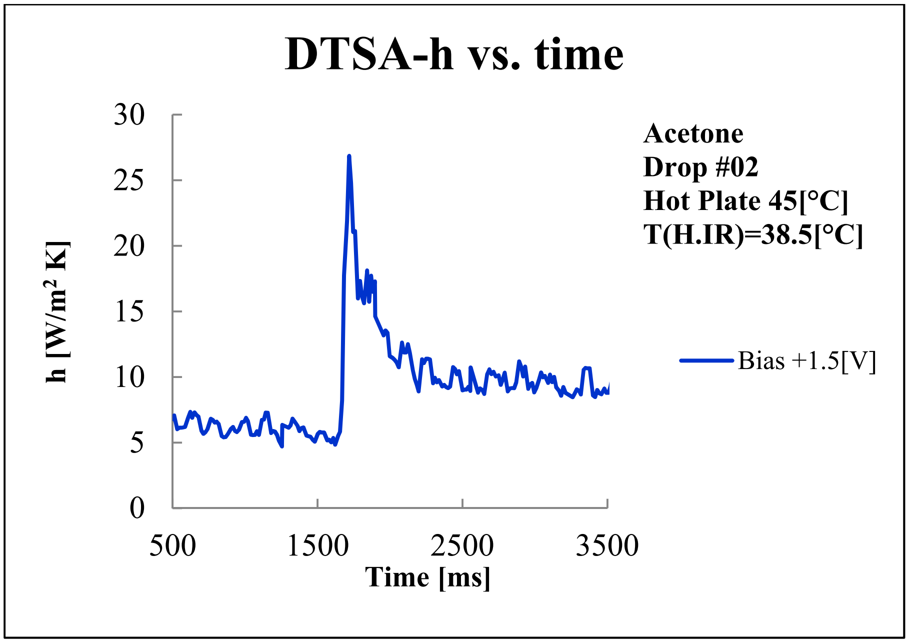
DTSA-h vs. time
30
25
20
15
10
5
0
h [W/m^2 K]
500
1500
2500
3500
Time [ms]
Acetone
Drop #02
Hot Plate 45[°C]
T(H.IR)=38.5[°C]
Bias +1.5[V]

Drop#03

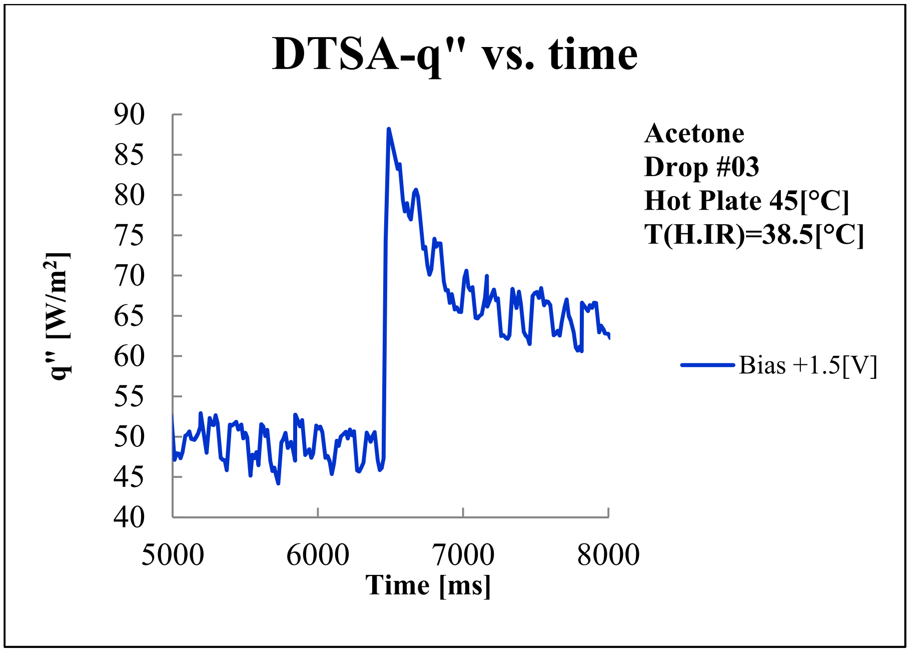
DTSA-q" vs. time
q" [W/m²]
90
85
80
75
70
65
60
55
50
45
40
5000
6000
7000
8000
Time [ms]
Acetone
Drop #03
Hot Plate 45[°C]
T(H.IR)=38.5[°C]
Bias +1.5[V]

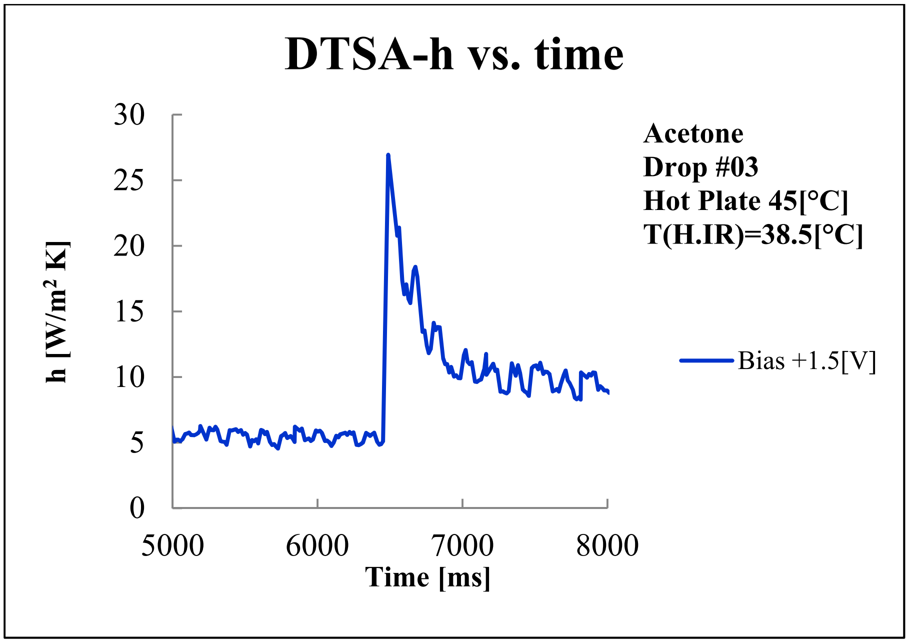
DTSA-h vs. time
h [W/m² K]
30
25
20
15
10
5
0
5000
6000
7000
8000
Time [ms]
Acetone
Drop #03
Hot Plate 45[°C]
T(H.IR)=38.5[°C]
Bias +1.5[V]

Drop#04

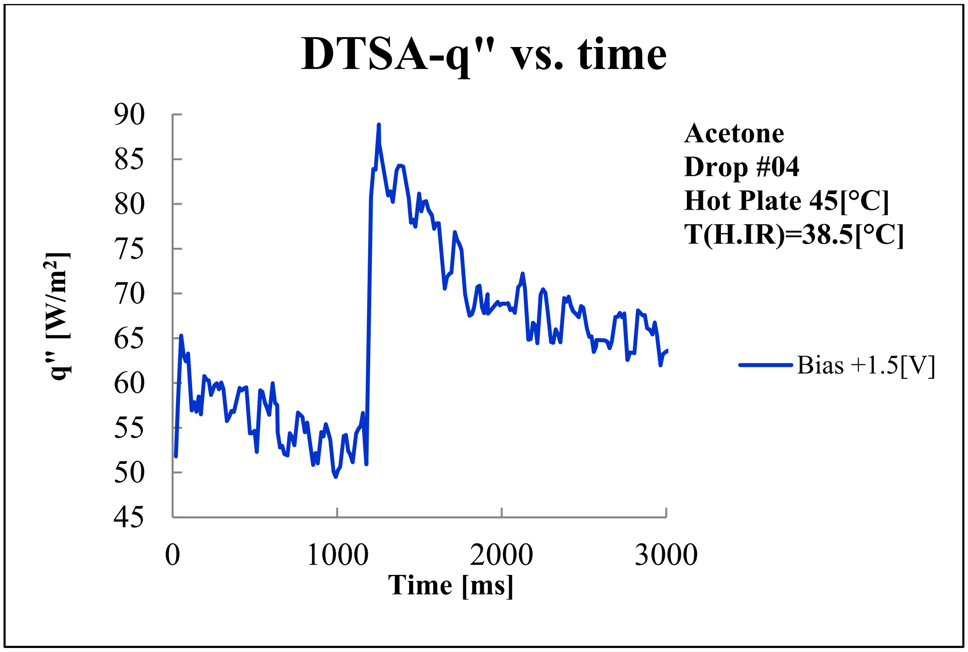
DTSA-q" vs. time
q" [W/m^2]
90
85
80
75
70
65
60
55
50
45
0
1000
2000
3000
Time [ms]
Acetone
Drop #04
Hot Plate 45[°C]
T(H.IR)=38.5[°C]
Bias +1.5[V]

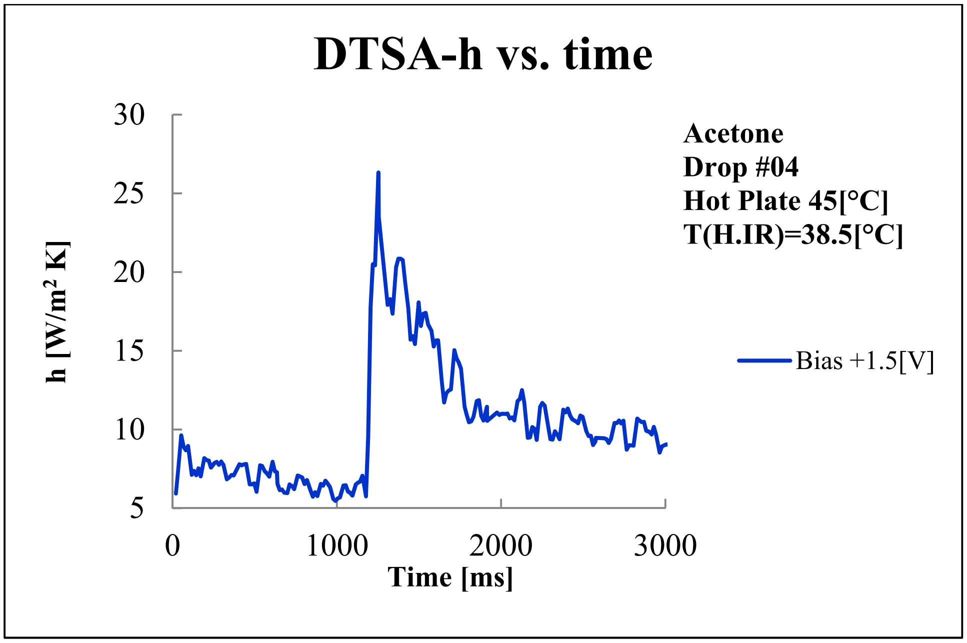
DTSA-h vs. time
h [W/m^2 K]
30
25
20
15
10
5
0
1000
2000
3000
Time [ms]
Acetone
Drop #04
Hot Plate 45[°C]
T(H.IR)=38.5[°C]
Bias +1.5[V]

Drop#05

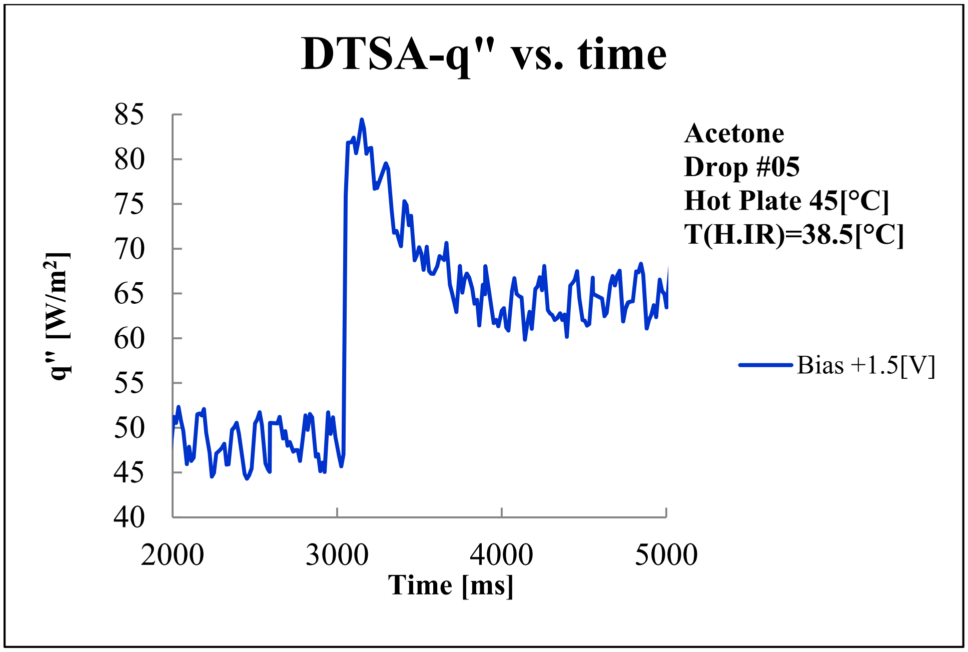
DTSA-q" vs. time
q" [W/m^2]
85
80
75
70
65
60
55
50
45
40
2000
3000
4000
5000
Time [ms]
Acetone
Drop #05
Hot Plate 45[°C]
T(H.IR)=38.5[°C]
Bias +1.5[V]

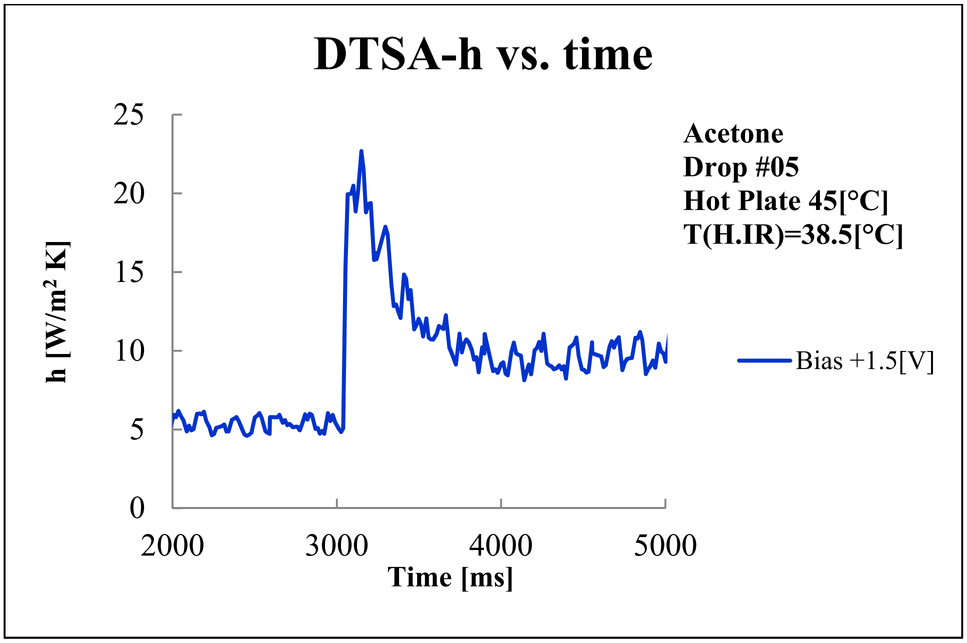
DTSA-h vs. time
h [W/m^2 K]
25
20
15
10
5
0
2000
3000
4000
5000
Time [ms]
Acetone
Drop #05
Hot Plate 45[°C]
T(H.IR)=38.5[°C]
Bias +1.5[V]

Drop#06

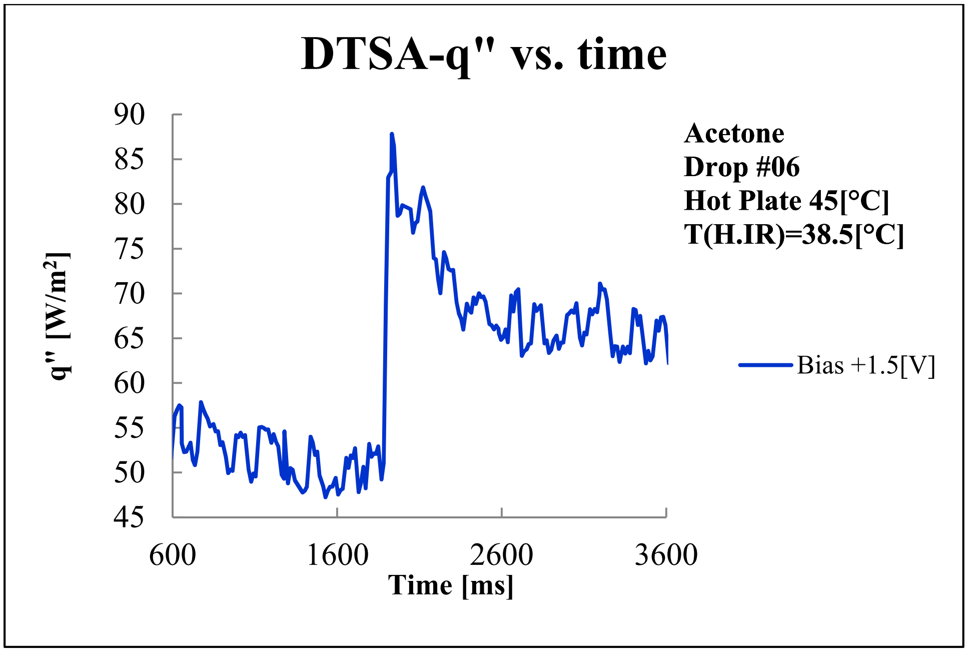
DTSA-q" vs. time
q" [W/m²]
90
85
80
75
70
65
60
55
50
45
600
1600
2600
3600
Time [ms]
Acetone
Drop #06
Hot Plate 45[°C]
T(H.IR)=38.5[°C]
Bias +1.5[V]

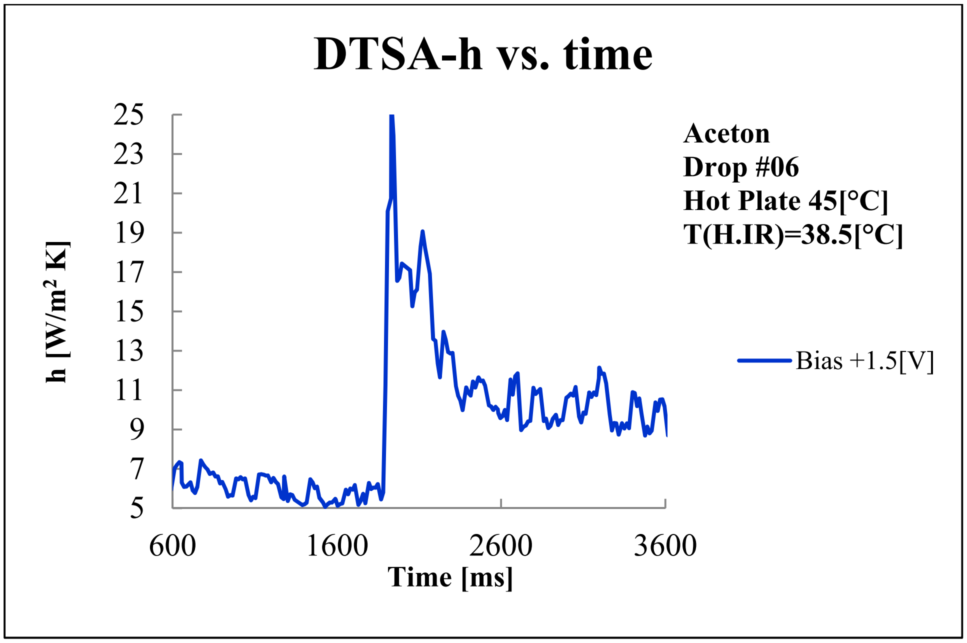
DTSA-h vs. time
h [W/m² K]
25
23
21
19
17
15
13
11
9
7
5
600
1600
2600
3600
Time [ms]
Aceton
Drop #06
Hot Plate 45[°C]
T(H.IR)=38.5[°C]
Bias +1.5[V]

Drop#07

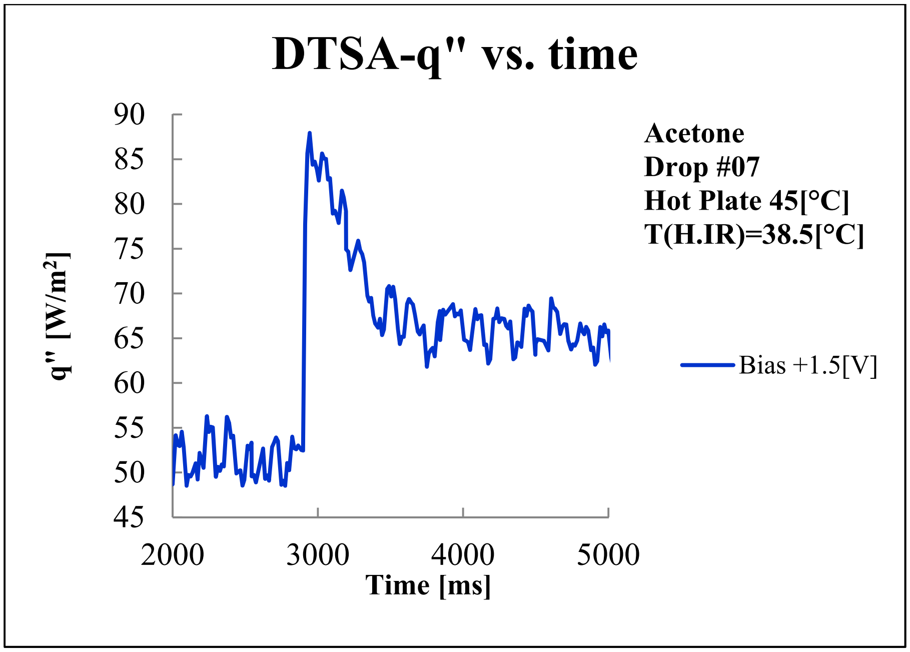
DTSA-q" vs. time
q" [W/m²]
90
85
80
75
70
65
60
55
50
45
2000
3000
4000
5000
Time [ms]
Acetone
Drop #07
Hot Plate 45[°C]
T(H.IR)=38.5[°C]
Bias +1.5[V]

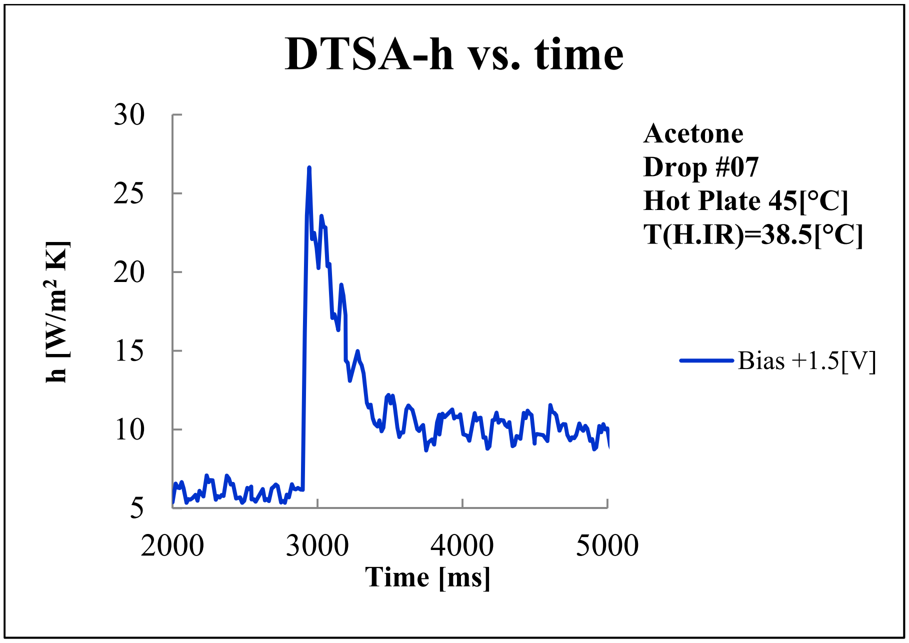
DTSA-h vs. time
h [W/m² K]
30
25
20
15
10
5
2000
3000
4000
5000
Time [ms]
Acetone
Drop #07
Hot Plate 45[°C]
T(H.IR)=38.5[°C]
Bias +1.5[V]

Drop#08

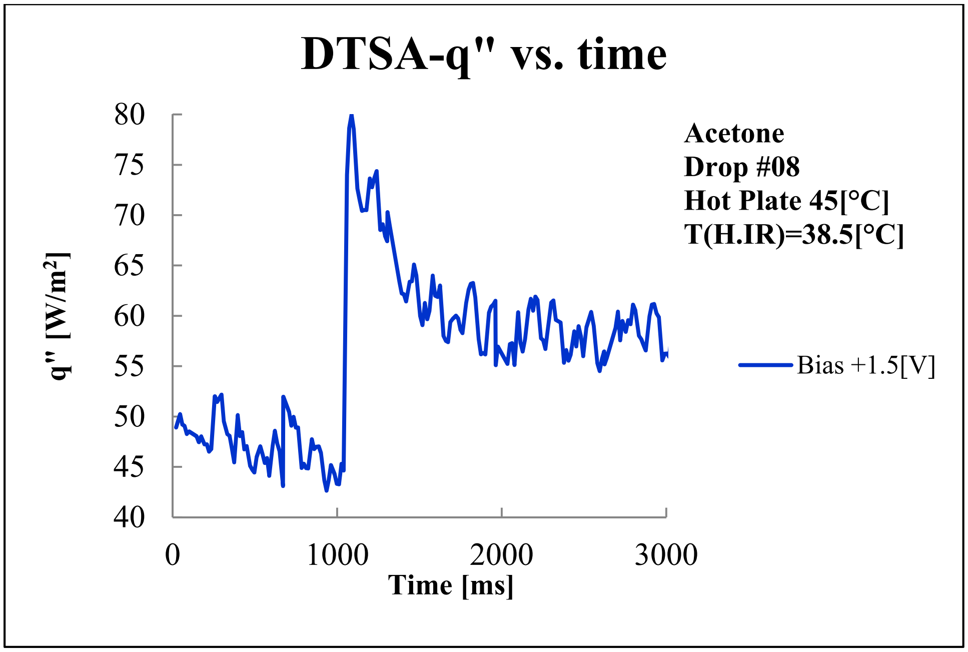
DTSA-q" vs. time
q" [W/m^2]
80
75
70
65
60
55
50
45
40
0
1000
2000
3000
Time [ms]
Acetone
Drop #08
Hot Plate 45[°C]
T(H.IR)=38.5[°C]
Bias +1.5[V]

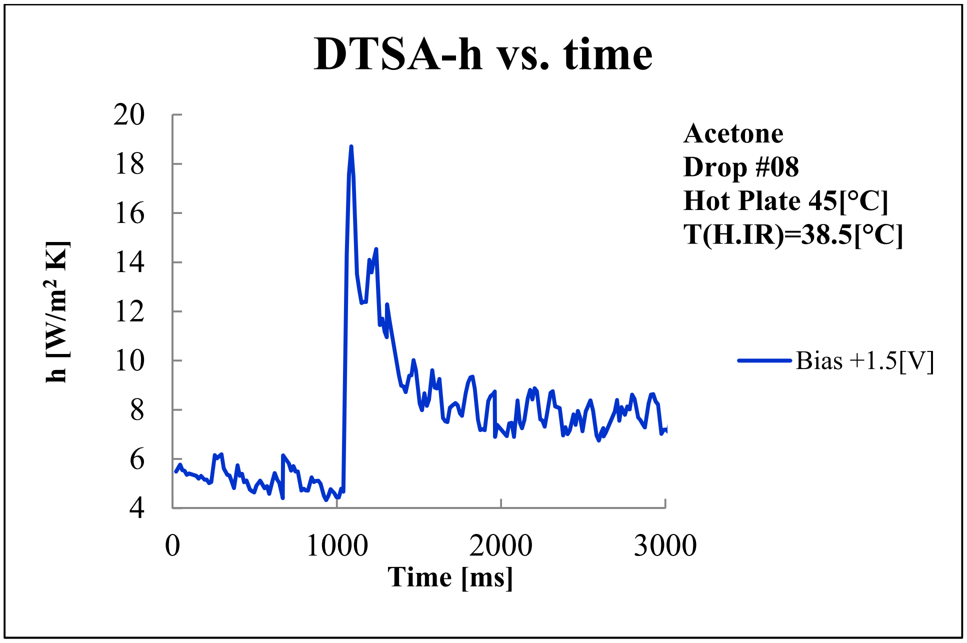
DTSA-h vs. time
h [W/m^2 K]
20
18
16
14
12
10
8
6
4
0
1000
2000
3000
Time [ms]
Acetone
Drop #08
Hot Plate 45[°C]
T(H.IR)=38.5[°C]
Bias +1.5[V]

Drop#09

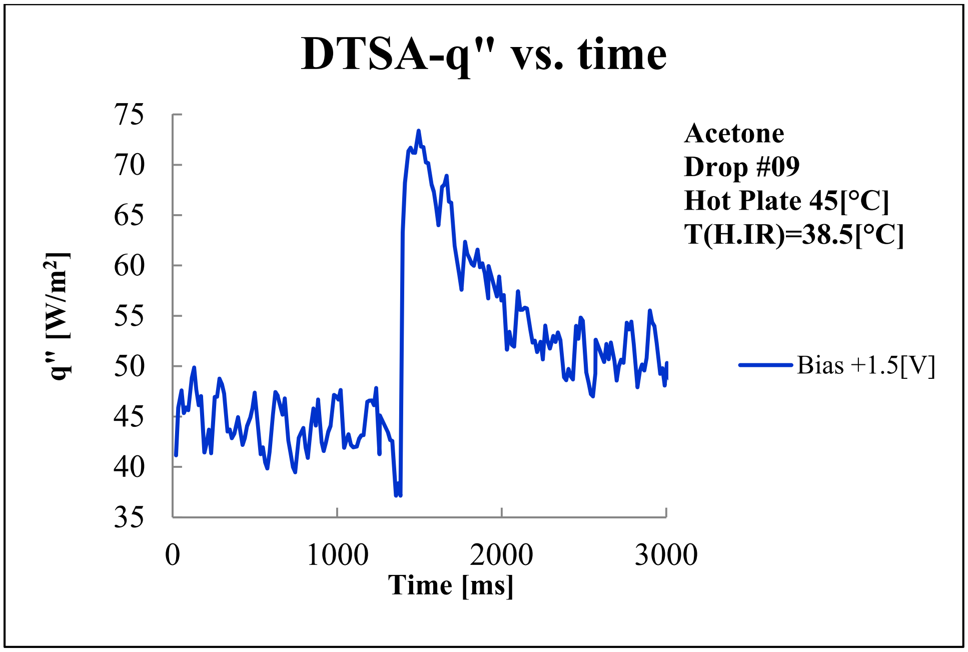
DTSA-q" vs. time
Acetone
Drop #09
Hot Plate 45[°C]
T(H.IR)=38.5[°C]
Bias +1.5[V]
q" [W/m2]
Time [ms]
75
70
65
60
55
50
45
40
35
0
1000
2000
3000

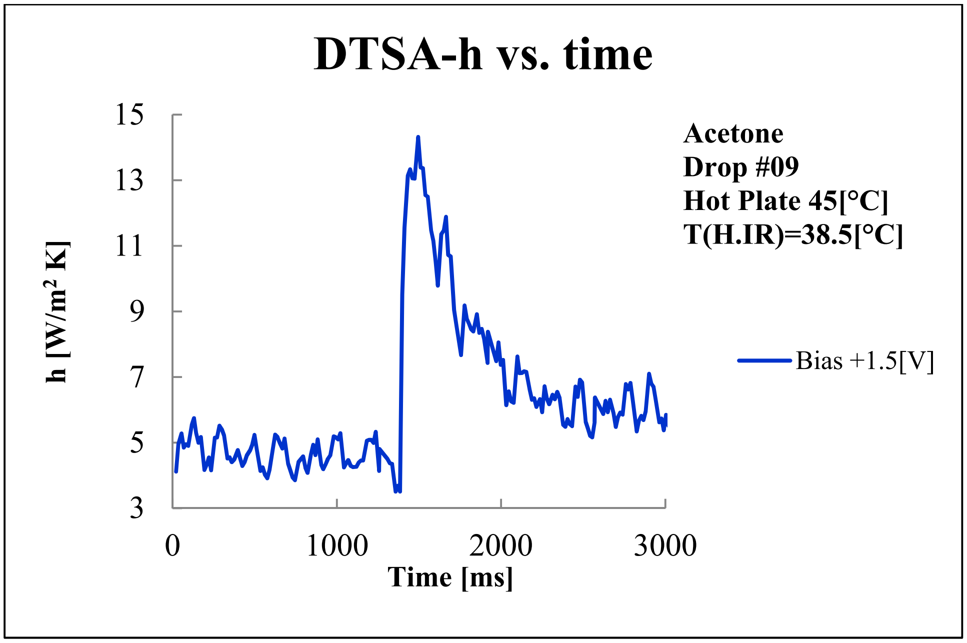
DTSA-h vs. time
Acetone
Drop #09
Hot Plate 45[°C]
T(H.IR)=38.5[°C]
Bias +1.5[V]
h [W/m2 K]
Time [ms]
15
13
11
9
7
5
3
0
1000
2000
3000

Drop#10

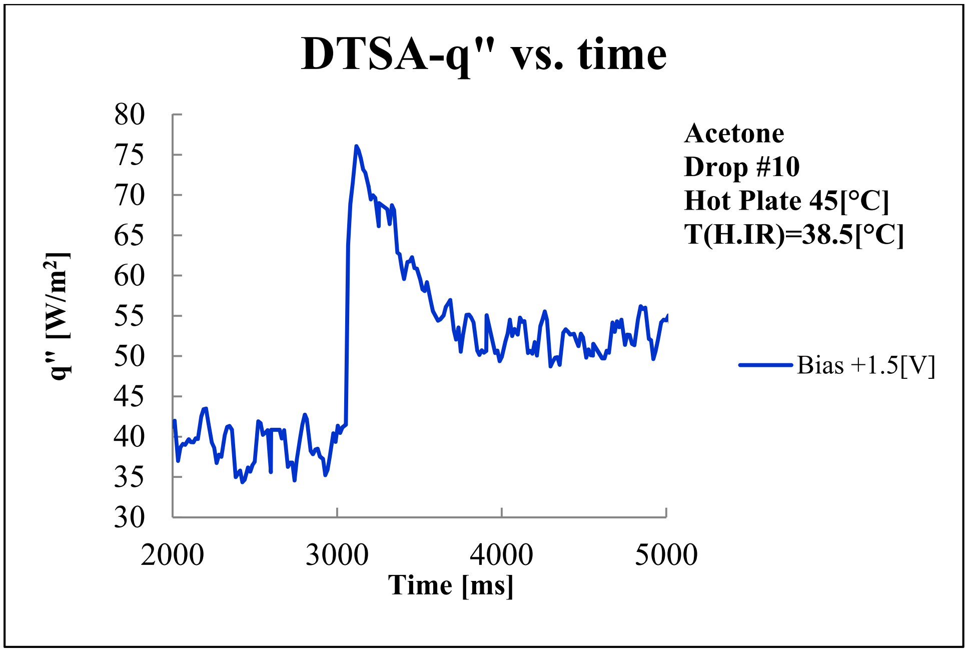
DTSA-q" vs. time
q" [W/m^2]
80
75
70
65
60
55
50
45
40
35
30
2000
3000
4000
5000
Time [ms]
Acetone
Drop #10
Hot Plate 45[°C]
T(H.IR)=38.5[°C]
Bias +1.5[V]

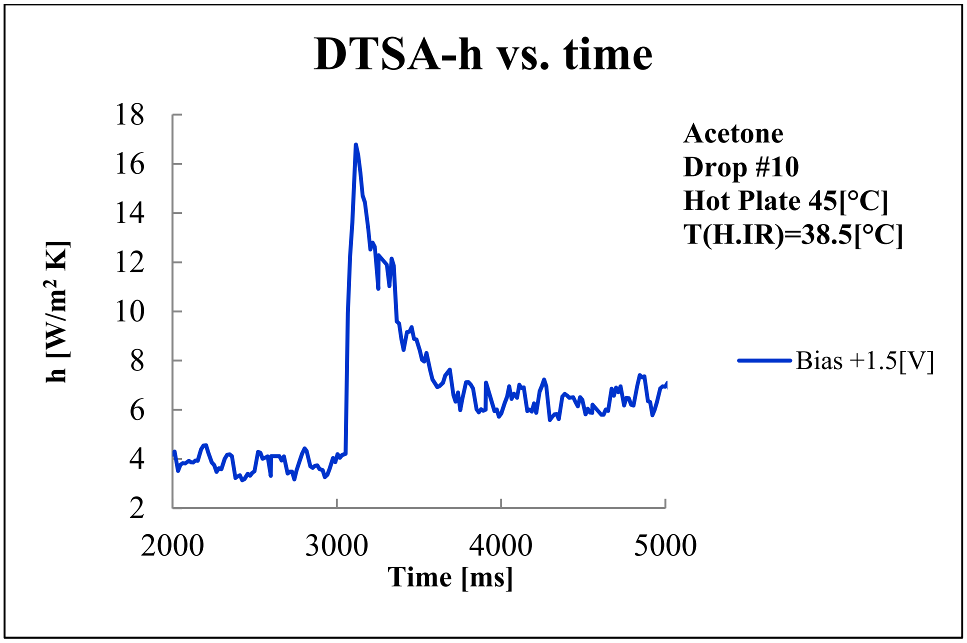
DTSA-h vs. time
h [W/m^2 K]
18
16
14
12
10
8
6
4
2
2000
3000
4000
5000
Time [ms]
Acetone
Drop #10
Hot Plate 45[°C]
T(H.IR)=38.5[°C]
Bias +1.5[V]

2) Acetone – 50, Drop #01

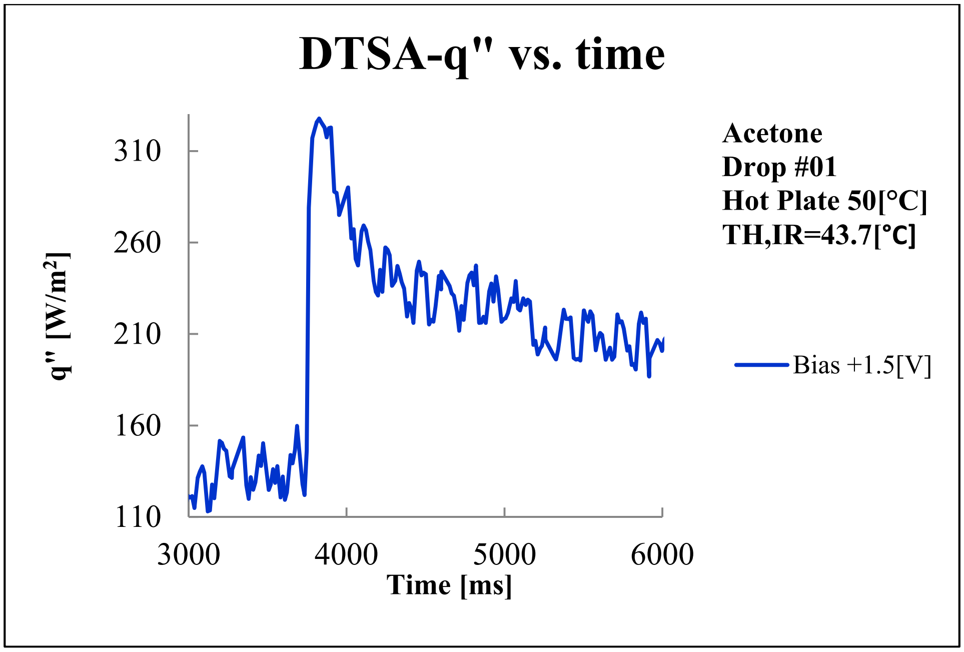

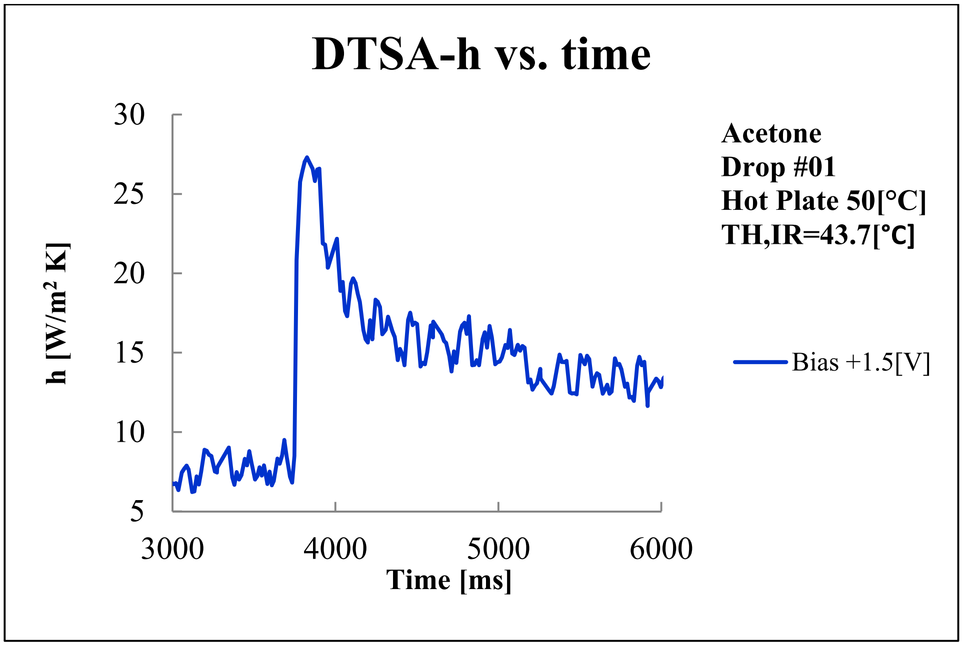

Drop#02

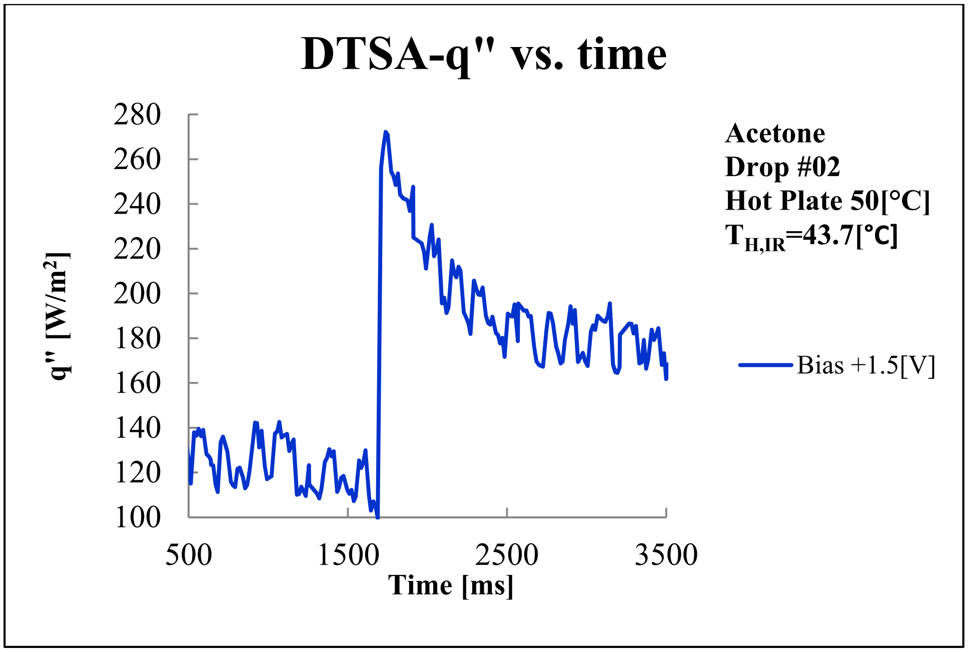
DTSA-q" vs. time
q" [W/m²]
280
260
240
220
200
180
160
140
120
100
500
1500
2500
3500
Time [ms]
Acetone
Drop #02
Hot Plate 50[°C]
T_H,IR=43.7[°C]
Bias +1.5[V]

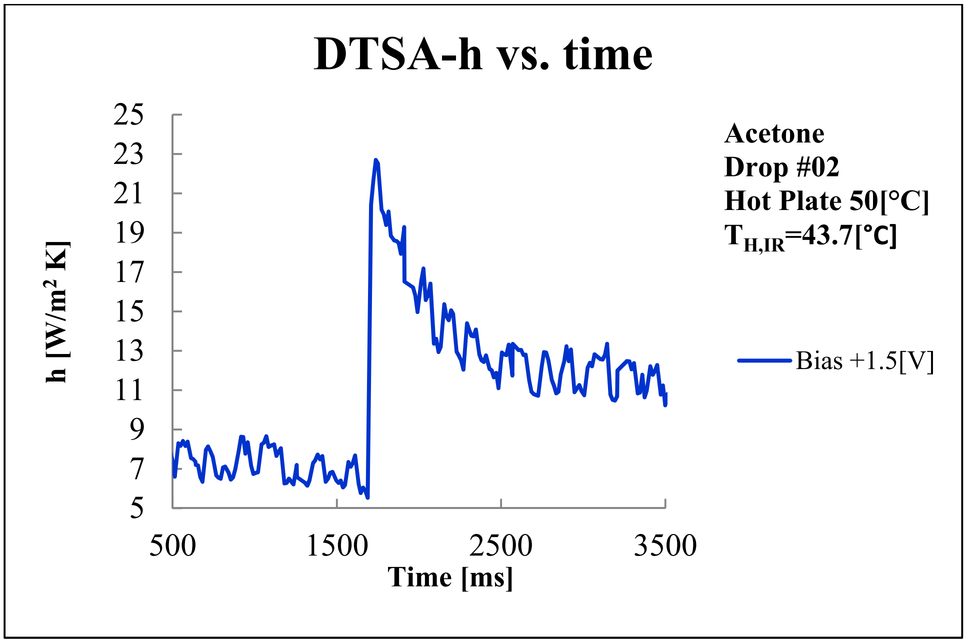
DTSA-h vs. time
h [W/m² K]
25
23
21
19
17
15
13
11
9
7
5
500
1500
2500
3500
Time [ms]
Acetone
Drop #02
Hot Plate 50[°C]
T_H,IR=43.7[°C]
Bias +1.5[V]

Drop#05

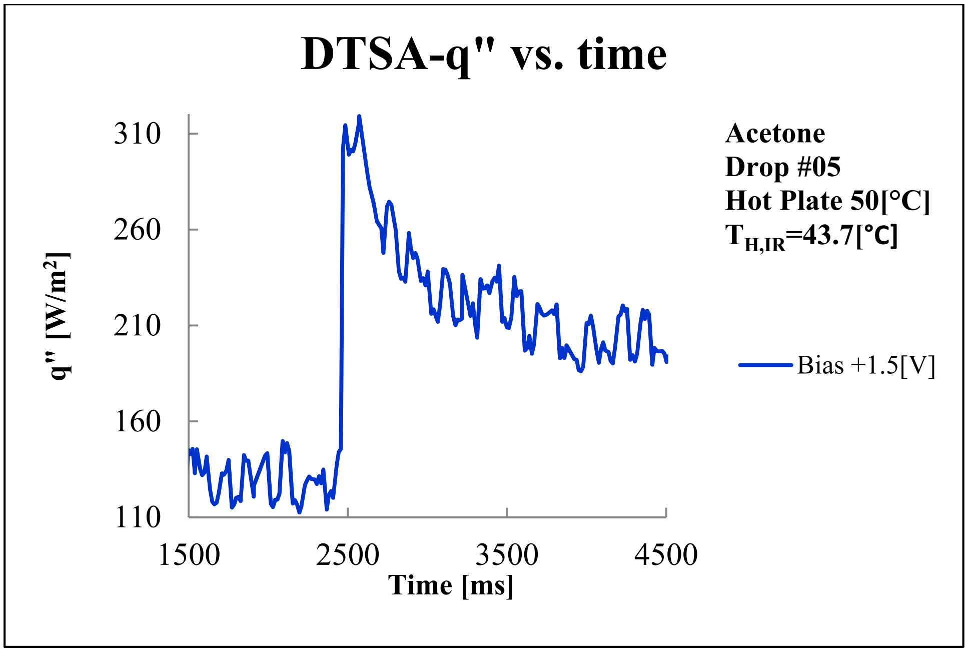
DTSA-q" vs. time
q" [W/m²]
310
260
210
160
110
1500
2500
3500
4500
Time [ms]
Acetone
Drop #05
Hot Plate 50[°C]
T_H,IR=43.7[°C]
Bias +1.5[V]

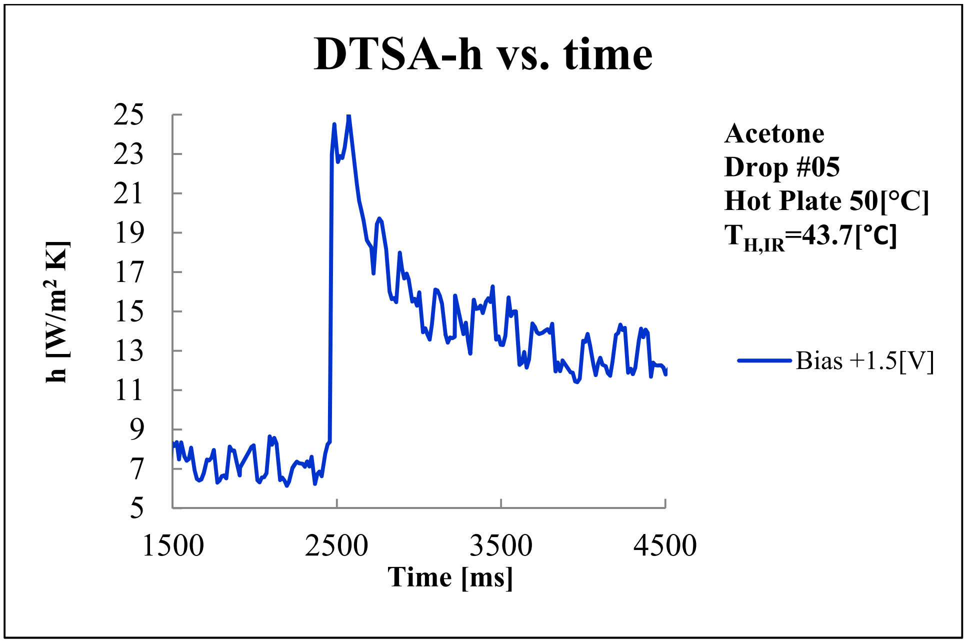
DTSA-h vs. time
h [W/m² K]
25
23
21
19
17
15
13
11
9
7
5
1500
2500
3500
4500
Time [ms]
Acetone
Drop #05
Hot Plate 50[°C]
T_H,IR=43.7[°C]
Bias +1.5[V]

Drop#06

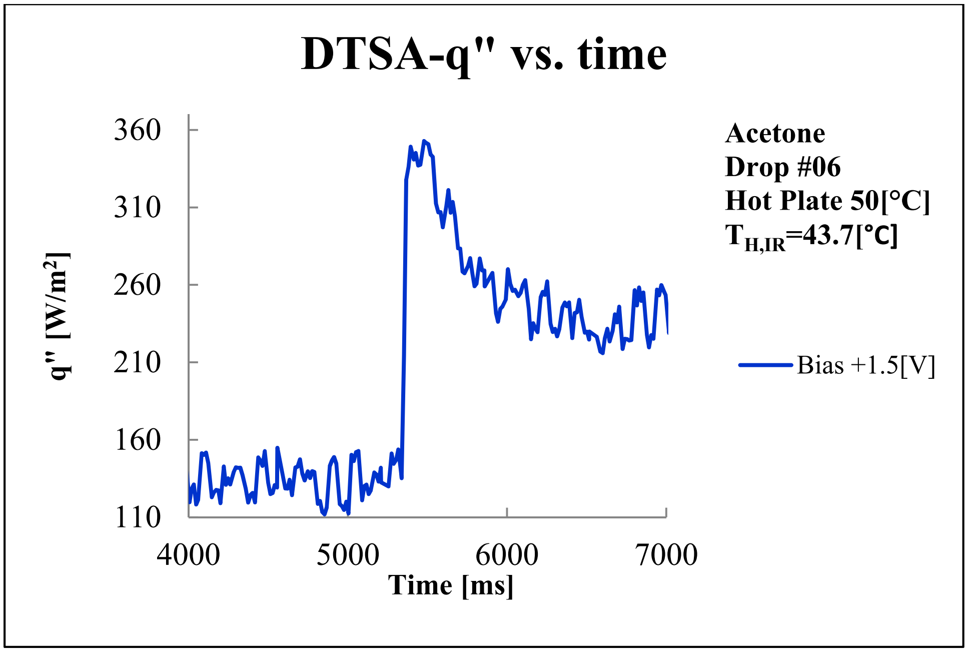
DTSA-q" vs. time
Acetone
Drop #06
Hot Plate 50[°C]
$T_{H,IR}$=43.7[°C]
Bias +1.5[V]
q" [W/m²]
360
310
260
210
160
110
4000
5000
6000
7000
Time [ms]

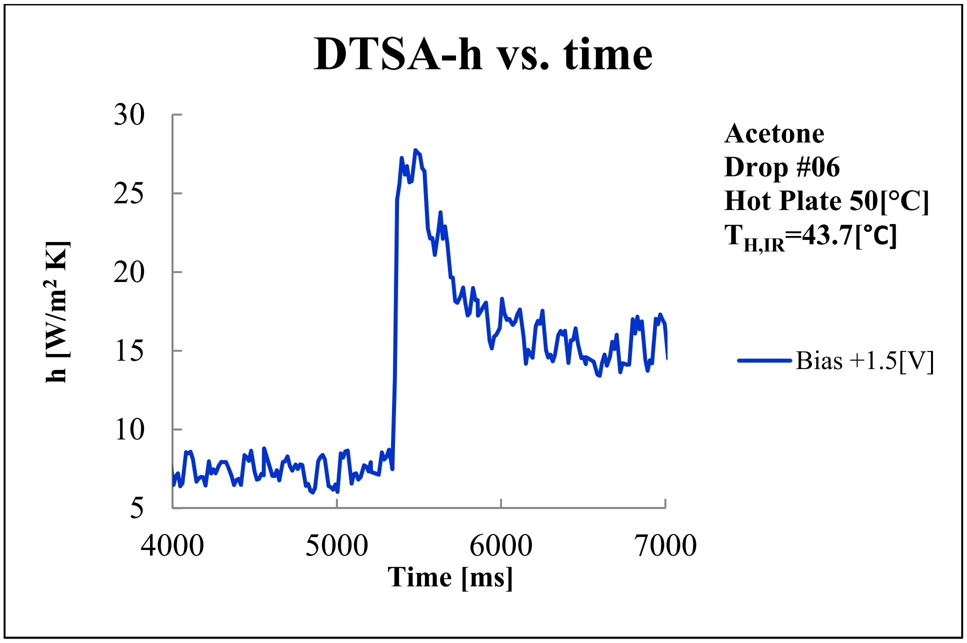
DTSA-h vs. time
Acetone
Drop #06
Hot Plate 50[°C]
$T_{H,IR}$=43.7[°C]
Bias +1.5[V]
h [W/m² K]
30
25
20
15
10
5
4000
5000
6000
7000
Time [ms]

Drop#07

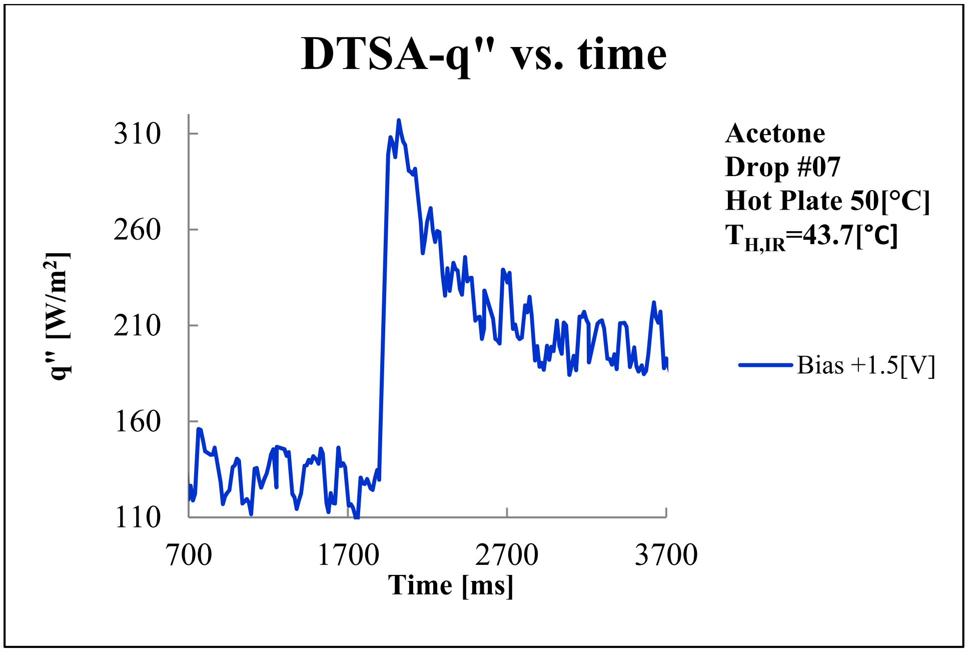
DTSA-q" vs. time
q" [W/m^2]
310
260
210
160
110
700
1700
2700
3700
Time [ms]
Acetone
Drop #07
Hot Plate 50[°C]
$T_{H,IR}$=43.7[°C]
Bias +1.5[V]

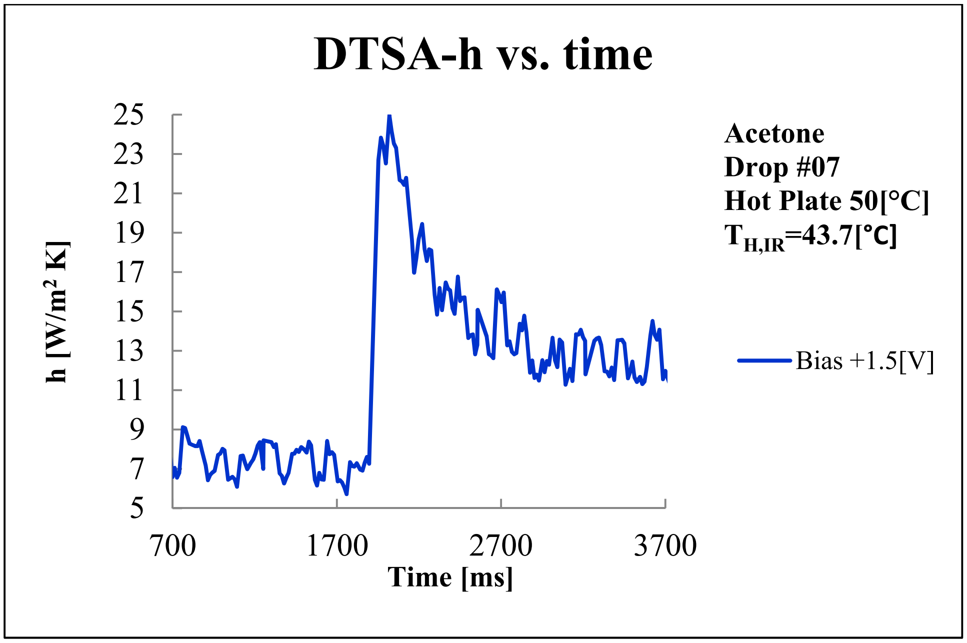
DTSA-h vs. time
h [W/m^2 K]
25
23
21
19
17
15
13
11
9
7
5
700
1700
2700
3700
Time [ms]
Acetone
Drop #07
Hot Plate 50[°C]
$T_{H,IR}$=43.7[°C]
Bias +1.5[V]

Drop#08

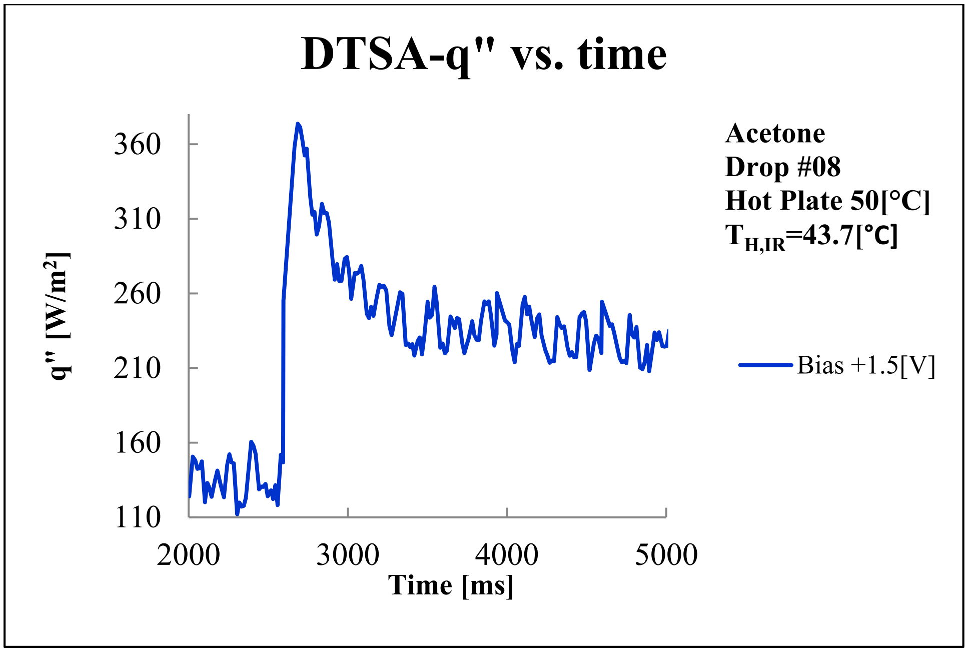
DTSA-q" vs. time
Acetone
Drop #08
Hot Plate 50[°C]
$T_{H,IR}$=43.7[°C]
q" [W/m^2]
360
310
260
210
160
110
2000
3000
4000
5000
Time [ms]
Bias +1.5[V]

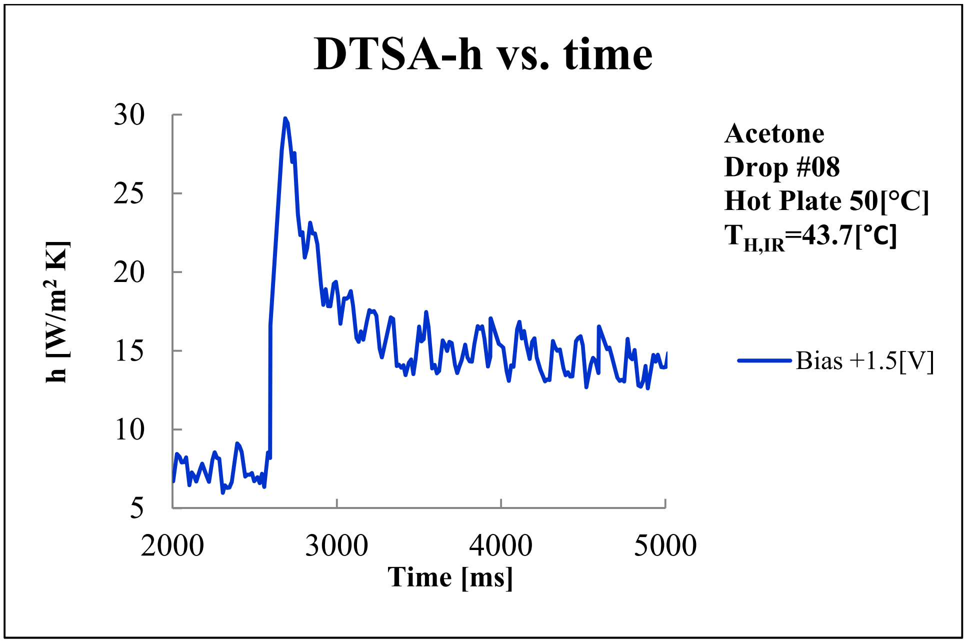
DTSA-h vs. time
Acetone
Drop #08
Hot Plate 50[°C]
$T_{H,IR}$=43.7[°C]
h [W/m^2 K]
30
25
20
15
10
5
2000
3000
4000
5000
Time [ms]
Bias +1.5[V]

Drop#09

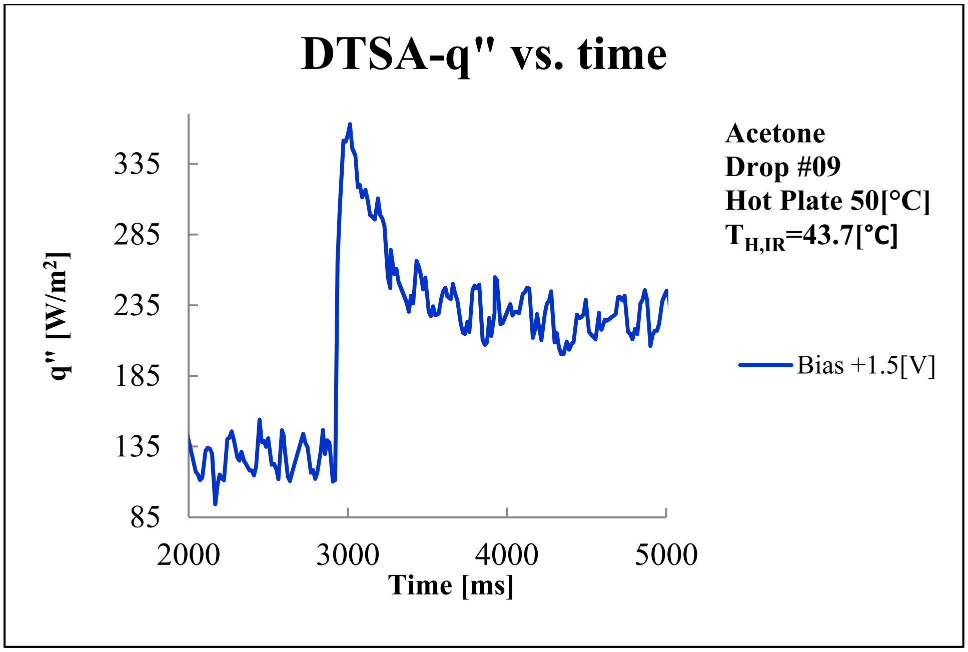
DTSA-q" vs. time
Acetone
Drop #09
Hot Plate 50[°C]
T_H,IR=43.7[°C]
Bias +1.5[V]
q" [W/m²]
335
285
235
185
135
85
2000
3000
4000
5000
Time [ms]

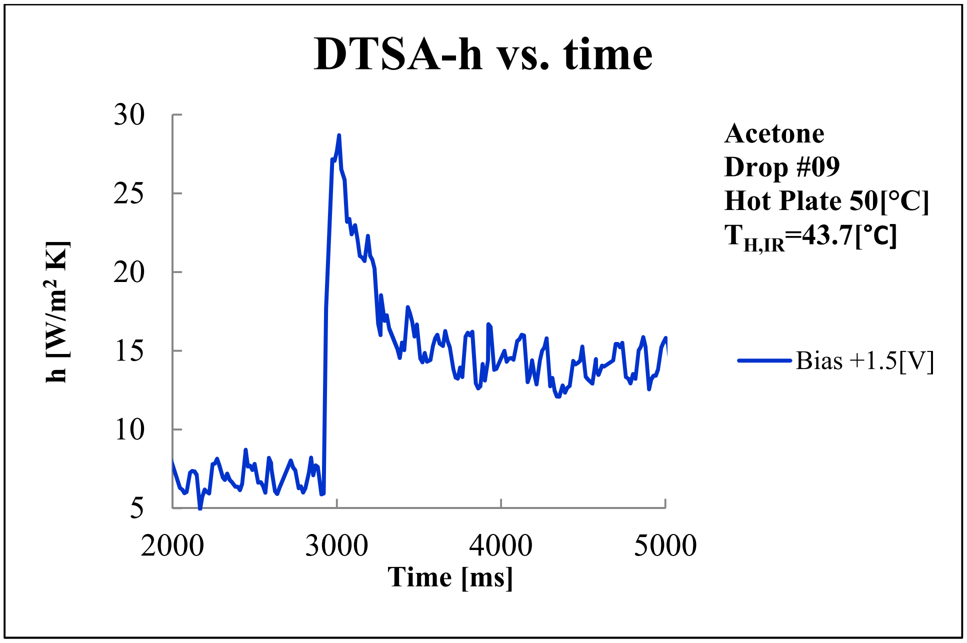
DTSA-h vs. time
Acetone
Drop #09
Hot Plate 50[°C]
T_H,IR=43.7[°C]
Bias +1.5[V]
h [W/m² K]
30
25
20
15
10
5
2000
3000
4000
5000
Time [ms]

Drop#10

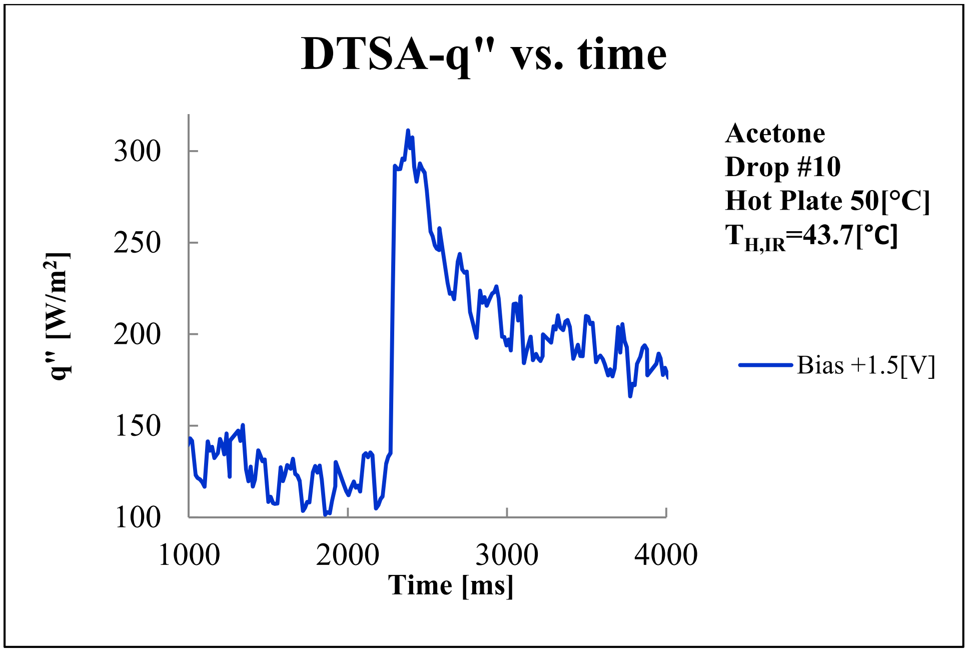
DTSA-q" vs. time
q" [W/m²]
300
250
200
150
100
1000
2000
3000
4000
Time [ms]
Acetone
Drop #10
Hot Plate 50[°C]
T H,IR=43.7[°C]
Bias +1.5[V]

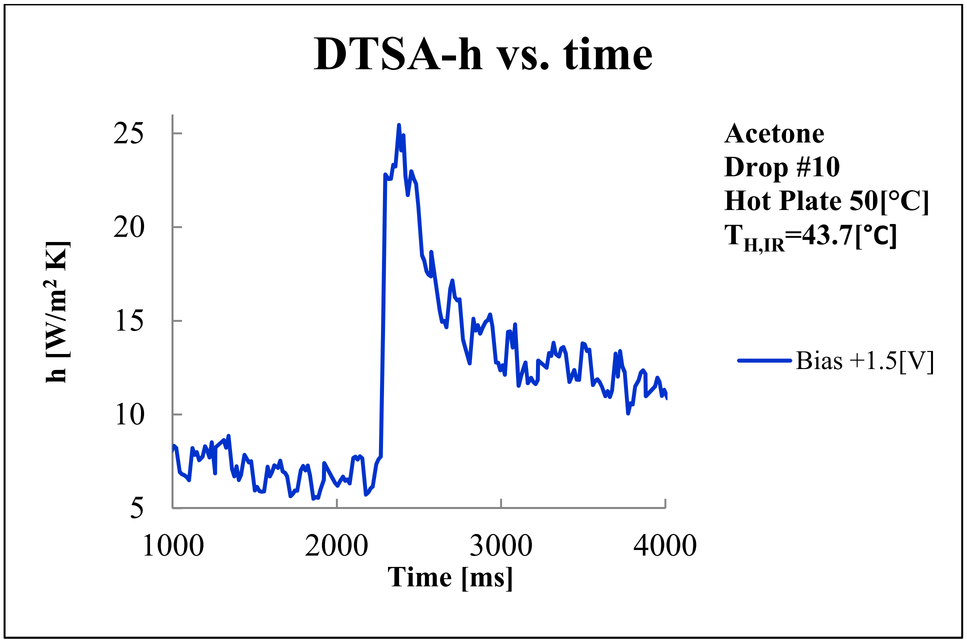
DTSA-h vs. time
h [W/m² K]
25
20
15
10
5
1000
2000
3000
4000
Time [ms]
Acetone
Drop #10
Hot Plate 50[°C]
T H,IR=43.7[°C]
Bias +1.5[V]

3) Acetone – 55, Drop#01

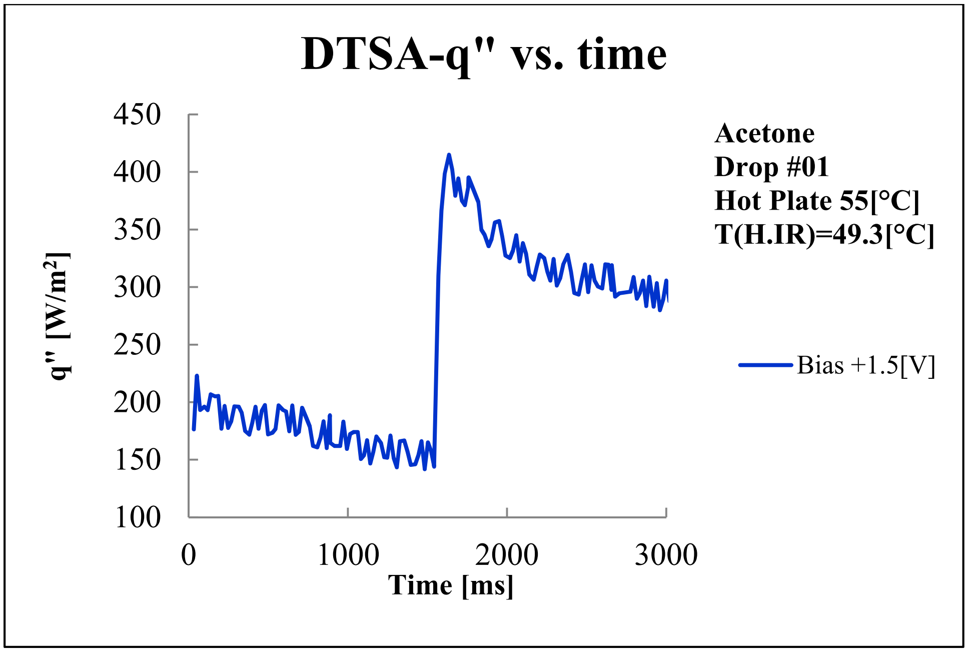

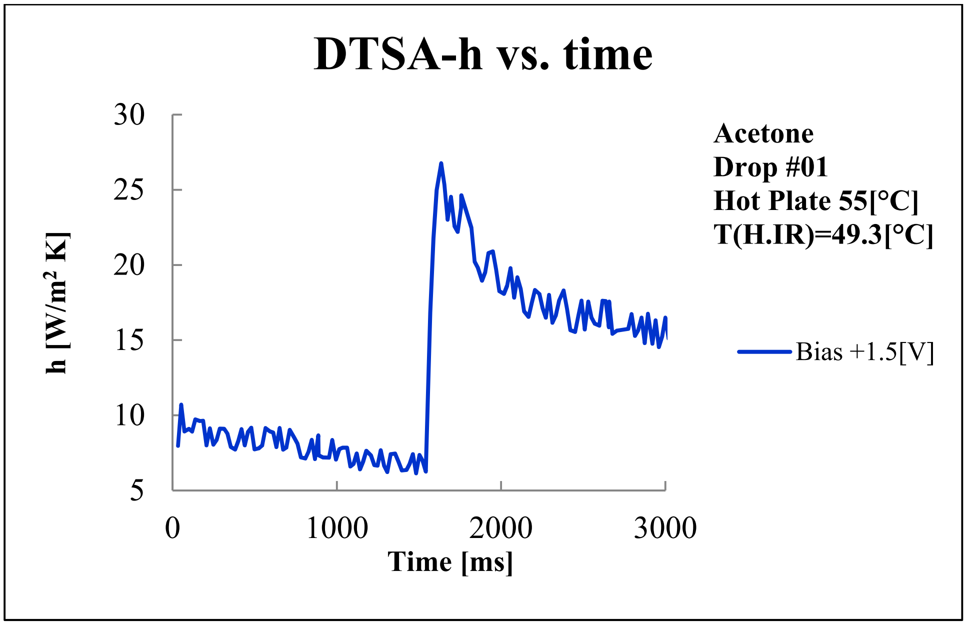

Drop#03

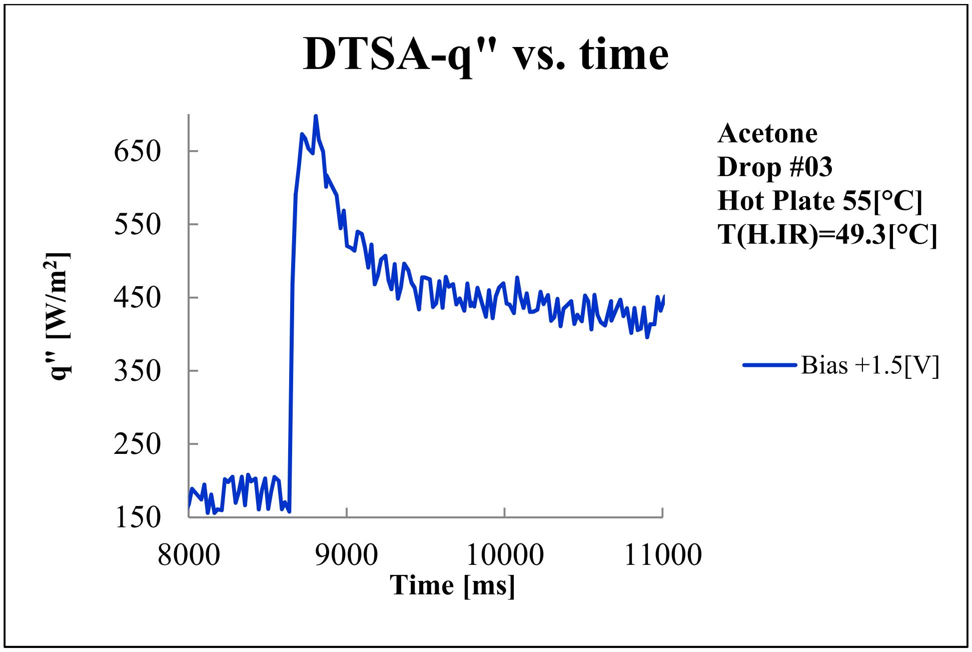
DTSA-q" vs. time
Acetone
Drop #03
Hot Plate 55[°C]
T(H.IR)=49.3[°C]
Bias +1.5[V]
q" [W/m²]
650
550
450
350
250
150
8000
9000
10000
11000
Time [ms]

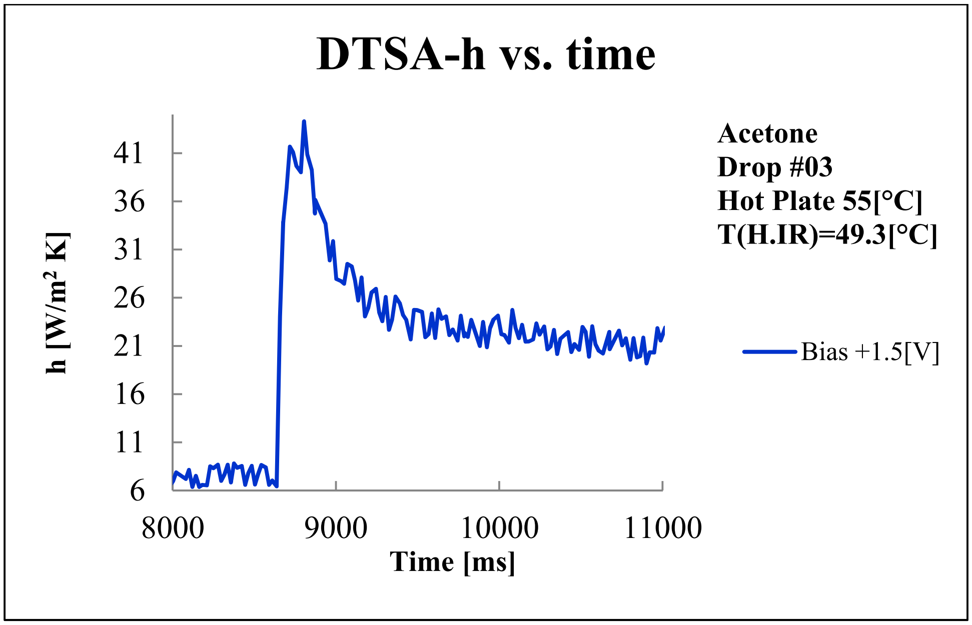
DTSA-h vs. time
Acetone
Drop #03
Hot Plate 55[°C]
T(H.IR)=49.3[°C]
Bias +1.5[V]
h [W/m² K]
41
36
31
26
21
16
11
6
8000
9000
10000
11000
Time [ms]

Drop#04

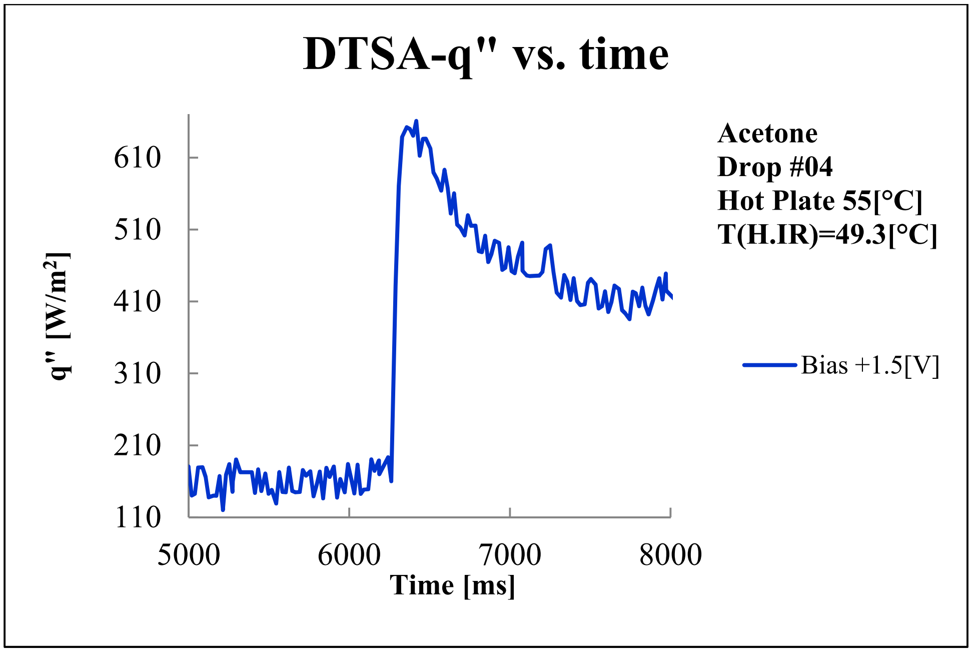
DTSA-q" vs. time
q" [W/m²]
610
510
410
310
210
110
5000
6000
7000
8000
Time [ms]
Acetone
Drop #04
Hot Plate 55[°C]
T(H.IR)=49.3[°C]
Bias +1.5[V]

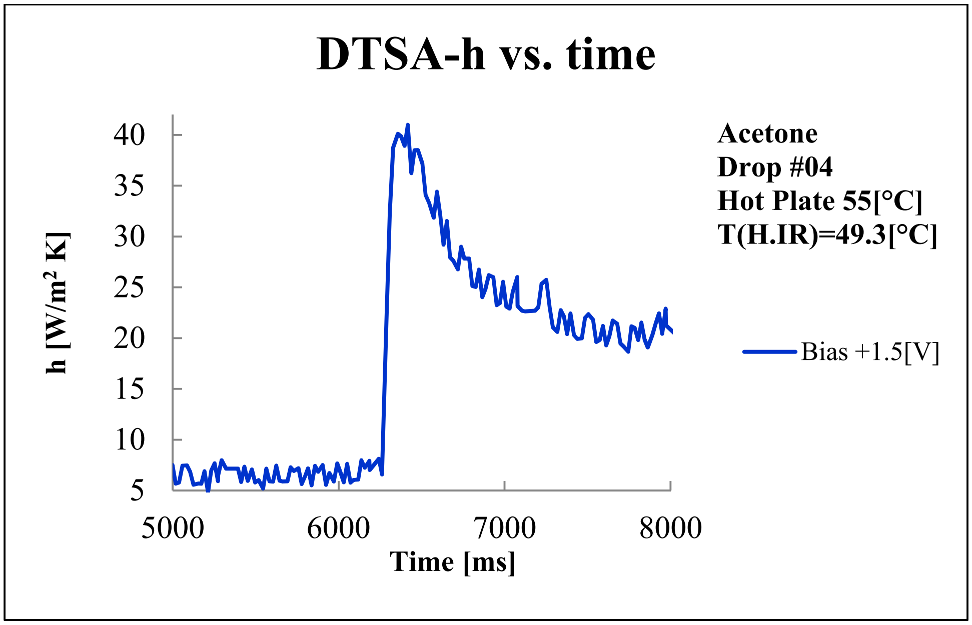
DTSA-h vs. time
h [W/m² K]
40
35
30
25
20
15
10
5
5000
6000
7000
8000
Time [ms]
Acetone
Drop #04
Hot Plate 55[°C]
T(H.IR)=49.3[°C]
Bias +1.5[V]

Drop#05

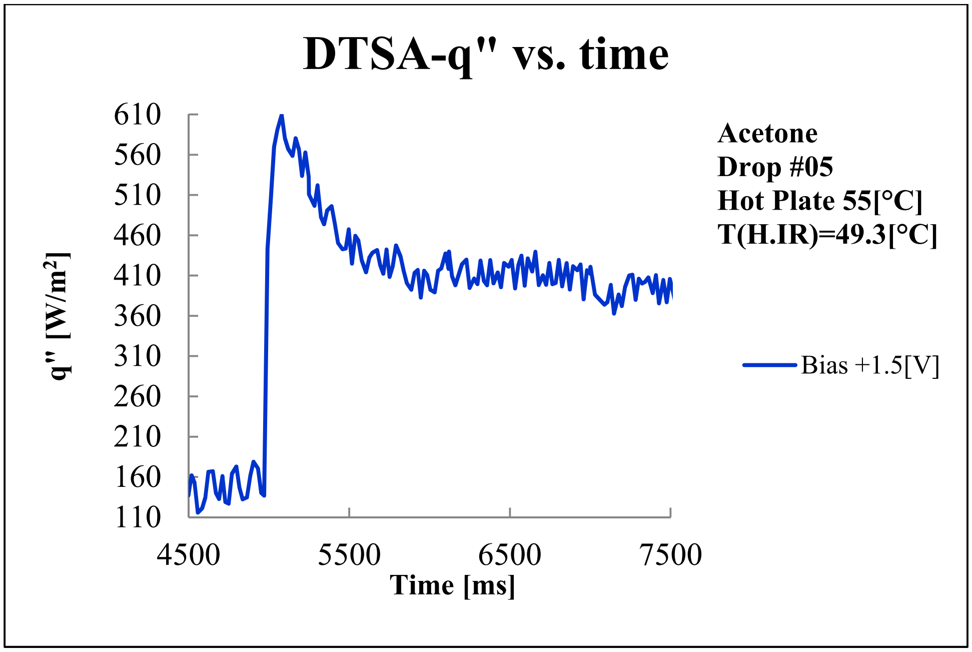
DTSA-q" vs. time
610
560
510
460
410
360
310
260
210
160
110
q" [W/m²]
4500
5500
6500
7500
Time [ms]
Acetone
Drop #05
Hot Plate 55[°C]
T(H.IR)=49.3[°C]
Bias +1.5[V]

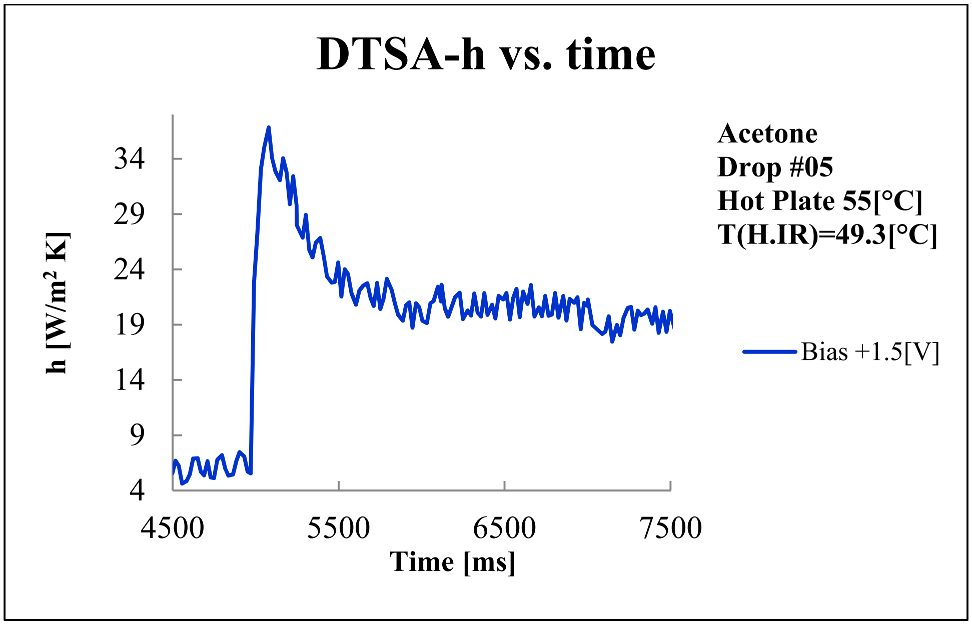
DTSA-h vs. time
34
29
24
19
14
9
4
h [W/m² K]
4500
5500
6500
7500
Time [ms]
Acetone
Drop #05
Hot Plate 55[°C]
T(H.IR)=49.3[°C]
Bias +1.5[V]

Drop#06

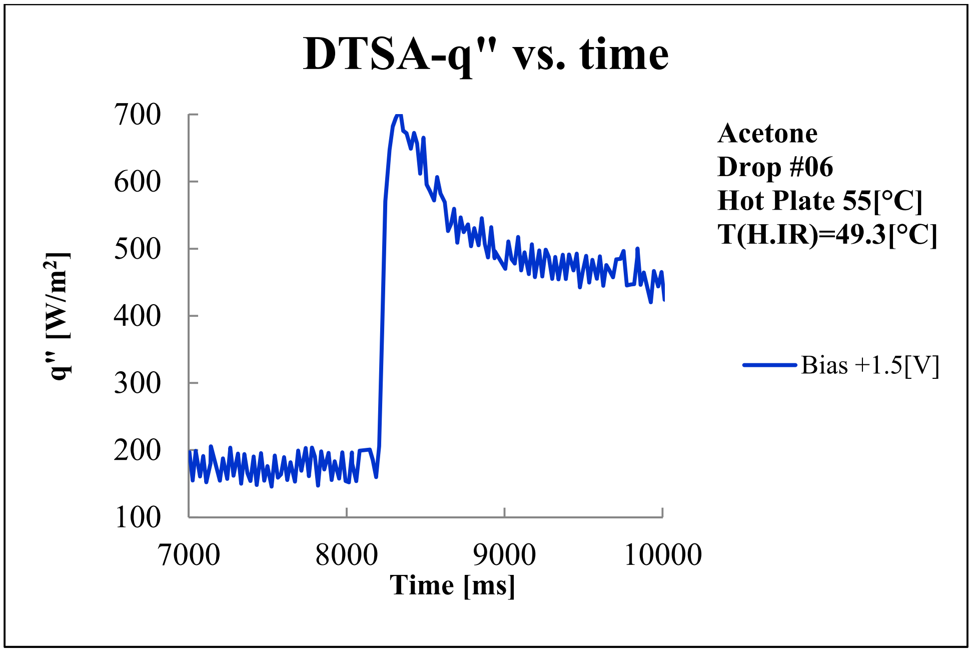
DTSA-q" vs. time
q" [W/m²]
700
600
500
400
300
200
100
7000
8000
9000
10000
Time [ms]
Acetone
Drop #06
Hot Plate 55[°C]
T(H.IR)=49.3[°C]
Bias +1.5[V]

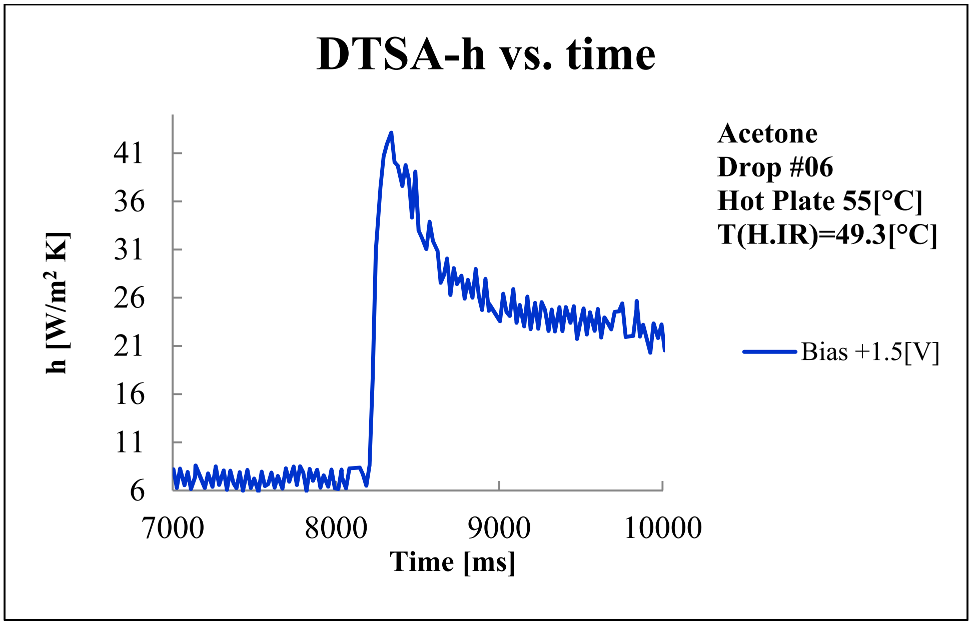
DTSA-h vs. time
h [W/m² K]
41
36
31
26
21
16
11
6
7000
8000
9000
10000
Time [ms]
Acetone
Drop #06
Hot Plate 55[°C]
T(H.IR)=49.3[°C]
Bias +1.5[V]

Drop#07

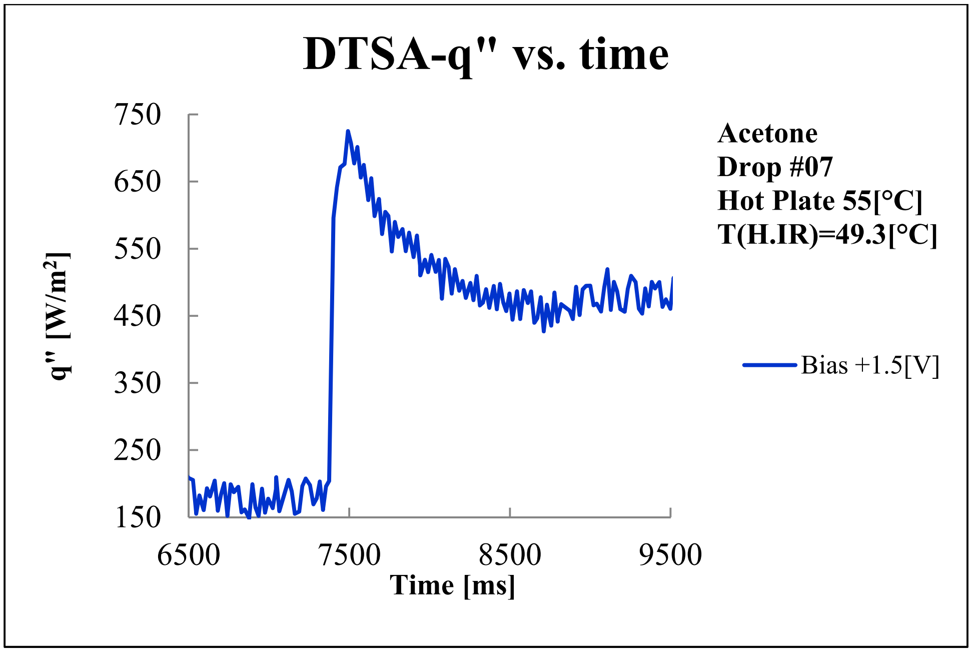
DTSA-q" vs. time
Acetone
Drop #07
Hot Plate 55[°C]
T(H.IR)=49.3[°C]
Bias +1.5[V]
q" [W/m²]
750
650
550
450
350
250
150
6500
7500
8500
9500
Time [ms]

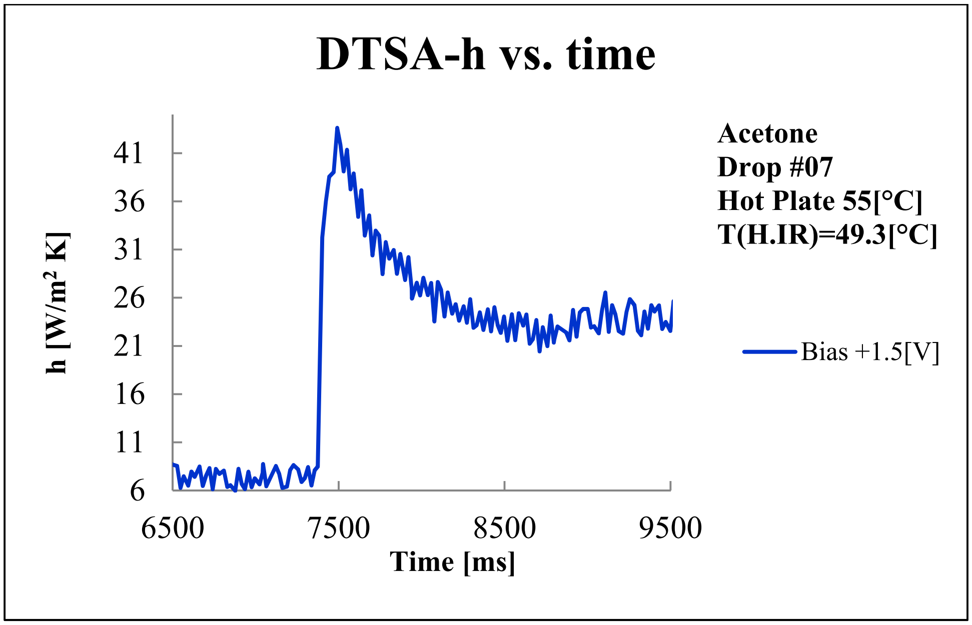
DTSA-h vs. time
Acetone
Drop #07
Hot Plate 55[°C]
T(H.IR)=49.3[°C]
Bias +1.5[V]
h [W/m² K]
41
36
31
26
21
16
11
6
6500
7500
8500
9500
Time [ms]

Drop#09

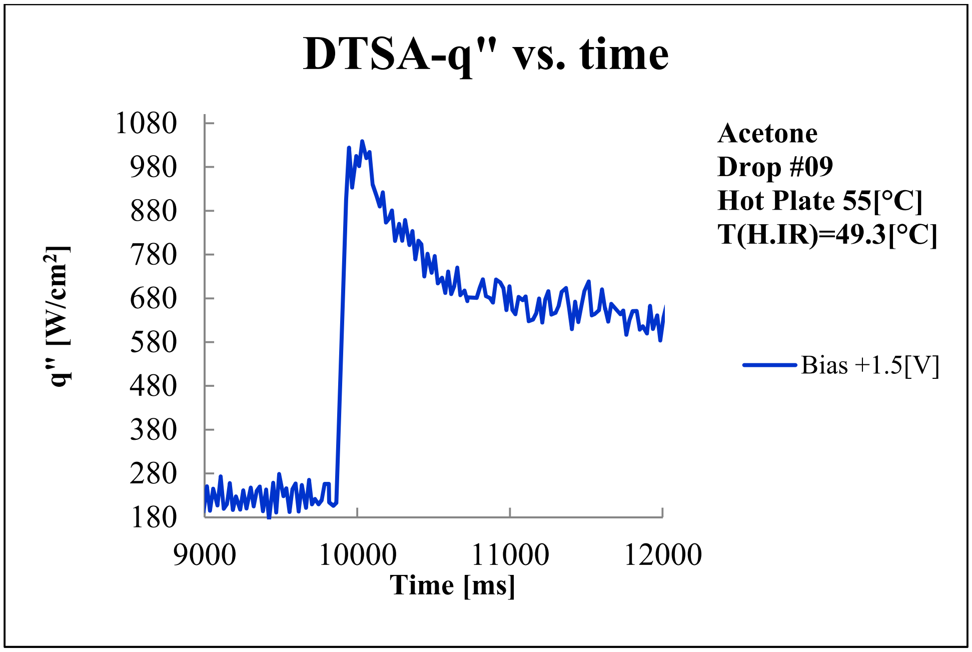
DTSA-q" vs. time
q" [W/cm²]
1080
980
880
780
680
580
480
380
280
180
9000
10000
11000
12000
Time [ms]
Acetone
Drop #09
Hot Plate 55[°C]
T(H.IR)=49.3[°C]
Bias +1.5[V]

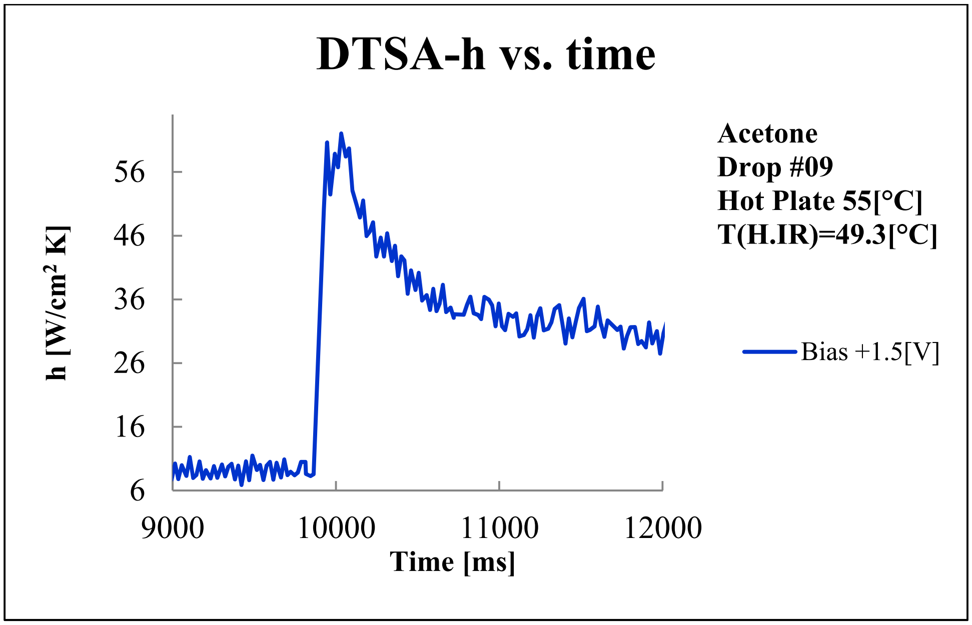
DTSA-h vs. time
h [W/cm² K]
56
46
36
26
16
6
9000
10000
11000
12000
Time [ms]
Acetone
Drop #09
Hot Plate 55[°C]
T(H.IR)=49.3[°C]
Bias +1.5[V]

Drop#10

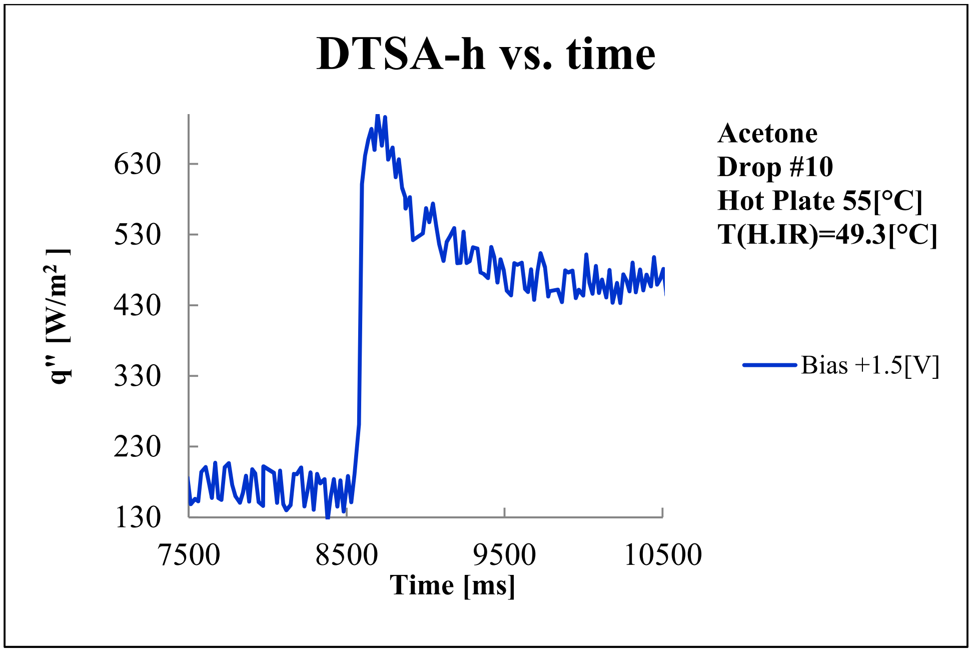
DTSA-h vs. time
q" [W/m²]
630
530
430
330
230
130
7500
8500
9500
10500
Time [ms]
Acetone
Drop #10
Hot Plate 55[°C]
T(H.IR)=49.3[°C]
Bias +1.5[V]

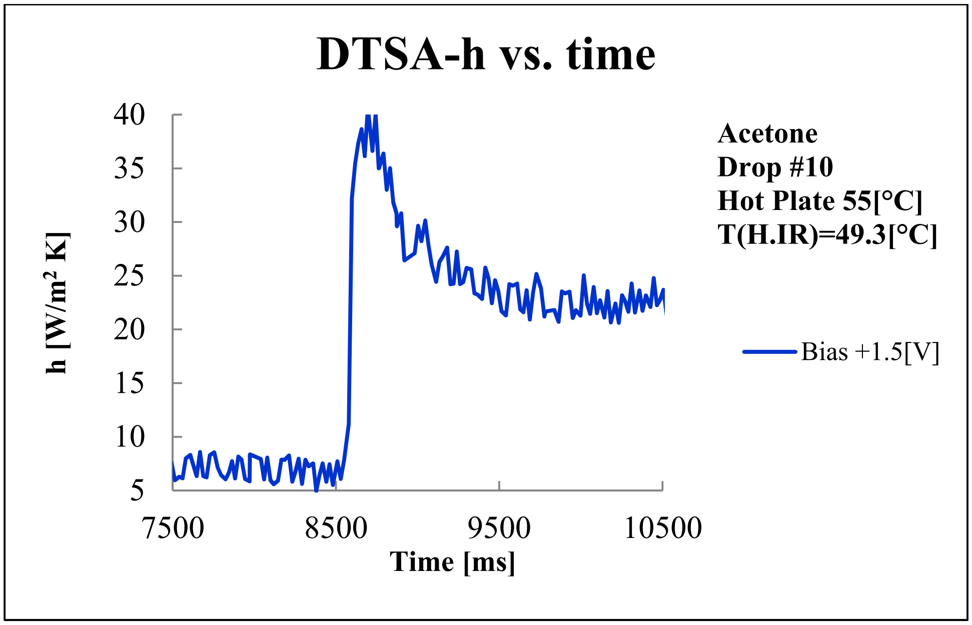
DTSA-h vs. time
h [W/m² K]
40
35
30
25
20
15
10
5
7500
8500
9500
10500
Time [ms]
Acetone
Drop #10
Hot Plate 55[°C]
T(H.IR)=49.3[°C]
Bias +1.5[V]

4) Ethanol – 45, Drop#01

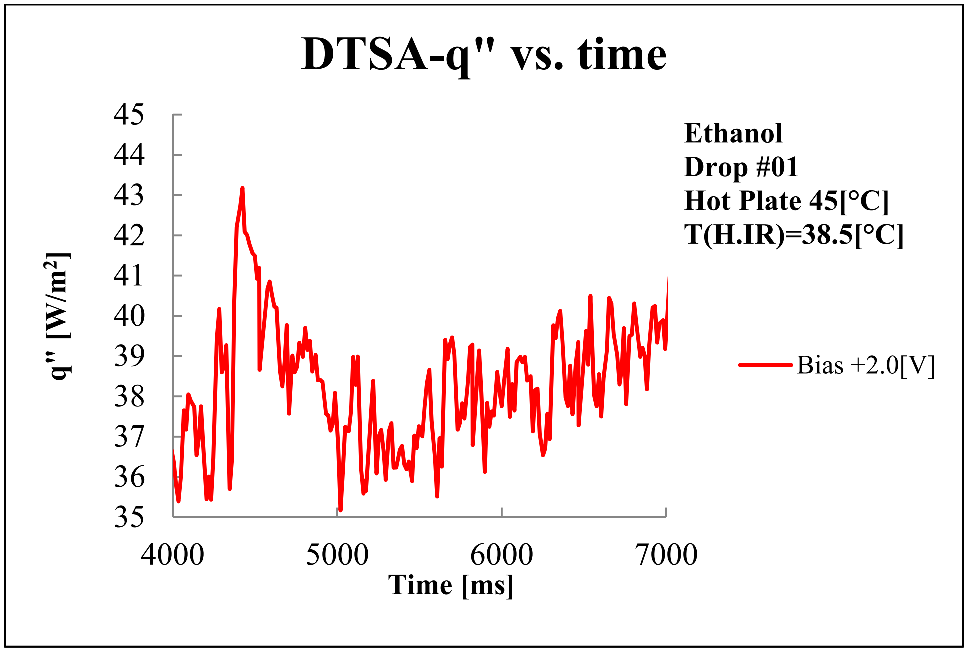

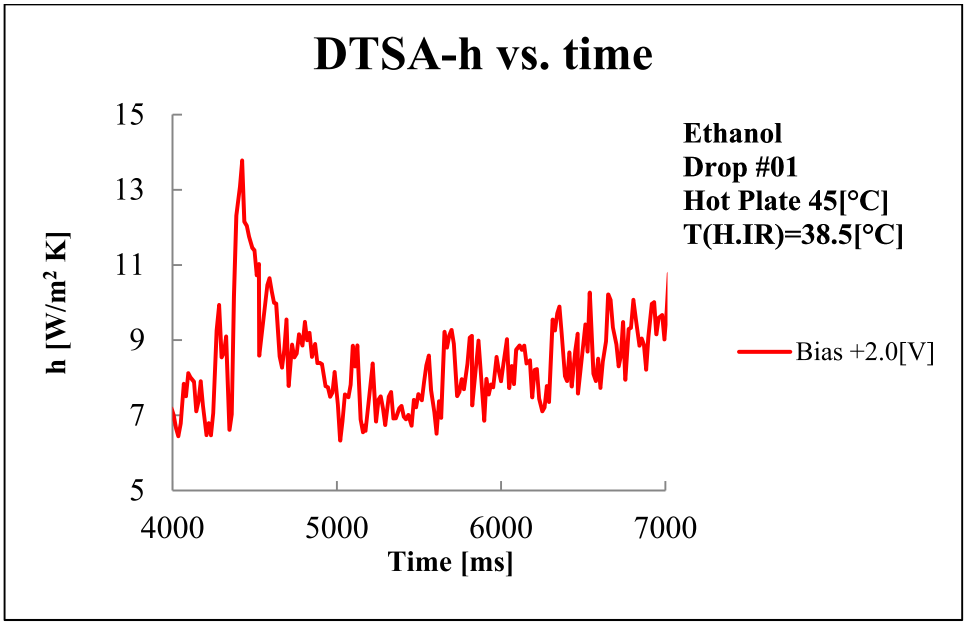

Drop#02

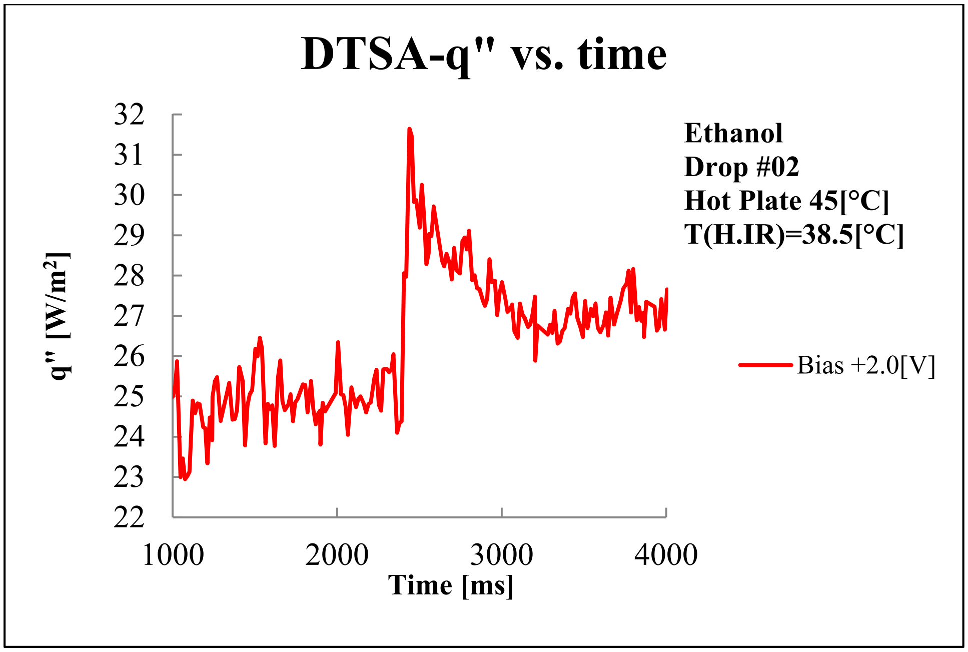
DTSA-q" vs. time
q" [W/m²]
32
31
30
29
28
27
26
25
24
23
22
1000
2000
3000
4000
Time [ms]
Ethanol
Drop #02
Hot Plate 45[°C]
T(H.IR)=38.5[°C]
Bias +2.0[V]

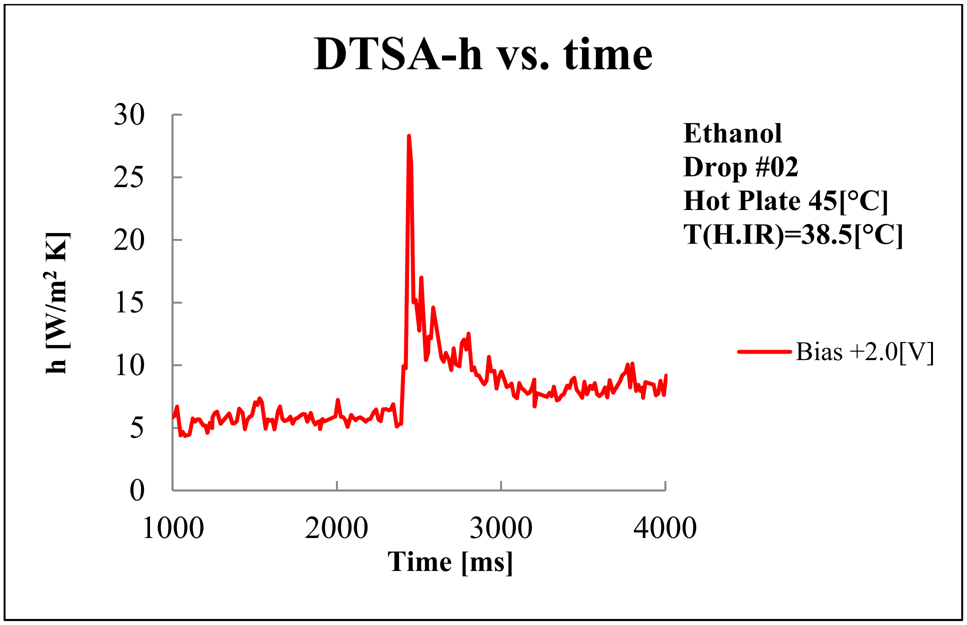
DTSA-h vs. time
h [W/m² K]
30
25
20
15
10
5
0
1000
2000
3000
4000
Time [ms]
Ethanol
Drop #02
Hot Plate 45[°C]
T(H.IR)=38.5[°C]
Bias +2.0[V]

Drop#05

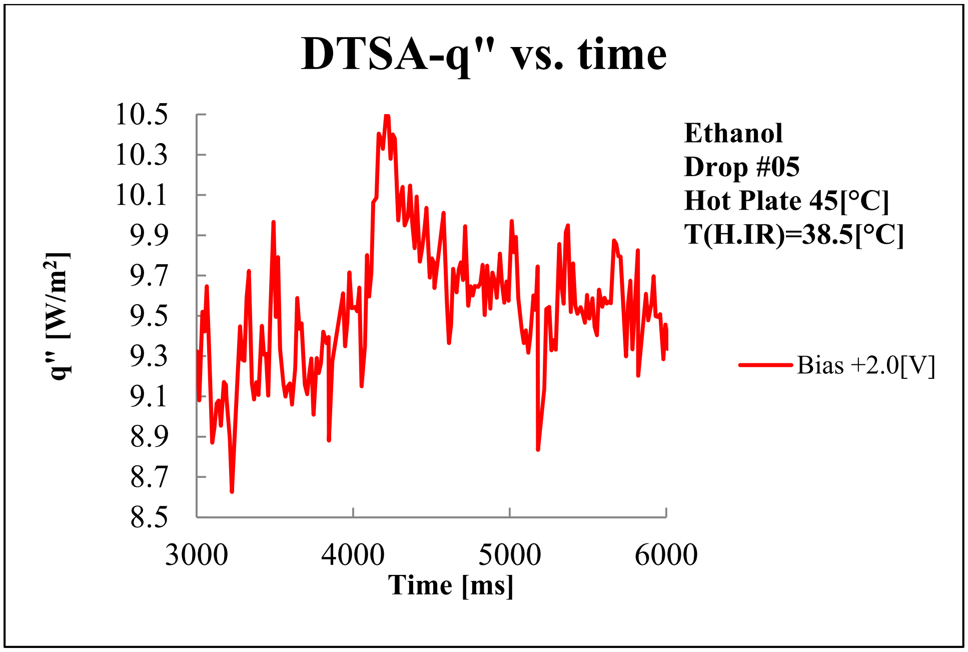
DTSA-q" vs. time
10.5
10.3
10.1
9.9
9.7
9.5
9.3
9.1
8.9
8.7
8.5
q" [W/m²]
3000
4000
5000
6000
Time [ms]
Ethanol
Drop #05
Hot Plate 45[°C]
T(H.IR)=38.5[°C]
Bias +2.0[V]

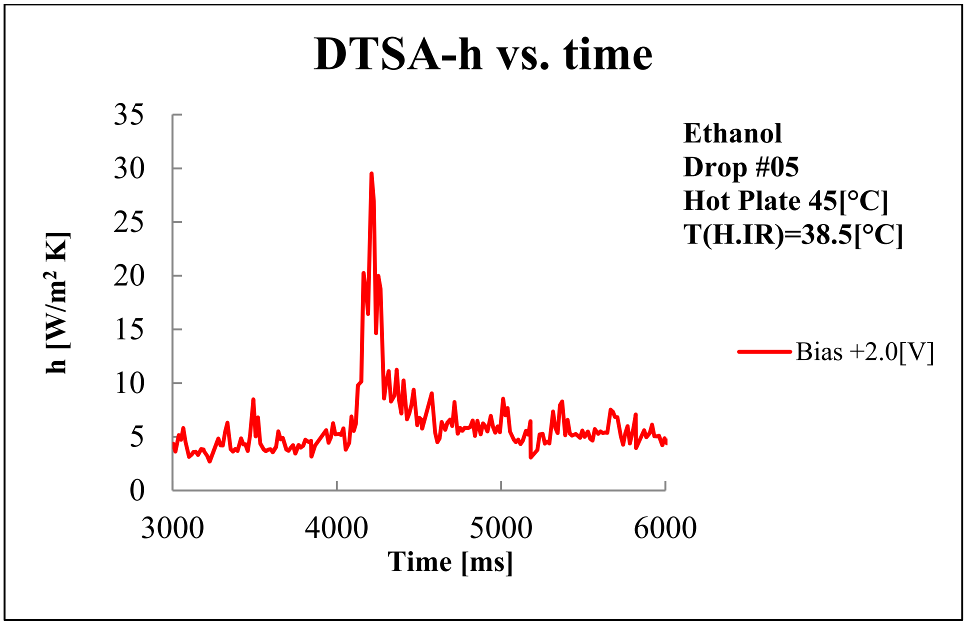
DTSA-h vs. time
35
30
25
20
15
10
5
0
h [W/m² K]
3000
4000
5000
6000
Time [ms]
Ethanol
Drop #05
Hot Plate 45[°C]
T(H.IR)=38.5[°C]
Bias +2.0[V]

Drop#06

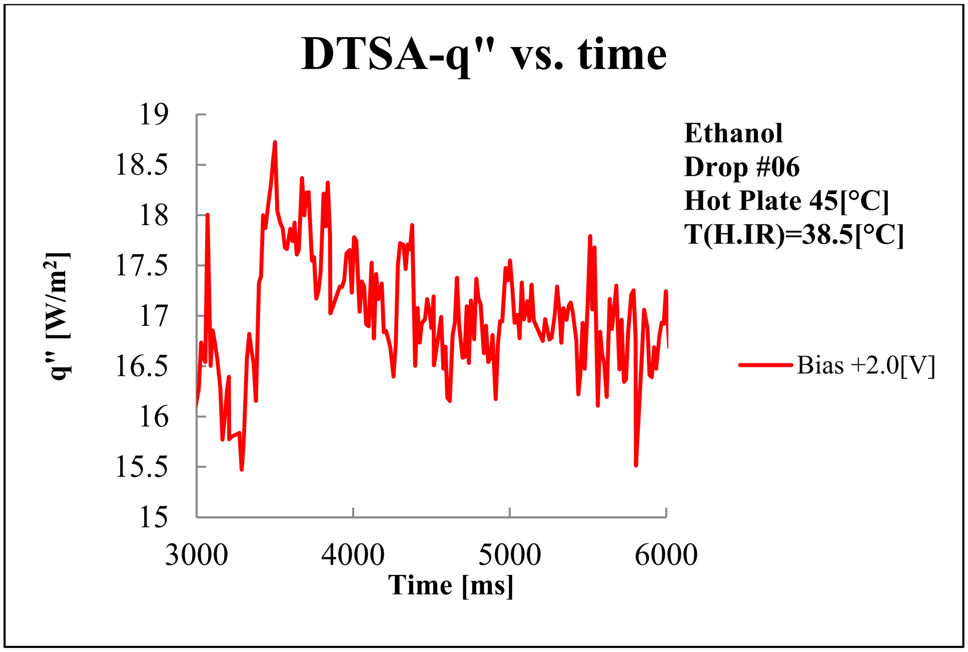
DTSA-q" vs. time
q" [W/m^2]
19
18.5
18
17.5
17
16.5
16
15.5
15
3000
4000
5000
6000
Time [ms]
Ethanol
Drop #06
Hot Plate 45[°C]
T(H.IR)=38.5[°C]
Bias +2.0[V]

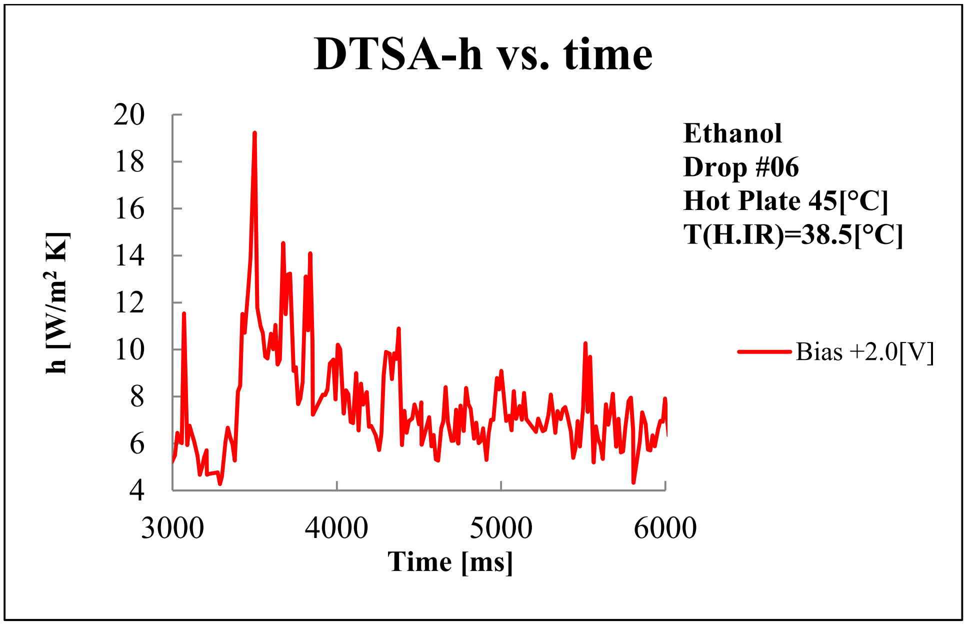
DTSA-h vs. time
h [W/m^2 K]
20
18
16
14
12
10
8
6
4
3000
4000
5000
6000
Time [ms]
Ethanol
Drop #06
Hot Plate 45[°C]
T(H.IR)=38.5[°C]
Bias +2.0[V]

Drop#07

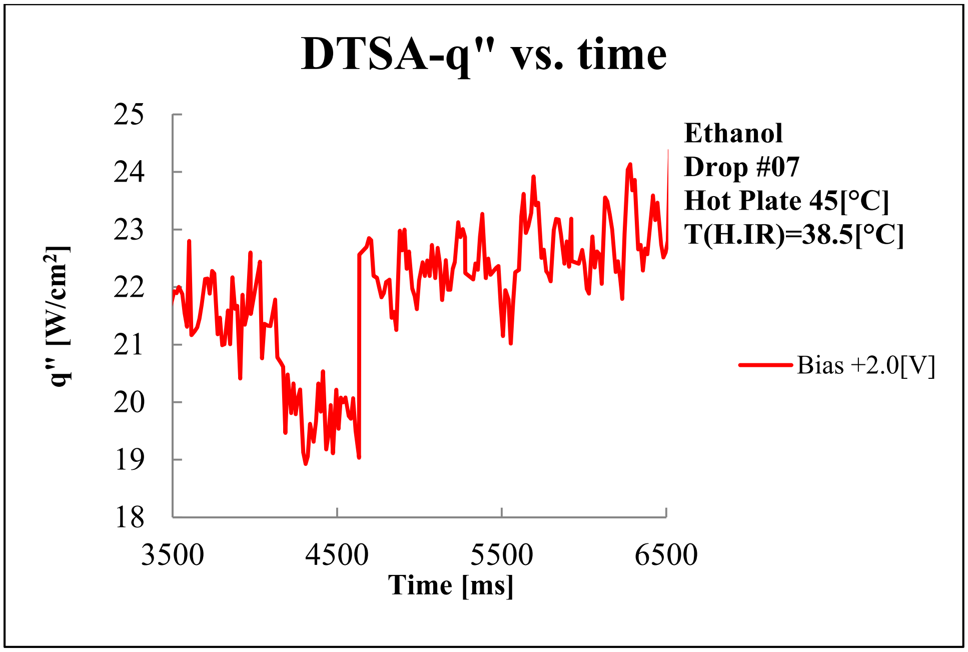
DTSA-q" vs. time
q" [W/cm^2]
25
24
23
22
21
20
19
18
3500
4500
5500
6500
Time [ms]
Ethanol
Drop #07
Hot Plate 45[°C]
T(H.IR)=38.5[°C]
Bias +2.0[V]

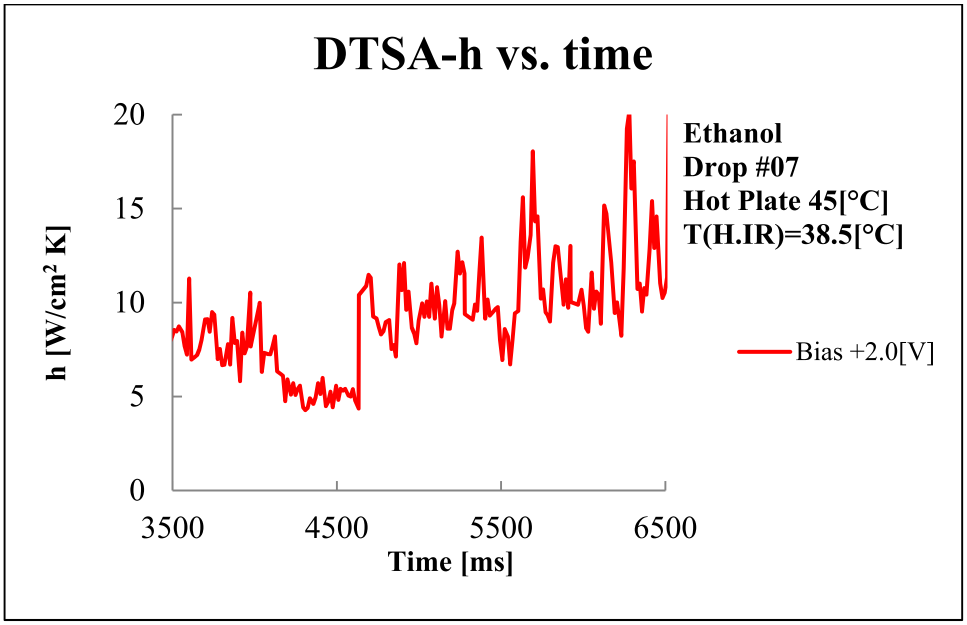
DTSA-h vs. time
h [W/cm^2 K]
20
15
10
5
0
3500
4500
5500
6500
Time [ms]
Ethanol
Drop #07
Hot Plate 45[°C]
T(H.IR)=38.5[°C]
Bias +2.0[V]

5) Ethanol – 55, Drop#03

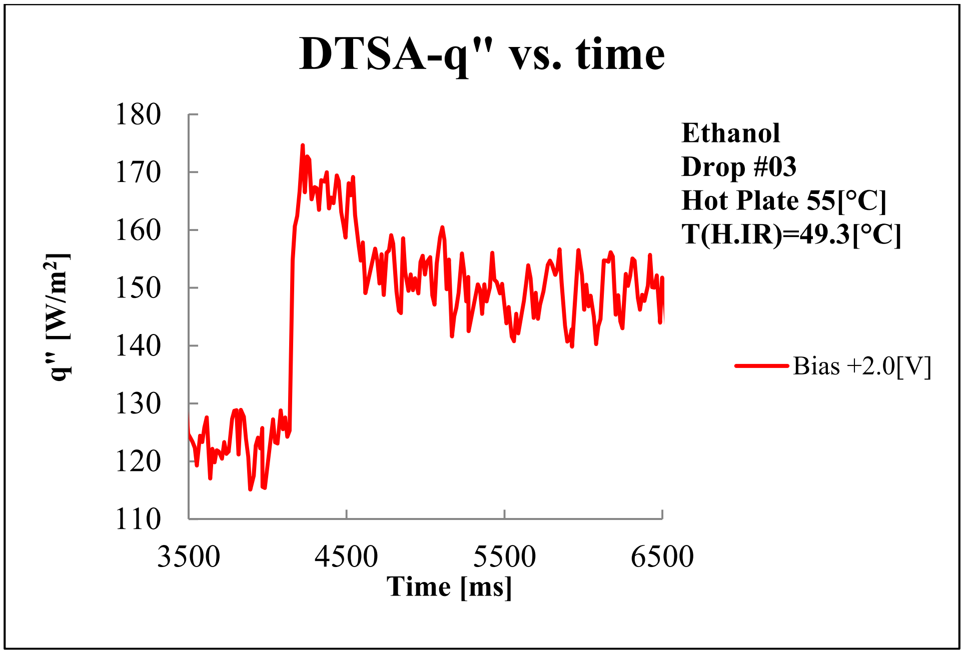

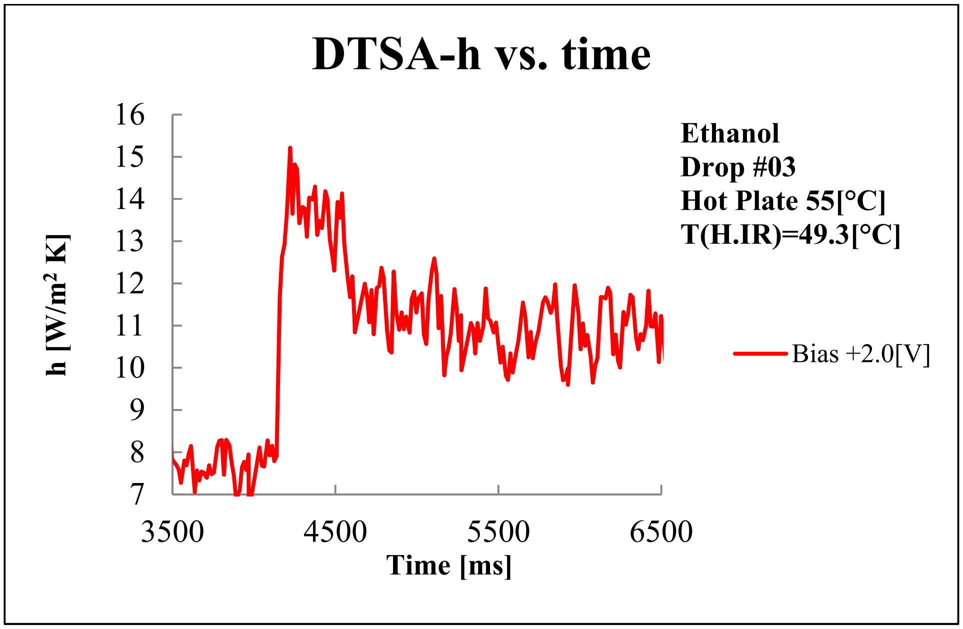

Drop#05

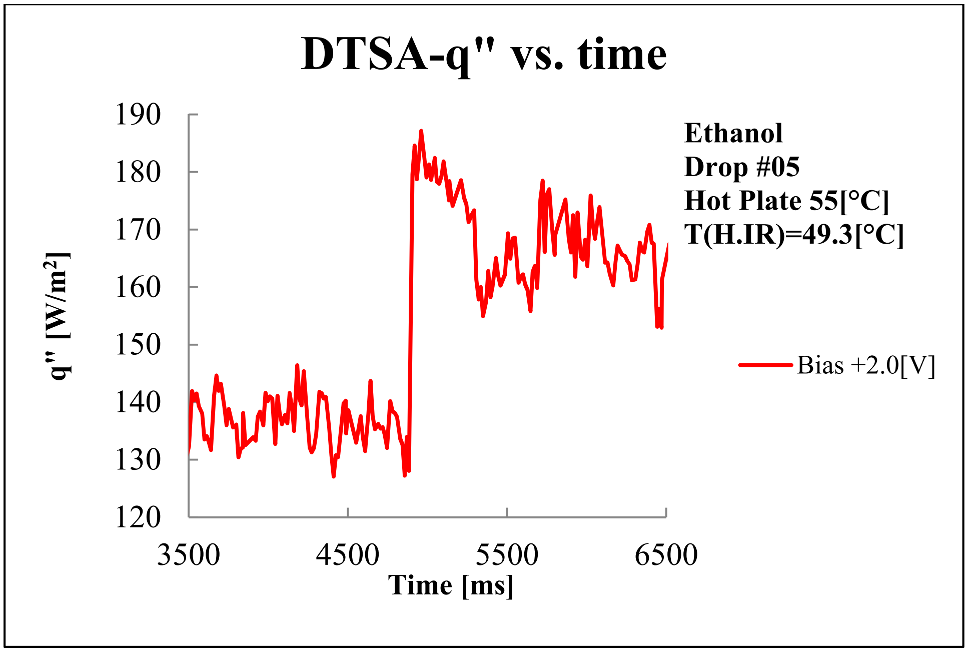
DTSA-q" vs. time
190
180
170
160
150
140
130
120
q" [W/m^2]
3500
4500
5500
6500
Time [ms]
Ethanol
Drop #05
Hot Plate 55[°C]
T(H.IR)=49.3[°C]
Bias +2.0[V]

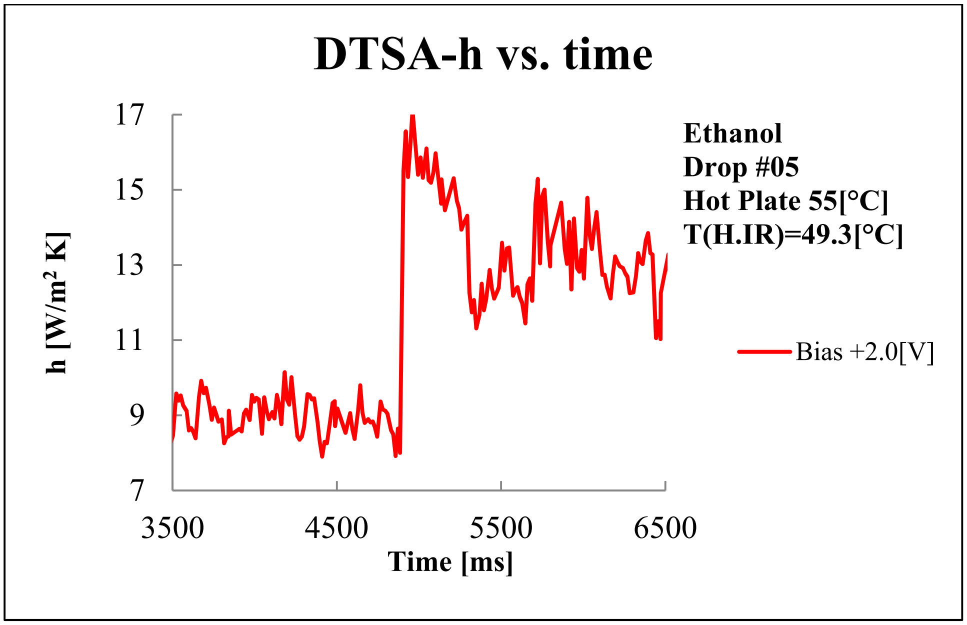
DTSA-h vs. time
17
15
13
11
9
7
h [W/m^2 K]
3500
4500
5500
6500
Time [ms]
Ethanol
Drop #05
Hot Plate 55[°C]
T(H.IR)=49.3[°C]
Bias +2.0[V]

Drop#06

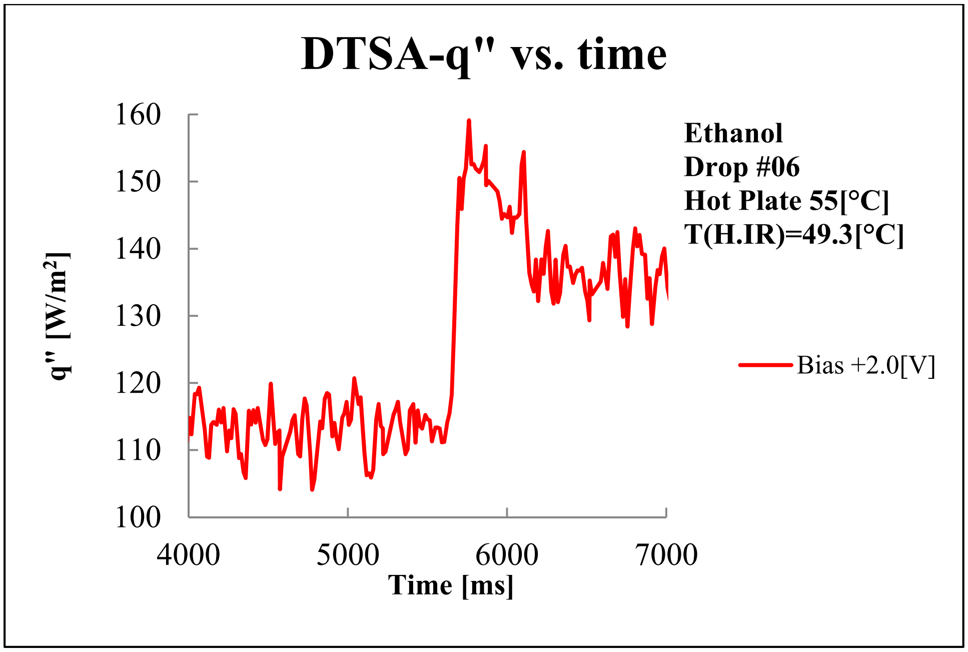
DTSA-q" vs. time
160
150
140
130
120
110
100
4000
5000
6000
7000
Time [ms]
q" [W/m²]
Ethanol
Drop #06
Hot Plate 55[°C]
T(H.IR)=49.3[°C]
Bias +2.0[V]

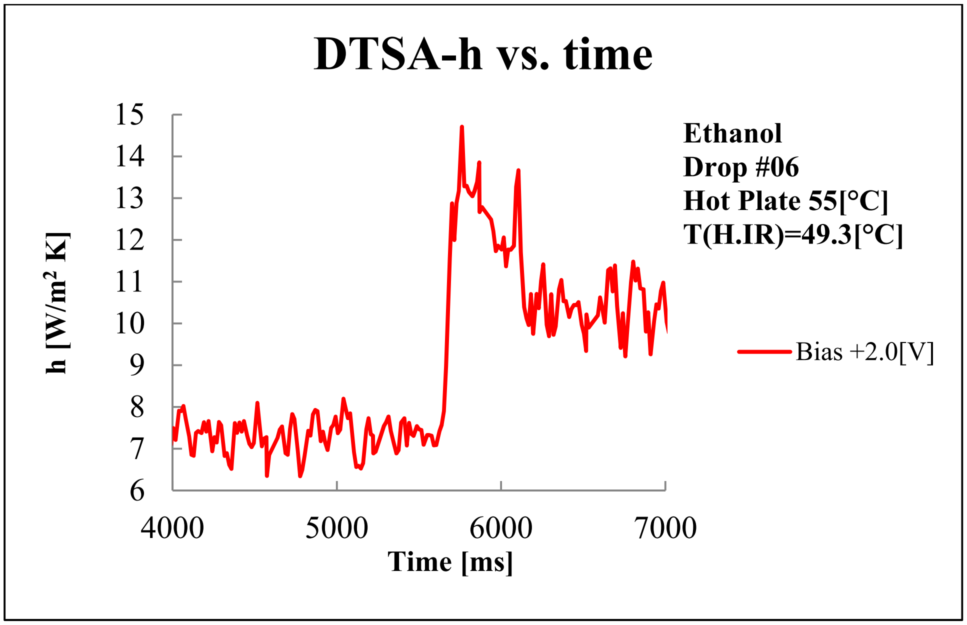
DTSA-h vs. time
15
14
13
12
11
10
9
8
7
6
4000
5000
6000
7000
Time [ms]
h [W/m² K]
Ethanol
Drop #06
Hot Plate 55[°C]
T(H.IR)=49.3[°C]
Bias +2.0[V]

Drop#08

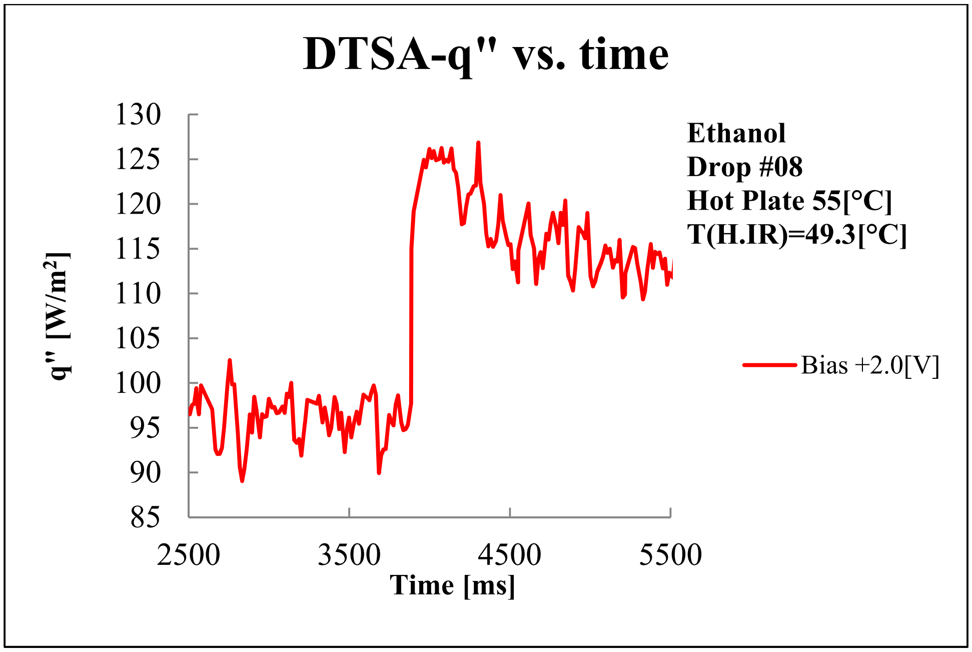
DTSA-q" vs. time
130
125
120
115
110
105
100
95
90
85
2500
3500
4500
5500
Time [ms]
q" [W/m²]
Ethanol
Drop #08
Hot Plate 55[°C]
T(H.IR)=49.3[°C]
Bias +2.0[V]

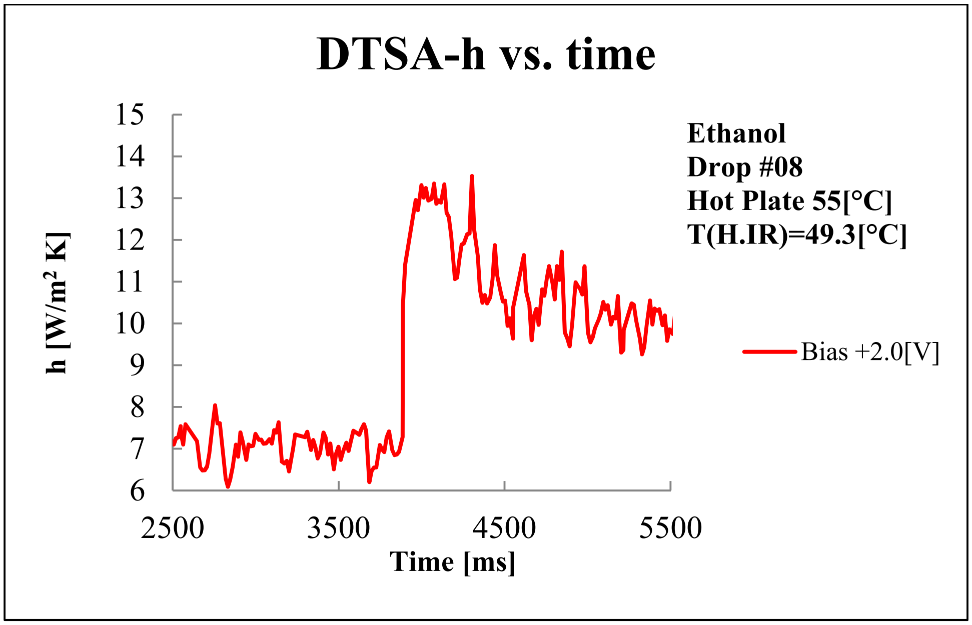
DTSA-h vs. time
15
14
13
12
11
10
9
8
7
6
2500
3500
4500
5500
Time [ms]
h [W/m² K]
Ethanol
Drop #08
Hot Plate 55[°C]
T(H.IR)=49.3[°C]
Bias +2.0[V]

Drop#09

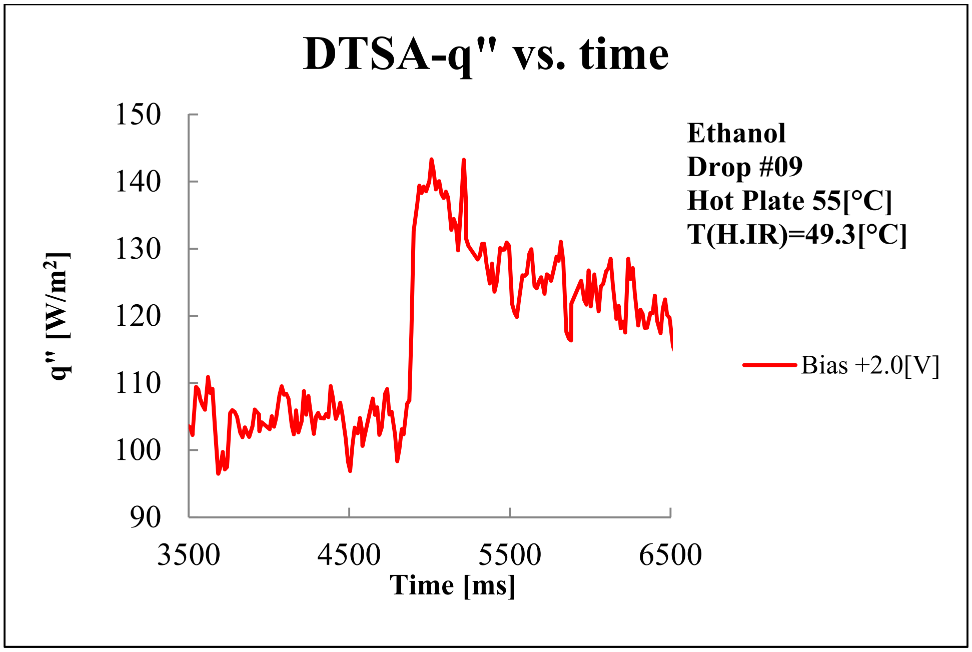
DTSA-q" vs. time
Ethanol
Drop #09
Hot Plate 55[°C]
T(H.IR)=49.3[°C]
q" [W/m^2]
150
140
130
120
110
100
90
3500
4500
5500
6500
Time [ms]
Bias +2.0[V]

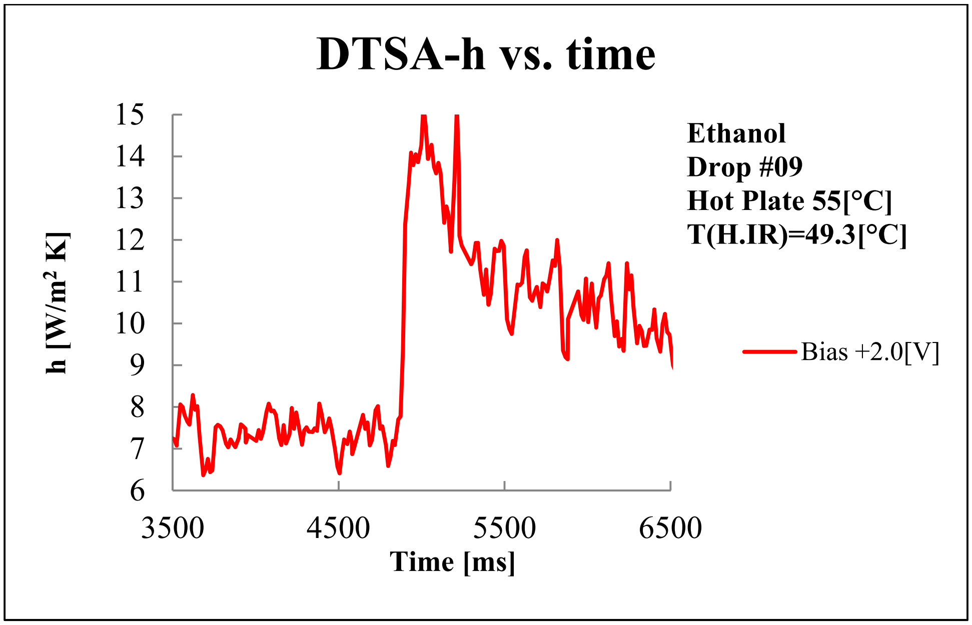
DTSA-h vs. time
Ethanol
Drop #09
Hot Plate 55[°C]
T(H.IR)=49.3[°C]
h [W/m^2 K]
15
14
13
12
11
10
9
8
7
6
3500
4500
5500
6500
Time [ms]
Bias +2.0[V]

Drop#10

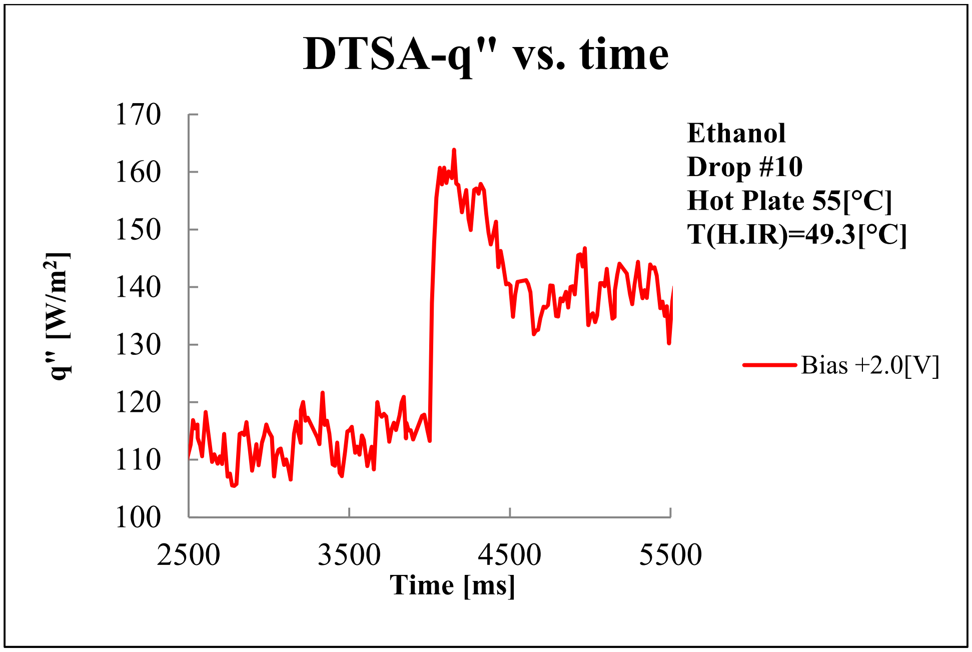
DTSA-q" vs. time
q" [W/m^2]
170
160
150
140
130
120
110
100
2500
3500
4500
5500
Time [ms]
Ethanol
Drop #10
Hot Plate 55[°C]
T(H.IR)=49.3[°C]
Bias +2.0[V]

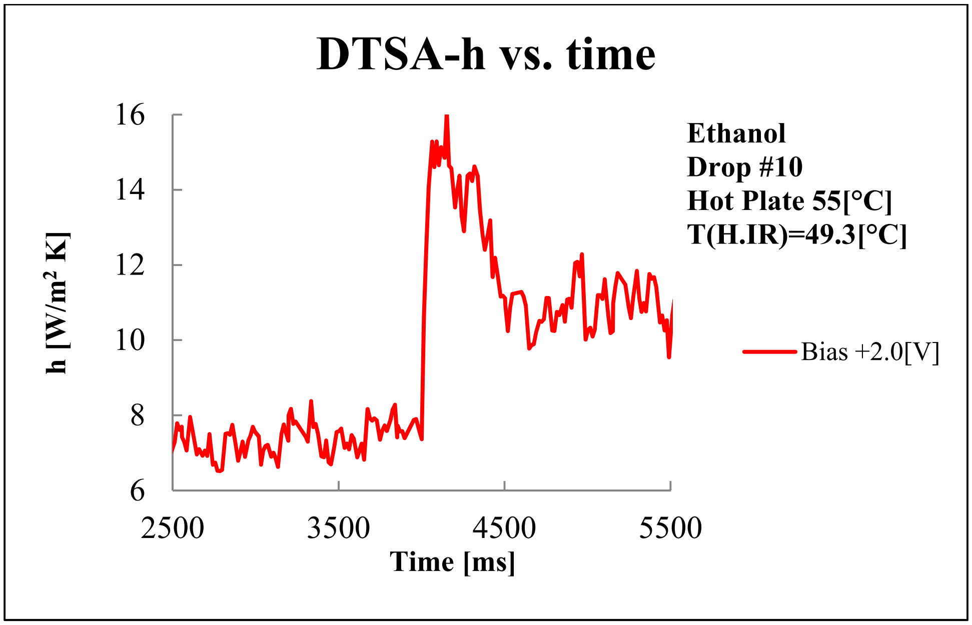
DTSA-h vs. time
h [W/m^2 K]
16
14
12
10
8
6
2500
3500
4500
5500
Time [ms]
Ethanol
Drop #10
Hot Plate 55[°C]
T(H.IR)=49.3[°C]
Bias +2.0[V]

6) Ethanol – 65, Drop#01

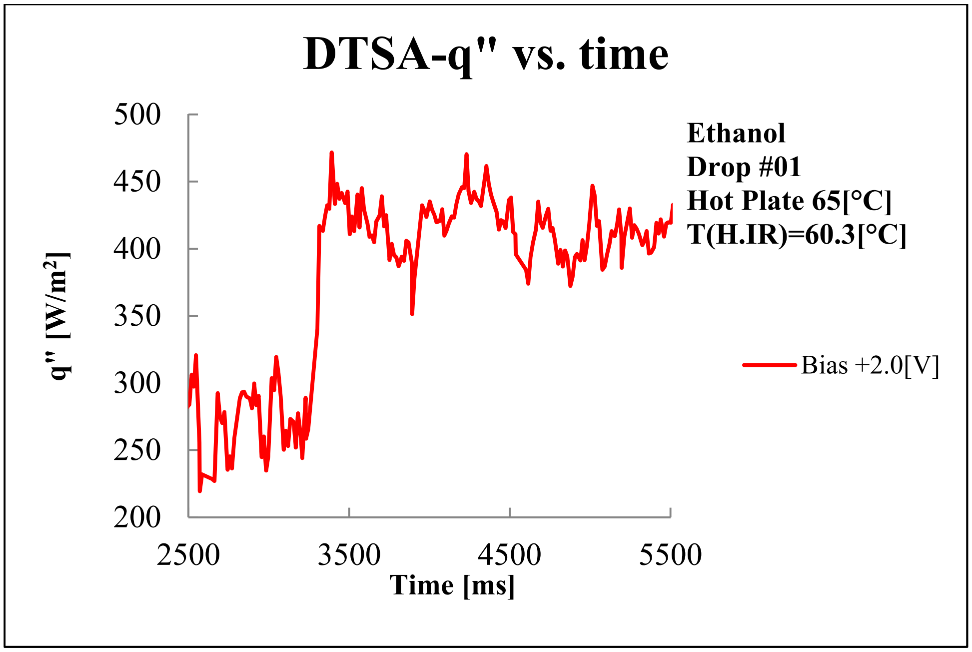

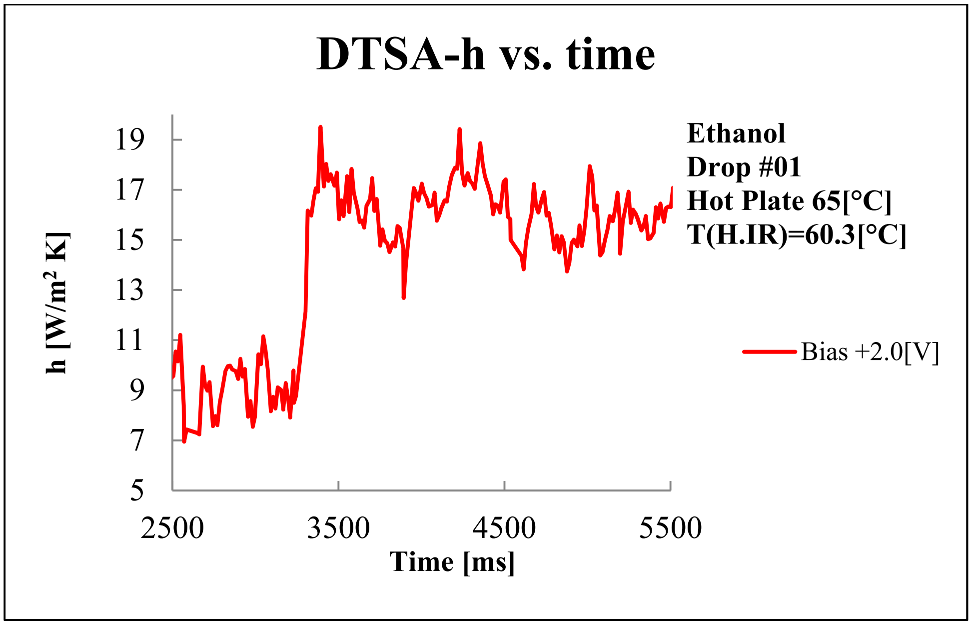

Drop#02

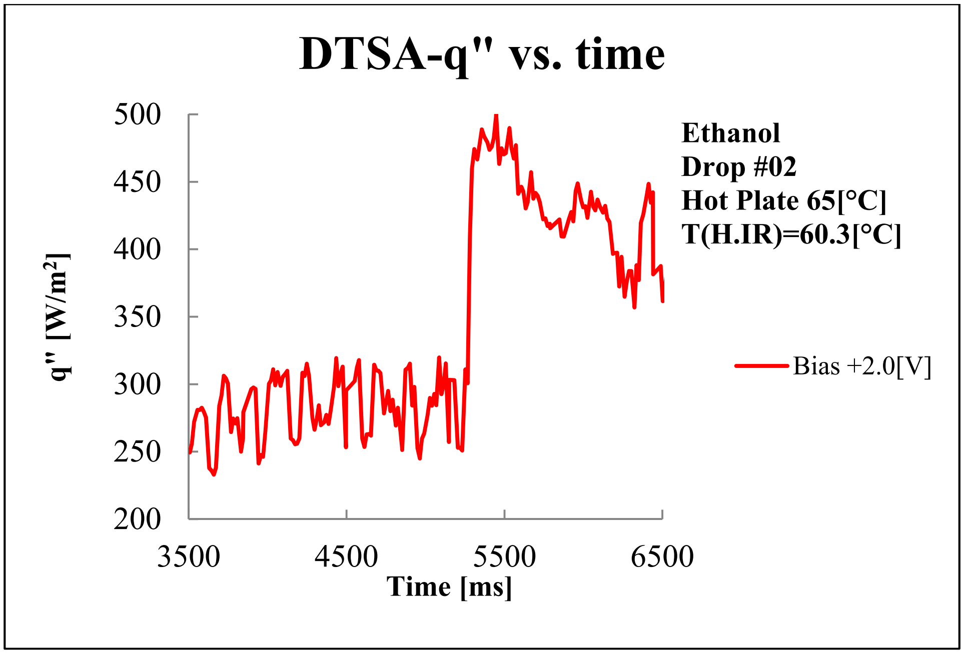
DTSA-q" vs. time
500
450
400
350
300
250
200
3500
4500
5500
6500
Time [ms]
q" [W/m²]
Ethanol
Drop #02
Hot Plate 65[°C]
T(H.IR)=60.3[°C]
Bias +2.0[V]

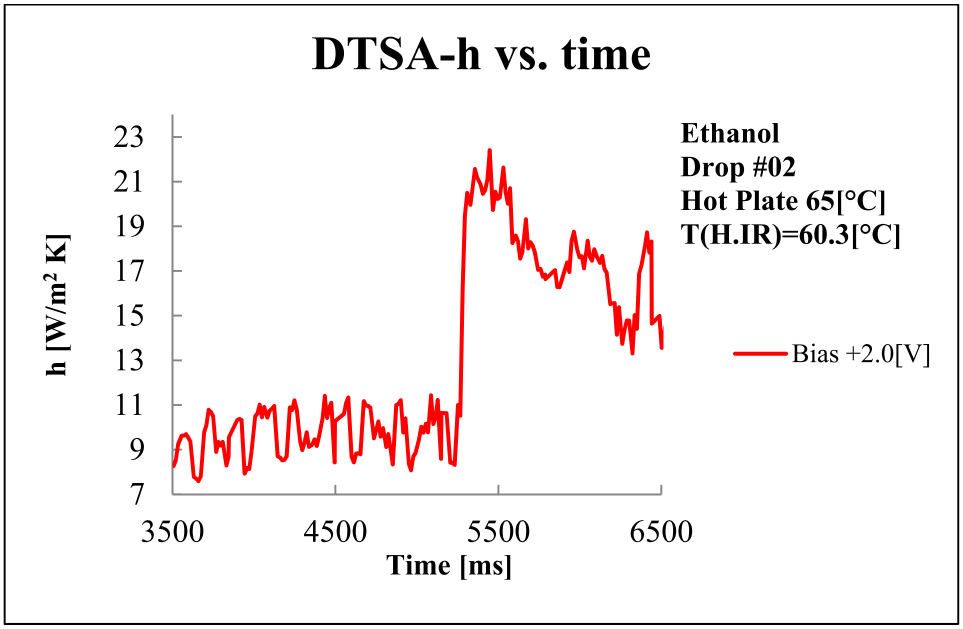
DTSA-h vs. time
23
21
19
17
15
13
11
9
7
3500
4500
5500
6500
Time [ms]
h [W/m² K]
Ethanol
Drop #02
Hot Plate 65[°C]
T(H.IR)=60.3[°C]
Bias +2.0[V]

Drop#03

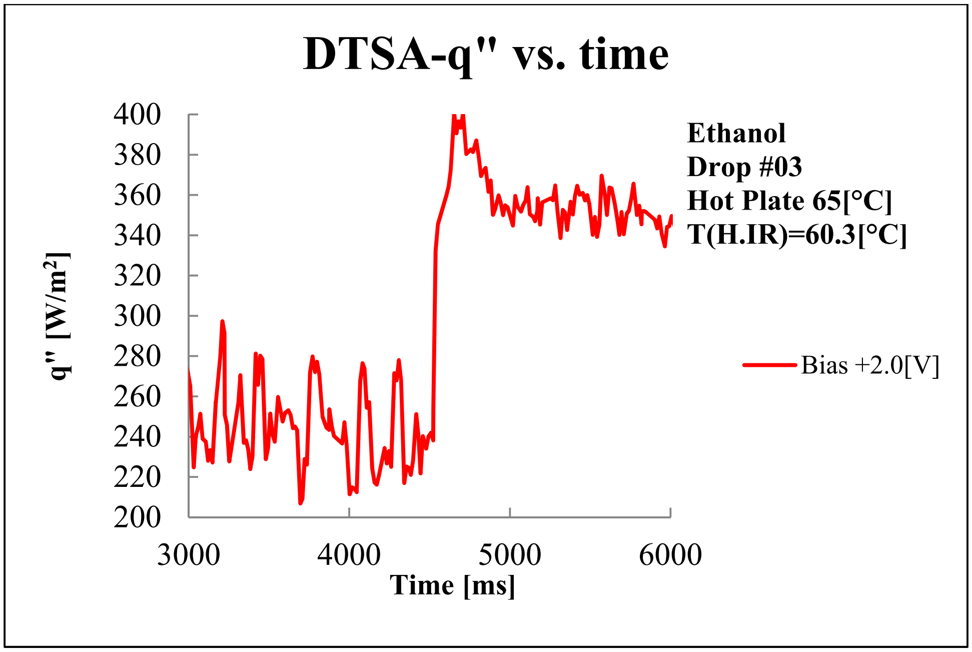
DTSA-q" vs. time
q" [W/m^2]
400
380
360
340
320
300
280
260
240
220
200
3000
4000
5000
6000
Time [ms]
Ethanol
Drop #03
Hot Plate 65[°C]
T(H.IR)=60.3[°C]
Bias +2.0[V]

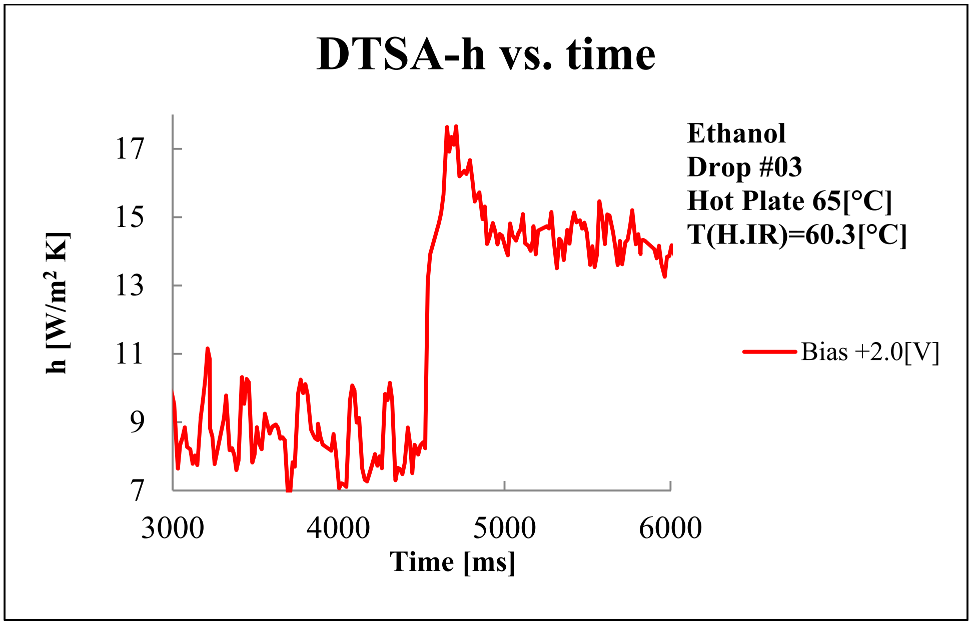
DTSA-h vs. time
h [W/m^2 K]
17
15
13
11
9
7
3000
4000
5000
6000
Time [ms]
Ethanol
Drop #03
Hot Plate 65[°C]
T(H.IR)=60.3[°C]
Bias +2.0[V]

Drop#04

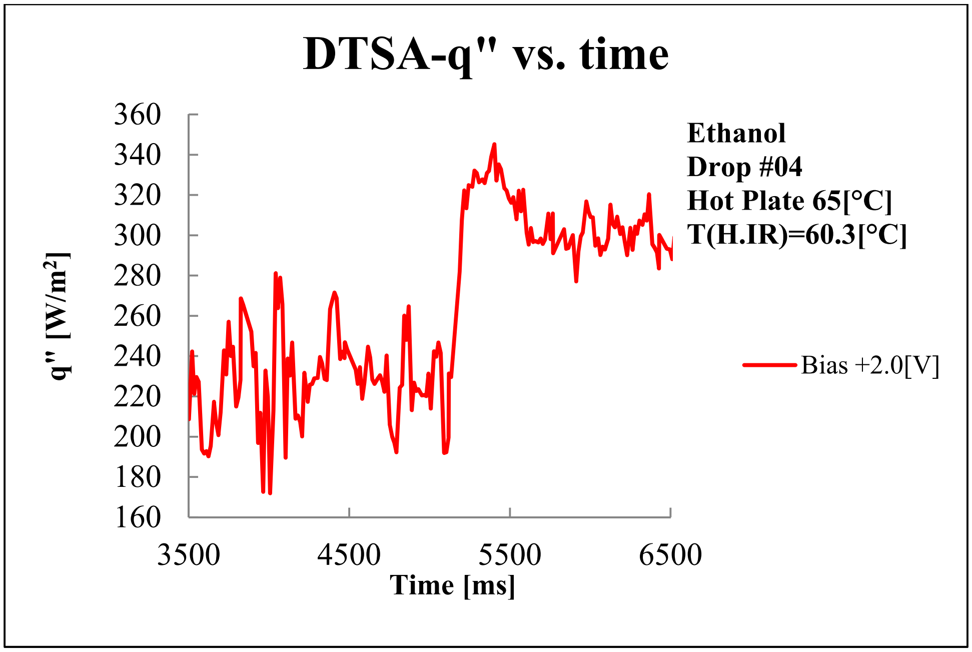
DTSA-q" vs. time
360
340
320
300
280
260
240
220
200
180
160
q" [W/m^2]
3500
4500
5500
6500
Time [ms]
Ethanol
Drop #04
Hot Plate 65[°C]
T(H.IR)=60.3[°C]
Bias +2.0[V]

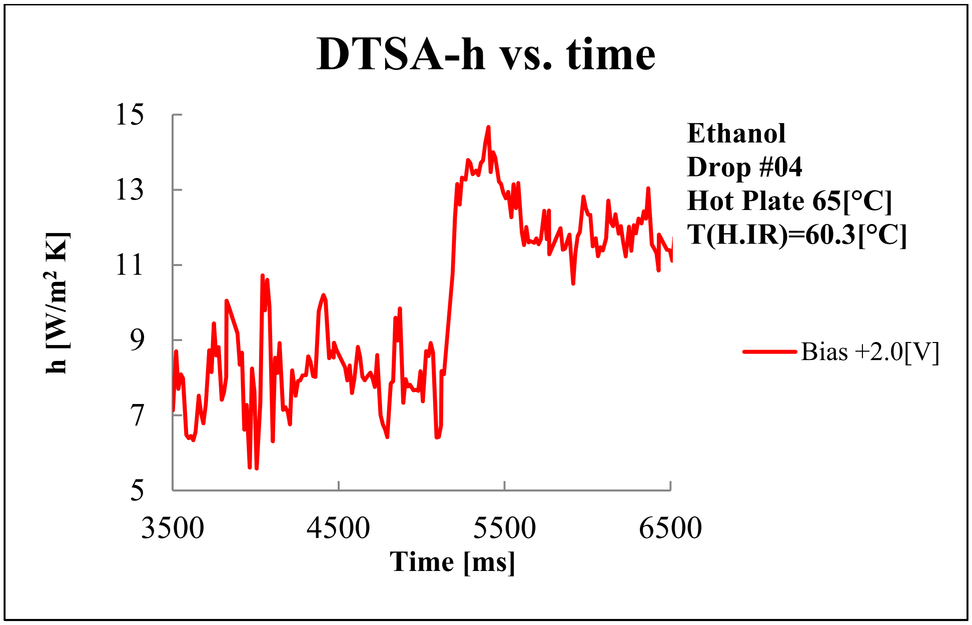
DTSA-h vs. time
15
13
11
9
7
5
h [W/m^2 K]
3500
4500
5500
6500
Time [ms]
Ethanol
Drop #04
Hot Plate 65[°C]
T(H.IR)=60.3[°C]
Bias +2.0[V]

Drop#06

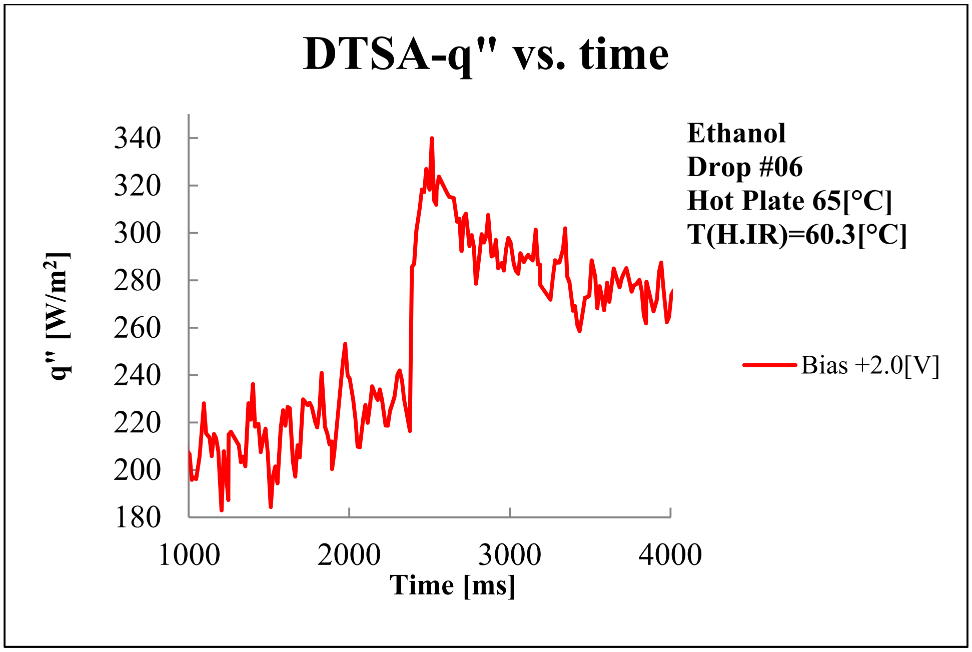
DTSA-q" vs. time
Ethanol
Drop #06
Hot Plate 65[°C]
T(H.IR)=60.3[°C]
q" [W/m²]
340
320
300
280
260
240
220
200
180
1000
2000
3000
4000
Time [ms]
Bias +2.0[V]

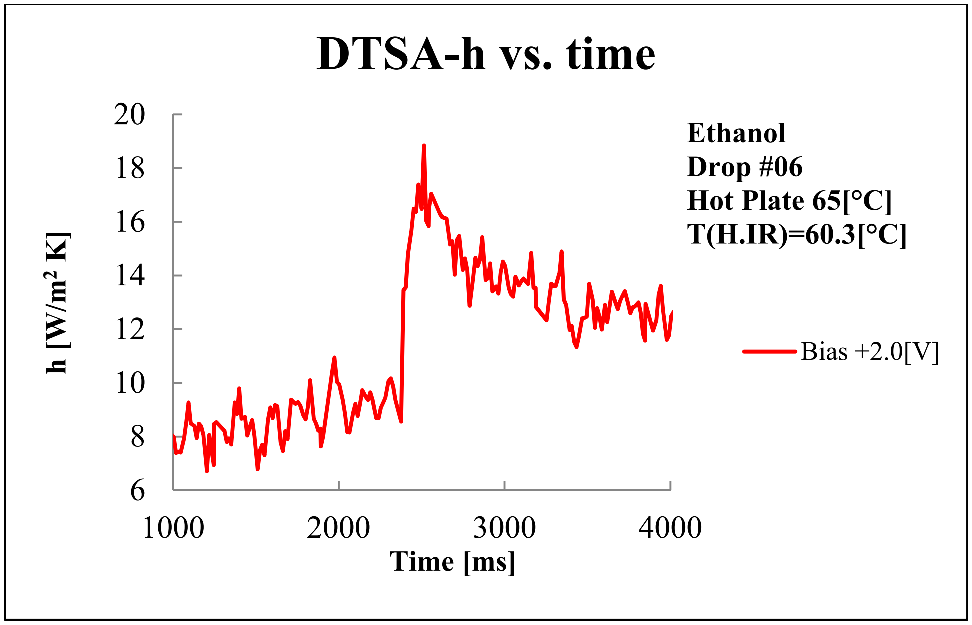
DTSA-h vs. time
Ethanol
Drop #06
Hot Plate 65[°C]
T(H.IR)=60.3[°C]
h [W/m² K]
20
18
16
14
12
10
8
6
1000
2000
3000
4000
Time [ms]
Bias +2.0[V]

Drop#07

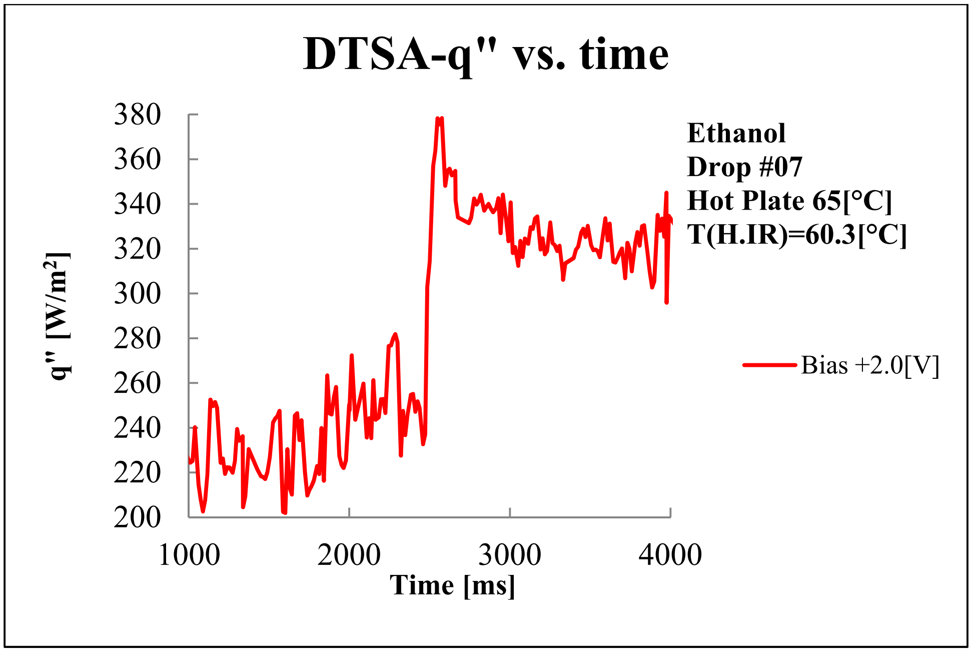
DTSA-q" vs. time
380
360
340
320
300
280
260
240
220
200
q" [W/m²]
1000
2000
3000
4000
Time [ms]
Ethanol
Drop #07
Hot Plate 65[°C]
T(H.IR)=60.3[°C]
Bias +2.0[V]

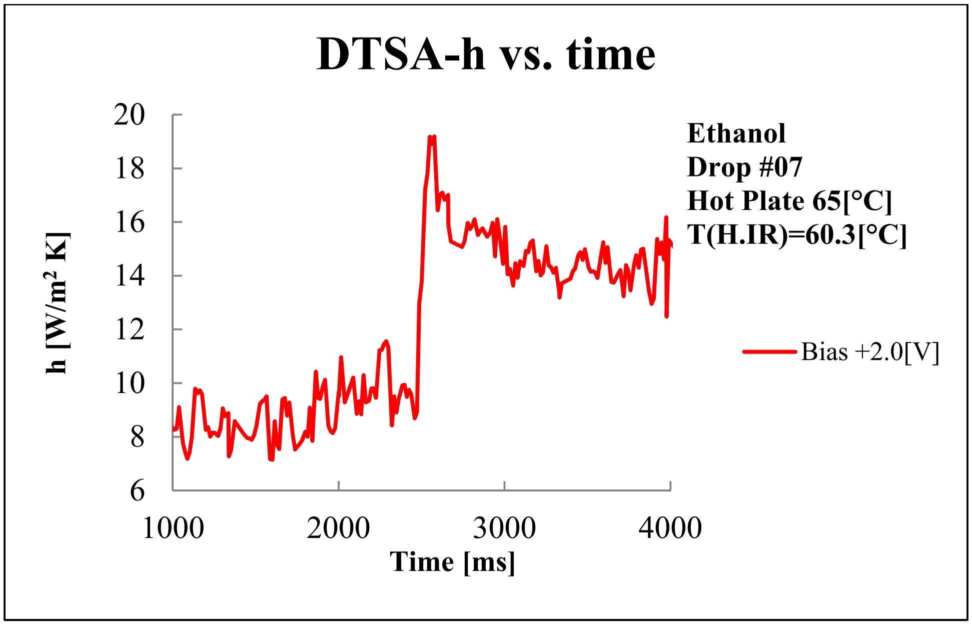
DTSA-h vs. time
20
18
16
14
12
10
8
6
h [W/m² K]
1000
2000
3000
4000
Time [ms]
Ethanol
Drop #07
Hot Plate 65[°C]
T(H.IR)=60.3[°C]
Bias +2.0[V]

Drop#08

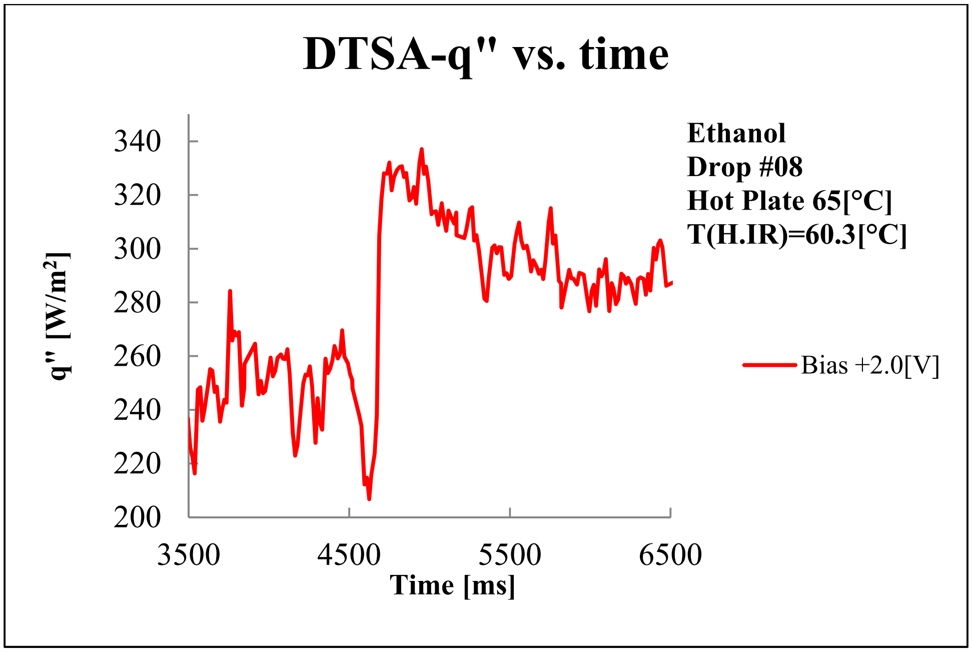
DTSA-q" vs. time
Ethanol
Drop #08
Hot Plate 65[°C]
T(H.IR)=60.3[°C]
q" [W/m2]
340
320
300
280
260
240
220
200
3500
4500
5500
6500
Time [ms]
Bias +2.0[V]

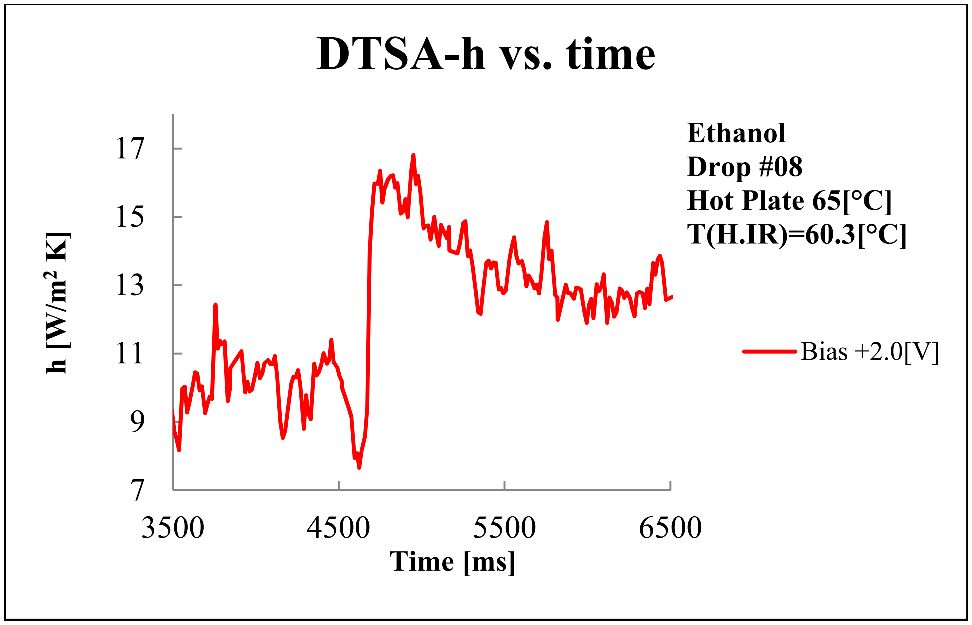
DTSA-h vs. time
Ethanol
Drop #08
Hot Plate 65[°C]
T(H.IR)=60.3[°C]
h [W/m2 K]
17
15
13
11
9
7
3500
4500
5500
6500
Time [ms]
Bias +2.0[V]

Drop#10

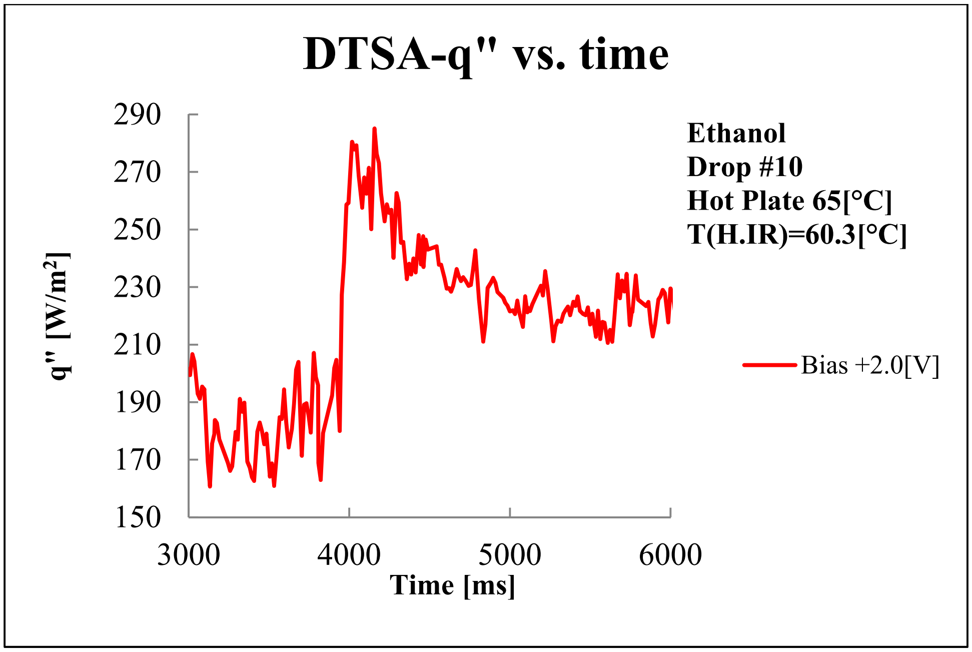
DTSA-q" vs. time
q" [W/m²]
290
270
250
230
210
190
170
150
3000
4000
5000
6000
Time [ms]
Ethanol
Drop #10
Hot Plate 65[°C]
T(H.IR)=60.3[°C]
Bias +2.0[V]

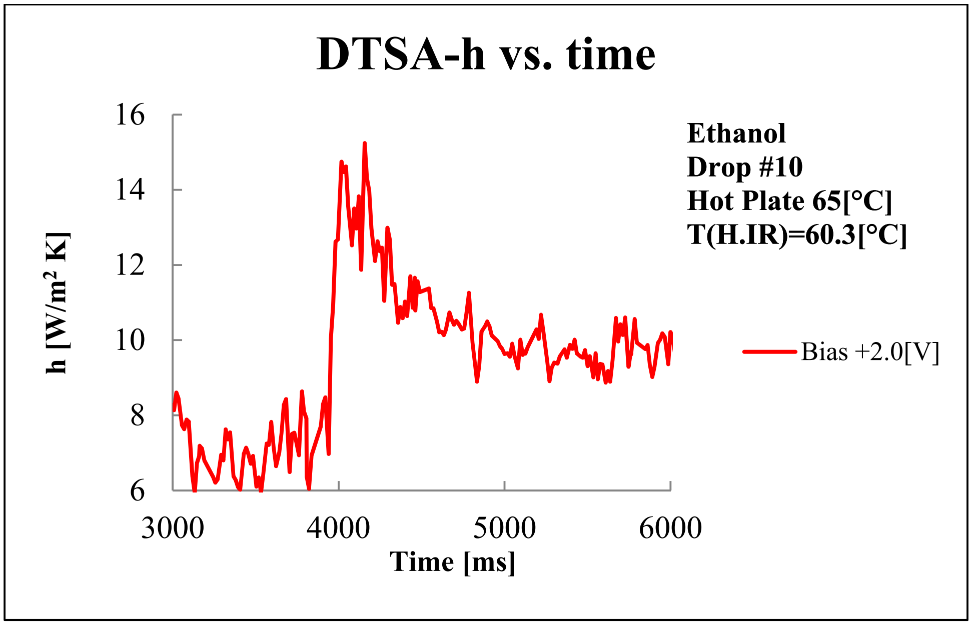
DTSA-h vs. time
h [W/m² K]
16
14
12
10
8
6
3000
4000
5000
6000
Time [ms]
Ethanol
Drop #10
Hot Plate 65[°C]
T(H.IR)=60.3[°C]
Bias +2.0[V]

APPENDIX D

DROPLET COOLING EXPERIMENT RESULTS USING TFT

(1) Hot Plate Indicator: 45°C, Sampling Rate: 6Hz

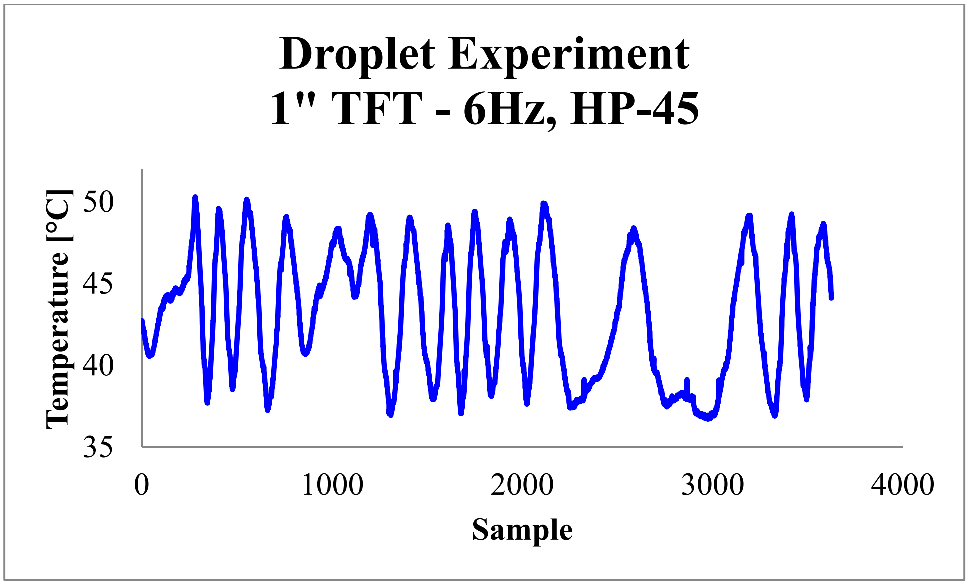

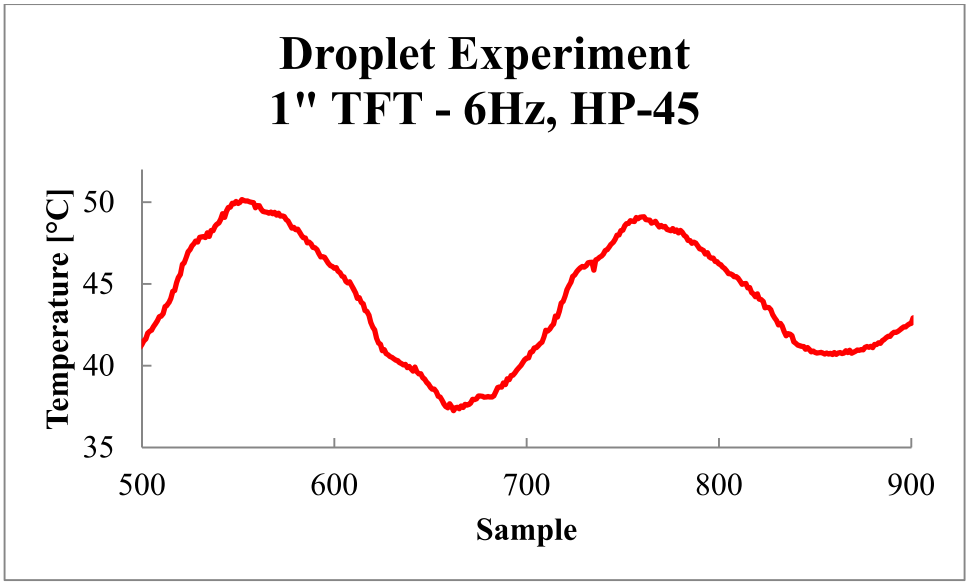

(2) Hot Plate Indicator: 45°C, Sampling Rate: 200Hz

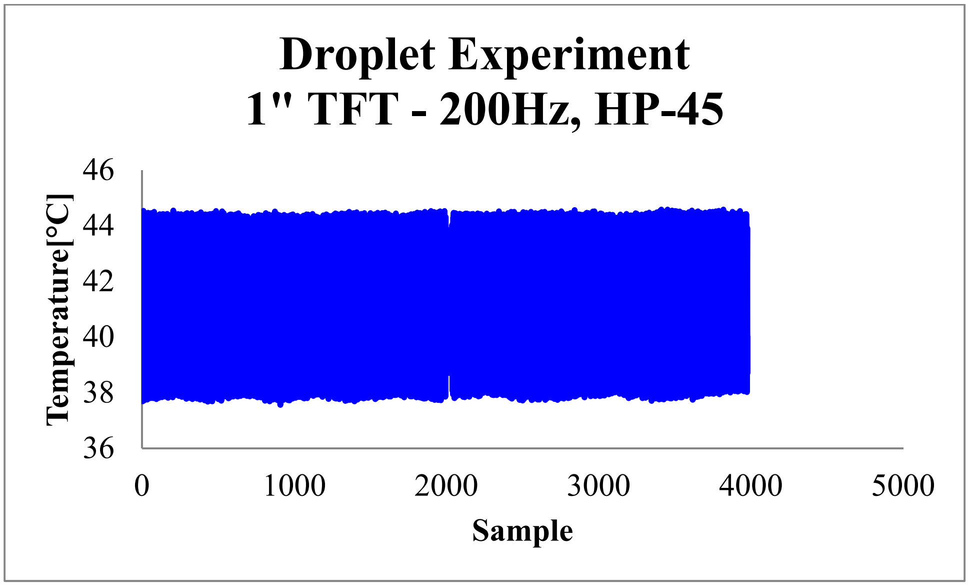

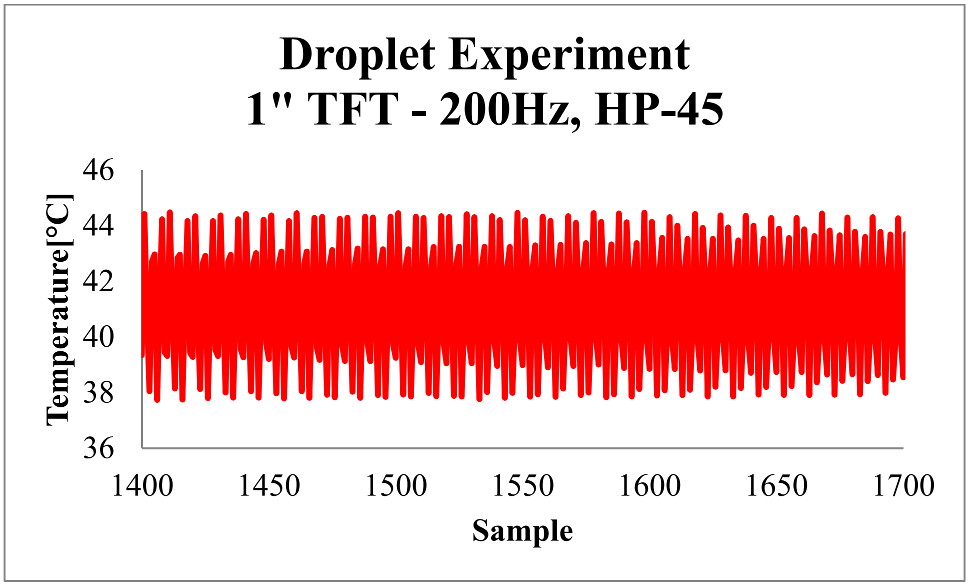

(3) Hot Plate Indicator: 60°C, Sampling Rate: 200Hz

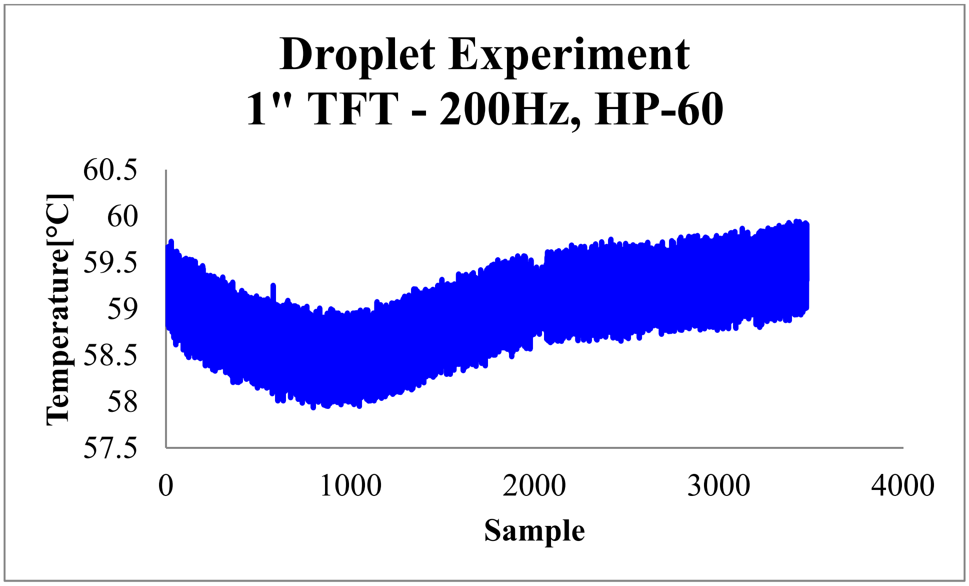

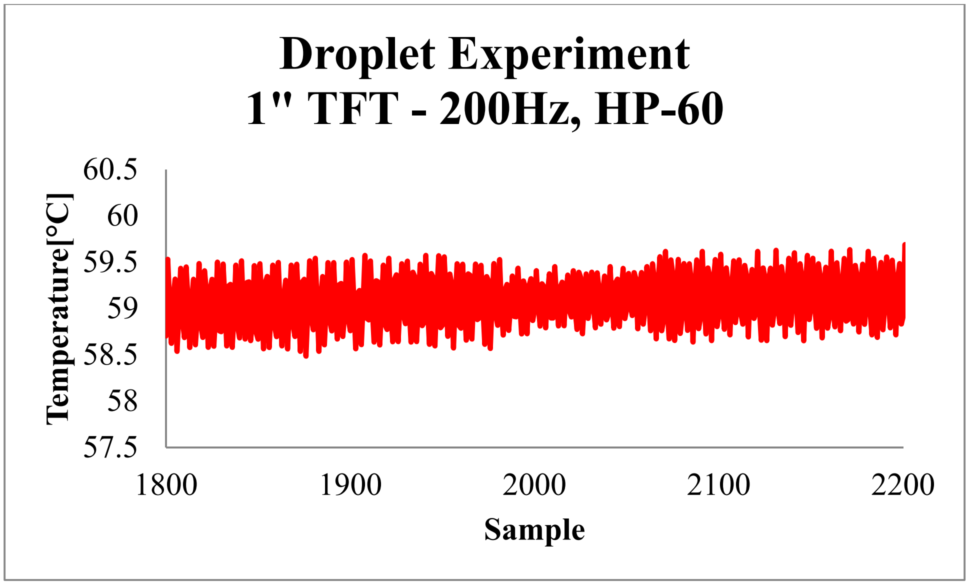

(4) Hot Plate Indicator: 70°C, Sampling Rate: 6Hz

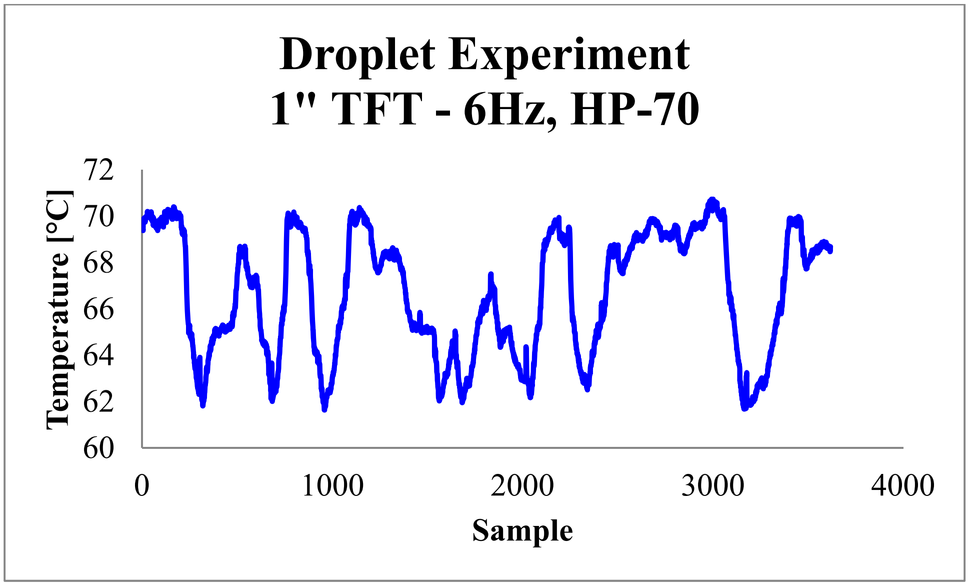

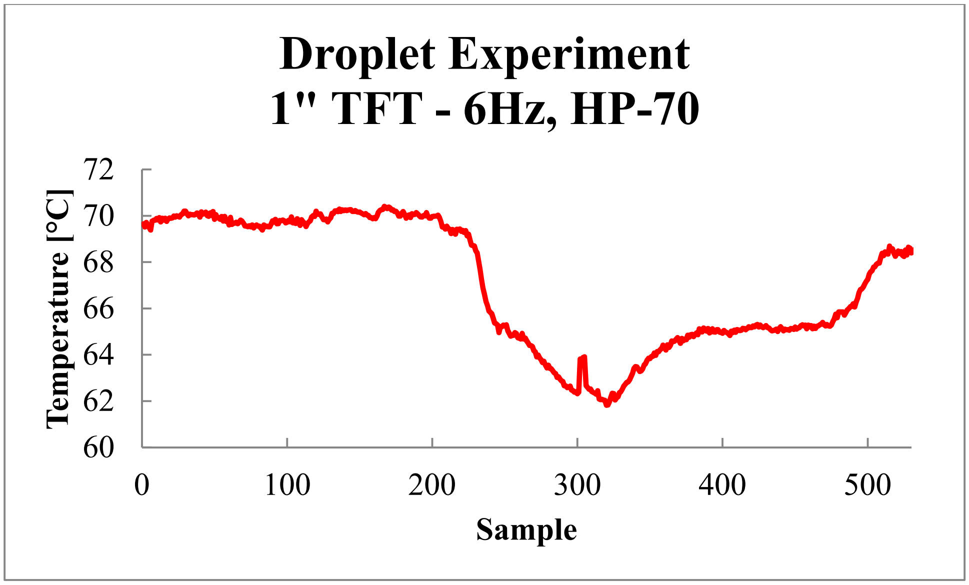

(5) Hot Plate Indicator: 80°C, Sampling Rate: 200Hz

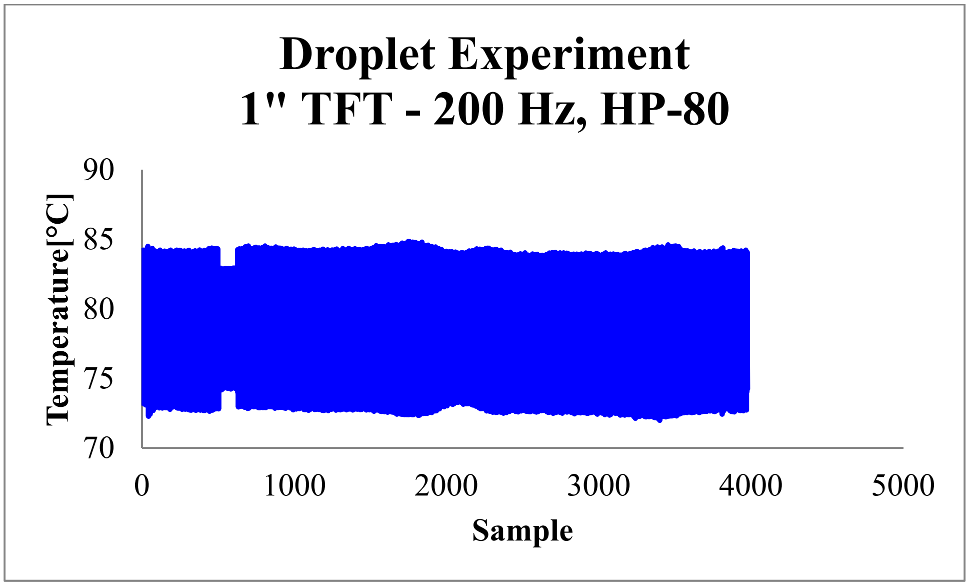

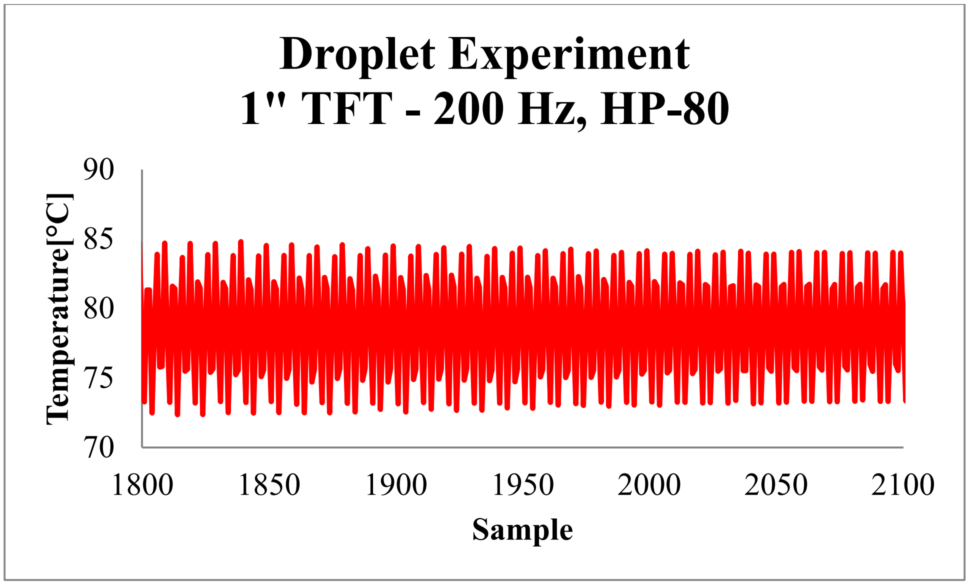

(6) Hot Plate Indicator: 90°C, Sampling Rate: 6Hz

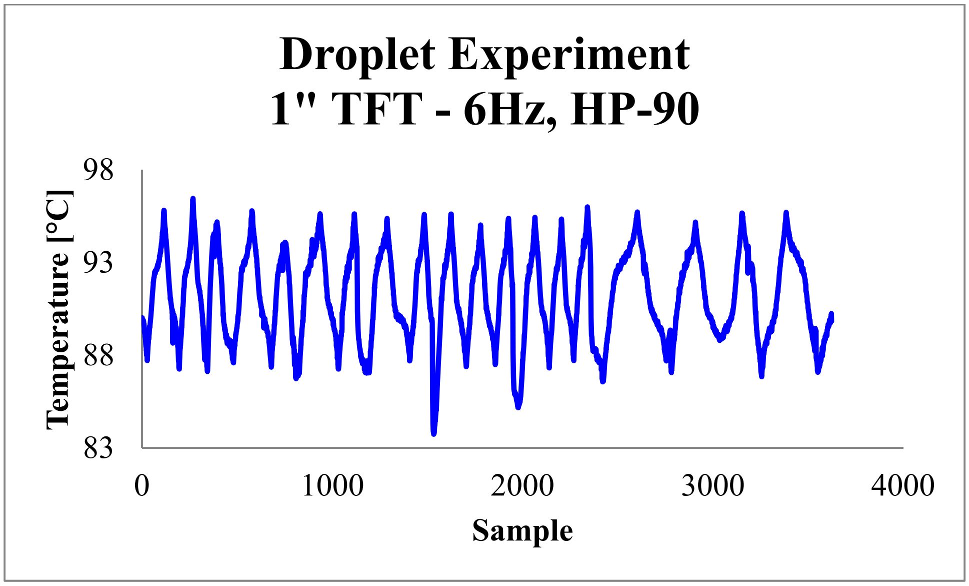

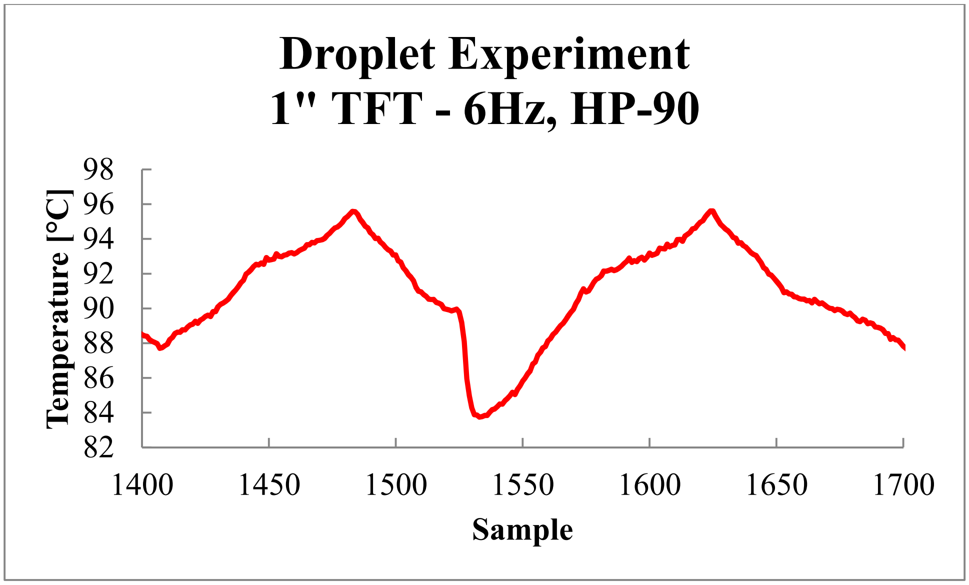

APPENDIX E

THE COMPACT CONDENSER EXPERIMENT (P-H DIAGRAM)

	Flat		Micropost	
	Average	stdev	Average	stdev
ΔP [kPa]	11.7 (1.07 psi)	0.15	81.5 (11.82 psi)	0.48
T_{sat4} - T_4 [K]	4.40	0.31	5.11	0.60
T_3-T_4 [K]	1.38	0.05	1.77	0.30
h [W/m^{2}K]	2672.6	241.2	3873.2	192.7

- Amount of refrigerant: 28.3 g (1.10 oz.)
- 45% enhancement in heat transfer coefficient when micropost is utilized.

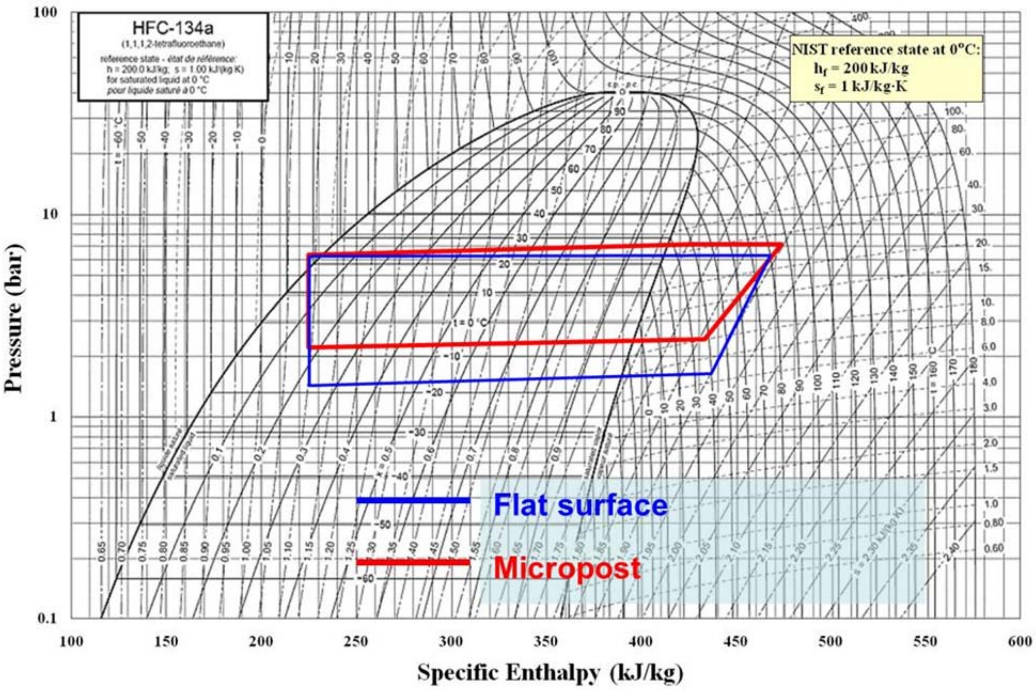

VITA

Sae Il Jeon received his Bachelor of Engineering degree in Mechanical Engineering and Design from Korea Aerospace University in 2002. He entered the Turbomachinery Laboratory at Seoul National University in March 2002 and received his Master of Science degree in February 2004. He worked for four years at Renault Samsung Motors with the Powertrain Design Team as an internal combustion engine component and system designer. In August 2008, he joined Texas A&M University to pursue a doctoral degree in College Station. He performed his research in the area of heat transfer and fluid dynamics for the flow boiling experiment, and as a sub-major expanded the research area for sensor fabrication collaboration with the electrical engineering department. He worked in the Multi-phase Flows and Heat Transfer Laboratory under the supervision of Dr. D. Banerjee in the Mechanical Engineering Department. He received his Ph.D degree in August 2011. His research interests include multi-phase flows and heat transfer on nano-structured surfaces using nano-sensors. He plans to expand the research in these topics, focusing on the industrial applications of these techniques. Sae Il is currently employed at Volvo Technologies. His current address is: 3123, TAMU, Department of Mechanical Engineering, College Station, TX 77843.